RESPONSIVE POLYMER-BASED COLLOIDS FOR DRUG DELIVERY AND BIOCONVERSION

A Dissertation
Submitted to the Graduate Faculty
of the
North Dakota State University
of Agriculture and Applied Science

By

Olena Kudina

In Partial Fulfillment
for the Degree of
DOCTOR OF PHILOSOPHY

Major Department:
Coatings and Polymeric Materials

July 2014

Fargo, North Dakota

North Dakota State University
Graduate School

Title
RESPONSIVE POLYMER-BASED COLLOIDS FOR DRUG DELIVERY AND BIOCONVERSION

By

Olena Kudina

The Supervisory Committee certifies that this ***disquisition*** complies with North Dakota State University's regulations and meets the accepted standards for the degree of

DOCTOR OF PHILOSOPHY

SUPERVISORY COMMITTEE:

Dr. Andriy Voronov
Chair

Dr. Dean Webster

Dr. Stuart Croll

Dr. Scott Pryor

Approved:

July 3, 2014	Dr. Dean Webster
Date	Department Chair

ABSTRACT

Responsive polymer-based colloids (RPBC) are the colloidal structures containing responsive polymeric component which is able to adapt its physico-chemical properties to the environment by undergoing chemical and/or conformational changes.

The goal of the dissertation is to develop and characterize several groups of RPBC with different morphological complexity and explore their potential in drug delivery and bioconversion. The role of RPBC morphology for these specific applications is discussed in details. Three groups of RPBC were fabricated: i. polymeric micelles; ii. mixed polymeric micelles; iii. hybrid polymer-inorganic particles. All fabricated RPBCs contain polymeric component in their structure. The dissertation investigates how the changes of the responsive polymeric component properties are reflected in morphologies of RPBC.

The first group of RPBC, polymeric micelles, was formed by the self-assembly of amphiphilic invertible polymers (AIPs) synthesized in our group. AIPs self-assemble into invertible micellar assemblies (IMAs) in solvents of different polarity. In this work, IMAs ability to invert the structure as a response to the change in solvent polarity was demonstrated using ^{1}H NMR spectroscopy and SANS. It was shown that the IMAs incorporate hydrophobic cargo either in the core or in the shell, depending on the chemical structure of cargo molecules. Following in vitro study demonstrates that loaded with drug (curcumin) IMAs are cytotoxic to osteosarcoma cells.

Mixed polymeric micelles represent another, more complex, RPBC morphologies studied in the dissertation. Mixed micelles were fabricated from AIPs and amphiphilic oligomers synthesized from pyromellitic dianhydride, polyethylene glycol methyl ethers, and alkanols/cholesterol. The combination of selected AIP and oligomers based on cholesterol results in mixed micelles with an increased drug-loading capacity (from 10% w/w loaded curcumin in single component IMAs to 26%w/w in mixed micelles).

Even more complex colloids are hybrid polymer-inorganic particles, the third RPBC group studied in dissertation. Material was designed as core–shell particles with superparamagnetic core engulfed by grafted polymer brushes. These particles were loaded with enzymes (cellulases), thus, are turned into enzymogels for cellulose bioconversion. The study demonstrates that such RPBCs can be used multiple times during hydrolysis and provide an about four-fold increase in glucose production in comparison to free enzymes.

ACKNOWLEDGEMENTS

I would like to express my heartfelt gratitude to my supervisor Professor Dr. Andriy Voronov. I could not have asked for better role model: inspirational, supportive, and patient.

I would also like to thank my Examination Committee Members, Professor Stuart Croll, Professor Scott Pryor and Professor Dean Webster for the assistance they provided at all levels of my graduate research. Also, I would like to thank Dr. Victoria Gelling, former Member of my Examination Committee for encouraging and constructive feedback.

My sincere gratitude goes to current and former members of Dr. Voronov's team: Dr. Ihor Tarnavchyk, Dr. Ivan Hevus, Dr. Ananiy Kohut for help and support with experiment setup and data interpretation. I appreciate the valuable help from Andriy Popadyuk and Oksana Zholobko for their assistance with some of the experiments. Especial thanks to the students I had an honor to supervise over the years: Gina Weiss and Mugienkeun Oh during their undergraduate studies; Brielle Van Orman, Melissa Fritz and Derek J Lehmann during Governor's Schools program.

Very special thanks goes to our collaborators – Power Professor Dr. Sergiy Minko (The University of Georgia, Athens, GA, USA), Dr. Leonind Ionov (Institute of Polymer Research, Dresden. Germany) and members of Dr. Pryor's group: at Nurun Nahar, Ashani Samaratunga and Dr. Bishnu Karki for working with our group on the enzymogels, for their support, guidance and helpful suggestions.

I wish to thank our collaborators from Mayo Clinic for wonderful time I spent there as a Research Trainee. Also, I would like to acknowledge Dr. Avudaiappan Maran, Kris Shogren and James Herrick for all the help and support during my stay in Rochester.

Separate gratitude goes to Oak Ridge National Laboratory and Tennessee EPSCoR for granting us beamtime to conduct neutron scattering experiments and for funding our travel to Oak Ridge. I would like to acknowledge Dr. Yuri Melnichenko and Lilin He for help and on-site assistance when working on CG-2 (HFIR) and Dr. William Heller, Changwoo Do and Carrie Gao for helping us on BL-6 EQ SANS (SNS).

I thank Shane Stafslien and Justin Daniels for the help with fluorescent microscopy experiments at CNSE (NDSU).

I wish to thank Dr. Angel Ugrinov and Dr. John Bagu for their assistance on using instruments at the Department of Chemistry and Biochemistry.

I would like to offer my greatest appreciation for faculty, staff and fellow students in Coatings and Polymeric Materials Department for wonderful and friendly atmosphere all these years.

I would also like to thank my grandmother Alla Sylantjeva for all the support and encouragement she gave me through the good and bad times.

And finally I wish to thank to all my dear friends, especially Zoja Majorova and Daria Moshkovskaya, for proofreading my dissertation and being there for me in so many ways.

DEDICATION

I dedicate my dissertation work to my family and dear friends.

I would never have been able to complete this journey without you support. I really am grateful for being there for me and many hours spent helping me with proofreading.

TABLE OF CONTENTS

CHAPTER 7. HIGHLY EFFICIENT PHASE BOUNDARY BIOCATALYSIS WITH ENZYMOGEL NANOPARTICLES……………………………………………………...142

LIST OF TABLES

LIST OF FIGURES

LIST OF SCHEMES

LIST OF ABBREVIATIONS

AFM	Atomic Force Microscopy
AIPs	Amphiphilic Invertible Polymers
ATRP	Atom-Transfer Radical-Polymerization
BSA	Bovine Serum Albumin
CEL	Cellulase Enzymes
Chol	Cholesterol
CMC	Critical Micelle Concentration
CPPPC	Chol-PMDA-PEG-PMDA-Chol Oligomer
DBP	Dibutyl Phthalate
DEPA	Diesters of Pyromellitic Acid
DLS	Dynamic Light Scattering
DMEM	Dulbecco's Modified Eagle Medium
FTIR	Fourier Transform Infrared Spectroscopy
DMFA	Dimethylformamide
FDP	Fractal Dimension Parameter
HBSS	Hank's Balanced Salt Solution
HLB	Hydrophilic-Lipophilic Balance
IMAs	Invertible Micellar Assemblies
KFRO	Kinetic Fractal Rate Order
LA	Lactic Acid
MEK	Methyl Ethyl Ketone

Mn	Number Average Molecular Weight
Mw	Weight Average Molecular Weight
NMR	Nuclear Magnetic Resonance
NOESY	Nuclear Overhauser Effect Spectroscopy
P2VP	Poly(2-Vinylpyridine)
PA	Poly(Amide)
PAA	Poly(Acrylic Acid)
PDI	Polydispersity Index
PDMS	Poly(Dimethylsiloxane)
PDMA	Pyromellitic Dianhydride
PEG	Poly(Ethylene Glycol)
PEO	Poly(Ethylene Oxide)
PHEMA	Poly(Hydroxyethylmethacrylate)
PMAA	Poly(Methacrylic Acid)
PPC	PEG-PMDA-Chol Oligomer
PPPHM	Poly(6-[4-(4-Pyridylazo)Phenoxy]Hexyl Methacrylate)
PS	Poly(Styrene)
PTHF	Poly(Tetrahydrofuran)
RPBC	Responsive Polymer-Based Colloids
SANS	Small Angle Neutron Scattering
SEM	Scanning Electron Microscopy
SLD	Scattering Length Density
SRB	Sudan Red B

TEA……………………………......Triethylamine

TEM…………………………......Transmission Electron Microscopy

UV-vis……………………………...Ultraviolet–Visible Spectroscopy

CHAPTER 1. INTRODUCTION: RESPONSIVE NANOSTRUCTURED POLYMER COLLOIDS

1.1. Introduction to Responsive Nanostructured Polymer-Based Colloids

Responsive polymer-based colloids (RPBC) are the colloidal structures containing responsive polymeric component which is able to adapt its physico-chemical properties to the environment by undergoing chemical and/or conformational changes.

The rapid development of responsive polymer-based colloids (RPBC) emerged from the combination of colloid and polymer science as a result of accumulated knowledge on the colloidal behavior of polymeric materials. RPBC are able to adjust to surrounding media by undergoing chemical and conformational changes [1-3]. Increase of complexity in the developed RPBC will result in broad variety of multifunctional polymer-based systems designed for important technological applications. Responsive behavior of polymer-based colloids is used to change wettability and adhesion of materials, convert chemical/biochemical signals into optical, electrical and even mechanical response and vice versa [2-3]. RPBC find numerous applications in stabilization, destabilization, inversion of colloidal systems, catalysis, sensors, drug delivery systems, etc. [1-3].

The stimuli-responsive behavior of RPBC can be considered as a sequence of events: reception of external signal (driving force), related chemical or physical changes in RPBC and transduction of the RPBC changes into significant event on micro/macroscopical scale [1, 3].

Reception of external stimuli is based on physical or chemical interactions between polymer functional groups and respective stimuli [4-7]. For example, multiple studies reported on the specific chemical interactions between functional groups of RPBC and biologically active molecules such as DNA [8-9], enzymes [10-11], antibodies [12] and other biologically active species [13-16]. Another example is pH-triggered conformation changes of PE chains pronounced as coil-to-globule transitions [17-18].

In most cases the reception of external signal would result in changes in chemical structure and/or interactions of RPBC with environment. Often such changes are followed by conformational changes of polymers resulting in phase transitions [1, 3, and 4]. These changes ultimately result in reversible or irreversible changes of a variety of material properties: mechanical, optical, surface properties, permeability, charge, etc. Engineering of combination of response and external stimuli on all stages can program the RPBC system for the specific application. RPBC materials are used in a diverse range of applications: intelligent drug delivery [19-20], removal of toxins [20], diagnostics [19], cell and tissue engineering [21], optical systems [1-5], biosensors [1-2], intelligent catalysis [22-23], personal care [1-2], coatings [24], microelectronics [1-5], textiles [1-3], etc [1-5].

1.2. Types of Responsive Nanostructured Polymeric Colloids

The RPBC are typically core-shell structures formed through self-assembly of amphiphilic copolymers or through surface modification of particles of organic, inorganic or hybrid nature with functional polymers (Fig.1.1 a-d) [1-3].

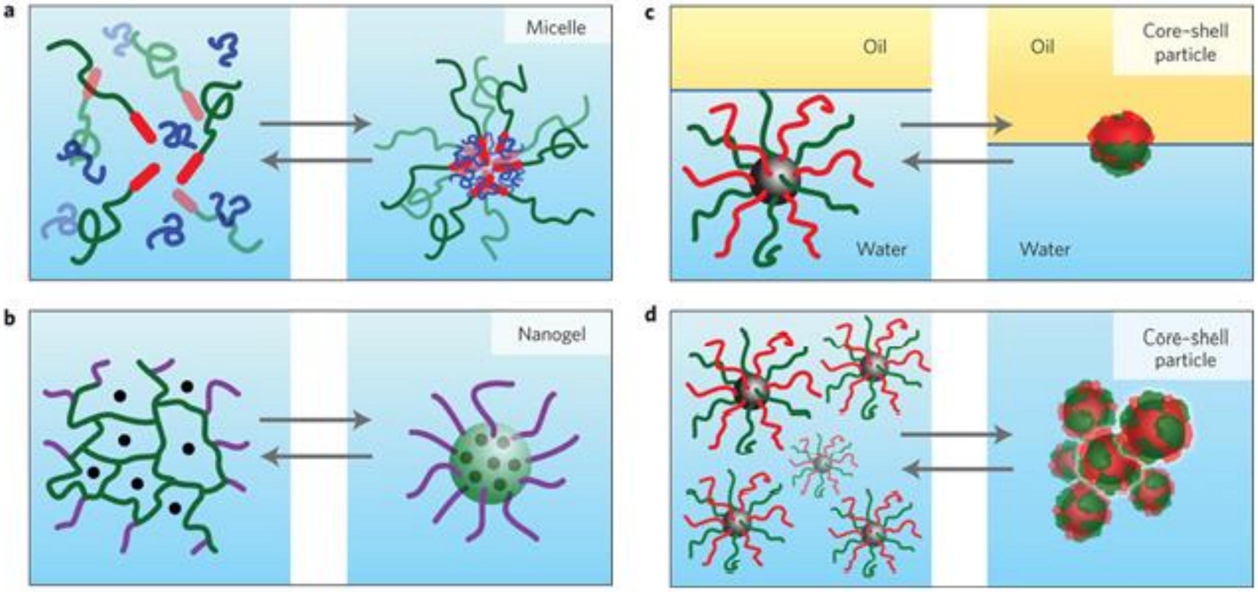

Fig.1.1. Examples of responsive nanostructured polymeric colloids (Reproduced from [25]). Reversible responses from different polymer-based systems a – self-assembly of polymer macrochains into responsive micelles, b – formation of responsive nanogels in highly cross-linked systems, c – formation of responsive core-shell Janus particles at the interphase, d – formation of responsive core-shell particles in solution.

In RPBC the polymeric component is associated with the responsive behavior. One or several responsive polymeric components can be localized in the core, shell or in both. External stimuli can induce the response in these components leading to degradation, aggregation, swelling and/or adsorption of RPBC [1-5]. The major types of RPBC such as block copolymer self-assemblies, polymersomes, nanogels, mixed micelles, hybrid materials, etc. are discussed below.

Block copolymers are among the most commonly used types of polymers for RPBC fabrication [26-27]. Such copolymers have been reported to form a variety of self-assembled structures: from micelles with different shape and size to continuous bilayers, depending on the interactions of their constituent fragments with the solvent [1-2, 28]. External stimuli may trigger the changes of block copolymer self-assemblies size, architecture and/or composition [5]. For example the transition of self-assemblies from spherical to cylindrical architectures (i.e. sphereto-rod transitions) may occur, accompanied by the interchange of blocks between the core and the corona of self-assemblies [1-4, 28].

Polymer vesicles or polymersomes are another interesting example of self-assembled RPBC [29]. Polymersomes are structures resembling liposomes, with internal compartment containing aqueous media being surrounded by amphiphilic copolymer shell (Fig.1.2) [1, 29-30]. Similarly to the liposome membrane, polymersome shell components regulate the permeability of the shell by controlling the transport of molecules in and out of polymersome [29-30]. The responsive behavior of shell components provides the possibility to tune the permeability of the polymersome [30]. Moreover, the shells of polymersomes can be designed to degrade upon external stimuli [29-31]. The presence of pH-responsive fragments in copolymers forming the polymersome renders the capability of polymersome's shell to transport hydrophilic molecules, thus resembling the transmembrane ion channel in the membranes of living cells [31].

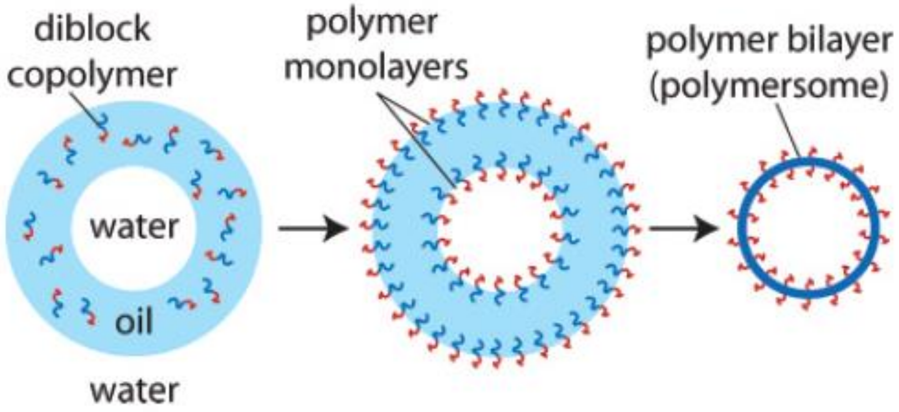

Fig.1.2. Polymersome formation (Reproduced from [31]).

Nanogels are nanoparticles with internal network structure composed of hydrophobic or amphiphilic polymer chains (Fig.1.3) [32]. Nanogels were developed as carriers for drug delivery, and hence can incorporate a variety of cargos, including biologically active molecules, genes, synthetic drug candidates, etc. [32-35] The incorporation of the cargo is carried out through the formation of salt bonds, hydrogen bonds, or hydrophobic interactions [33]. Due to high crosslink density nanogels were reported to resemble the properties of hydrogels – i.e. swelling, degradation, and chemical functionality [31-33]. Responsive nanogels can be designed to reversibly respond to several external stimuli: e.g. temperature and redox-potential [34].

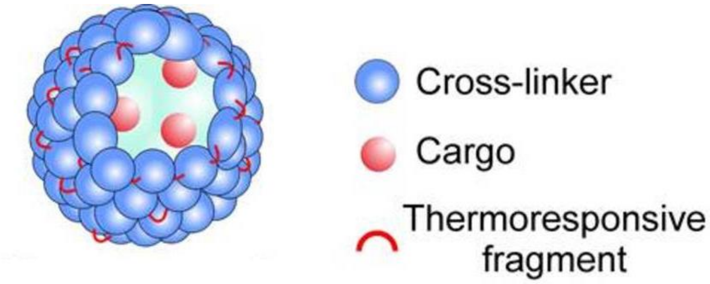

Fig.1.3. Thermosensitive nanogel scheme [35].

Responsive macromolecules can be incorporated in hybrid colloidal particles, serving as the core or shell component [36]. The properties of the responsive shell can be controlled through the external stimuli, hence providing the control over the behavior of the hybrid system [37]. This tunability results in reversible regulation of micro- and microscopic properties of hybrid colloidal systems [36-37]. For example the responsive behavior of mixed polymer brush grafted to the surface of inorganic particles can be used for a reversible particle aggregation, switching between w/o and o/w emulsions, etc [36-37].

Responsive polymeric capsules can be produced from micrometer and sub micrometer-sized particles using layer-by-layer (LbL) assembly of responsive macromolecules [39-40]. After the formation of the shell using LbL deposition, the core of the particles can be dissolved resulting in fabrication of hollow responsive capsules (Fig.1.4) [39]. The behavior of the resulting responsive capsules resembles the behavior of LbL films [40]. The responsive capsules demonstrated higher capacity when encapsulating a wide range of functional molecules, including dyes and polypeptides [41]. Reported high capacity combined with the controlled response properties can be used for stimuli-triggered control of permeability of the encapsulated materials along with capsule manipulation and targeting [41-42].

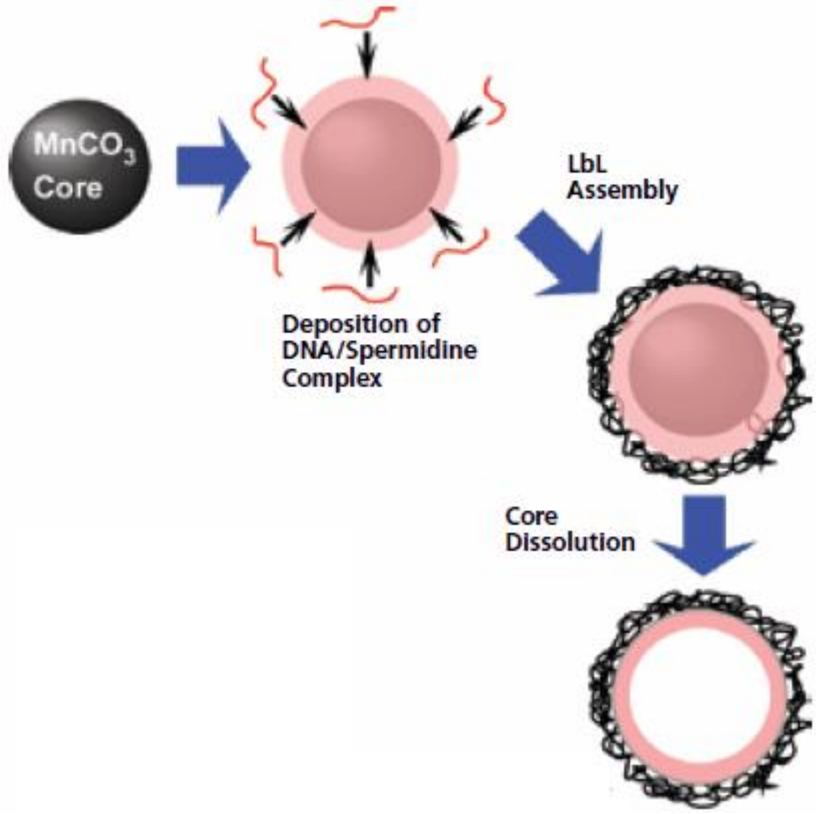

Fig.1.4. Formation of hollow capsules using LbL deposition [110].

Recent progress in studies of RPBC resulted in the design and fabrication of structures with stimuli-responsive formation, degradation, inversion behavior, etc. Such behavior can find use in numerous applications in chemical, cosmetics, detergent and food industries, as well as in medicine for drug delivery and diagnostics for the development of new technologies and products [5]. The major types of the RPBC relevant to current studies are further discussed in detail.

1. 3. Responsive Polymeric Micelles

Responsive micellar structures, as RBPC generated by the self-assembly of responsive copolymers, are among the most studied subjects in nanoscience and nanotechnology [42]. The most common polymers used for the fabrication of responsive micelles are amphiphilic diblock (hydrophilic—hydrophobic) or triblock (hydrophilic—hydrophobic—hydrophilic) copolymers. Additional structures may include graft (hydrophilic-hydrophobic) or ionic (hydrophilic-ionic) copolymers. Due to regulated biocompatibility, toxicity, enhanced blood circulation time responsive polymeric micelles are promising in the area of drug and gene delivery [43-45].

In aqueous media the responsive polymeric micelles typically have a hydrophobic core and a hydrophilic exterior [42]. The hydrophobic fragments form the core of the micelle, which is stabilized by the interactions of external hydrophilic fragments with surrounding aqueous media. The major driving force behind self-assembly of amphiphilic macromolecules into micelles is the decrease of free energy of the system. This decrease in free energy is a result of removal of hydrophobic fragments from the aqueous surroundings (‘hydrophobic effect’) with the formation of a micelle core stabilized with hydrophilic fragments oriented towards water [43].

Like any micellar structure, responsive micellar structures are formed as a result of the self-assembly of copolymers. The self-assembly of copolymers starts at a concentration higher than certain minimal concentration called ‘critical micelle concentration’ (CMC). At low polymer concentration, there is insufficient number of macrochains to form micelles and instead the polymer macromolecules are found distributed throughout the solution and/or adsorbing at the air—water or aqueous—organic solvent interface. As the concentration of polymer increases, more macrochains are adsorbed at the interface. Eventually a concentration is reached at which both the bulk solution and interface are saturated with polymer chains — this is the CMC. Any further addition of amphiphilic macromolecules results in the self-assembly of polymer chains into micelles, so that the free energy of the system is reduced [42-43]. The micellization is accompanied by a sudden change of physicochemical properties, which is used for the experimental studies of micelle formation [1-3, 40-43]. In aqueous media amphiphilic copolymers can form a variety of stable responsive micellar structures: spherical, worm-like or cylindrical, polymersomes, etc [1-5, 42-43].

The kinetic stability of the polymeric micelles is relatively high. Some micelles with ‘solid’ cores, with the glass transition temperature Tg, above physiological temperature, may survive for many hours and even days upon dilution below the CMC [42]. A number of factors was reported to affect the polymer self-assembly: such as the molecular weight of block copolymer, aggregation number of polymer macromolecules, ratio and distribution of hydrophilic and lipophilic fragments, preparation procedure, solvent-polymer interactions [44-47]. The major factor determining the morphology of block copolymer self-assembly is the hydrophilic volume ratio called the packing factor (p), which can be calculated according to the equation 1.1 [48]:

$$p = \frac{v}{a l_c} \qquad (1.1)$$

where v is the volume occupied by the densely packed copolymer fragments (such as hydrophobic fragments in aqueous media), l_c – is the statistical critical length normal to the interphase (correlates with contour length of the polymer chain), *a* – is the effective cross-sectional area per polymer macromolecule at the interphase [2, 44-47].

The packing factor can be used to differentiate between the types of aggregates (Fig.1.5) [2, 44-48]. Copolymers with p below 1/3 typically self-assemble into spherical micelles, when p is between 1/3 and 1/2 the shape of the micelles can vary from spherical to cylindrical (rod-like, worm -like) [46-47]. In case of p values between 1/2 and 1 a gradual transition from cylindrical micelles to polymersomes is reported [47]. At values of p ~ 1 the formation of planar bilayers is expected. And in case of $p>1$ the systems of inverted aggregates can form [48]. Changes in the environment (e.g. solvent, radiation, etc.) can lead to changes of p and as a result in the reorganization of the self-assembled structure – i.e. responsive behavior. This versatility of behavior of polymeric micelles provides great potential to design systems with controlled sharp or gradual responses to the external stimuli [45-48].

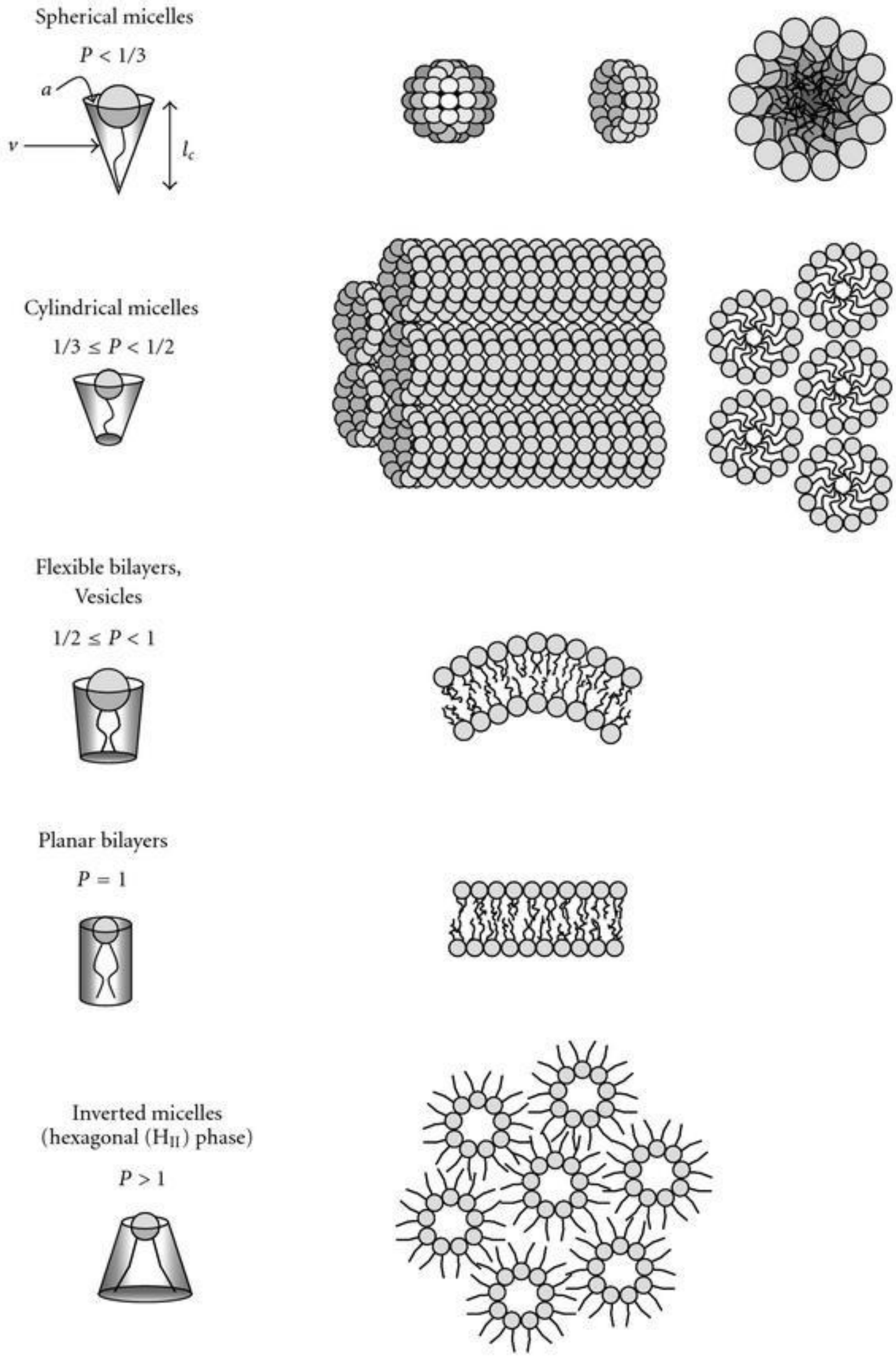

Fig.1.5. The types of aggregates according to the packing parameter (Reproduced from [49]).

Two different approaches can be used for the classification of polymeric micelles: either i. based on the stimuli affecting them (e.g. pH, radiation, etc.) or ii. by the type of the system response (change of colloidal stability, mechanical or optical properties, etc.). Below both classification approaches are discussed followed by corresponding examples of respective responsive micellar systems.

Responsive polymeric micelles have been reported to respond to a significant number of external stimuli– pH, thermal, ionic strength of solution, redox stimuli, osmotic shock, ion exchange, solvent composition and polarity (for non-aqueous systems), different types of radiation, etc [1-4, 44-48]. For example, copolymers such as poly(N-isopropylacrylamide) (PNIPAAm) with a cloud point or some other poly(N-alkylacrylamide) around 32°C forming temperature-responsive micelles were investigated for potential drug delivery formulations [50-51]. These micelles incorporate a lipophilic drug above certain temperature and temperature-responsive drug release would require local cooling of tumor tissue [51]. Good stability, low toxicity, and long circulation time of micelle-encapsulated drugs was achieved by Pluronic P-105 micelles [52-53]. These Pluronic-based mixed micelles were effectively accumulated in tumor interstitial space while retaining their drug load [52-53]. The on-demand release of drugs from mixed micelles and effective intracellular drug uptake by the tumor cells was achieved by local ultrasound treatment of the tumor at a specific time after the drug injection [53]. The polymeric micelles, with lipophilic drug attached to the side chain of the core-forming segment via an acid-labile hydrazone bond were stable at physiological pH (7.0–7.4) but degraded at lower pH (5.0–5.5) [54-56]. A biodistribution study revealed a minimal leakage of free drug into circulation and a selective accumulation in solid tumors where it was released from the carrier upon intracellular uptake via endocytosis [54-56].

Some polymeric micelles can have different responses to several external stimuli – multiresponsive systems [42-44]. For example, dual pH and temperature sensitivity was reported for PAA-b-PNIPAAm, which was presented in the change of drug uptake [57]. At the optimum of pH 7.2 and 25°C the drug was forming complexes with PAA fragments of copolymers. With the changes of either pH or temperature complex was disintegrating releasing the drug. For triple-responsive system fabricated from poly(3-acrylamidophenylboronic acid) and PAPBA-b-PNIPAAm self-assemblies changed composition depending on pH, temperature and presence of selected chemicals [57].

The nature of the response achieved from responsive polymeric micelles varies depending on their structure and composition and is typically used for delivering and release non-soluble cargo in the interior of the micelles [1-2, 40-42]. The most common and useful responses with the examples of existing responsive systems are described below.

The most commonly explored response of polymeric micelles is the transition between the dissolved random-coiled state and self-assembled state, as well as transition between different types of self-assemblies. Thermoresponsive PEO-b-PPPHM diblock copolymers can reversibly form spherical micellar structures with the phase transition temperature 42-55°C [58]. This self-assembly – solution transition is successfully used to load and release different cargo molecules (e.g. drugs for the drug delivery systems) [1-4]. The introduction of specific targeting functional fragments into the shell of micellar structure facilitates the targeting of loading and release of cargo [1-3].

Controlled change of the size or type of responsive polymeric self-assemblies is another promising type of the response for polymeric micelles [1-2]. For example, for specialty poly(ethylene)-based block copolymers [57-59] the size of micellar structures was controlled by change of pH and ionic strength of the solution. Several structures were reported to undergo stimuli-responsive transition between different types of self-assemblies. pH responsive triblock copolymer P2VP-b-PAA-PBMA was reported to form centrosymmetric core-shell micelles, spherical micelles, flowerlike micelles and pH-sensitive networks, toroidal nanostructures at different pH values and copolymer concentrations which can be used to deliver and release different cargos [59].

External stimuli can also affect the optical properties of responsive polymeric self-assemblies [42-48, 60-61]. During pH-controlled reversible complexation was reported for the pyrene-labeled PCL-b-PMAA28 [60-61]. In the reported system the fluorescence was gradually decreasing from 100% to 0.1% with the pH decrease.

An example of the stimuli-triggered change of mechanical properties is the shear-thinning response observed for giant rod-like micelles formed by butadiene-oxirane block copolymers. The shear thinning was caused by critical slowing of orientational Brownian motion, breaking and stress-induced merging of worms [42, 62].

A more complex behavior is expressed by the systems where the external stimuli trigger the interchange of fragments between the corona and the core. For amphiphilic invertible polymers containing fragments of PEG and dicarboxylic acids, the partial inversion was reported in response to the solvent polarity [62].

Interesting for potential applications in multifunctional systems are responsive polymeric micelles with two responses. For PNIPAAm-b-PS block copolymers the change of the size of micellar assemblies was accompanied by the change of fluorescent properties [63].

Responsive block copolymer self-assemblies can be further modified transforming them into different architectures such as: nanogels, capsules, and even composite/hybrid materials.

The progress in the applications of responsive polymeric micelles is based on engineering stable responsive micellar systems capable of encapsulating a broad range of agents (mostly for chemotherapy and other treatments). Developing internal or external stimuli-responsive micelles enhances the degree of targeting and allows modulating and directing intracellular drug trafficking. Application of responsive polymeric micelles in therapy may offer new life to potent bioactive compounds and facilitate their clinical applications.

1.4. Responsive Mixed Polymeric Micelles

For successful application of responsive polymeric micelles several important parameters should be optimized: micelle size and size distribution, stability, responsive behavior, etc [64-66]. In the drug delivery application the intravenous injections of micellar solutions are associated with extreme dilutions in blood flow (usually about 25-fold dilution at bolus injection or a much higher dilution at infusion) and some specialty temperature and pH environments. If micelles are prematurely disassembled, this may result in the release of encapsulated drug into the blood and could be dangerous because a poorly soluble drug may precipitate inside blood vessels. Polymeric micelles fabricated from single copolymers are often lacking the ability to regulate one or more of crucial parameters due to limitation on length and number of fragments [66]. To address these issues it is often practical to combine responsive copolymer with other macromolecules to form responsive mixed micelles. The comicellization of such RPBC is an efficient way to avoid sophisticated synthetic schemes [66 - 67].

The advantages of mixed micelles as RPBC over individual components include significant improvements in thermodynamic and kinetic stability, regulated loading capacity, exquisite control over size to prevent precipitation, etc. [3, 64 - 66] Ideally, the relevant property of the mixed micelles system can be mathematically derived from the molar fractions of the constituents [3, 66 - 67].

Mixed responsive polymeric micelles can be classified according to the interactions involved in their formation and stabilization: hydrophobic interactions, stereocomplexation, hydrogen bonding, ionic interactions and chemical cross-linking (Fig.1.6) [2-3, 65-66]. Responsive mixed micelles fabricated through different types of interactions are expected to have different responsive behavior [64-66]. Described below are the examples of typical responsive mixed polymeric micelles formed by different types of interactions.

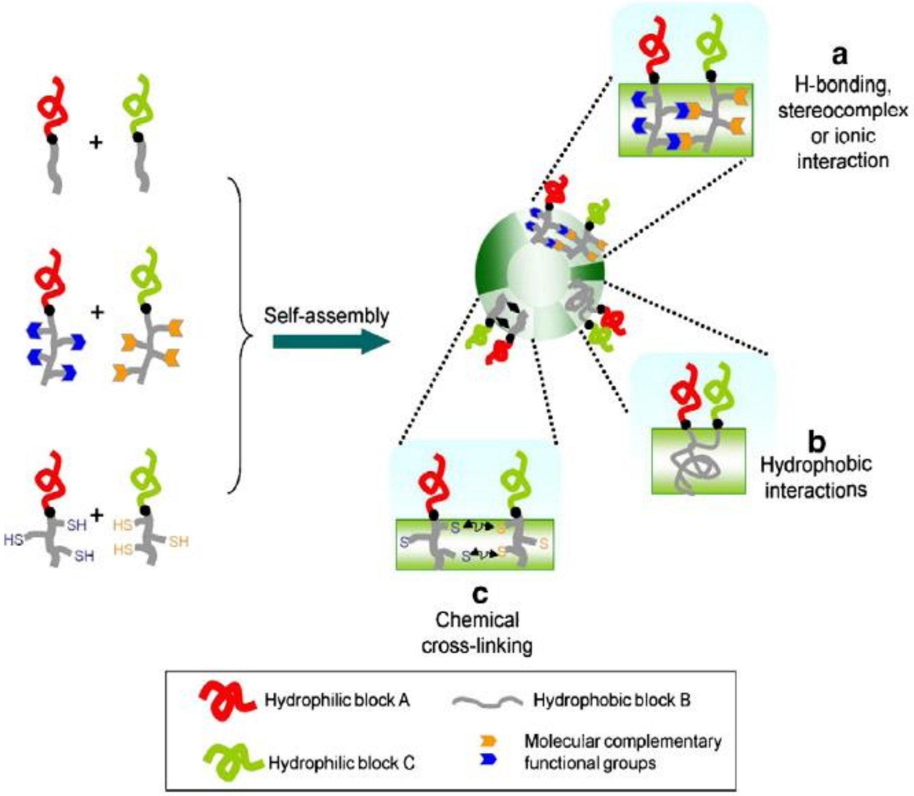

Fig.1.6. Schematic presentation of the formation of mixed micelles through various core interactions. (a) Hydrogen bonding, stereocomplexation or ionic interaction; (b) Hydrophobic interactions; and (c) Chemical cross-linking (e.g. disulfide bond) [2-3].

The frequently observed types of non-covalent interactions during comicellization are hydrophobic interactions (Fig.1.6 b) [68-70]. In this case the stable responsive mixed micelles are formed through the hydrophobic interactions between the hydrophobic blocks of participating macromolecules. To fabricate mixed micelles governed by hydrophobic interactions amphiphilic copolymer was mixed with i. other one or several amphiphilic copolymers [68-69] or ii. other macromolecules: modified phospholipids [70-71], vitamin E, D-α-tocopheryl polyethylene glycol succinate [72-73], etc. For example, mixed micelles fabricated from two Pluronic copolymers, Pluronic L61 and Pluronic L101 with different HLB values have shown improved stability and capacity [74]. The reported Pluronic L61/ L101 system was approved for clinical trials as drug delivery vehicle for doxorubicin [75]. Typically such systems undergo transition from dissolved random-coiled state into self-assembled state as a response to changes of temperature [1-2, 72-73].

In addition to improving drug loading capacity, stability and size, proper formulation of mixed micelles can be used to control the sensitivity of response by changing critical solution parameters – CMC, critical solution temperature (LCST), etc [1-5, 72-75]. For example, after mixing temperature-responsive copolymer mPEG-b-P(NmPAAm-coVlm), which is unable to form stable micelles at room temperature (LCST 35°C), with mPEG-b-PLA the resulting mixed micelles were stable at room conditions. The decrease of LCST to 21°C in mixed system was caused by the decrease of mobility of mPEG-b-P(PNIPAAm-coVlm). The decrease of LCST allowed fabricating stable responsive mixed micelles at room temperature and thus controlling the temperature response by preventing the premature drug release [75].

Stereocomplexation is an alternative promising approach for the formation of responsive mixed micelles. The major advantage of mixed systems formed by this interaction type is the precise structural control and thus sustainable character of response (release of cargo). Typical enantiomers used for stereocomplexation are polyoxiranes, polylactides, polylactones, etc [76-

80]. For example, for system based on PEG-PEGLA and PNIPAAm-PLLA the formation of mixed micelles in water was based on stereoselective association between enantiomeric PLA blocks which are supported by PEG and PNIPAAm fragments [77]. The resulting responsive spherical micelles showed temperature-responsive behavior. In addition to homocomplexes, formed from enantiomers with identical chemical composition, the formation of heterocomplexes was reported. Heterocomplexes were fabricated from dissimilar block copolymers, such as for example L-peptides and poly(D-PLA). The responsive behavior of the L-peptide/poly(D-PLA) was facilitated by polylactive degradation [78].

Similarly to stereocomplexation, the hydrogen bonds are formed due to close-range interactions (Fig.1.6a). Responsive mixed micelles are formed due to interactions of hydrophobic blocks and then are stabilized by hydrogen bonds in the hydrophobic core [81]. Reported examples of mixed micelles formed by hydrogen bonding include macromolecules containing urea functional groups [82-83], which are able to form strong hydrogen bonds between each other. The properties of responsive mixed micelles formed using hydrogen bonding can be regulated through the parameters regulating hydrogen bonding: temperature, pH, etc [84-85].

In addition to the short-range interactions, discussed above, long-range ionic interactions can also take part in the formation of responsive mixed micelles. In this case the strong electrostatic interactions can act as a driving force during the micellization: oppositely charged functional groups of macromolecules come together to form stable mixed micelles called polyion complexes. Such micelles have the additional advantage of solubilizing ionic cargo molecules, e.g. folic acid [86], DNA [87], etc. Ionic interactions can provide sensitivity to pH, temperature, ionic composition of solution thus increasing the scope the possible external stimuli to trigger the responsive release of drug [88-90].

Chemical cross-linking is a versatile and promising approach for the fabrication of responsive mixed polymeric micelles (Fig.6c). This approach allows forming responsive mixed micelles from compositions, which are unable to form stable mixed micelles by any other approach [83-84]. This approach allows to selectively adjust the responsive behavior of mixed polymeric micelles components by stabilizing/destabilizing them – chemical cross-linking is often involved in stabilization of either core or shell [91-92]. For example, in PEO/PHEMA system PPO core was chemically cross-linked by UV-induced free radical polymerization to improve core stability against methanol [93-94]. Chemical cross-linking in the shell stabilizes micelles configuration and thus allows controlling the presence of functional groups on the surface [95].

Fabrication of responsive mixed micelles is a versatile and simple approach to improve the responsive polymeric micelles for practical applications. Mixing functional macromolecules to form single mixed system allows avoiding challenging synthetic schemes for the synthesis of complex copolymers with multiple functionalities. The versatility of mixed micelles also offers an opportunity to optimize the properties of responsive micellar system, as well as to control the surface densities of functional groups.

1.5. Hybrid Responsive Polymer-Inorganic Colloids

Polymer-based colloids described above show responsive behavior by changing colloidal, mechanical and optical properties as a response external stimuli. However, the scope of response for polymeric materials is limited as they are unable to express the most of magnetic, catalytic, electronic, or spectroscopic responses characteristic for inorganic materials. Therefore one of the most practical solutions is the fabrication of hybrid polymer-inorganic responsive nanostructured colloids from the combination of polymeric and inorganic materials (Scheme 1.1). Such materials offer a new level of responsive behavior by combining properties both of the inorganic and the polymer constituents: e.g. the mechanical behavior, solubility, and processability of the polymer, and the magnetic, catalytic, electronic, and spectroscopic features of the inorganic component [95]. The reported synergistic effects in such materials can result in their high efficiency as catalysts and biocatalysts [94-96]. Often the hybrid composition is able to provide additional storage stability by preserving the colloidal structure when the responsive hybrid particles are dried and redispersed. In this case inorganic component preventing complete perturbation of polymer chains in dry material and preserving the essential colloid properties and organic component provides the ability of responsive hybrid particles to be redispersed [94-95]. Because the scope of the responsive colloid hybrid materials, ranging from nanometers to centimeters in size, involving complex individual and synergistic, discussed below are only responsive hybrid colloids composed from inorganic core covered by polymer shell.

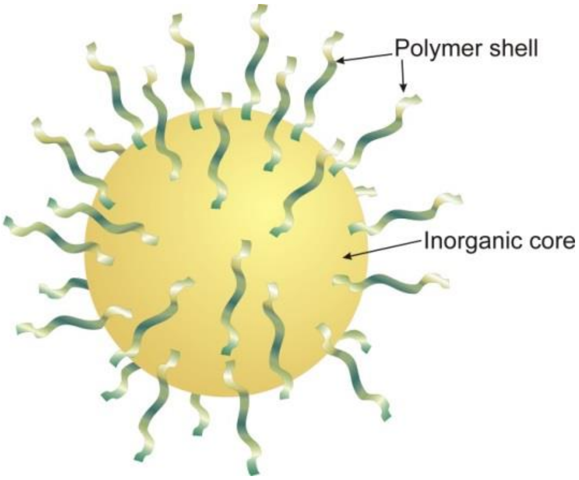

Scheme 1.1. Scheme of hybrid polymer-inorganic responsive nanostructured colloid [1–2, 94-96].

The technological challenge in the fabrication of responsive hybrid polymer-inorganic colloids is mutual incompatibility of polymer and inorganic components. The interfacial tension in hybrid system depends on the stabilization of the polymer/inorganic interface. In order to fabricate stable polymer/inorganic hybrid colloids, the polymer/inorganic interface has to be sufficiently stabilized to provide adhesion between the polymer and inorganic microphase [94-95]. Such adhesion can be provided by functional fragments of copolymers that bind to the inorganic material (P2VP, P4VP, PDMS, PEO, PA, etc.) forming the shell of the hybrid colloid. The most common inorganic components used in hybrid systems are silica [96], alumina [97], ceolite [98], iron oxide [99-100] and noble metals [101-103].

The colloidal properties of polymer/inorganic hybrid materials depend largely on the properties of the polymeric component. The polymer component should not have excessive thermodynamic stability since this could prevent the formation of the desired colloid. Growing the desired inorganic colloids within microdomains of suitable size and shape formed by polymeric materials can give the control over the size and shape of the hybrid colloids [94].

The typical synthetic routes for the controlled formation of responsive hybrid colloids may involve following steps: formation of inorganic core and grafting of one/several polymeric components. The succession of these steps is variable.

The core-forming inorganic particles can be reacted either with the monomer (i.e.‘grafting from’ procedure) or with the polymer (i.e. ‘grafting to’ procedure) (Scheme 1.2) or can be incorporated into polymeric micelles by adsorption [94-96].

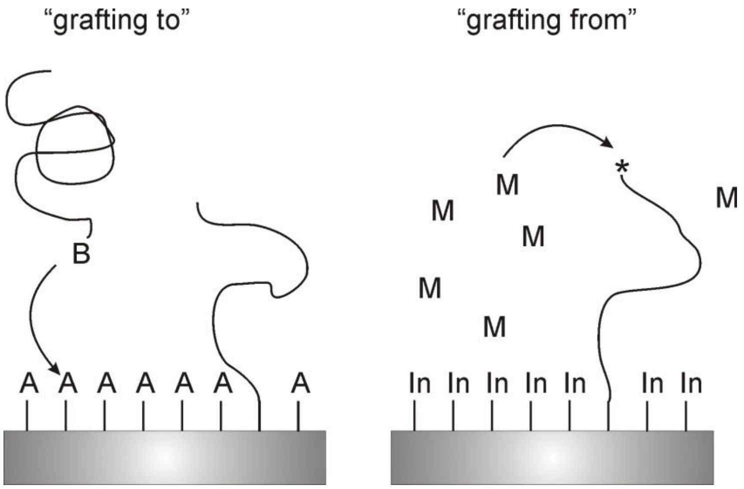

Scheme 1.2. Synthesis of polymer brushes using "grafting to" and "grafting from" approaches [1-3]. A – active group on the surface, B – polymer macromolecule reacting with A, In – initiator on the surface, M – monomer molecules in solution.

Grafting techniques involve the chemical attachments of functional polymers to the surface of inorganic particles. "Grafting from" and "grafting to" are the two major approaches used for the covalent binding of polymer component to the inorganic component [97-100]. The 'grafting to' techniques involve chemical reaction of functional polymer with the corresponding groups on the inorganic particle surface. The advantages of this approach are the robustness and the use of premade polymers with known properties. In the same time 'grafting from' involves the initiation of polymerization of organic component using initiator on the inorganic particle surface [90-91]. A number of different polymerization techniques can be used on this stage, including ATRP, living ionic polymerization, hyperbranching, etc [97-102]. The major advantage of this approach is the possibility to regulate the density of the grafting by regulating the density of the surface-bound initiator [97-101]. The grafted polymer interior can consist of single polymer component or can combine a number of different macrochains forming mixed polymer brushes [109].

The control of magnetic properties can be achieved by optimizing the morphology and size of hybrid colloids [113]. The complete transition of the colloidal behavior from paramagnetic to superparamagnetic to ferromagnetic was obtained, depending on the type of block copolymer and the reaction conditions. The response of hybrid particles can be used to separate particles from bulk solution and also for magnetic targeting of colloids to specific areas [113].

The control and installation of special optical properties was achieved by means of the synthesis of CdS colloids in ordered block copolymer films. The resulting modular hybrid can be used to replace the standard organic UV-absorbers [113-115].

The hybrid Pd catalysts are the examples of catalytic behavior of hybrid particles as they combine the advantages of homogeneous and heterogeneous catalysis. Due to the polymeric shell, the Pd colloids can be dissolved in organic solvents very much like low molecular weight homogeneous catalysts [116]. The catalytic properties of micellar-stabilized Pd or Pt colloids have been investigated in case of hydrogenation [114] and the Heck reaction [116]. In most reactions, the hybrid systems remain catalytically active even after more than 50 000 turnover cycles.

The incorporation of enzymes into hybrid responsive polymer-inorganic structures provides new horizons in biocatalysis [118, 119]. Hybrid particles composed of inorganic cores and grafted polymeric shells were reported to efficiently immobilize enzymes for novel heterogeneous catalysis [120]. The advantages of responsive hybrid polymer-inorganic colloids are in providing a large surface area to bind an appropriate number of enzyme molecules for efficient enzyme-substrate ratio [119-120]. In such hybrid particles the responsive polymer component allows reversibly bind the enzymes in the same maintaining their biological functionality. The inorganic core provides the structural stability, storage stability during drying and provides additional benefits during the separation/recovery of hybrid particles from the solution [117]. For example, responsive hybrid particles containing magnetic cores can be easily removed from the bulk solution using magnet [120].

Hence, the change of morphological complexity for RPBC can be considered as a tool in regulating the interaction between the responsive polymeric component of RPBC and cargo molecules (for example, hydrophobic drugs or enzymes). The results of this study can be used to fabricate and/or optimize the RPBC structures with an appropriate morphology and properties for the specific applications in drug delivery and bioconversion.

1. 6. References

[1]. Motornov, M.; Roiter, Y.; Tokarev, I.; Minko, S. Stimuli-responsive nanoparticles, nanogels and capsules for integrated multifunctional intelligent systems. *Progress in Polymer Science* **2010**, 35, 174–211

[2]. Motornov, M.; .Sheparovych, R; Lupitskyy, E; MacWilliams, S; Minko, S. Responsive colloidal systems: reversible aggregation and fabrication of superhydrophobic surfaces. *Journal of Colloid and Interface Science* **2007**, *310*, 481–488

[3]. Bajpai, A.K.; Shukla, S. K.; Bhanu, S.; Kankane, S. Responsive polymers in controlled drug delivery. *Progress in Polymer Science* **2008**, *33*, 1088–1118

[4]. Chen, G.H; Hoffman, A.S. Graft copolymers that exhibit temperature-induced phase transitions over a wide range of pH. *Nature* **1995**, *373*, 49–52.

[5]. Qiu ,Y; Park, K. Environment-sensitive hydrogels for drug delivery. *Advanced Drug Delivery Reviews* **2001**, *53*, 321–339.

[6]. Gil, E.S; Hudson, S.A. Stimuli - responsive polymers and their bioconjugates. *Progress in Polymer Science* **2004**, *29*, 1173–1222.

[7]. Chilkoti, A; Dreher, M.R; Meyer, D.E; Raucher, D. Targeted drug delivery by thermally responsive polymers. *Advanced Drug Delivery Reviews* **2002**, *54*, 613–630.

[8]. Li, Z; Zhang, Y; Fullhart, P; Mirkin, C.A. Reversible and chemically programmable micelle assembly with DNA block copolymer amphiphiles. *Nano Letters* **2004**, *4*, 1055–1058.

[9]. Yurke, B, Lin, D.C, Langrana, N.A. *Use of DNA nanodevices in modulating the mechanical properties of polyacrylamide gels. Carbone.* Pierce NA, editors. Lecture notes in computer science, vol. 3892. Springer-Verlag: Berlin, **2006**. p. 417–426

[10]. Miyata, T; Uragami, T; Nakamae, K. Biomolecule-sensitive hydrogels. *Advanced Drug Delivery Reviews* **2002**, *54*, 79–98.

[11]. Ulijn, R.V. Enzyme-responsive materials: a new class of smart biomaterials. *Journal of Materials Chemistry* **2006**, *16*, 2217–2225.

[12]. Miyata, T; Asami, N; Uragami, T. A reversibly antigen-responsive hydrogel. *Nature* **1999**, *399*, 766–769.

[13]. Cutler, S.M; Garcia, A.J. Engineering cell adhesive surfaces that direct integrin $\alpha_5\beta_1$ binding using a recombinant fragment of fibronectin. *Biomaterials* **2003**, *24*, 1759–1770.

[14]. Rosso, F; Marino, G; Giordano, A; Barbarisi, M; Parmeggiani, D; Barbarisi, A. Smart materials as scaffolds for tissue engineering. *Journal of Cellular Physiology* **2005**, *203*, 465–470.

[15]. Stayton, P.S; Shimoboji, T; Long, C; Chilkoti, A; Chen GH, Harris, J.M; Hoffman, A. S. Control of protein–ligand recognition using a stimuli-responsive polymer *Nature* **1995**, *378*, 472–474.

[16]. Hoffman, A.S. Bioconjugates of intelligent polymers and recognition proteins for use in diagnostics and affinity separations. *Clinical Chemistry* **2000**, *46* (9), 1478–1486

[17]. Minko, S; Roiter, Y. AFM single molecule studies of adsorbed polyelectrolytes. *Current Opinion in Colloid & Interface Science* **2005**, *10*, 9–15.

[18]. Roiter, Y; Minko, S. AFM Single Molecule Experiments at the Solid-Liquid Interface: In Situ Conformation of Adsorbed Flexible Polyelectrolyte Chains. *Journal of the American Chemical Society* **2005**, 127, 15688–15689.

[19]. Jhaveri, S. J; Hynd, M. R.; Dowell-Mesfin, N.; Turner, J. N.; Shain, W.; Ober, C. K. Release of Nerve Growth Factor from HEMA Hydrogel-coated substrates and its effect on the differentiation of neural cells. *Biomacromolecules* **2009**, *10*, 174–183.

[20]. Hoffman, A. S. The origins and evolution of “controlled” drug delivery systems. *Journal of Controlled Release* **2008**, 132, 153–163.

[21]. Liu, Z. S.; Calvert, P. Multilayer hydrogels as muscle-like actuators. *Advanced Materials* **2000**, *12*, 288–291.

[22]. Lu, Y.; Mei, Y.; Drechsler, M.; Ballauff, M. Thermosensitive core–shell particles as carriers for Ag nanoparticles: modulating the catalytic activity by a phase transition in networks. *Angewandte Chemie International Edition* **2006**, *45*, 813–816.

[23]. Lu, Y.; Proch, S.; Schrinner, M.; Drechsler M.; Kempe R.; Ballauff. M. Thermosensitive core-shell microgel as a “nanoreactor” for catalytic active metal nanoparticles. *Journal of Materials Chemistry* **2009**, *19*, 3955–3961.

[24]. Senaratne, W.; Andruzzi, L.; Ober, C. K. Self-assembled monolayers and polymer brushes in biotechnology: current applications and future perspectives. *Biomacromolecules* **2005**, *6*, 2427–2448.

[25]. Cohen Stuart, M. A.; Huck, W. T. S.; Genzer, J.; Müller, M.; Ober, C.; Stamm, M.; Sukhorukov, G. B.; Szleifer, I. ; Tsukruk, V. V.; Urban, M.; Winnik, F.; Zauscher, S.; Luzinov, I.; Minko, S. Emerging applications of stimuli-responsive polymer materials. *Nature Materials* **2010**, *9*, 101–113

[26]. Discher, D. E.; Ortiz, V., Srinivas, G.; Klein, M. L.; Kim, Y.; Christian, D.; Cai, S.; Photos, P.; Ahmed F. Emerging applications of polymersomes in delivery: From molecular dynamics to shrinkage of tumors. *Progress in Polymer Science* **2007**, *32*, 838–857.

[27]. Blanazs, A.; Armes, S. P.; Ryan, A. Self-Assembled Block Copolymer Aggregates: From Micelles to Vesicles and their Biological Applications. *Macromolecular Rapid Communications* **2009**, *30*, 267–277.

[28]. Mathur, A.M.; Drescher, B.; Scranton, A. B.; Klier J. Polymeric emulsifiers based on reversible formation of hydrophobic units. *Nature* **1998**, *392*, 367-370.

[29]. Yan, Y.; Besseling N.; de Keizer, A.; Marcelis, A.; Drechsler, M.; Cohen, S. Hierarchical Self-Assembly in Solutions Containing Metal Ions, Ligand, and Diblock Copolymer. *Angewandte Chemie International Edition* **2007**, 46, 1807–1809.

[30]. Hayward, R. C.; Utada, A. S.; Dan, N.; Weitz D. A. Dewetting instability during the formation of polymersomes from block copolymer-stabilized double emulsions. *Langmuir* **2006**. *22*, 4457-4461.

[31]. Chiu, H. C.; Lin, Y. W.; Huang, Y. F.; Chuang, C. K.; Chern, C. S. Polymer Vesicles Containing Small Vesicles within Interior Aqueous Compartments and pH-Responsive Transmembrane Channels. *Angewandte Chemie International Edition 2008, 47,* 1875–1878

[32]. Oh, J. K.; Drumright, R.; Siegwart, D. J.; Matyjaszewski K. The development of microgels/nanogels for drug delivery applications. *Prog. Polym.Sci.* **2008**, *33*, 448–477.

[33]. Morimoto, N.; Qiu, X. P.; Winnik, F. M.; Akiyoshi, K. Dual stimuli-responsive nanogels by self-assembly of polysaccharides lightly grafted with thiol-terminated poly(N-isopropylacrylamide) chains. *Macromolecules* **2008**, *41*, 5985–5987.

[34]. Morimoto, N.; Winnik, F. M.; Akiyoshi, K. Botryoidal Assembly of Cholesteryl−Pullulan/Poly(N-isopropylacrylamide) Nanogels. *Langmuir* **2007**, **23**, 217–223.

[35]. Asadian, M.; Cuggino, J.; Steinhilber, D.; Souza, A.; Calderón M. Functional nanogels for biomedical applications. *Current Medicinal Chemistry* **2012**, *19* (29), 5029-5043.

[36]. Motornov, M.; Zhou, J.; Pita, M.; Gopishetty, V.; Tokarev, I.; Katz, E.; Minko, S. “Chemical Transformers” from Nanoparticle Ensembles Operated with Logic. *Nano Letters* **2008**, *8*, 2993–2997.

[37]. Perro, A.; Reculusa, S.; Bourgeat-Lami, E.; Duguet, E.; Ravaine S. Synthesis of hybrid colloidal particles: from snowman-like to raspberry-like morphologies. *Colloids and Surfaces A: Physicochemical and Engineering Aspects* **2006**, *284–285*, 78–83

[38]. Donath, E.; Sukhorukov, G. B.; Caruso, F.; Davis, S. A.; Möhwald, H. Novel hollow polymer shells by colloid-templated assembly of polyelectrolytes. *Angewandte Chemie International Edition* **1998**, *37*, 2202–2205.

[39]. Zelikin, A. N.; Li, Q.; Caruso, F. Disulfide-stabilized poly(methacrylic acid) capsules: formation, cross-linking, and degradation behavior. *Chemistry of Materials* **2008**, *20*, 2655–2661.

[40]. Levy, T.; Dejugnat, C.; Sukhorukov, G. B. Polymer Microcapsules with Carbohydrate-Sensitive Properties. *Advanced Functional Materials* **2008**, *18*, 1586–1594.

[41]. Kozlovskaya, V.; Kharlampieva, E.; Mansfield, M. L.; Sukhishvili, S. A. Poly(methacrylic acid) hydrogel films and capsules: Response to pH and ionic strength, and encapsulation of macromolecules. *Chemistry of Materials* **2006**, *18*, 328–336.

[42]. W.Loh. *Encyclopedia of Surface and Colloid Science.* **2002**, CRC Press: New York.

[43]. Gohy, J. Block copolymer micelles. *Advances in Polymer Science* **2005**, *190*, 65-136

[44]. Israelachvili, J.N; Mitchell, D.J.; Ninham B;W. Theory of self-assembly of hydrocarbon amphiphiles into micelles and bilayers. *Journal of the Chemical Society, Faraday Transactions* **1976**, 2(72), 1525–68.

[45]. Israelachvili, J.N. *Intermolecular and surface forces.* Academic Press:San Diego, 1991.

[46]. Discher, D.E; Ortiz, V.; Srinivas, G.; Klein, M.L.; Kim, Y.; David, C.A.; Cai, S.; Photos, P.; Fariyal, A. Emerging applications of polymersomes in delivery: From molecular dynamics to shrinkage of tumors. *Progress in Polymer Science* **2007**, *32*, 838–857.

[47]. Blanazs, A., Armes, S.P, Ryan, A.J. Self-Assembled Block Copolymer Aggregates: From Micelles to Vesicles and their Biological Applications. *Macromolecular Rapid Communications* **2009**, *30*, 267–277.

[48]. Discher, B.M.; Won, Y.Y.; Ege, D.S.; Lee, J.C.M.; Bates, FS, Discher, D.E.; Hammer, D. A. Polymersomes: Tough Vesicles Made from Diblock Copolymers. *Science* **1999**, *284*, 1143–6.

[49]. Balazs, D. A.; Godbey, WT. Liposomes for use in gene delivery. *Journal of Drug Delivery* **2010**, *2011*, 1-12.

[50]. Zhou; X. Y. X; Zhang, G. Thermoresponsive triblock copolymer aggregates investigated by laser light scattering. *The Journal of Physical Chemistry B* **2007**, *111* (19), 5111–5115.

[51]. Neradovic, D.; Soga, O.; Van Nostrum, C. F.; Hennink, W. E. The effect of the processing and formulation parameters on the size of nanoparticles based on block copolymers of

poly(ethylene glycol) and poly(N-isopropylacrylamide)with and without hydrolytically sensitive groups. *Biomaterials* **2004**, *25*, 2409–2418.

[52]. Gao, Z.; Fain, H.; Rapoport, N. Controlled and targeted tumor chemotherapy by micellar-encapsulated drug and ultrasound. *Journal of Controlled Release* **2005**, *102*, 203–221.

[53]. Gao, Z.; Fain H. D.; Rapoport, N. Ultrasound-enhanced tumor targeting of polymeric micellar drug carriers. *Molecular Pharmaceutics* **2004**, *1*, 317–330.

[54]. Bae, Y.; Jang, W.; Nishiyama, N.; Fukushima, S.; Kataoka, K. Multifunctional polymeric micelles with folate-mediated cancer cell targeting and pH-triggered drug releasing properties for active intracellular drug delivery. *Molecular BioSystems* **2005**, *1*, 242–250.

[55]. Bae, Y.; Fukushima, S.; Harada, A.; Kataoka, K. Design of environment-sensitive supramolecular assemblies for intracellular drug delivery: polymeric micelles that are responsive to intracellular pH change. *Angewandte Chemie International Edition* **2003**, *42*, 4640–4643.

[56]. Bae, Y.; Nishiyama, N.; Fukushima, S.; Koyama H.; Matsumura,Y.; Kataoka, K. Preparation and biological characterization of polymeric micelle drug carriers with intracellular pH-triggered drug release property: tumor permeability, controlled subcellular drug distribution, and enhanced *in vivo* antitumor efficacy. *Bioconjugate Chemistry* **2005**, *16*, 122–130.

[57]. Li, G.Y.; Song, S.; Guo, L.; Ma, S.M. Self-assembly of thermo- and pH-responsive poly(acrylic acid)-b-poly(N-isopropylacrylamide) micelles for drug delivery. *ournal of Polymer Science Part A: Polymer Chemistry* **2008**, *46*, 5028–5035.

[58]. Nishihara, M.; Murakami, Y.; Shinoda, T.; Yamamoto, J.; Yokoyama, M. Synthesis and characterization of a temperature-responsive amphiphilic block copolymer containing a liquid crystalline unit. *Chemistry Letters* **2008**, *37*, 1214–1215.

[59]. Tsitsilianis, C.; Roiter, Y.; Katsampas, I.; Minko, S. Diversity of nanostructured self-assemblies from a pH-responsive ABC terpolymer in aqueous media. *Macromolecules* **2008**, *41*, 925–934.

[60]. Lee, S.C.; Kim, K.J.; Jeong, Y.K.; Chang, J.H.; Choi, J. pH-Induced reversible complexation of poly(ethylene glycol) and poly(ε-caprolactone)-b-poly(methacrylic acid) copolymer micelles. *Macromolecules* **2005**, 38, 9291 – 9297.

[61]. Lee, S.C.; Lee, H.J. Reversible Vesicle Restraint in Response to Spatiotemporally Controlled Electrical Signals: A Bridge between Electrical and Chemical Signaling Modes. *Langmuir* **2007**, 23, 88–95.

[62]. Kohut, A., Voronov, A. Hierarchical micellar structures from amphiphilic invertible polyesters: ^{1}H NMR spectroscopic study. *Langmuir* **2009**, *25* (8), 4356 – 4360.

[63]. Zeng, J.G.; Shi, K.Y.; Zhang, Y.Y.; Sun X.H.; Zhang, B.L. Construction and micellization of a non-covalent double hydrophilic block copolymer. *Chemical Communications* **2008**, *32,* 3753–3755.

[64]. Allen, C.; Maysinger, D.; Eisenberg, A. Nano-engineering block copolymer aggregates for drug delivery. *Colloids and Surfaces B: Biointerfaces* **1999**, *16*, 3–27.

[65]. Kim, S.; Shi, Y.; Kim, J.; Park, K.; Cheng, J. New inhibitors of the mammalian target of rapamycin signaling pathway for cancer. *Expert Opinion on Drug Delivery* **2010**, *7*, 49–62.

[66]. Rapoport, N. Physical stimuli-responsive polymeric micelles for anticancer drug delivery. *Progress in Polymer Science* **2007**, *32,* 962–90.

[67]. Riess, G. Micellization of block copolymers. *Progress in Polymer Science* **2003**, 28, 1107–1170.

[68]. Vakil, R.; Kwon, G. Poly(ethylene glycol)-b-poly(ε-caprolactone) and PEG-phospholipidform stable mixed micelles in aqueous media. *Langmuir* **2006**, *22*, 9723–9729.

[69]. Gao, Z.; Fain, H.; Rapoport, N. Controlled and targeted tumor chemotherapy by micellar-encapsulated drug and ultrasound. *Journal of Controlled Release* **2005**, *102*, 203–222.

[70]. Wang, J.; Wang, R.; Li, L. Preparation and properties of hydroxycamptothecin-loaded nanoparticles made of amphiphilic copolymer and normal polymer. *Journal of Colloid and Interface Science* **2009**, *336*, 808–813.

[71]. Mu, L.; Elbayoumi T.; Torchilin, V. Mixed micelles made of poly(ethylene glycol)–phosphatidylethanolamine conjugate and d-α-tocopheryl polyethylene glycol 1000 succinate as pharmaceutical nanocarriers for camptothecin. *International Journal of Pharmaceutics* **2005,** 306, 142–9.

[72]. O‘Neil, C.; van der Vlies, A.; Velluto, D.; Wandrey, C.; Demurtas, D.; Dubochet, J.; Hubbell, J. A. Extracellular matrix binding mixed micelles for drug delivery applications. *Journal of Controlled Release* **2009**, *137*, 146–151.

[74]. Lo C; Lin S; Tsai H; Chan W; Tsai C; Cheng C; Chien-Hsin D; Cheng, G.H. H. Mixed micelle systems formed from critical micelle concentration and temperature-sensitive diblock copolymers for doxorubicin delivery. *Biomaterials* **2009**, *30*, 3961–3970.

[75]. Tsuji, H. *In vitro* Enzymatic Degradation of Nanoparticles Prepared from Hydrophobically-Modified Poly(γ-glutamic acid). *Macromol Biosci* **2005**, *5*, 569–597.

[76]. Skey, J.; Hansell, C; O'Reilly, R. Stabilization of amino acid derived diblock copolymer micelles through favorable D: L side chain interactions. *Macromolecules* **2010**, *43*, 1309–1318.

[77]. Fukushima, K; Kimura ,Y. Stereocomplexed polylactides (Neo-PLA) as high-performance bio-based polymers: their formation, properties, and application. *Polymer International* **2006**, *55*, 626–42.

[78]. Fukushima, K.; Sogo, K.; Miura, S.; Kimura, Y. Production of D-Lactic Acid by Bacterial Fermentation of Rice Starch. *Macromolecular Bioscience* **2004**, *4*, 1021–1027.

[79]. Jeong, B.; Bae, Y.; Lee, D.; Kim, S. Biodegradable block copolymers as injectable drug-delivery systems. *Nature* **1997**, *388*, 860–862.

[80]. Uhrich, K.; Cannizzaro, S.; Langer, R.; Shakesheff, K. Polymeric systems for controlled drug release. *Chemical Reviews* **1999**, *99*, 3181–3198.

[81]. Tan, J.; Kim, S.; Nederberg, F.; Fukushima, K.; Coady, D.; Nelson, A; Yang, Y.Y; Hedrick, J.L. Delivery of anticancer drugs using polymeric micelles stabilized by hydrogen-bonding urea groups. *Macromolecular Rapid Communications* **2010**, *31*, 1187–1192.

[82]. Podhajecka, K.; Stepanek, M.; Prochazka, K.; Brown, W. Hybrid polymeric micelles with hydrophobic cores and mixed polyelectrolyte/nonelectrolyte shells in aqueous media. 2. Studies of the shell behavior. *Langmuir* **2001**, *17*, 4245–4250.

[83]. Stpanek, M.; Podhajecka, K.; Tesaova, E.; Prochazka, K.; Tuzar, Z.; Brown, W. Hybrid polymeric micelles with hydrophobic cores and mixed polyelectrolyte/nonelectrolyte shells in aqueous media. 1. Preparation and basic characterization. *Langmuir* **2001**, *17*, 4240–4244.

[84]. Lefevre, N.; Fustin, C.; Gohy, J. Reorganization of hydrogen-bonded block copolymer complexes. *Langmuir* **2007**, *23*, 4618–2462.

[85]. Luo, Y.; Yuan, J.; Liu, X.; Xie, H.; Gao, Q. Fabrication and characterization of electrospun PLGA/MWNTs/hydroxyapatite biocomposite scaffolds for bone tissue engineering. *Journal of Bioactive and Compatible Polymers* **2010**, *25*, 292–304.

[86]. Luo, Y.; Yao, X.; Yuan, J.; Ding, T.; Gao, Q. Preparation and drug controlled-release of polyion complex micelles as drug delivery systems. *Colloids and Surfaces B* **2009**, *68*, 218–224.

[87]. Katayose, S; Kataoka, K. Water-soluble polyion complex associates of DNA and poly(ethylene glycol)-poly(L-lysine) block copolymer. *Bioconjugate Chemistry* **1997**, *8*, 702–707.

[88]. Lee, S.; Kim, S.; Park, T. Intracellular siRNA delivery system using polyelectrolyte complex micelles prepared from VEGF siRNA-PEG conjugate and cationic fusogenic peptide. *Biochemical and Biophysical Research Communications* **2007**, *357*, 511–516.

[89]. Hermans, T.; Broeren, M.; Gomopoulos, N.; Van Der Schoot, P.;Van Genderen, M.; Sommerdijk, N.; Sommerdijk, N. A. J. M.; Fytas, G.; Meijer, E. W. Self-assembly of soft nanoparticles with tunable patchiness. *Nature Nanotechnology* **2009**, *4*, 721–726.

[90]. Petrov, P.; Bozukov, M.; Burkhardt, M.; Muthukrishnan, S.; Müller, A.; Tsvetanov, C.; Stabilization of polymeric micelles with a mixed poly(ethylene oxide)/poly(2-hydroxyethyl methacrylate) shell by formation of poly(pentaerythritol tetraacrylate) nanonetworks within the micelles. *Journal of Materials Chemistry* **2006**, *16*, 2192–2199.

[91]. Hui, T.; Chen, D.; Jiang, M. A one-step approach to the highly efficient preparation of core-stabilized polymeric micelles with a mixed shell formed by two incompatible polymers. *Macromolecules* **2005**, *38*, 5834–5837.

[92]. Kakizawa, Y.; Harada, A.; Kataoka, K. Environment-sensitive stabilization of core-shell structured polyion complex micelle by reversible cross-linking of the core through disulfide bond. *Journal of the American Chemical Society* **1999**, *121*, 11247–11248.

[93]. Joralemon, M.; Murthy, K.; Remsen, E.; Becker, M.; Wooley, K. Synthesis, characterization, and bioavailability of mannosylated shell cross-linked nanoparticles. *Biomacromolecules* **2004**, *5*, 903–913.

[94]. Förster, S.; Antonietti, M. Amphiphilic block copolymers in structure-controlled nanomaterial hybrids. *Advanced Materials* **1998**, *10* (3), 195-217.

[95]. Buitenhuis, J.; Förster, S. Block copolymer micelles-viscoelasticity and interaction potential of soft spheres. *The Journal of Chemical Physics* **1997**, *107*, 262.

[96]. Lapeyre, V.; Renaudie, N.; Dechezelles, J.F.; Saadaoui, H.; Ravaine, S.; Ravaine, V. Multiresponsive hybrid microgels and hollow capsules with a layered structure. *Langmuir* **2009**, *25*, 4659–4667.

[97]. Ash, B.J.; Siegel, R.W.; Schadler, L.S. Glass transition behavior of alumina/polymethylmethacrylate nanocomposites. *Journal of Polymer Science Part B: Polymer Physics* **2004**, *42*, 4371–4383.

[98]. Ziesmer, S.; Stock, N. Synthesis of bifunctional core–shell particles with a porous zeolite core and a responsive polymeric shell. *Colloid & Polymer Science* **2008**, *286*, 831–836.

[99]. Arias, J.L.; Gallardo, V.; Gomez-Lopera S.A.; Plaza, R.C.; Delgado, A.V. Synthesis and characterization of poly(ethyl-2-cyanoacrylate) nanoparticles with a magnetic core. *Journal of Controlled Release* **2001**, *77*, 309–321.

[100]. Deng, Y.H.; Yang, W.L.; Wang, C.C.; Fu, S.K. Responsive poly(NIPAM-co-AA) particle-functionalized magnetic microspheres. *Advanced Materials* **2003**, 15, 1729–1732.

[101]. Kazemi, A.; Lahann, J. Environmentally responsive core/shell particles via electrohydrodynamic co-jetting of fully miscible polymer solutions. *Small* **2008**, *4*, 1756–1762.

[102].Hain, J.; Schrinner, M.; Lu, Y.; Pich, A. Design of multicomponent microgels by selective deposition of nanomaterials. *Small* **2008**, 4, 2016–2024.

[103]. Kim, J.H.; Lee, T.R. Hydrogel-templated growth of large gold nanoparticles: synthesis of thermally responsive hydrogel–nanoparticle composites. *Langmuir* **2007**, *23,* 6504–9.

[104]. Cohnheim, P. C.; Laxly, T. V.; Price, C.; Stubbersfield, R. B. Faraday Discussions of the Chemical Society I 1980, *76*, 1857.

[105]. Brittain, W.J; Minko, S. A structural definition of polymer brushes. *Journal of Polymer Science Part A: Polymer Chemistry* **2007**, *45*, 3505–3512.

[106]. Luzinov, I.; Voronov, A.; Minko, S.; Kraus, R.; Wilke ,W.; Zhuk, A. Encapsulation of fillers with grafted polymers for model composites . *Journal of Applied Polymer Science* **1996**, *61,* 1101–1109.

[107]. Luzinov, I.; Minko, S.; Tsukruk, V. Responsive brush layers: from tailored gradients to reversibly assembled nanoparticles. *Soft Matter* **2008**, *4*, 714–725.

[108]. Advincula, R.C. Surface initiated polymerization from nanoparticle surfaces. *Journal of Dispersion Science and Technology* **2003**, *24*, 343–61.

[109]. Usov, D.; Gruzdev, V.; Nitschke, M.; Stamm, M.; Hoy, O.; Luzinov, I.; Tokarev, I.; Minko, S. Three-dimensional analysis of switching mechanism of mixed polymer brushes. *Macromolecules* **2007**, *40*, 8774–8783.

[110]. Minko S, Muller M, Usov D, Scholl A, Froeck C, Stamm M. Mixed polyelectrolyte brush from oppositely charged polymers for switching of surface charge and composition in aqueous environment. *Physical Review Letters* **2002**, 88, 035502/1–4.

[111]. Brittain, W.J.; Boyes, S.G.; Granville, A.M.; Baum, M.; Mirous, B.K.; Akgun, B.; Zhao, B.; Blickle, C.; Foster, M. D. Surface rearrangement of diblock copolymer brushes—stimuli responsive films. *Advances in Polymer Science* **2006**, *198,* 125–147.

[112]. Spatz, J. P.; Mossmer, S.; Möller, M. Ordered deposition of inorganic clusters from micellar block copolymer films. *Angewandte Chemie International Edition* **1996**, *35*, 1510.

[113]. Platonova, O. A.; Bronstein, L. M.; Sododovnikov, S. P.; Yanovskaya, I. M.; Obolonkova, E. S.; Valetsky, P. M.; Wenz, E.; Antonietti, M. Cobalt nanoparticles in block copolymer micelles: Preparation and properties. *Colloid & Polymer Science* **1997**, *275*, 426-431.

[114]. Mayer, A. B. R.; Mark, J. E. Transition metal nanoparticles protected by amphiphilic block copolymers as tailored catalyst systems. *Colloid & Polymer Science***1997**, *275*, 333-340.

[115]. Mayer, A. B. R.; Mark, J. E. Colloidal gold nanoparticles protected by water-soluble homopolymers and random copolymers. *European Polymer Journal* **1998**, *34* (1), 103–108.

[116]. Seregina, M. V.; Bronstein, L. M.; Platonova, O. A.; Chernyshov, D. M.; Valetsky, P. M.; Wenz, E.; Antonietti, M. Preparation of noble-metal colloids in block copolymer micelles and their catalytic properties in hydrogenation. *Chemistry of Materials* **1997**, *9*, 923–931.

[117]. Shchukin, D.; Patel, A. A.; Sukhorukov, G. B.; Lvov, Y. Nanoassembly of Biodegradable Microcapsules for DNA Encasing. *Journal of the American Chemical Society* **2004**, *126*, 3374-3375.

[118]. Wittemann, A.; Ballauff, M. Secondary structure analysis of proteins embedded in spherical polyelectrolyte brushes by FT-IR spectroscopy. *Analytical Chemistry* **2004**, *76*, 2813 – 2819.

[119]. Wittemann, A.; Ballauff M. Synthesis, Characterization and Behavior in Aqueous Solution of Star-Shaped Poly(acrylic acid). *Macromolecular Bioscience* **2005**, *5*, 13 – 20.

[120]. Puretskiy, N.; Ionov, L. Synthesis of Robust Raspberry-like Particles Using Polymer Brushes. *Langmuir* **2011**, *27* (6), 3006–3011.

CHAPTER 2. RESEARCH SCOPE

Responsive polymer-based colloids (RPBC) are colloidal structures containing responsive polymeric components which are able to adapt their physicochemical properties to the environment by undergoing chemical and/or conformational changes.

Despite extensive research efforts dedicated to the development and characterization of different responsive (smart) polymer-based colloids, little attention has been paid to studies of how the colloids' morphology with regard to the composition of RPBC responsive polymeric component impacts their properties and applications. Polymeric colloids (e.g. micelles) fabricated from common block copolymers are often lacking thermodynamic stability or the ability to regulate one or more crucial functional parameters due to the various limitations, including limitation on length and number of fragments. To address these issues, it is often practical to design more complex polymeric morphologies or to combine the polymers with other organic or inorganic components.

In this study it was assumed that the increasing morphological complexity of the developed RPBCs can help to broaden their functionality and fabricate a variety of polymer-based colloid materials, specifically for drug delivery and bioconversion applications.

The goal of the current work is to develop and characterize several groups of RPBC with different morphological complexity and explore their potential in drug delivery and bioconversion. The role of RPBC morphology for these specific applications is discussed in details. Three groups of RPBC were fabricated: i. polymeric micelles; ii. mixed polymeric micelles; iii. hybrid polymer-inorganic particles. All fabricated RPBCs contain a polymeric component in their structure. The dissertation investigates how the changes of the responsive polymeric component are reflected in morphological properties of RPBC.

Chapter 1 of the dissertation introduces major polymer-based colloids reported in literature, their properties and possible applications. In addition, this chapter provides a literature overview on three RPBC groups described in the dissertation.

Chapter 3 is dedicated to the study of morphology and responsive behavior of the first RPBC group in this dissertation, polymeric micelles fabricated from amphiphilic invertible polymers (AIPs) synthesized in our group. AIPs macromolecules self-assemble into invertible micellar assemblies (IMAs) in solvents of different polarity. IMAs are able to rapidly change their conformation and structure in response to changes in solvent polarity. The structural study was conducted for detailed exploration of morphology and invertibility of IMAs. Small-angle neutron scattering (SANS) was used to study the morphology of IMAs at different concentrations, temperatures in selected solvents (water and toluene).

Chapter 4 explores data on the feasibility of IMAs in drug delivery applications. In this chapter IMAs were used to solubilize two different water-insoluble cargo molecules (Sudan Red B and dibutyl phthalate) and poorly water-soluble drug (curcumin). The solubilization of Sudan Red B and dibutyl phthalate was used to determine the role of cargo’s chemical structure and cargo's limited aqueous solubility for the solubilization mechanism. IMAs loaded with drug (curcumin) were tested in vitro to study their therapeutic effect on osteosarcoma (bone cancer) cells.

Chapters 5 and 6 are dedicated to the studies of mixed micelles, another RPBC group with more complex morphology. They were fabricated from AIPs and amphiphilic oligomers synthesized in this work from pyromellitic dianhydride, polyethylene glycol methyl ethers, and alkanols/cholesterol. These chapters describe the synthesis and characterization of amphiphilic oligomers. In addition, Chapter 5 includes the ‘proof of concept’ study on the fabrication of mixed micelles from selected AIP macromolecules and amphiphilic oligomers containing cholesterol and on loading these mixed micelles with drug (curcumin) molecules.

Even more complex colloids, hybrid polymer-inorganic particles representing the third RPBC group are described in Chapters 7 and 8 of this dissertation. These colloids were designed as core–shell particles with superparamagnetic core engulfed by grafted polymer brushes. The particles were loaded with enzymes (cellulases) and, thus, turned into a new material, enzymogels, for cellulose bioconversion. Chapter 7 describes the synthesis and characterization of the enzymogel particles and presents novel phase boundary catalysis mechanism based on the discovered in this work mobility of the enzymes immobilized in the polymeric brushes of enzymogels. In Chapter 8, kinetic studies were conducted to investigate role of the mobility of the immobilized enzymes for their hydrolytic activity. For this purpose, the hydrolytic performance of enzymogels was compared to the latter of free enzymes and enzymes chemically grafted to dispersed carrier particles (silica).

CHAPTER 3. SOLVENT-RESPONSIVE SELF-ASSEMBLY OF AMPHIPHILIC INVERTIBLE POLYMERS DETERMINED WITH SANS

(Published in *Langmuir* **2014**, *30*, 3310−3318)

3.1. Abstract

Amphiphilic invertible polymers (AIPs) are a new class of macromolecules that self-assemble into micellar structures and rapidly change structure in response to changes in solvent polarity. Using small angle neutron scattering (SANS) data, we obtained a quantitative description of the invertible micellar assemblies (IMAs). The detailed composition and size of the assemblies (including the effect of temperature) were measured in aqueous and toluene polymer solutions. The results show that the invertible macromolecules self-assemble into cylindrical core−shell micellar structures. The composition of the IMAs in aqueous and toluene solutions was used to reveal the inversion mechanism by changing the polarity of the medium. Our experiments demonstrate that AIP unimers self-assemble into IMAs in aqueous solution, predominantly through interactions between the hydrophobic moieties of macromolecules. The hydrophobic effect (or solvophobic interaction) is the major driving force for self-assembly. When the polarity of the environment is changed from polar to nonpolar, poly(ethylene glycol) (PEG) and aliphatic dicarboxylic acid fragments of AIP macromolecules tend to replace each other in the core and the shell of the IMAs. However, neither the interior nor the exterior of the IMAs consists of fragments of a single component of the macromolecule. In aqueous solution, with the temperature increasing from 15 to 35°C, the IMAs' mixed core from aliphatic dicarboxylic acid and PEG moieties and PEG based shell change the structure. As a result of the

progressive dehydration of the macromolecules, the hydration level (water content) in the micellar core decreases at 25°C, followed by dehydrated PEG fragments entering the interior of the IMAs when the temperature increases to 35°C.

3.2. Introduction

Macromolecular conformation in solution is governed by the balance between polymer fragments' interactions with the solvent and interactions between the fragments themselves [1]. Amphiphilic block copolymer macromolecules contain chemically different fragments ("building blocks") that contribute to both types of macromolecular interactions in solution. This factor makes adjusting the balance between the two types of interactions for block copolymers even more complex and results in the macromolecules' tendency to self-assemble into micelles in selective solvents (similarly to low-molecular-weight surfactants in solution). In a solvent that is a good choice for one of the blocks but a rather poor one for the other, block segregation and microphase separation occur. As the concentration increases, the block copolymer micelles aggregate into micellar structures as a consequence of the self-assembling tendency. Thus, diverse ordered morphologies are formed, such as spheres, cylinders, lamellae, or various bicontinuous microstructures [3, 4]. The physical and colloidal properties of the micellar aggregates can be tuned by varying the structure of the macromolecules, the concentration, and the temperature to target a much broader range of applications. These applications, for example, involve potential drug and DNA carriers, nanoreactors, and nanocontainers [1, 5].

Linear block copolymers typically self-assemble into spherical [16−12] or cylindrical [13−17] structures with a corona from the highly solvated fragments of one block and a closely packed inner core from other block fragments [18, 19]. Many reports have shown that a much broader range of possible morphologies with different sizes of microdomains are found for nonlinear block copolymers, multiblock copolymers, and polymer blends [20−22]. In terms of applications using block copolymers, the right building blocks for macromolecules must be found, and the conditions of their self-assembly into aggregates must be controlled to target the desired stable morphology of the block copolymer micellar assemblies.

Using a selective solvent is one approach to developing size controlled polymeric assemblies (including micellar assemblies) as well as nanoscale materials based on these assemblies [24 − 26]. In many applications, solvents are present during the processing or in the final material, thus introducing additional conformational freedom of block copolymer macromolecular chains.

Recently, we developed a library of amphiphilic invertible polymers (AIPs), a new class of macromolecules that can self-assemble into micellar structures and rapidly change structure in response to changes in solvent polarity (Fig.3.1) [27−34]. The major difference that distinguishes the new macromolecules from the current block copolymers is that the incompatibility of the fragments in a backbone is achieved at a much smaller fragment length. It allows greater tunability of the micellar assembly formation and a fast response to the changing polarity of the medium [27−29]. The latter is approached by alternating the distribution of hydrophilic and hydrophobic short fragments with well-defined length in AIP macromolecules (Fig.3.1A). The difference in the hydrophilic−lipophilic balance (HLB) affects the AIP surface activity and the ability to self - assemble [30−32]. Using 1H NMR spectroscopy, we revealed environment-dependent self-assembly for various IMAs with various HLBs [32−34]. Macromolecules form micellar assemblies with unique inversion behavior when the solvent polarity is changed (Fig.3.1B) [28−34].

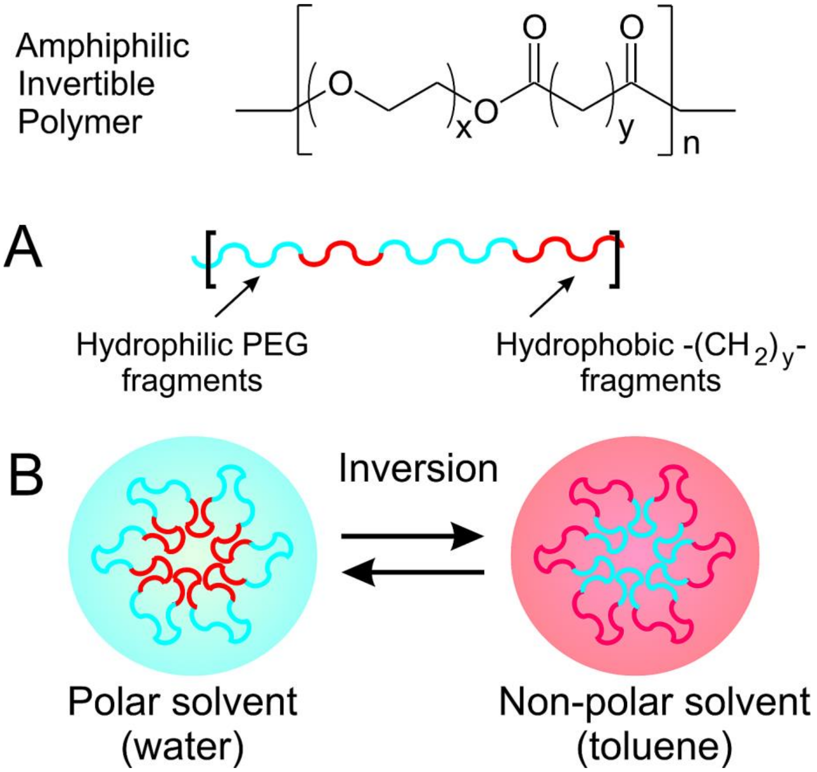

Fig.3.1. AIP structure and micellar architecture in polar and nonpolar solvents.

We observed that, in dilute polymer solutions in toluene, the exterior of the micelles is made of lipophilic -$(CH_2)_n$- moieties, and the interior consists of polar PEG fragments [32]. In turn, micelles with a hydrophobic inner part and a hydrophilic exterior are formed in aqueous solution (Fig.3.1B). With increasing polymer concentration, the hydrophilic and hydrophobic domains are formed in toluene and an aqueous medium as a result of unimer aggregation. Furthermore, the ability of micellar assemblies to sequester hydrophobic molecules in water has been observed. The loaded micellar assemblies cross the polar/nonpolar interface and transfer their cargo to a nonpolar phase [35, 36]. The ability to encapsulate molecules that are insoluble in nonpolar solvents has also been revealed [33]. The amount transferred through the polar/nonpolar interface and encapsulated in a nonpolar solvent material has been shown to depend primarily on the micellar loading capacity. The loading capacity is mainly governed by the hydrophilic lipophilic balance of the AIP macromolecules [35, 36]. In a nonpolar medium, it has been additionally demonstrated that the micellar exterior and interior can interact with “guest” molecules, thus potentially increasing the encapsulation and transferring capacity of micellar assemblies.

Although ^{1}H NMR spectroscopy is commonly used to demonstrate polymer self-assembly and to determine the composition of the assemblies [37−39], the small-angle neutron scattering (SANS) technique is advantageous because it can determine the shape, size, internal structure, and composition of the scattering objects (micellar assemblies) [40]. Both techniques are often complementary, as demonstrated by the fact that NMR spectroscopy measurements can be helpful in producing an accurate model for SANS data. At the same time, SANS can provide information on the micellar structure and intermicellar interactions in solution because the scattering curves are governed by the micellar size and morphology as well as by their contrast with solvents [41−44]. For example, the core− corona structure of polymeric micellar assemblies in solution can be described in terms of the properties of the core and the corona as a result of monitoring the deuterated solvent distribution between the core and the corona [45, 46]. As a rule, this distribution is uneven, with a more solvated corona and “drier” core domains.

In this work, motivated by the recently discovered properties of IMAs and their potential inversion behavior in solvents of different polarities, we studied SANS on AIP micellar assemblies in aqueous and toluene solutions of various concentrations at various temperatures. Our main interest was in using SANS to establish the inversion behavior of micellar assemblies when the solvent polarity was changed and in determining the assemblies’ size and morphology for AIPs with different chemical structures.

3. 3. Experimental

3.3.1. Materials

Poly(ethylene glycol) (PEG, molecular weights 300, 600, and 1000 g/mol), sebacic acid, toluene-d8, and deuterium oxide were purchased from Sigma-Aldrich. Dodecanedioic acid was obtained from TCI.

AIP Synthesis. Amphiphilic invertible polymers (Table 3.1) were synthesized using previously reported methods [27,47] from PEG-300 and sebacic acid (S3), PEG-600 and sebacic acid (S6), PEG-1000 and sebacic acid (S10), PEG-300 and dodecanedioic acid (D3), and PEG-1000 and dodecanedioic acid (D10) using the polycondensation of poly(ethylene glycol)s with aliphatic dicarboxylic acids.

Table 3.1. Characteristics of the AIPs.[a].

AIPs	**HLB**	**M_n, g/mol**	**PDI**	**x**	**y**
S3	10.1	6.900	1.58	6.4	8
S6	12.4	6.500	1.42	13.2	8
S10	15.4	6.000	1.59	22.3	8
D3	9.2	5.500	1.44	6.4	10
D10	14.4	5.000	1.53	22.3	10

[a] x and y are the number of ethylene oxide units in hydrophilic fragments and methylene groups in hydrophobic fragments in the main AIP backbone, respectively (corresponding to the chemical structure in Fig.3.1).

3.3.2. SANS Measurements

The measurements were performed at the Oak Ridge National Laboratory, U.S. Department of Energy, Knoxville, TN, using a general-purpose small-angle neutron scattering diffractometer (CG-2). Scattering intensity data were recorded at various temperatures in the range of 15–35°C (most experiments at 25°C). Two detector settings (1.5 and 20 m) and a neutron wavelength of $\lambda = 6$ Å were used to cover scattering vectors ranging from 0.004 to 1.000 Å^{-1}. The intensity was recorded with an area detector over 5.1×5.1 cm^2. The AIP solutions at varying concentrations in deuterated water and toluene were placed in 0.5- cm-long quartz "banjo" cells sealed with parafilm.

3.3.3. SANS Data Reduction

The scattering patterns were radially transformed into 1D scattering functions. Corrections for inhomogeneity in the detector response, empty cell scattering, sample transmission, background noise, and solvent interference were applied. The resulting corrected intensities were normalized to absolute cross-section units with the uncertainty of absolute calibration estimated at 10%. The scattering intensity, I(q), according to the Bragg equation, is shown as a function of the modulus of the scattering vector

$$q = 4\pi(\sin \theta)/\lambda \qquad (3.1)$$

where 2θ is the scattering angle and λ is the neutron wavelength [46,48-51].

For the data analysis, the experimental points were fitted using nonlinear least-squares routine developed at Oak Ridge National Laboratory according to previously reported procedures [46, 48–51]. The scattering data were modeled using appropriate analytical models and optimized with a weighted least-squares procedure.

3.3.4. SANS Data Analysis

SANS data were analyzed with model independent approaches (e.g., the power law approach and Guinier analysis) and subsequent model-dependent analysis.

Porod Plots (Power Law Approach). A power law was used as a primary model-independent approach to estimate the morphology of structures of AIPs in D_2O and toluene-d_8 solutions. The Porod exponents have been determined as a slope of the scattering curve plotted in logarithmic coordinates at high scattering angles.

Guinier Analysis. Three types of Guinier approximations (for spherical, cylindrical (rod-like), and flat objects) were applied to estimate the possible scattering object shape. The validity of the Guinier approximation was assessed using the criteria $q_{max} \times R_g \approx 1$ for spherical objects, $q_{max} \times R_c < 1$ for cylindrical objects, and $q_{max} \times R_t < 1$ for flat objects, where R_c and R_t are the radius of gyration of the cylindrical and the flat scattering object, respectively. Subsequently, a model-dependent analysis of scattering data was used to determine the size and morphology of the micellar assemblies [46−48].

Form-Factor for Core−Shell Cylinders. In this study, the experimental SANS data were characterized using models developed for the core−shell cylinder structures (Fig.3.2) [49, 50]. The following is the form factor function for the core−shell cylinder model:

$$P(q) = \int_0^{\pi/2} \sin\theta d\theta \left[V_c(\rho_c - \rho_o) \frac{\sin\frac{qH_c\cos\theta}{2}}{\frac{qH\cos\theta}{2}} \frac{2J_1(qR_c\sin\theta)}{QR_c\sin\theta} + V_s(\rho_c - \rho_s) \frac{\sin\frac{qH_s\cos\theta}{2}}{\frac{qH_s\cos\theta}{2}} \frac{2J_1(qR\ \sin\theta)}{QR\sin\theta} \right]^2 \quad (3.2)$$

$$V_c = \pi R_c^2 H_x \ (3), \qquad V_s = \pi(r+t)^2 H \quad (3.4)$$

where $J_1(x)$ is the first-order Bessel function, θ is the angle between the cylinder axis and the scattering vector, R is the total radius of the core−shell structure, and R_c and H are the radius and length of the core, respectively.

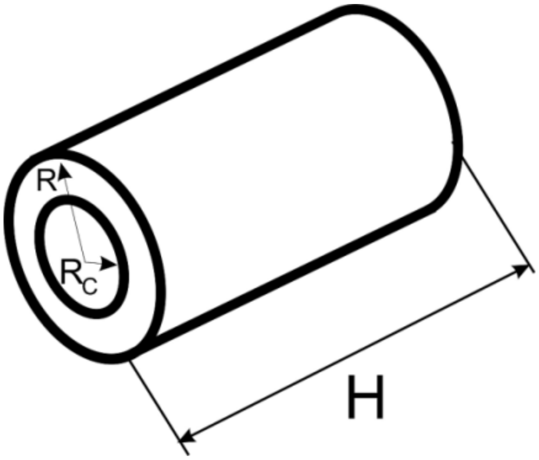

Fig.3.2. Core−shell cylinder structure.

The characteristic scattering length density (SLD) of the hydrophilic (poly(ethylene glycol)) and hydrophobic (aliphatic dicarboxylic acids) fragments of the AIP macromolecules shows that a measurable contrast between the domains can be provided by SANS measurements after the fragments self-assemble (Table 3.2). Using the scattering length density of the AIP fragments and solvents, we can estimate the hydrophilic (PEG) and hydrophobic (aliphatic dicarboxylic acids) fragment content in self-assembled micellar domains (core or shell). The average discrepancy between experimental data and fitted data is $\chi = 1.59 \pm 0.05$.

Table 3.2. Scattering length density of AIP fragments and solvents [50-53].

Fragment	**$\rho \times 10^{-10}$, cm^{-2}**
PEG 300	2.64
PEG 600	1.82
PEG 1,000	1.62
Diester of sebacic acid	-0.49
Diester of dodecanedioic acid	-0.50
D_2O (deuterium oxide)	6.37
$C_6D_5CD_3$ (toluene-d8)	5.66

3.4. Results and Discussion

In this work, we conducted a SANS study on aqueous and toluene polymer solutions of various concentrations (0.1−5% w/v) at various temperatures (15−35°C). Our goal was to determine the size and morphology of the micellar assemblies from polymers with different chemical structures and to establish their inversion when the solvent polarity is changed. Two levels of modeling were used for the interpretation of the SANS data obtained. First, model-independent (Porod (power law) and Guinier) approximations were applied to demonstrate the aggregation of the AIP macromolecules in solvents strongly differing in polarity and to determine the overall geometry of micellar assemblies. Afterward, the dimensions of the micellar assemblies were estimated using model-dependent analysis. To confirm the ability of the assemblies to invert by changing polarity, the size and composition of hydrophilic and hydrophobic micellar domains from selected AIPs were approached in polar (water) and nonpolar (toluene) media.

3.4.1. Model-Independent Analysis

Using Guinier analysis, one can determine the radius of gyration (R_g) of an arbitrarily shaped (isotropic) particle from experimental SANS patterns [46,48]. At the same time, Porod's approximation can be applied to the initial analysis of the particle geometry in solution. In this work, these two model-independent approaches were employed to demonstrate the aggregation of AIP unimolecular micelles into micellar assemblies in solution at increasing concentration in both polar (water) and nonpolar (toluene) media.

Although the power law does not provide direct information on the size and morphology of experimental scattering objects in SANS, the overall shape of these objects can be determined using this analysis. Afterward, the obtained information can be used in model-dependent analysis, particularly to determine the size and the morphology of the self-assembled structures.

Using the experimental SANS patterns, we calculated Porod exponents for AIP solutions of various concentrations in water and toluene and used this parameter as a primary criterion for the characterization of the overall AIP geometry. Thus, an exponent value of −1 indicates the presence of cylinder structures, −2 implies the presence of 2D (planar or flat) structures, and a value between −3 and −4 refers to the self-assembly of 2D aggregates into 3D superstructures [54]. Porod exponent values of 0−0.7 were assumed to be the result of the scattering of a transitional structure where no objects with a distinct shape are present if confirmed with Guinier analysis. A drastic change in AIP micellar geometry was observed for most aqueous polymer solutions with changing AIP concentration (Fig.3.3).

The calculated power-law approximation data are in good agreement with the results obtained using Guinier analysis. In particular, the latter analysis carried out for rod-like structures confirms the presence of elongated structures in AIP solutions with a calculated Porod slope parameter approaching −1 (flat cylindrical structure). Guinier analysis of 2D (sheet-like) polymer structures meets the validating condition (qmax × Rt < 1) for AIP assemblies with a Porod slope parameter close to −2 (2D aggregates).

The modeling tools were also applied in this study to examine macromolecule behavior in toluene solutions at different concentrations. The obtained results show that the AIP macromolecules form cylindrical structures in toluene at higher concentrations (at least 1% w/v), and these structures do not undergo further aggregation under the chosen experimental conditions (Fig.3.3).

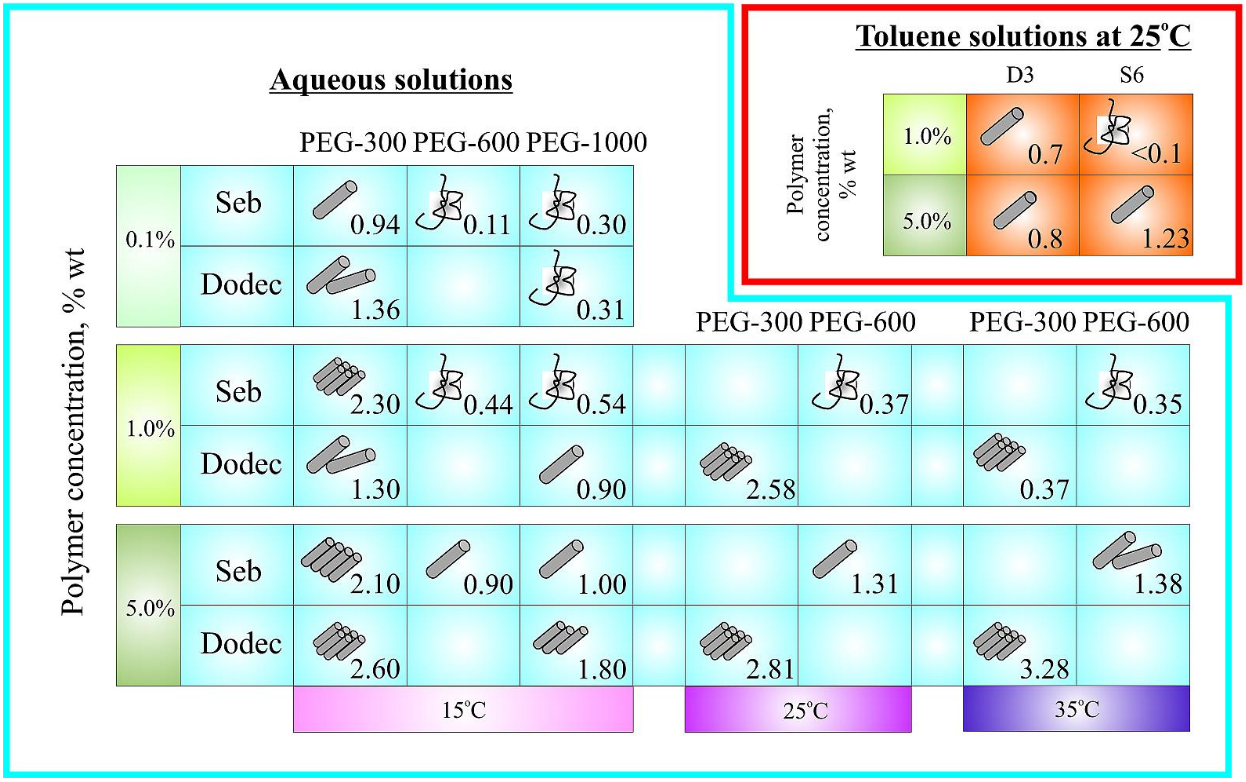

Fig.3.3. Absolute values of Porod exponents determined for AIP aqueous and toluene solutions of various polymer concentrations. (Each box contains the expected micelle structure and absolute value of the Porod parameter).

Although the Porod and Guinier approximations successfully provide information on the formation of cylindrical morphology for AIP assemblies at certain concentrations in aqueous and toluene solutions, these modeling tools cannot give insight into the dimensions and composition of the micellar assemblies. These parameters were approached in this study using model dependent SANS analysis.

3.4.2. Model-Dependent Analysis

In the model-independent analysis, we observed that AIP macromolecules with lower HLB (D3 and S3) self-assemble in cylindrical structures in water at a lower concentration (0.1% w/v, Fig.3.3). These two polymer samples were chosen for model-dependent analysis along with

S6, D10, and S10, where the presence of cylindrical structures was justified in aqueous solution at higher concentrations. To confirm the ability of polymer micellar assemblies to invert by changing polarity, model-dependent analysis was performed for macromolecules of 5%w/v S6 aqueous and toluene solutions. The same polymer sample (5%w/v S6) was chosen to study the effect of temperature on AIP self-assembly in aqueous solution.

Generally, model-dependent SANS analysis compares experimental scattering data and theoretical density profiles or structure factors of self-assemblies and accounts for the form factor contribution to the description of the scattering data. In this work, a cylindrical core−shell form factor function was used to evaluate the composition of the AIP micellar domains formed in water and toluene in terms of the distribution of the hydrophilic and hydrophobic macromolecular fragments. Using the same model, we also obtained information on the size of the micellar domains for various polymers at various concentrations and on the effect of temperature on AIP self-assembly in aqueous solutions.

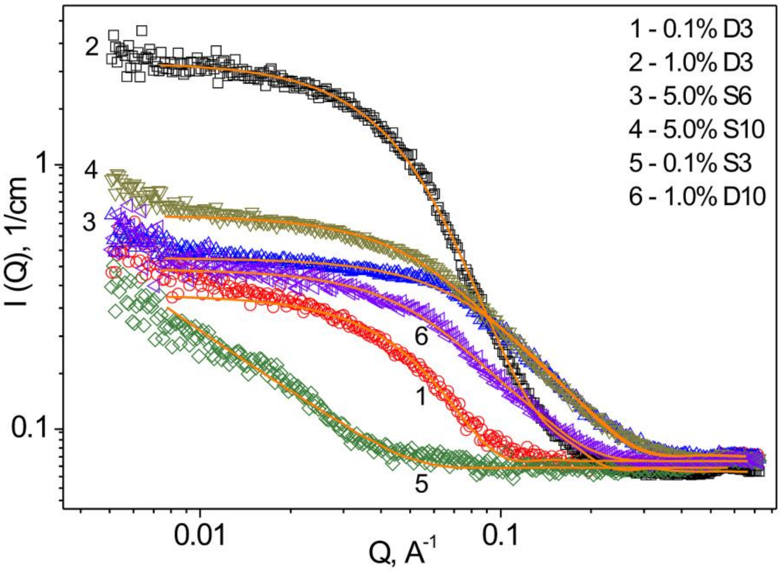

Fig.3.4. SANS scattering curves for various AIP micellar solutions in D_2O at 15°C. Solid lines represent the fits obtained using a core−shell cylindrical form factor.

Fig.3.4 shows SANS scattering plots for various AIPs at 0.1; 1.0 and 5.0%w/v micellar solutions in D_2O at 15°C and the fits obtained using a core−shell cylindrical form factor. Using the scattering data, the total radius of the core−shell micellar assemblies, R, the shell thickness, h, and the radius and the length of the core, Rc and H, respectively, were calculated (Table 3.3).

Table 3.3. Parameters of AIP self-assembly in aqueous solution at 15°C (% w/v).

Parameter	**D3 (0.1%)**	**D3 (1%)**	**D10 (1%)**	**S3 (0.1%)**	**S6 (5%)**	**S10 (5%)**
R (nm)[a]	5.2	3.0	2.5	3.4	2.3	2.8
R_c (nm)[a]	3.3	1.5	1.4	1.6	0.8	1.0
h (nm) [b]*	1.9	1.5	1.1	1.8	1.5	1.8
H (nm)[c]	7.2	6.8	7.5	12.8	7.8	7.6
ρ_{core} ($\times 10^{-10}$ cm^{-2}) [d]	1.5	0.7	4.3	2.5	4.7	5.0
ρ_{shell}($\times 10^{-10}$ cm^{-2}) [d]	4.2	4.9	4.8	4.2	5.4	5.6

*h is the shell thickness (R − Rc) (nm). Standard deviations do not exceed [a] 2.5%; [c] 7.1%. [d] 2.0%. [e] 2.5%.

A comparison of the ρ_{core} values for the polymer micelles formed in aqueous solutions and those of the hydrophobic fragments, sebacic and dodecanedioic acid moieties (Table 3.3), indicates that the interior of the assemblies from more hydrophobic D3/S3 polymers mostly contains fragments of aliphatic dicarboxylic acids (increasing with polymer concentration), but some water and/or PEG fragments are located in the micellar interior as well. Obviously, the water/PEG content in the mixed micellar core increases with increasing PEG fragment length in AIP macromolecules (as demonstrated for D10, S6, and S10).

SLD values for the shell of micellar assemblies in Table 3.3 are close to the ρ value of water (Table 3.2). It could be concluded that the shell of the AIP assemblies contains PEG fragments that are highly solvated in water, so hydrophobic fragments of AIP macromolecules are all obviously located in the micellar core. The size of the assemblies (Table 3.3) does not depend substantially on the chemical structure of the polymer but rather changes with the change in length of the hydrophobic fragment in the macromolecular backbone. S3 forms significantly larger structures at the same concentration compared to D3.

This may indicate that AIP unimers self-assemble into micellar assemblies in aqueous solution, predominantly through interactions between their hydrophobic moieties. In fact, similar results were reported in the literature on self-assemblies from Pluronics, amphiphilic block copolymers from PEG and poly(propylene oxide) blocks [25,26]. The morphology of Pluronic assemblies is determined by interactions between their hydrophobic poly(propylene oxide) blocks rather than between hydrophilic PEG sequences.

Similar to Pluronics, the hydrophobic effect (or solvophobic interactions) [55] can be considered to be the major driving force for the self-assembly of AIP micelles. The main reason for the low solubility of nonpolar substances in water, the hydrophobic effect, generally reflects interactions linked to the reorganization of water molecules. What actually drives these solvophobic interactions is neither a repulsion between water molecules and polymer chains nor strong interaction between the macromolecules themselves but instead the decreasing entropy of the system as a result of the increasing number of ordered elements in the structure of water. When less-polar macromolecules (compared to water) transfer from their own phase into aqueous solution, the free energy of the system, $\Delta G = \Delta H - T\Delta S$, increases, making it thermodynamically less favorable [56, 57]. At room temperature, the enthalpy change (ΔH) is negligible, but the entropy change (ΔS) becomes negative as a result of the reorganization of the hydrogen bonds and the changes in the structure of water [57]. In fact, the interaction between the water molecules is much stronger when compared to the polymer−polymer and polymer−water interactions.

Obviously, when AIP macromolecules enter the aqueous solution, a specific interface forms between them and water. The water molecules form cages in the spatial pattern of water where the dissolved AIP macromolecules are localized, leading to the entropy decrease [55, 57]. The clustering together of the macromolecules (self-assembly) reduces the amount of contact surface area (interface area) between the macromolecules and the aqueous phase and turns some free water molecules from their more ordered arrangement at the interface. Because of the solvophobic interactions, the water tends to exclude less-polar macromolecules and increase (regain) some entropy. It is then obvious that this effect is stronger for the AIP macromolecules with a greater number of hydrophobic methylene -CH_2- groups in the aliphatic dicarboxylic acid moieties. The longer -$(CH_2)_{10}$- sequences of D3 obviously undergo stronger interactions compared to shorter -$(CH_2)_8$- fragments of S3, resulting in the formation of smaller assemblies.

To this end, the hydrophobic effect reflects this tendency of water to provide the formation on the most compact macromolecular structures (assemblies) from AIP as a result of the presence of hydrophobic fragments and facilitate the smallest possible contact between these assemblies and water. The presence of even two additional methylene groups in the hydrophobic fragment of the AIP [$(CH_2)_{10}$ vs $(CH_2)_8$] will result in a greater entropy of water and a more favorable thermodynamic state of the system by excluding the $(CH_2)_{10}$ fragments from water.

With the established formation peculiarities of AIP self-assemblies in aqueous solution, the mechanism of their inversion by changing solvent polarity was considered next. Our recent ^{1}H NMR spectroscopy study [32, 33] shows that self-assembled AIP macromolecules undergo conformational changes in solvents whose polarity strongly differs. This makes the micellar assemblies responsive to the changing polarity of the environment. We assume that, when the solvent polarity changes (for example, from polar water to nonpolar toluene), the aliphatic fragments of dicarboxylic acids, which are insoluble in water, may move from the hydrophobic core to the assembly's shell. Although the PEGs (300, 600, and 1000 g/ mol) are soluble in toluene, it is possible that when the medium changes from water to toluene, entirely hydrophilic PEG fragments may relocate to the assembly's interior to form a micellar core in toluene. The reverse effect occurs when the nonpolar solvent is further replaced with the polar one. Using experimental scattering curves recorded in toluene and water, we determined the fraction change of each species in the shell and core region of 5% w/v S6 micellar solutions.

Comparing the scattering curves with the data obtained using the core − shell cylindrical form factor reveals the formation of cylindrical micellar assemblies for 5% w/v S6 in a polar aqueous medium and a nonpolar organic solvent (Fig.3.5). Using the scattering plots recorded for polymer solutions in water and toluene at 25°C, the shell thickness, h, and the radius and length of the core, Rc and H, were calculated for the two solvents (Table 3.4).

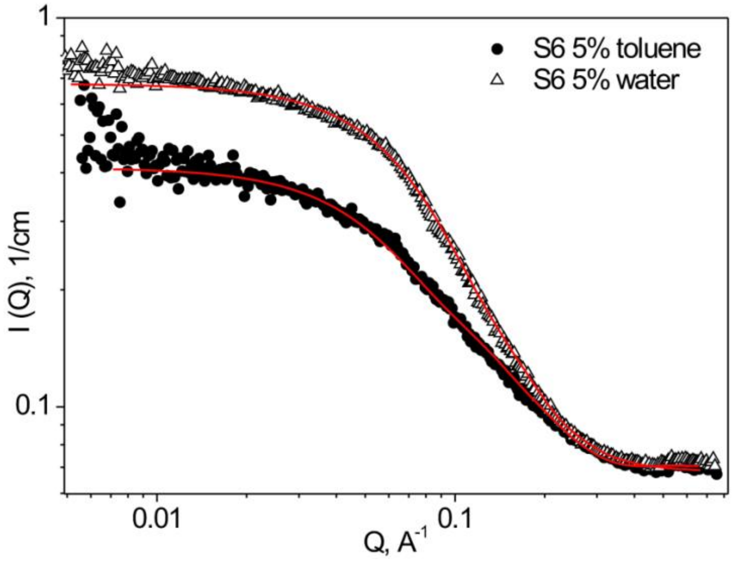

Fig.3.5. SANS scattering curves for micellar solutions of S6 (5% w/v) in water and toluene at 25°C. Solid lines represent the fits obtained using a core−shell cylindrical form factor.

Table 3.4. Parameters of S6 (5% w/v) self-assemblies in aqueous and toluene solution at 25°C and schematic assembly structures in water and toluene (inset).

Parameter	**S6 (5% w/v)**		
	toluene	**water**	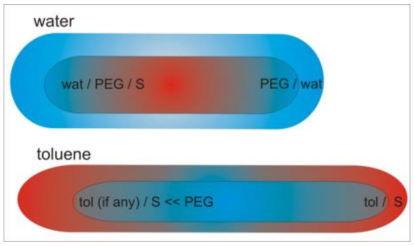
ρ_{core} ($\times 10^{-10}$ cm^{-2})	1.6	3.4	
ρ_{shell} ($\times 10^{-10}$ cm^{-2})	2.8	4.2	
R_c (nm) core radius*	0.7	2.2	
h (nm) shell thickness ^{a} *	1.2	1.0	
H (nm) length*	12.3	10.4	

[a] h is the shell thickness $(R - R_c)$ (nm), and standard deviations do not exceed 7%* and 1%**.

Although the size of the micellar assemblies in the two solvents does not differ significantly (being slightly larger in toluene), there is a notable difference in the location of the hydrophilic and hydrophobic fragments within the structure of self-assemblies when the polarity of the environment has been changed. If the micellar core/shell SLD values are compared to those of macromolecular components and solvents (Table 3.2), then one can conclude that PEG and sebacic acid fragments of AIP macromolecules indeed tend to replace each other in the core and the shell by changing the medium from water to toluene. Similar to experiments in water at 15°C, the micellar shell exclusively contains PEG fragments solvated in water; thus, all sebacic moieties' units are obviously located in the core. Furthermore, the sebacic acid fragments, PEG, and water are found in the micellar interior as well, as the SLD value of the core shows.

When the micellar assemblies are formed in toluene, the PEG species move from the shell to the interior of the self-assemblies, and hydrophobic dicarboxylic acid moieties tend to relocate from the core to the exterior. As a result, the micellar interior contains mostly PEG fragments (the SLD of the core is very similar to that of PEG-600; see Table 3.2), with a small amount of sebacic acid and very little toluene, if any. A comparison of the ρ_{shell} value of the micelles formed in toluene and those of the solvent and macromolecular components (PEG-600, sebacic acid, and toluene) indicates that the shell of the S6 assemblies contains solvated sebacic acid fragments. However, neither the interior nor the exterior of the assemblies consists of just a single component of the macromolecule. Hydrophilic and hydrophobic fragments are present in the mixed micellar core and shell in the nonpolar solvent. The assemblies' S6 structures that are inverted as a result of changes in the polarity of the environment are schematically shown in an inset of Table 3.4.

In fact, using the ^{1}H NMR technique, we recently studied the solubilization of hydrophobic cyclohexasilane, Si_6H_{12}, in micellar assemblies in toluene and determined the presence of "guest" molecules in the core and shell regions. This finding is in good agreement with the observation that the hydrophobic fragments of AIP macromolecules are present not only in the exterior but also in the micellar assemblies' interior [33].

Previously, self-assembly over a wide range of polymer concentrations using ^{1}H NMR spectroscopy in aqueous and toluene media for S6 was studied [32], and similar behavior exhibited by hydrophilic and hydrophobic fragments of AIP was observed during the macromolecule inversion.

Because one of our goals was to establish the formation of micellar assemblies under different experimental conditions, we performed SANS measurements on 5% w/v S6 aqueous solutions at three different temperatures: 15, 25, and 35°C. Our interest was in how the size and composition of the assemblies (core and shell) change when macromolecules self-assemble in aqueous solution at various temperatures.

Typical neutron scattering curves with the fits obtained using a core−shell cylindrical form factor recorded for 5% w/v aqueous solutions of S6 at three different temperatures are shown in Fig.3.6. There is a good correlation between the modeling and experimental results for

S6. The SLD parameters for the S6 self-assemblies at various temperatures are presented in Table 3.5.

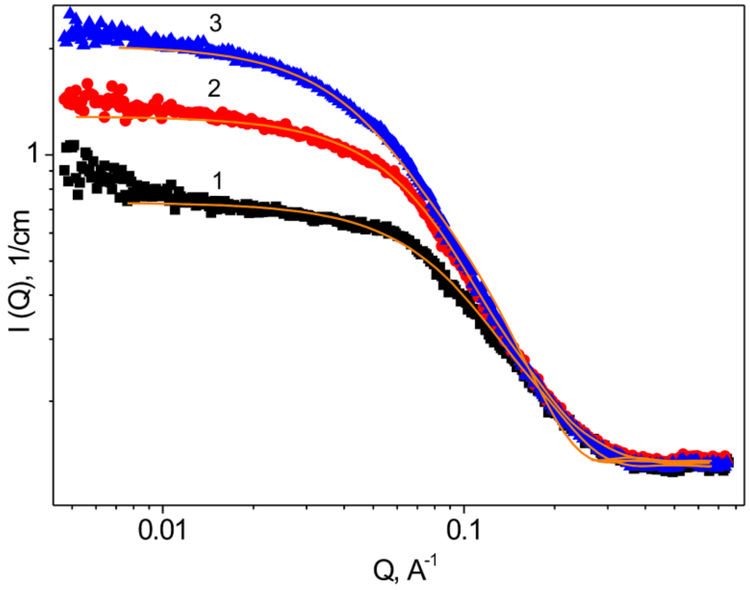

Fig.3.6. SANS scattering curves for D_2O micellar solutions of 5% w/v S6 at 1−15; 2−25 and 3−35°C. Solid lines represent the fits obtained using a core−shell cylindrical form factor.

Table 3.5. SLDs of 5% w/v S6 self-assemblies at various temperatures in aqueous solution.

Parameter	**15°C**	**25°C**	**35°C**
ρ_{core} ($\times 10^{-10}$ cm^{-2})	4.7	3.4	4.5
ρ_{shell} ($\times 10^{-10}$ cm^{-2})	5.4	4.2	5.7

[a] Standard deviations do not exceed 1.0%.

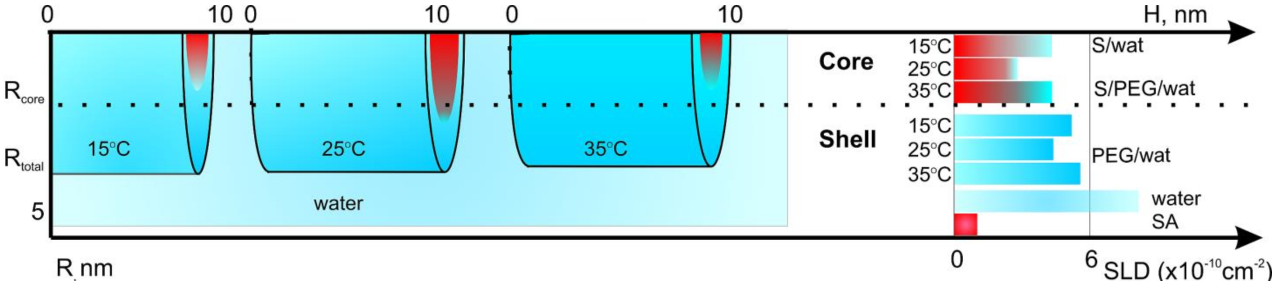

Fig.3.7. Scheme of core and the shell changes for S6 (5% w/v) micellar assemblies by changing the temperature in aqueous solution.

The ρ_{core} value of the assemblies becomes smaller at 25°C compared to the value recorded at 15°C. This indicates that micellar assemblies are initially well hydrated at 15°C, but when the temperature increases, the driving phenomenon for the ρ_{core} decrease is the progressive loss of water. In fact, the micellar shell from PEG is always well-hydrated and has a higher water fraction [58]. The micellar core is composed of the aliphatic dicarboxylic acid fragments, PEG, and water, and this aqueous fraction in the core decreases when the temperature increases, resulting in a ρ_{core} value drop at 25°C. The following increase in the ρ_{core} value due to the temperature of 35°C can be attributed to the changes in the core and shell composition.

One can expect that the progressive dehydration of the core with further increasing temperature leads to the stronger interaction of hydrophobic fragments, closely packed inner-core hydrophobic regions, and finally PEG fragments from the shell (where a loss of water occurs as well) entering the interior of the assemblies. Thus, when the temperature is increased from 25°C to 35°C, the ρ_{core} value increases as a result of the increasing presence of dehydrated PEG species contributing to the formation of the interior of the assemblies.

In Fig.3.7, we demonstrate the scheme of changes in the composition of the fragments forming the S6 core and the shell by changing the temperature of the aqueous solution. Although the core consists of polymer fragments and water molecules at 15°C, it starts to dry out at 25°C. More PEG fragments enter the core as a result of further increases in the temperature from 25 to 35°C.

3.5. Conclusions

Amphiphilic invertible polymers (AIPs) are a new class of macromolecules that self-assemble and rapidly change structure in response to changes in solvent polarity. The difference in the hydrophilic−lipophilic balance of the macromolecule affects the AIP surface activity and their ability to self-assemble into invertible micellar assemblies (IMAs). Using SANS measurements and their fitting according to a core−shell cylindrical model, detailed quantitative parameters of the IMA structures were obtained. The size and detailed composition of the micelles (including the effect of temperature on the size and composition of the assemblies) was measured in aqueous and toluene polymer solutions.

The hydrophobic effect (or solvophobic interactions) is the major driving force for the AIP self-assembly in water. The macromolecules self-assemble in aqueous solution, predominantly through block segregation and microphase separation. The presence of two additional methylene groups in the hydrophobic fragment of the AIP results in a more favorable state of the system by excluding the longer fragments from water into the micellar core. The longer -$(CH_2)_{10}$- sequences of dodecanedioic acid undergo stronger interactions compared to shorter -$(CH_2)_8$- fragments of sebacic acid, resulting in their closer packing in the core and the formation of smaller assemblies.

Using calculated SLD and the known scattering length densities of the solvents and the polymer components, the inversion mechanism of IMAs has been demonstrated. By changing the polarity of the environmental medium from polar to nonpolar, PEG and aliphatic dicarboxylic acid fragments of AIP macromolecules tend to replace each other in the core and shell of the IMAs. In toluene solutions, the PEG species move from the shell to the interior of the self-assemblies, whereas hydrophobic aliphatic dicarboxylic acid moieties tend to relocate from the core to the exterior of self-assemblies. However, neither the interior nor the exterior of the IMAs consists of just a single component of the macromolecule. Both the hydrophilic and hydrophobic fragments are present in the micellar core and shell in the nonpolar solvent.

In aqueous solution at 15°C, the IMA mixed core from aliphatic dicarboxylic acid, PEG moieties, and the PEG-based shell changes its composition when the temperature increases. As a result of the progressive loss of water by the macromolecules, the hydration level (water content) in the micellar core significantly decreases at 25°C, followed by dehydrated PEG fragments in the shell entering the interior of the assemblies when the temperature increases to 35°C.

The invertibility of the micellar assemblies is promising for rapid and controlled self-assembly in applications that require simultaneous utility in polar and nonpolar media (e.g., for the development of new drug-delivery systems).

3.6. References

[1]. *Encyclopedia of Surface and Colloid Science*; Hubbard, A. T.Marcel Dekker: New York, **2002**.

[2]. Alexandridis, P.; Lindman, B. *Amphiphilic Block Copolymers: Self- Assembly and Applications*; Elsevier Science B.V.: Amsterdam, **2000**.

[3]. Spontak, R. J.; Alexandridis, P. Solvent-regulated ordering in block copolymers. *Current Opinion in Colloid & Interface Science* **1999**, *4*, 140−146.

[4]. Lohse, D. J.; Hadjichristidis, N. Microphase separation in block copolymers. *Current Opinion in Colloid & Interface Science* **1997**, *2*, 171−176.

[5]. Martin, A., Swarbrick, J., Cammarata, A. *Physical Chemistry*; Lea & Febiger Press: Philadelphia, PA, **1983**.

[6]. Pedersen, J. S.; Svaneborg, C. Scattering from block copolymer micelles. *Current Opinion in Colloid & Interface Science* **2002**, *7*, 158−166.

[7]. Mortensen, K.; Pedersen, J. S. Structural study on the micelle formation of poly(ethylene oxide)-poly(propylene oxide) -poly(ethylene oxide) triblock copolymer in aqueous solution. *Macromolecules* **1993**, *26*, 805−812.

[8]. Butun, V.; Armes, S. P.; Billingham, N. C.; Tuzar, Z.; Rankin, A.; Eastoe, J.; Heenan, R. K. The remarkable "flip-flop" self-assembly of a diblock copolymer in aqueous solution. *Macromolecules* **2001**, *34*, 1503−1511.

[9]. Svensson, B.; Olsson, U.; Alexandridis, P.; Mortensen, K. A. A SANS investigation of reverse (water-in-oil). micelles of amphiphilic block copolymers. *Macromolecules* **1999**, *32*, 6725−6733.

[10]. Goldmints, I.; Yu, G.-E.; Booth, C.; Smith, K. A.; Hatton, T. A. Structure of (deuterated PEO)− (PPO)−(deuterated PEO) block copolymer micelles as determined by small angle neutron scattering. *Langmuir* **1999**, *15*, 1651−1656.

[11]. Liu, Y.; Chen, S.-H.; Huang, J. S. Relationship between the microstructure and rheology of micellar solutions formed by a triblock copolymer surfactant. *Macromolecules* **1998**, 31, 2236−2244.

[12]. Chen, S.-H.; Liao, C.; Fratini, E.; Baglioni, P.; Mallamace, F. Interaction, critical, percolation and kinetic glass transitions in pluronic L-64 micellar solutions. *Colloids and Surfaces A* **2001**, *183−185*, 95−111.

[13]. Won, Y.-Y.; Davis, H. T.; Bates, F. S. Giant wormlike rubber micelles. *Science* **1999**, *283*, 960−963.

[14]. Lang, P.; Willner, L.; Pyckhout-Hintzen, W.; Krastev, R. Isotropic to nematic transition in solutions of cylindrical PB−PEO block copolymer micelles close to a wall. *Langmuir* **2003**, *19*, 7597− 7603.

[15]. Minatti, E.; Viville, P.; Borsali, R.; Schappacher, M.; Deffieux, A.; Lazzaroni, R. Micellar morphological changes promoted by cyclization of PS-b-PI copolymer: DLS and AFM experiments. *Macromolecules* **2003**, *36*, 4125−4133.

[16]. Hamley, I. W.; Pedersen, J. A.; Booth, C.; Nace, V. M. A smallangle neutron scattering study of spherical and wormlike micelles formed by poly [oxyethylene]-based diblock copolymers. *Langmuir* **2001**, *17*, 6386−6388.

[17]. Mortensen, K.; Brown, W. Poly(ethylene oxide)-poly(propylene oxide)-poly(ethylene oxide) triblock copolymers in aqueous solution. The influence of relative block size. *Macromolecules* **1993**, *26*, 4128−4135.

[18]. Mortensen, K.; Brown, W. Poly(ethylene oxide)-poly(propylene oxide)-poly(ethylene oxide) triblock copolymers in aqueous solution. The influence of relative block size. *Macromolecules* **1993**, *26*, 4128-4135.

[19]. Noolandi, J.; Hong, K. M. Theory of block copolymer micelles in solution. *Macromolecules* **1983**, *16*, 1443-1448.

[20]. Hasegawa, H. Block copolymers generic phase behaviour compared to surfactant phase behaviour. *Current Opinion in Colloid & Interface Science* **1998**, *3*, 264−269.

[21]. Thomas, E. L.; Alward, D. B.; Kinning, D. J.; Martin, D. C.; Handlin, D. L.; Fetters, U. Ordered bicontinuous double-diamond structure of star block copolymers: a new equilibrium microdomain morphology. *Macromolecules* **1986**, *19*, 2197−2202.

[22]. Hajduk, D. A.; Harper, P. E.; Gruner, S. M.; Honeker, C. C.; Thomas, E. L.; Fetters, U. A reevaluation of bicontinuous cubic phases in starblock copolymers. *Macromolecules* **1995**, *28*, 2570−2573.

[23]. Alexandridis, P.; Spontak, R. J. Solvent-regulated ordering in block copolymers. *Current Opinion in Colloid & Interface Science* **1999**, 4, 130−139.

[24]. Alexandridis, P. Poly(ethylene oxide)-poly(propylene oxide) block copolymer surfactants. *Curr. Opin. Colloid Interface Sci.* **1997**, *2*, 478−489.

[25]. Alexandridis, P.; Ivanova, R.; Lindman, B. Effect of glycols on the self-assembly of amphiphilic block copolymers in water. 1. Phase diagrams and structure identification. *Langmuir* **2000**, *16*, 3676−3689.

[26]. Yang, L.; Alexandridis, P. Small-angle neutron scattering investigation of the temperature-dependent aggregation behavior of the block copolymer Pluronic L64 in aqueous solution. *Langmuir* **2000**, *16*, 4819−4829.

[27]. Kohut, A.; Voronov, A.; Gevus, O.; Tokarev, V.; Voronov, S.; Peukert, W. Invertible architectures from amphiphilic polyesters. *Langmuir* **2006**, *22*, 1946- 1948.

[28]. Voronov, A.; Kohut, A.; Peukert, W. Synthesis of amphiphilic silver nanoparticles in nanoreactors from invertible polyester. *Langmuir* **2007**, *23*, 360−363.

[29]. Voronov, A.; Kohut, A.; Vasylyev, S.; Peukert, W. Mechanism of silver ion reduction in amphiphilic invertible nanoreactors formed in a non-polar solvent at ambient conditions. *Langmuir* **2008**, *24*, 12587− 12594.

[30]. Voronov, A.; Vasylyev, S.; Kohut, A.; Peukert, W. Surface activity of new invertible amphiphilic polyesters based on poly-(ethylene glycol) and aliphatic dicarboxylic acids. *Journal of Colloid and Interface Science* **2008**, *323*, 379–385.

[31]. Martinez Tomalino, L.; Voronov, A.; Kohut, A.; Peukert, W. Study of amphiphilic polyester micelles by Hyper-Rayleigh scattering: invertibility and phase transfer. *The Journal of Physical Chemistry* **2008**, *112*, 6338.

[32]. Kohut, A.; Voronov, A. Hierarchical micellar structures from amphiphilic invertible polyesters: ^{1}H NMR spectroscopic study. *Langmuir* **2009**, *25*, 4356−4360.

[33]. Kohut, A.; Dai, X.; Pinnick, D.; Schulz, D. L.; Voronov, A. ‘‘Host−guest’’ interaction between cyclohexasilane and amphiphilic invertible macromolecules. *Soft Matter* **2011**, *7*, 3717−3720.

[34]. Kohut, A.; Kudina, O.; Dai, X.; Schulz, D. L.; Voronov, A. Host-guest interactions between non-micellized amphiphilic invertible polymer and insoluble cyclohexasilane in acetonitrile. *Langmuir* **2011**, *27*, 10356−10359.

[35]. Hevus, I.; Kohut, A.; Voronov, A. Interfacial micellar phase transfer using amphiphilic invertible polymers. *Polymer Chemistry* **2011**, *2*, 2767−2770.

[36]. Hevus, I.; Modgil, A.; Daniels, J.; Kohut, A.; Sun, C.; Stafslien, S.; Voronov, A. Invertible micellar polymer assemblies for delivery of poorly water-soluble drugs. *Biomacromolecules* **2012**, *13*, 2537−2545.

[37]. Malmsten, M.; Lindman, B. Self-assembly in aqueous block copolymer solutions. *Macromolecules* **1992**, *25*, 5440−5445.

[38]. Kriz, J.; Masar, B.; Plestil, J.; Tuzar, Z.; Pospisil, H.; Doskocilova, D. Three-layer micelles of an ABC block copolymer: NMR, SANS, and LS study of a poly(2−ethylhexyl acrylate) block-poly(methyl methacrylate)- block-poly(acrylic acid) copolymer in D_2O. *Macromolecules* **1998**, *31*, 41−51.

[39]. Rodriguez-Hernandez, J.; Lecommandoux, S. Reversible insideout micellization of pH-responsive and water-soluble vesicles based on polypeptide diblock copolymers. *Journal of the American Chemical Society* **2005**, 127, 2026− 2027.

[40]. Hamley, I. W.; Castelletto, V. Small-angle scattering of block copolymers: in the melt, solution and crystal states. *Progress in Polymer Science* **2004**, 29, 909−948.

[41]. Mortensen, K.; Pedersen, J. S. Structural study on the micelle formation of poly(ethylene oxide)-poly(propylene oxide)-poly-(ethylene oxide) triblock copolymer in aqueous solution. *Macromolecules* **1993**, 26, 805−812.

[42]. Glatter, O.; Scherf, G.; Schillen, K.; Brown, W. Characterization of a poly[ethylene oxide].-poly[propylene oxide]. triblock copolymer [EO27-PO39-EO27]. in aqueous solution. *Macromolecules* **1994**, *27*, 6046−6054.

[43]. Jain, N. J.; Aswal, V. K.; Goyal, P. S.; Bahadur, P. Micellar structure of an ethylene oxide−propylene oxide block copolymer: a small-angle neutron scattering study. *The Journal of Physical Chemistry B* **1998**, *102*, 8452−8458.

[44]. Goldmints, I.; Yu, G. E.; Booth, C.; Smith, K. A.; Hatton, T. A. Structure of (deuterated PEO)−(PPO)−(deuterated PEO) block copolymer micelles as determined by small angle neutron scattering. *Langmuir* **1999**, *15*, 1651−1656.

[45]. Yang, L.; Alexandridis, P. Small-angle neutron scattering investigation of the temperature-dependent aggregation behavior of the block copolymer Pluronic L64 in aqueous solution. *Langmuir* **2000**, *16*, 8555−8561.

[46]. Higgins, J. S., Benoit, H. C. Polymer and Neutron Scattering; Oxford University Press: Oxford, U.K., **1996**.

[47]. Sieburg, L.; Kohut, A.; Kislenko, V.; Voronov, A. Amphiphilic invertible polymers for adsolubilization on hydrophilic and hydrophobized silica nanoparticles. *Journal of Colloid and Interface Science* **2010**, *351*, 116−121.

[48]. Guinier, A.; Fournet, G. *Small Angle Scattering of X-rays*; Wiley: New York, **1955**.

[49]. Sears, V. F. Neutron scattering lengths and cross sections. *Neutron News* **1992**, *3*, 26−37.

[50]. May, R. P.; Ibel, K.; Haas, J. The forward scattering of cold neutrons by mixtures of light and heavy water. *Journal of Applied Crystallography* **1982**, *15*, 15−19.

[51]. Glinka, C. J. Incoherent neutron scattering from multi-element materials. *Journal of Applied Crystallography* **2011**, *44*, 618−624.

[52]. Pedersen, J. S. Analysis of small-angle scattering data from colloids and polymer solutions: modeling and least-squares fitting. *Advances in Colloid and Interface Science* **1997**, *70*, 171−210.

[53]. Alexandridis, P.; Nivaggioli, T.; Hatton, T. A. Temperature effects on structural properties of pluronic P104 and F108 PEO-PPOPEO block copolymer solutions. *Langmuir* **1995**, *11*, 1468−1476.

[54]. Hammouda, B. Probing Nanoscale Structures: The SANS Toolbox; **2009**, book available online at http://www.ncnr.nist.gov/staff/ hammouda/the_SANS_toolbox.pdf.

[55]. Reichardt, C. *Solvents and Solvent Effects in Organic Chemistry*; VCH Verlagsgesellschaft mbH: Weinheim, Germany, **1988**.

[56]. Butler, J. A. Trans. Faraday Soc. **1937**, 33, 255.

[57]. Tanford, C. *The Hydrophobic Effect: Formation of Micelles and Biological Membranes*; John Wiley & Sons: New York, **1973**.

[58]. Manet, S.; Lecchi, A.; Imperor-Clerc, M.; Zholobenko, V.; Durand, D.; Oliveira, C. L. P.; Pedersen, J. S.; Grillo, I.; Meneau, F.; Rochas, C. Structure of micelles of a nonionic block copolymers determined by SANS and SAXS. *The Journal of Physical Chemistry B* **2011**, *115*, 11318− 11329.

CHAPTER 4. RESPONSIVE MICELLAR ASSEMBLIES FROM AMPHIPHILIC INVERTIBLE POLYMERS AS NANOCARRIERS FOR DRUG DELIVERY

4.1. Abstract

Two hydrophobic probes (Sudan Red B, dibutyl phthalate) with poor aqueous solubility were solubilized in invertible micellar structures (IMA's) from amphiphilic invertible polymers (AIP's) in order to study the role of cargo solubility on the incorporation into IMAs. ^{1}H NMR spectroscopy and SANS techniques were used to investigate the morphology of IMAs as well as the location of the cargo in micellar assemblies after the solubilization. The IMAs were shown to incorporate hydrophobic cargo molecules in a different manner. Depending on the chemical structure of the cargo, the hydrophobic molecules were incorporated either in the core or in the shell of micellar structures. Such selective incorporation of hydrophobic cargo into IMAs can potentially be used for the fabrication of multifunctional therapeutic formulations, where two different active therapeutic agents can be delivered at the same time.

In vitro testing of IMAs on normal cells and different cancer cell lines was used to test the therapeutic effect of loaded IMAs as drug carriers. IMAs loaded with natural drug candidate curcumin were tested in vitro using normal bone cells and bone cancer cells (human and mice osteosarcoma cell lines). Curcumin-loaded IMAs were found to be cytoxic against tested bone cancer cell lines whereas normal bone cells remain viable in presence of micellar curcumin. A significant amount of curcumin was observed in the cytoplasm of cancer cells in the same conditions.

4.2. Introduction

A lot of therapeutic agents and drug candidates have poor aqueous solubility and bioavailability, and can be incorporated into the drug carriers [1-4]. Drug delivery refers to the systems developed for transporting a therapeutic agent in the patient body to safely achieve the desired treatment effect [1]. Drug delivery can be used for: (1) controlled concentration of therapeutically active compounds in the human organism; (2) predictable and reproducible drug release rate over a long period of time (sustainable release); (3) protection of bioactive compounds unstable in aqueous media; (4) elimination of side effects and drug overdose; (5) optimized therapy and better patient compliance due to sustainable release of drugs, and (6) individualized therapy [2-4].

Micellar structures are among the most promising drug carriers due to small size, structural versatility and lower toxicity [4-6]. Polymeric micelles are stable towards dilution and hence exhibit much lower cytotoxicity [4, 6-7]. Lower toxicity and higher bioavailability make polymeric micelles suitable for intravenous administered drug delivery [4, 7-8]. Nanoscopic size of polymeric micelles prevents their removal from the blood circulation by filtration in kidneys [4-8]. Moreover, the small size of polymeric micelles as drug carriers minimizes the risk of their accumulation and clotting capillaries, in contrast to larger carriers such as liposomes, capsules, etc. [8-10] The hydrophilic shell of the micelle interacts with the blood components and cell membranes thus controlling biodistribution of the micellar polymeric drug carriers. Polymeric micelles are small enough to permeate through highly porous capillaries in the tumor site, accumulate in tumor tissue and then release the therapeutic cargo to treat the tumor (Fig.4.1) [10-13].

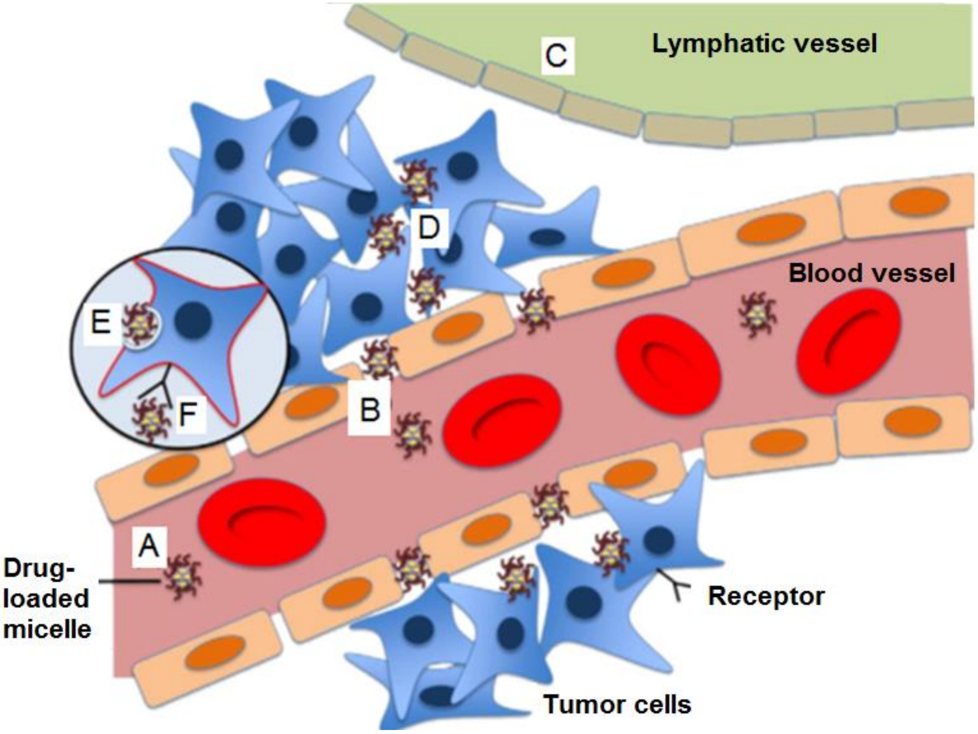

Fig.4.1. Performance of drug delivery system based on polymeric micelles: (A) block copolymer micelles effectively evade filtration in kidneys and other elimination mechanisms, resulting in prolonged blood circulation time; (B) nanosized micelles efficiently permeate through the highly porous tumor vasculature; (C) impaired lymphatic drainage in tumor tissues; (D) high interstitial concentration of drug-loaded micelles is retained in the tumor; (E) non-specific or (F) specific receptor-mediated internalization of drug-loaded micelles (Reproduced from [10]).

In most cases the hydrophobic drugs are incorporated inside the micelles due to non-specific interactions (e.g. hydrophobic interactions) [1-5]. Hence, there is no need to modify the chemical structure of the drugs to fabricate a carrier [3-4, 8]. The ‘smart’ properties of micelles fabricated from stimuli-responsive (pH, temperature sensitive) copolymers can be used for the formation of ‘smart’ drug carriers [2-8]. Such carriers can deliver the drug to the target location (tumor) and perform triggered release of the drug to treat the tumor [3-8].

There are at least two advantages of the drug incorporation into polymeric micelles. First, drug incorporation into micelles prevents premature elimination and clearance, increasing the concentration of drug, its blood circulation time and stability. Besides, the drug dose can be reduced thus preventing overdose. The latter helps in preventing non-specific organ toxicity (e.g. cardiotoxicity induced by doxorubicin) [7-8]. Hence, using polymeric micelles for drug delivery may prevent uncomfortable and dangerous side effects of the treatment [1-5, 14-16].

Recently synthesized amphiphilic invertible polymers (AIPs) were shown to be capable of (i). self-assembling into invertible micellar assemblies (IMAs) in response to changes in polarity of environment, polymer concentration, and structure, (ii). accommodating (solubilizing) substances, that are otherwise insoluble in water, and (iii). inverting their macromolecular conformation in response to changes in the polarity of the local environment [14-15, 25]. The IMAs capability to solubilize lipophilic drugs, deliver and release these cargo molecules was demonstrated by testing IMAs loaded with a phytochemical drug, curcumin [25]. The IMAs were shown to be nontoxic against normal human cells up to a concentration of 10 mg/L and cytoxic against breast carcinoma cells at this concentration [25].

In this study the incorporation of hydrophobic cargo molecules was studied using two hydrophobic cargo molecules – Sudan Red B and dibutyl phthalate. Selected hydrophopic molecules have significantly different aqueous solubility and were used to investigate the role of limited solubility of cargo molecules in their solubilization in IMAs. Different limited solubility of selected cargo molecules was expected to affect the amount of solubilized material. The solubilization study using ^{1}H NMR spectroscopy and small angle neutron scattering (SANS) methods was used to establish the morphology of loaded IMAs as well as the location of solubilized cargo in IMAs.

For in vitro testing IMAs were loaded with natural drug curcumin. In vitro testing of IMAs on normal cells and different cancer cell lines was used to determine the therapeutic effect of loaded IMAs as drug carriers. In current study curcumin-loaded IMAs were tested against a broad selection of osteosarcoma cell lines over the range of IMAs concentration, in order to discover the optimal performance range.

4.3. Experimental

4.3.1. Materials

Poly(ethylene glycol) (PEG, molecular weight 300 and 600 g/mol), poly(tetrahydrofuran) (PTHF, molecular weight 250 and 650 g/mol), carbon tetrachloride, methanol, and deuterium oxide were purchased from Sigma-Aldrich. Dodecanedioic acid was obtained from TCI, while curcumin was purchased from Alfa Aesar.

4.3.2. Synthesis of Amphiphilic Invertible Polymers (AIPs)

Amphiphilic invertible polymers (AIPs) were synthesized using previously reported methods [14, 15]. Polymer PEG$_{600}$PTHF$_{650}$ was fabricated from PEG with molecular weight 600 g/mol and PTHF with molecular weight 650 g/mol. Polymer D3 was synthesized from PEG with molecular weight 300 g/mol and dodecanedioic acid.

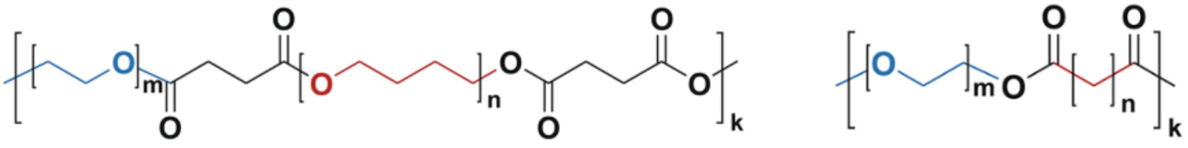

PEG$_{600}$-PTHF$_{650}$

D3

Fig.4.2. Chemical structure of the AIPs used in the study.

Table 4.1. Characterization of the AIPs used in the study.

AIP	**m**	**n**	**M_w**	**PDI**	**CMC, mg/L**
$PEG_{600}PTHF_{650}$	13.2	8.8	9700	1.52	3.5
D3	6.4	10	5500	1.44	10.4

4.3.3. Preparation of Loaded IMAs

IMAs loaded with hydrophobic cargo (SRB, DBP or curcumin) were prepared using thin film method [15]. Following this method, polymer (0.1 g) and methanol solution of hydrophobic cargo (Sudan Red B, dibutyl phthalate, curcumin) taken in excess amount (0.2 mL, 5 mg/mL) were mixed in carbon tetrachloride (10 mL). The solvent was removed by rotary evaporation at 60°C for 1 h to obtain a solid cargo/AIP film. Residual carbon tetrachloride remaining in the cargo/AIP matrix was evaporated overnight in vacuum. The resultant thin film was hydrated with Millipore water (10 mL). Unincorporated cargo was removed by filtration through 0.45 and 0.2 μm filters.

^1H NMR spectra were recorded on a JEOL ECA 400 MHz NMR spectrometer using chloroform-d and deuterium oxide as solvents.

4.3.4. SANS Experiments

The measurements were performed at the Oak Ridge National Laboratory, U.S. Department of Energy, Knoxville, TN, using the Extended Q-Range Small-Angle Neutron Scattering Diffractometer (BL-6) on the Spallation Neutron Source. Scattering intensity data were recorded at room temperature (25°C). Two neutron wavelengths of $\lambda = 3$ and 11 Å were used to cover scattering vectors ranging from 0.004 to 1.000 $Å^{-1}$. The intensity was recorded with 1 × 1 m low-angle detector. The AIP solutions at varying concentrations in deuterated water and toluene were placed in 0.5 cm quartz “banjo” cells sealed with parafilm.

SANS Data Reduction and Analysis. The SANS data were reduced and analyzed as described in Chapter 2.3.3.

4.3.5. In Vitro Testing of Curcumin-Loaded Responsive AIP Micelles

The curcumin-loaded IMAs were evaluated for cytotoxicity toward the osteosarcoma (bone cancer) cell lines 143B, MG63, KHOS, LM7 (human) (obtained from the American Type Culture Collection) and normal bone cells – human osteoblasts BAB552 (obtained from patients in Mayo Clinic, Rochester, NM). Cell cultures were maintained in Dulbecco’s modified Eagle medium (DMEM) supplemented with 10% w/v fetal bovine serum (FBS), penicillin (100 U/mL), streptomycin (100 μg/mL) and glutamine (2 mM). The cells were trypsinized and resuspended into fresh media. The cells were seeded into 12-well poly-L-lysine plates at an inoculum density of 5×10^4 cells/well. The plates were incubated at 37°C (5% CO_2) for 24 hours and then the DMEM was carefully removed from each well and replaced with fresh media. For treatment different dosages of micellar curcumin was added to the media. DMEM media without micellar curcumin was used as positive growth control. The plates were then incubated at 37°C growth chamber (5% CO_2). Following the selected incubation period, the curcumin-loaded IMAs and control samples were discarded and the entire plate was rinsed with saline.

Cell viability was determined using an MTS colorimetric assay (Promega) [17]. In particular, a 0.5 g/L solution of MTS in HBSS (0.033 mL) was added to each well of the plate and then incubated for 1 h at 37°C. Following the 1 h incubation period, the plates were transferred to a multiwell plate spectrophotometer and the absorbance values were measured at

570 nm. The mean absorbance values reported (n = 5) were considered to be directly proportional to the number of viable cells that survived after the curcumin-loaded IMAs and control sample treatments. Statistical analysis was performed using a JMP 7.0 statistical software package (SAS Institute Inc.). A one-way ANOVA was used to evaluate the differences in cell viability. The cell viability data were used to calculate cell survival according to equation 4.1:

$$Cell\ survival, \% = \frac{CV_{curcumin}}{CV_{polymer}} \times 100\% \qquad (4.1)$$

where $CV_{curcumin}$ and $CV_{polymer}$ are the colorimetric signals from MTS assay representing the proliferation of cells cultured in presence of micellar curcumin and non-loaded AIP respectively.

Cell proliferation was estimated by determining the total content of protein in cell lysate using Bradford protein assay (SigmaAldrich) [18]. In particular, a 0.5 g/L solution of lysing buffer was added to each flask and then incubated for 4 h at 37°C. Following the 4 h incubation period, the cell lysate was transferred to 96 poly-L-lysine well plate. 0.2 mL of Bradford reagent was added to each well of the plate. The plates were transferred to a multiwell plate spectrophotometer and the absorbance values were measured at 590 nm. The mean absorbance values reported (n = 5) were considered to be directly proportional to the number of viable cells that survived after the curcumin-loaded polymer micelles and control sample treatments. Statistical analysis was performed using a JMP 7.0 statistical software package (SAS Institute Inc.). A one-way ANOVA was used to evaluate the differences in cell viability. The cell proliferation was estimated as the ratio of protein content in the curcumin-treated sample to the protein content in the reference sample:

$$Cell\ proliferation,\% = \frac{P_{curcumin}}{P_{polymer}} \times 100\% \quad (4.2)$$

where $P_{curcumin}$ and $P_{polymer}$ total protein content in cells cultured in presence of micellar curcumin (curcumin-treated sample) and non-loaded micellar AIP (reference sample), respectively.

Fluorescent *confocal microscopy* was performed using Olympus BX61 microscope equipped with 20X and 40X water immersion objectives. An AsRed2 filter cube and bright field cube were used for fluorescent and bright field images, respectively.

4.4. Results and Discussion

The solubilization of hydrophobic cargo into IMAs was investigated using ^{1}H NMR spectroscopy and small-angle neutron scattering (SANS) techniques. The small-angle neutron scattering (SANS) technique was used to compare the morphology of loaded and non-loaded IMAs as well as to determine the location of hydrophobic cargo in the core/shell of IMAs. ^{1}H NMR spectroscopy was used to study the interactions between hydrophobic molecules (Sudan Red B or dibutyl phthalate) and hydrophobic and hydrophilic micellar fragments of loaded IMA’s.

In vitro testing was carried out in order to study the cytotoxicity (cell survival and cell proliferation) of the curcumin-loaded IMAs (micellar curcumin) towards cancer cell lines. The results were compared to the cell survival/proliferation in the presence non-loaded IMAs in the same conditions. Fluorescent microscopy was used to track the location of curcumin inside the normal and cancer cells during the treatment.

4.4.1. Solubilization of Poorly Water-Soluble Molecules by IMAs Studied using SANS And ^{1}H NMR Spectroscopy

Two different hydrophobic probes - Sudan Red B (SRB) and dibutyl phthalate (DBP) (Fig.4.3 and Table 4.1), with different poor aqueous solubility were selected to study their solubilization by IMAs. Both probes are expected to be stabilized in water by incorporation inside IMAs. Besides different aqueous solubility the selected cargos have different partition coefficient ($logK_{wo}$)[1] and dipole moments (Table 4.2). The partition coefficient can be used to estimate the distribution of hydrophobic molecules solubilized inside IMAs [27]. Higher $logK_{WO}$ of SRB (Table 4.2) indicates its higher affinity to the hydrophobic environment, such as core of IMAs comprised of hydrophobic fragments (see Chapter 3). At the same time, dipole moment values (Table 4.2) can be used to estimate the ability of molecules to participate in polar interactions. A larger dipole moment of DBP (compared with SRB) indicates its higher potential to polar intermolecular interactions.

IMAs loaded with hydrophobic cargo (SRB, DPB) were prepared using 1 and 5% w/v AIP solutions (Table 4.2). At these concentrations, the micelles are self-assembled into IMAs to solubilize hydrophobic cargo molecules [25].

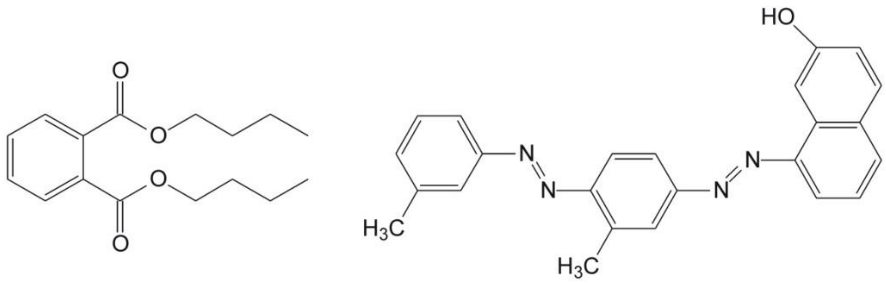

Sudan Red B (SRB) Dibutyl Phthalate (DBP)

Fig.4.3. Chemical structures of hydrophobic cargo molecules.

---

[1] Partition coefficient ($logK_{WO}$) calculated as the ratio of concentrations of a hydrophobic molecule in a mixture of two immiscible phases at equilibrium [27].

Table 4.2. Hydrophobic probes characteristics.

Characteristics	**SRB**	**DBF**
Aqueous solubility, mg/L	0.19	13
$logK_{WO}$	7.5	5.6
Dipole moment, D	0.95	6.94
Loading in 1%w/v D3 solution, % w/w	6.0	15.0
Loading in 5% w/v D3 solution, % w/w	3.6	9.5

Based on previous studies of IMAs morphology (see Chapter 3) in this study a core-shell form factor was selected for the fitting of experimental SANS plots. Fig.4.4. shows SANS scattering plots for 1 and 5% w/v blank and loaded IMAs from D3 in D2O at 25°C and the corresponding model fits obtained using a core shell cylindrical form factor [28-31]. The modeling of scattering data was used to calculate the scattering length density (SLD) values and the dimensions of IMAs: total radius of the core-shell micellar assemblies, R, the shell thickness, h, and the radius and the length of the core, Rc and H, respectively. Comparing the SLDs of core and shell of IMAs (Table 4.3) can help to estimate their composition [29-31]. The SLD values of selected hydrophobic cargo molecules are different in comparison with the SLDs of non-loaded core and shell constituents of IMAs (Table 4.3). So, the presence of hydrophobic probe in either the core or shell may lead to the changes in core or shell SLD values.

Table 4.3. SLD values ($\rho\times10^{-10}$, cm^{-2}) [29, 31].

Component	**$\rho\times10^{-10}$, cm^{-2}**
AIP components	
PEG fragment	2.64
dodecanedioic acid fragment	-0.49
Hydrophobic probes	
DBP	1.08
SRB	2.39
Solvent	
D_2O	6.37

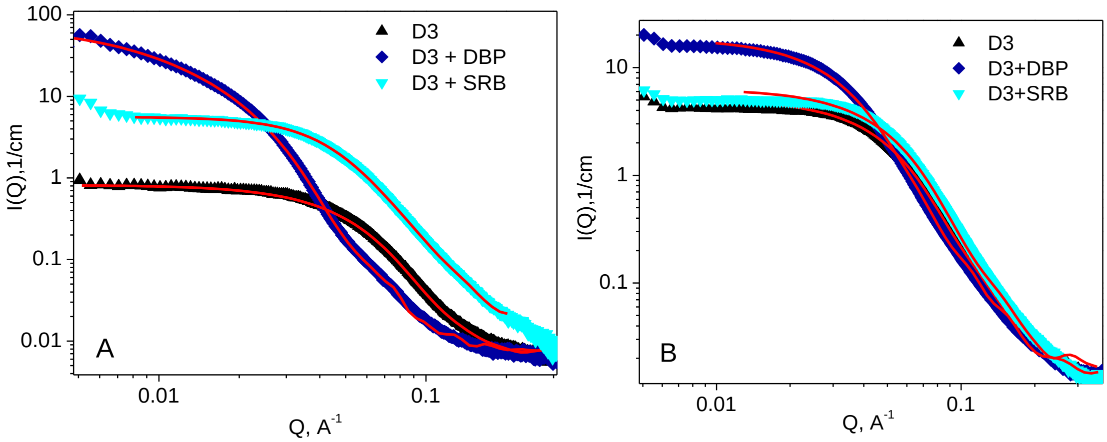

Fig.4.4. Scattering curves for loaded and non-loaded D3 micellar assemblies in D_2O at 15°C. A – 1% w/v, B – 5% w/v. Solid lines represent the fits obtained using a core−shell cylindrical form factor.

Fig.4.5. represents the calculated core and shell SLD values of IMAs loaded and non-loaded with hydrophobic cargos. The SLDs change significantly after the incorporation of hydrophobic cargo molecules. In SRB-loaded IMAs the SLD of core increases when compared with non-loaded IMAs, while the SLD of the shell remains unchanged. In DBP-loaded IMAs the situation is different. The SLD of shell decreases while the core SLD remains unchanged. This effect is consistent for both tested concentrations, but is more pronounced at concentration of 1% w/v.

These changes of IMAs SLD can possibly be explained by the selective incorporation of hydrophobic cargos, when SRB is primarily incorporated in the core of IMAs, and DBP is mostly located in the shell. Such distribution of cargo molecules can be explained by their logKWO and dipole moment values (Table 4.2). Higher logKWO of SRB indicates its higher affinity towards hydrophobic environment such as the core of IMAs. In the same time lower dipole moment of SRB indicates lower polarity of the molecule, and thus lower capability for polar interactions. These two factors can explain the SRB localization in the hydrophobic core of IMAs. Whereas the combination of lower logKWO and higher dipole moment for DBP molecules results in stronger polar interactions between DPB and PEG fragments of IMAs. Such polar interaction may lead to localization of DBP primarily in the shell of IMAs.

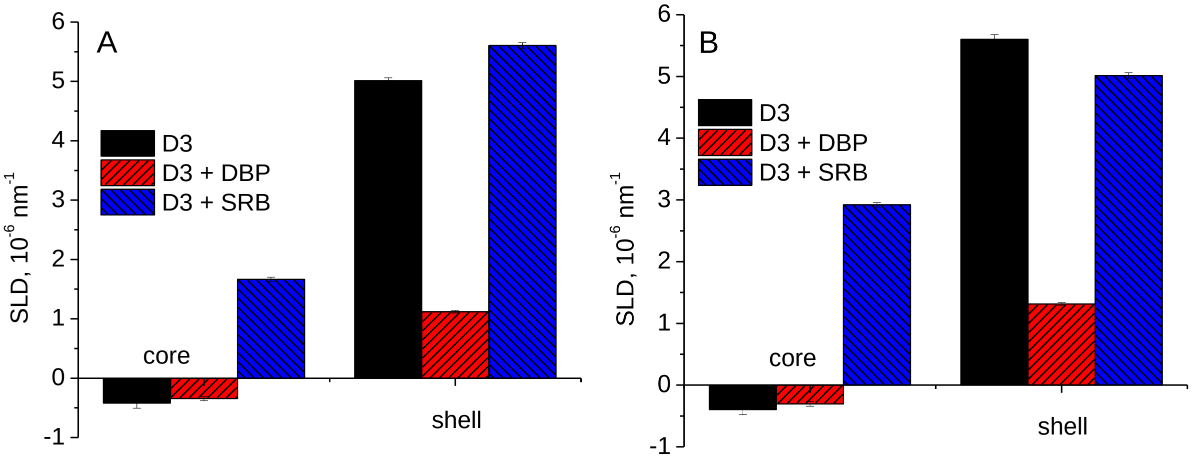

Fig.4.5. SLD values of D3 loaded and non-loaded micellar assemblies at different concentrations in aqueous media. A – 1% w/v, B - 5% w/v.

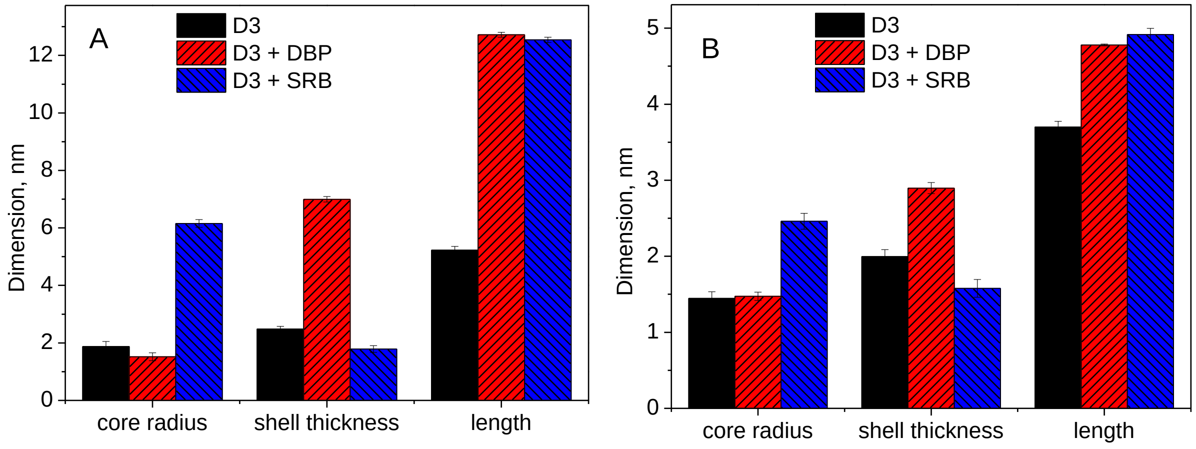

Fig.4.6. Morphology of D3 loaded and non-loaded micellar assemblies at different concentrations in aqueous media. A – 1% w/v, B – 5% w/v.

Fig.4.6. represents the calculated morphology of cylindrical core-shell IMAs. It is shown, that the size of the micellar assemblies changes significantly after the incorporation of

hydrophobic cargo (Table 4.4). The volume of core and shell of micellar structures was calculated according to the formulas 4.3 and 4.4.

$$V_{core} = 2\pi \cdot {R_c}^2 H \qquad (4.3)$$

$$V_{shell} = 2\pi \cdot R^2 H - 2\pi \cdot {R_c}^2 H \qquad (4.4)$$

where V_{core} and V_{shell} are the volumes of core and shell respectively, R - total radius of the core-shell micellar assemblies, h -shell thickness, R_c and H -and the radius and the length of the core.

Table 4.4. Volumes of cylindrical core-shell IMAs at 25°C in aqueous media, nm^3.

Volumes, nm^3	**D3**	**D3+DBP**	**D3-SRB**
		1% w/v solution	
core	57.6	91.9	1492.1
shell	253.8	2803.4	992.7
		5% w/v solution	
core	24.3	42.6	115.4
shell	113.4	234.8	171.2

The incorporation of SRB and DBP affects the micellar morphology in a different manner. In SRB-loaded IMAs the radius of hydrophobic core increases when compared with non-loaded IMAs, while the thickness of the hydrophilic shell remains unchanged. In DBP-loaded IMAs the situation is different – the shell thickness increases while the core radius remains unchanged. This effect is consistent for both tested concentrations, but is more pronounced at concentration of 1% w/v. Such characteristic changes of IMAs morphology may indicate that SRB is primarily incorporated in the core of IMAs and DBP is located in the shell, as it is discussed before.

^{1}H NMR spectroscopy can be used to track the changes of proton signals after the solubilization of hydrophobic molecules as the chemical shifts are known to be sensitive to the electronic structure of the corresponding protons [32]. Thus, ^{1}H NMR spectroscopy can give detailed insights into the loading of hydrophobic cargos inside IMAs, including information on the possible interactions between cargo molecules with hydrophobic and hydrophilic fragments of IMAs. The differences in the proton signals of loaded IMAs may indicate changes of the structural properties: conformation changes, specific interaction with hydrophobic probe, etc. [32-34]

^{1}H NMR spectra of 1% and 5% w/v D3 solutions have been recorded in D_2O before and after loading of hydrophobic cargo. Fig.4.8. shows the local expanded ^{1}H NMR spectra of each peak region corresponding to specific protons. The peaks in Fig.4.8 correspond to the proton labelling for D3 on Fig.4.7.

Protons A are represented as two different multiplets (Fig.4.8). The upfield multiplet (signals at 2.147, 2.169, 2.245 ppm) corresponds to the protons located in a micellar core. The presence of hydrophobic cargo causes the sudden downfield shifts for one of proton A multiplets from 2.147 to 2.245 ppm (Fig.4.8). Such change of chemical shift indicates that the corresponding hydrogen atoms are affected by polar interactions which results in partial deshielding of proton. It can be associated with the transfer of protons from nonpolar into polar microenvironment [32, 34]. The deshielding effect is more prominent for IMAs with solubilized SRB indicating that this particular hydrophobic probe is localized in the core taking part in polar interactions with ester group of dicarboxylic acid fragment.

Notably, a significant downfield shift is observed for broad peaks corresponding to the PEG fragments (protons E and F) in D3 micellar solutions loaded with DBP (Fig.4.8., Table 4.5). The increase of chemical shift values for protons E and F indicates the decrease of their shielding. It can be explained by specific interactions between PEG fragment and DBP, when PEG fragment acts as an electrophile. Aromatic ring of DBP with electron-withdrawing ester substituents acts as an electrophile interacting with electron pair of oxygen atom in PEG fragment (Scheme 4.1). This assumption correlates with notable change of chemical shifts for DBP protons A and B corresponding to DBP aromatic ring (Fig.4.9). We assume that DBP takes part in such interactions due to specific chemical structure, higher dipole moment and lower partition coefficient. Specific interaction between PEG fragment and DBP can explain drastic change of the shell size and shell SLD values of corresponding DBP-loaded IMAs determined by SANS (Fig.4.5. and 4.6., Table 4.3).

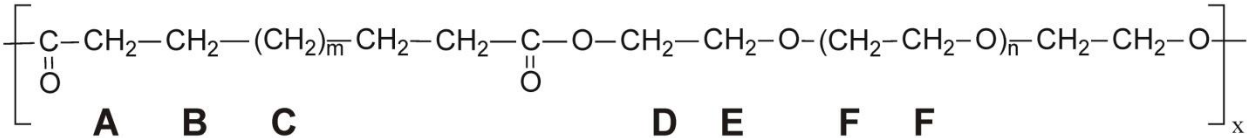

$$\left[-\underset{\overset{\|}{O}}{C}-CH_2-CH_2-(CH_2)_m-CH_2-CH_2-\underset{\overset{\|}{O}}{C}-O-CH_2-CH_2-O-(CH_2-CH_2-O)_n-CH_2-CH_2-O- \right]_x$$

Fig.4.7. Proton labelling for D3 macromolecule.

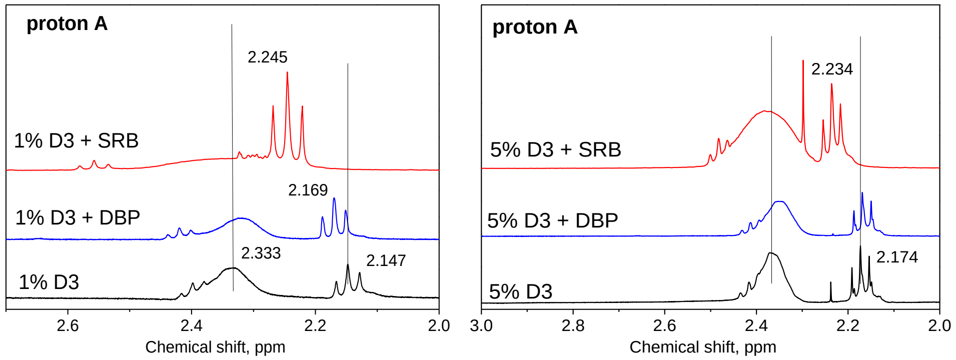

Fig.4.8. ^{1}H NMR spectra of non-loaded and loaded with DBP or SRB aqueous D3 solutions (%,w/v).

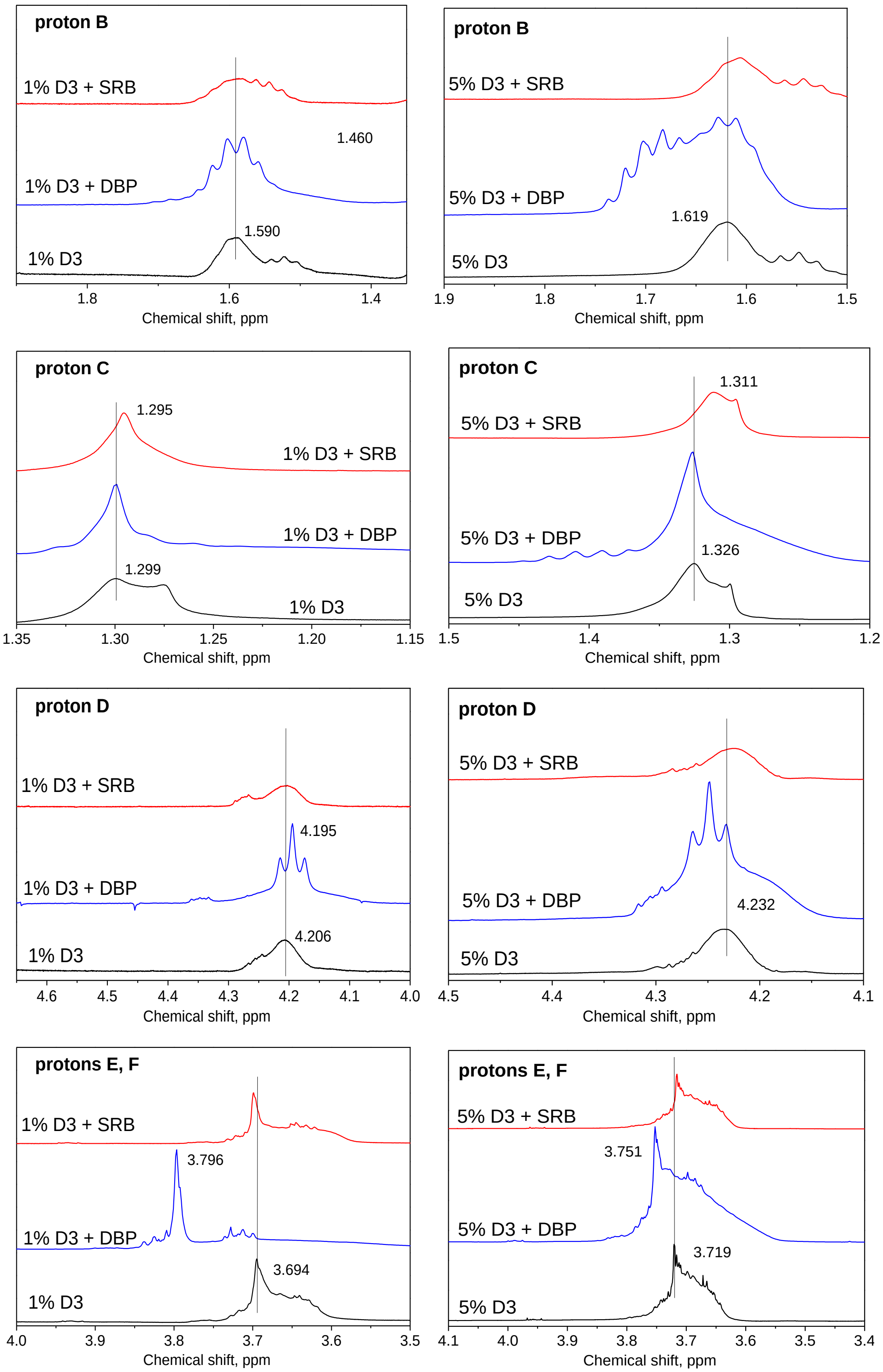

Fig.4.8. ^{1}H NMR spectra of non-loaded and loaded with DBP or SRB aqueous D3 solutions (%,w/v) (continued).

Table 4.5. Chemical shifts of non-loaded and loaded with DBP or SRB aqueous D3 solutions at different concentrations of D3 (%,w/v).

Proton	**1% D3**	**1% D3+ DBP**	**1% D3+ SRB**	**5% D3**	**5% D3+ DBP**	**5% D3+ SRB**
A	2.333/2.147	2.333/2.147	2.230/2.169	2.367/2.174	2.367/2.234	2.235/2.269
B	1.59	1.59	1.59	1.619	1.619	1.619
C	1.299	1.299	1.295	1.326	1.326	1.311
D	4.206	4.195	4.206	4.232	4.232	4.228
E, F	3.694	3.796	3.698	3.719	3.751	3.719

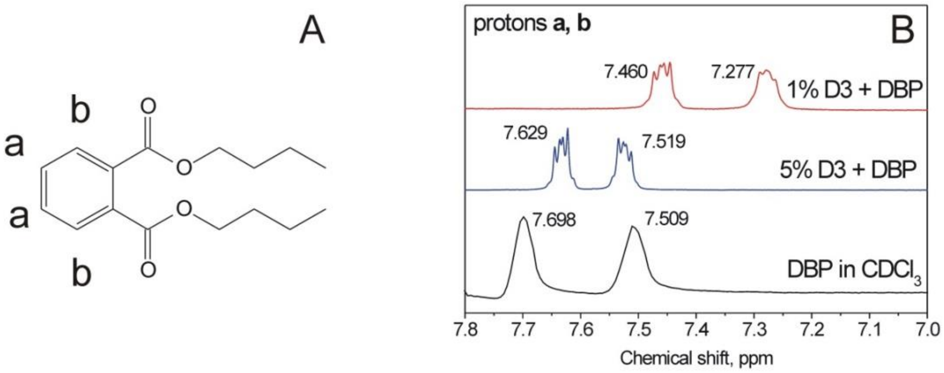

Fig.4.9. Expanded fragment of ^{1}H NMR spectra of D3 IMAs loaded with DBP, corresponding to protons of DBP aromatic ring, (%,w/v) (B) and respective DBP proton labels (A).

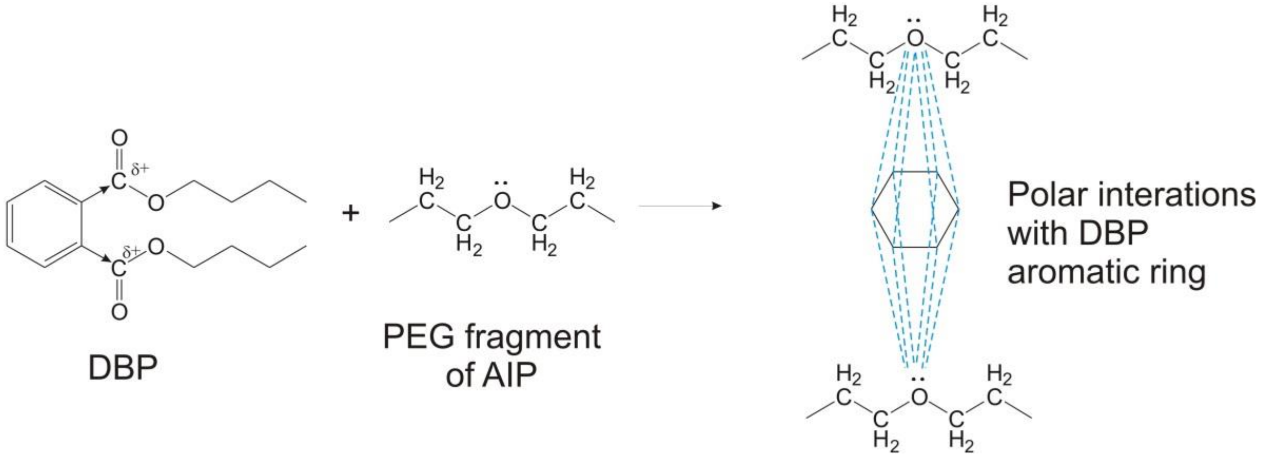

Scheme 4.1. Scheme of possible interactions between PEG fragments of IMAs and aromatic fragment of DBP.

The combined results of SANS and ^{1}H NMR spectroscopy studies indicate the ability of hydrophobic cargoes to be incorporated into different locations in IMAs. Depending on the chemical structure of the hydrophobic probe, it was incorporated either in core or shell of the IMAs. We suggest that selective incorporation of hydrophobic molecules can be possibly used for a variety of biomedical applications (Fig.4.10). The use of multifunctional carriers can minimize the undesired interactions between different cargo species, program interactions between the target cell and carrier thus facilitating the sustainable release. Such selective incorporation of hydrophobic cargo into IMAs can potentially be used for the fabrication of multifunctional therapeutic formulations, where two different active therapeutic agents are delivered at the same time.

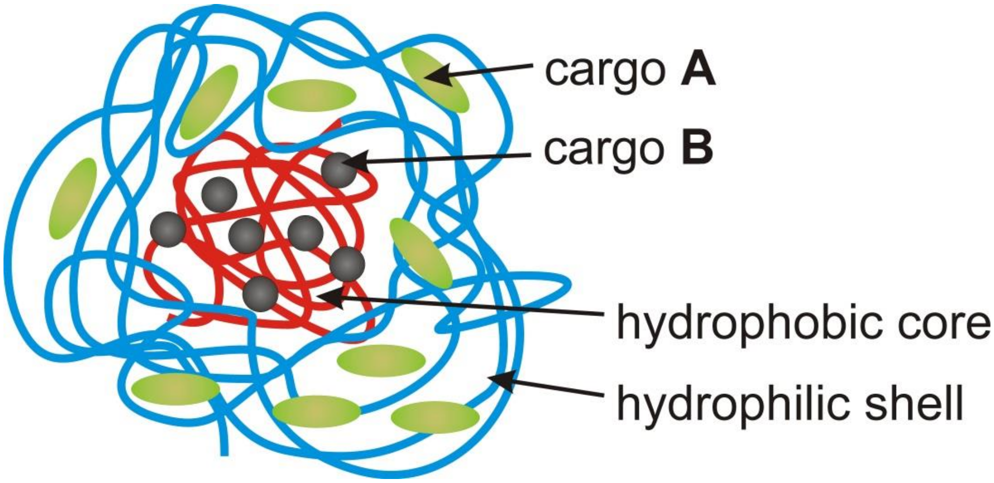

Fig.4.10. Multifunctional carrier loaded with two different cargo molecules.

4.4.2. Curcumin-Loaded IMAs as Drug Carriers in Osteosarcoma Treatment

Osteosarcoma is the malignant tumor of bones that is most prevalent among adolescents and young adults [19]. The prognosis is often poor and within one year of therapy about 30% of osteosarcoma patients are diagnosed with lung metastases [19-20]. Chemotherapy is often ineffective, resulting in high mortality rates. Hence, it is important that new therapeutic approaches are evaluated for this malignant disease [20].

Curcumin, a phenolic compound from the rhizome of the plant Curcuma longa was shown to have anti-inflammatory, antioxidant and anticancer effects [21-22]. Curcumin is found to have an inhibitory function towards a broad range of human and animal tumors [21-23]. The major benefit of curcumin as anticancer agent is the ability to affect the organism in a cell type dependent manner [21-23]. Curcumin was reported to selectively affect abnormal cancer cells without affecting normal cells [22-24]. However, curcumin has very low solubility in aqueous media and quickly degrades on contact with water [22]. To increase the solubility and thus bioavailability of curcumin, it can be incorporated into micellar systems [22-24].

In current study IMAs were loaded with curcumin in order to test their performance as drug carriers for treatment of osteosarcoma. Curcumin-loaded IMAs were prepared using 1% w/v PEG600-PTHF650 micellar solution which were demonstrated as the most effective curcumin-loaded IMAs formulations in previous studies [25].

The cell survival of cancer cell lines (K7M2, KHOS, LM7) was examined in the presence of blank and curcumin-loaded IMAs using standard MTS assay. The cell survival values (eq. 4.1 in Chapter 4.3.2) can be used to determine the net effect of curcumin-loaded IMAs, by eliminating the effect of presence of non-loaded IMAs. The effect of non-loaded micellar assemblies was eliminated by dividing the cell viability of curcumin-loaded IMAs by the cell viability of blank IMAs. Various concentrations of IMAs were used to plot dose curve for tested cancer cell lines (Fig.4.11). The curcumin-loaded IMA's show the maximal cytotoxicity against cancer cells at concentration of 0.75-1% w/v (Fig.4.11.A-B). In experimental conditions after testing curcumin-loaded IMA's at different treatment time (Fig.4.11B) the established optimal performance time was 3 days.

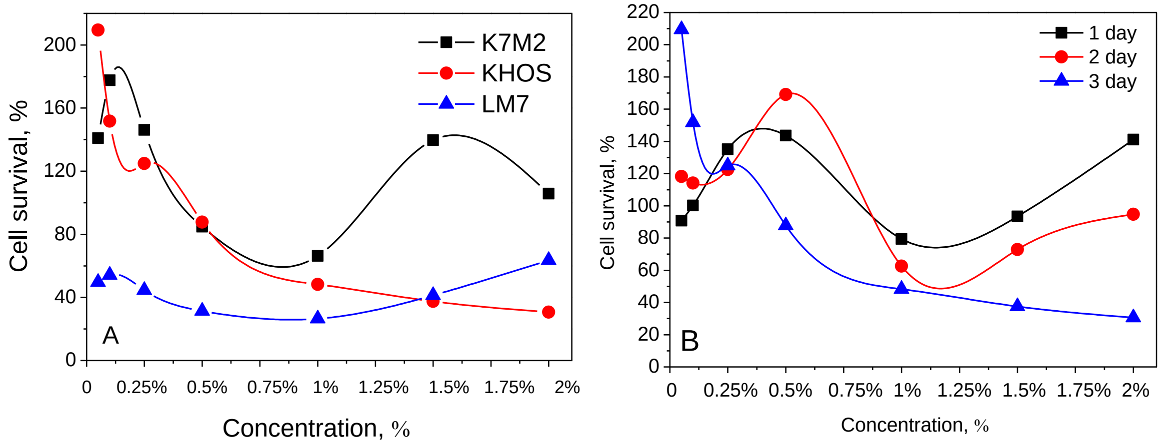

Fig.4.11. Cell survival of osteosarcoma cells treated with various concentrations of curcumin-loaded IMAs. A – dose curves for after 3 days of treatment, B – dose curves for KHOS cell line at different treatment time.

Based on the established time and concentration (Fig.4.11), curcumin-loaded IMAs were tested using a broad range of cancer and normal cells (Fig.4.12). As a potential drug carrier, the material has to be nontoxic for human organism and biocompatible. To establish the cytoxicity of curcumin-loaded IMAs and their feasibility as drug carriers, the cell survival of normal bone cells (HOB) was compared to the cell survival of cancer cells (K7M2, KHOS, LM7, 143B). The results of the testing show that curcumin-loaded IMAs as well as non-loaded IMAs are not toxic towards HOB (Fig.4.12). In the same time the survival of cancer cells after treatment with curcumin-loaded IMAs drops significantly. The latter observation can only be contributed to the presence of micellar curcumin, as non-loaded IMAs are not cytotoxic at the concentrations used in the experiment (Fig.4.12).

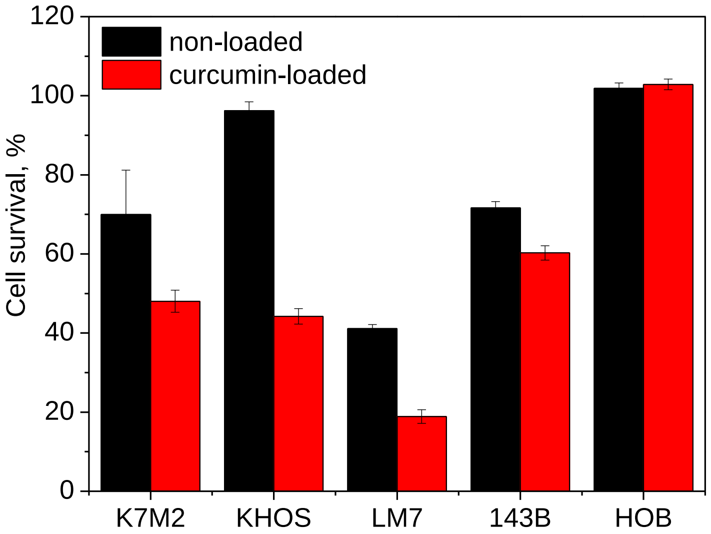

Fig.4.12. Cell survival of osteosarcoma cells (K7M2, KHOS, LM7, 143B) and normal cells (HOB) treated with 1% w/v non-loaded and curcumin-loaded IMAs.

Cell survival can give only rough estimate on the number of cells in the tested culture, as the same number of cells can exhibit different viability. To this end in order to confirm the cytotoxic effect of curcumin-loaded IMAs against the cancer cells, cell proliferation needs to be tested. The number of cells in curcumin-treated sample is directly proportional to the total protein content number in the sample. Hence, the calculation of the total number of protein in samples treated with IMAs can be used to estimate the change of cell proliferation in presence of non-loaded and curcumin-loaded IMAs (Fig.4.13). The rapid decrease of cancer cell proliferation (143B, MG63) was recorded after 16 hours of treatment with curcumin-loaded IMAs (Fig.4.13). In the same time the cell proliferation of HOB (normal cells) was not affected by the presence of micellar curcumin even after 24 hours of treatment (Fig.4.13). These results demonstrate the cytotoxicity of curcumin-loaded IMAs towards cancer cells, when normal bone cells are unaffected by micellar drug.

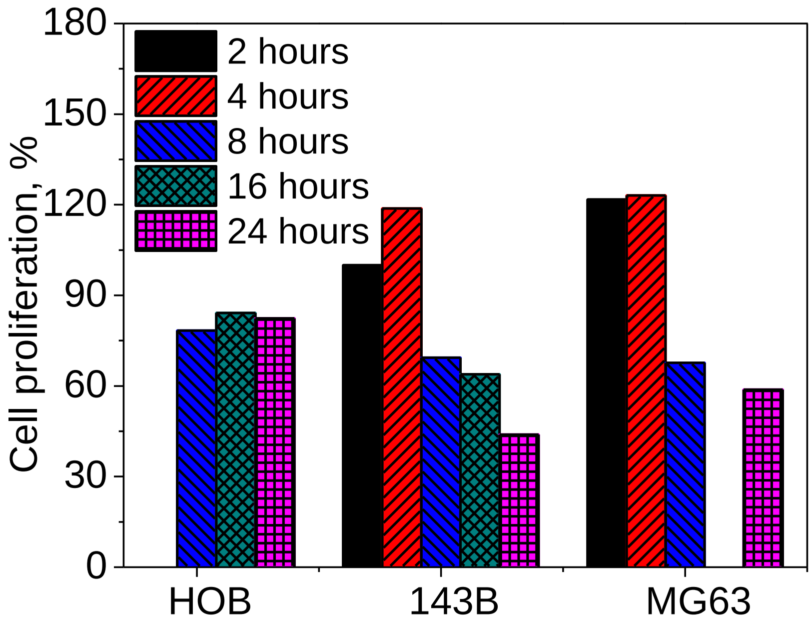

Fig.4.13. Cell proliferation of normal cells (HOB) and osteosarcoma (MG63, 143B) treated with 1% w/v curcumin-loaded IMAs.

To study the incorporation of micellar curcumin into cells and location of the drug after the incorporation fluorescent confocal microscopy was used (Fig.4.14. and 4.15). Natural fluorescent signal of curcumin (at excitation wavelength 535 nm) [26] was used to track the location of the drug inside the cells. The obtained results indicate the absence of curcumin in HOB (Fig.4.14B). In the same time over same treatment period notable amount of curcumin was incorporated by sample of MG63 cancer cells (Fig.4.14A). This observation correlates with cell survival and proliferation data, confirming lower toxicity of curcumin-loaded IMAs towards HOB.

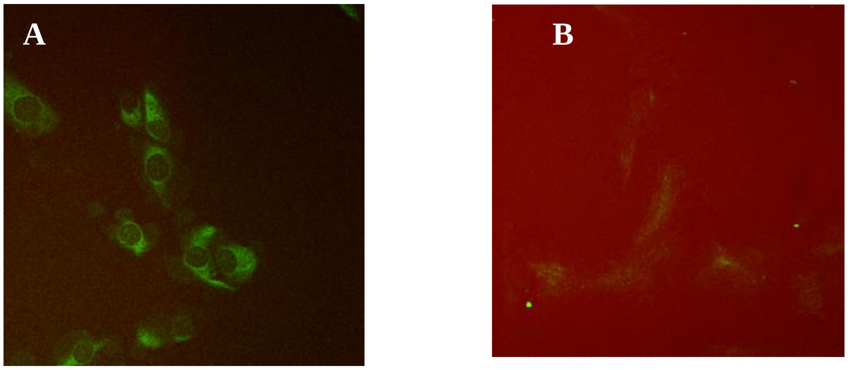

Fig.4.14. Fluorescent microscopic images of the incorporation of curcumin into MG63 cancer cells (A) and HOB (B). 1% w/v IMAs solution was used for the treatment for 30 minutes.

In order to track incorporation of curcumin into cancer cells, fluorescent images were taken at different treatment times (Fig.4.15). As it is shown in Fig.4.15A the curcumin is initialy incorporated in the cell cytoplasm (cell interior outside nucleus). At longer time of treatment, the curcumin progressively internalizes into the cell nuclei (Fig.4.15B) until the most of the cell interior is filled with drug (Fig.4.15C).

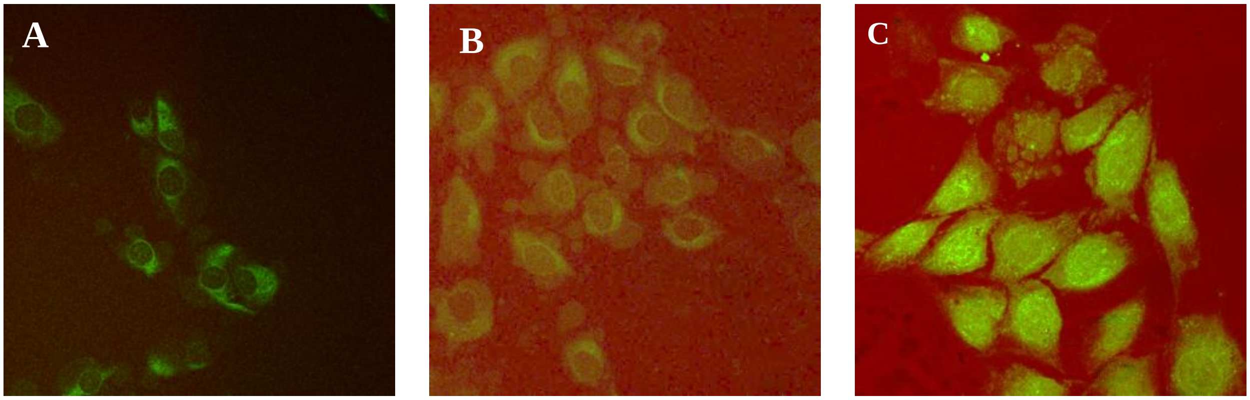

Fig.4.15. Fluorescent microscopic images of gradual incorporation of micellar curcumin into MG63 cancer cells delivered by 1% w/v IMAs. A – after 30 minutes, B – after 1 hour, C – after 2 hours.

In vitro tests demonstrate that curcumin-loaded IMAs possess a significant cytotoxic effect on multiple bone cancer cell lines while the normal bone cells remain unaffected by the micellar curcumin. The dose curve and time-resolved testing were used to determine the optimal concentration and time for micellar curcumin performance in treatment of osteosarcoma. Significant amounts of micellar curcumin were detected in the cytoplasm of cancer cells.

4.5. Conclusions

^{1}H NMR spectroscopy and SANS techniques were used to investigate the morphology of IMAs as well as the location of the hydrophobic cargo in micellar assemblies after the solubilization. The IMAs were shown to incorporate hydrophobic cargo molecules in a different manner. Depending on the chemical structure of the hydrophobic molecules, the cargos were incorporated either in core or in the shell of micellar structures. Such selective incorporation of hydrophobic cargo into IMAs can potentially be used for the fabrication of multifunctional therapeutic formulations, where two different active therapeutic agents are delivered at the same time.

In vitro testing of IMAs on normal cells and different cancer cell lines was used to determine the therapeutic effect of loaded IMAs as drug carriers. IMA's loaded with natural drug curcumin were tested *in vitro* as drug carriers on human and mice bone cancer cells as well as on normal bone cells. Curcumin-loaded IMAs were found to be toxic against multiple bone cancer cell lines whereas normal bone cells remain viable in presence of micellar curcumin. Significant amount of curcumin was observed in the cytoplasm of cancer cells, while the cytoplasm of normal cells contained only trace amounts of drug.

4.6. References

[1]. Ravi Kumar, M. N. V. *Handbook of Particulate Drug Delivery (2-Volume Set),* New York: American Scientific Publishers, **2008**.

[2]. Graham, N.B. *Polyethylene glycol chemistry*. In: Harris, J.M, editor. Biotechnical and biomedical application. New York: Plenum Press; **1992**. p. 1–13.

[3]. Kwon, G.S.; Okano, T.Polymeric micelles as new drug carriers. *Advanced Drug Delivery Reviews* **1996**, *21*, 107-116.

[4]. Bajpai, A.K.; Shukla, S. K.; Bhanu, S.; Kankane,S. Responsive polymers in controlled drug delivery. *Progress in Polymer Science* **2008**, *33*, 1088–1118.

[5]. Alarcon, C.D.L.; Penndam, S.; Alexander, C. Stimuli responsive polymers for biomedical applications. *Chemical Society Reviews* **2005**, *34*, 276–285.

[6]. Owen, S.C.; Chan, D.P.; Molly, Y.; Shoichet,S. Polymeric micelle stability. *Nano Today* **2012**, *7*, 53—65.

[7]. Goldberg, M.; Langer, R.; Jia, X. Nanostructured materials for applications in drug delivery and tissue engineering. *Journal of Biomaterials Science, Polymer Edition* **2007**, *18*(3), 241–268.

[8]. Adams, M.L.; Lavasanifar, A.; Kwon, G.S. Amphiphilic block copolymers for drug delivery. *Journal of Pharmaceutical Sciences* **2003**, *92*, 1343-1355.

[9]. Motornov, M.; Roiter, Y.; Tokarev, I.; Minko, S. Stimuli-responsive nanoparticles, nanogels and capsules for integrated multifunctional intelligent systems. *Progress in Polymer Science* **2010**, *35*, 174–211.

[10]. Kataoka, K.; Harada, A.; Nagasaki, Y. Block copolymer micelles for drug delivery: design, characterization and biological significance. *Advanced Drug Delivery Reviews* **2001**, *47* (1), 113–131.

[11]. Letchford, K.; Burt, H. A review of the formation and classification of amphiphilic block copolymer nanoparticulate structures: micelles, nanospheres, nanocapsules and polymersomes. *European Journal of Pharmaceutics and Biopharmaceutics* **2007**, *65*(3), 259–269.

[12]. Nishiyama, N.; Kataoka,K. Current state, achievements, and future prospects of polymeric micelles as nanocarriers for drug and gene delivery. *Pharmacology & Therapeutics* **2006**,*112*(3), 630–648.

[13]. Torchilin, V.; Lukyanov, A.; Gao, Z.; Papahadjopoulos-Sternberg,B. Immunomicelles: targeted pharmaceutical carriers for poorly soluble drugs. *Proceedings of National Academy of Science of USA* **2003**, *100*(10), 6039–6044.

[14]. Kohut, A.; Voronov, A. Hierarchical micellar structures from amphiphilic invertible polyesters: ^{1}H NMR spectroscopic study. *Langmuir* **2009**, *25*, 4356−4360.

[15].Kohut, A.; Sieburg, L.; Vasylyev, S.; Kudina, O.; Hevus, I.; Stafslien, S.; Daniels, J.; Kislenko, V.; Voronov, A. *In Amphiphiles: Molecular Assembly and Applications*; Nagarajan, R., Ed.; ACS Symposium Series 1070; American Chemical Society: Washington, DC, **2011**; 205−224 p.

[16]. Zhang, X.; Jackson, J. K.; Burt, H. M. Development of amphiphilic diblock copolymers as micellar carriers of taxol. *Int. J. Pharm*. **1996**, *132*, 195−206.

[17]. Papazisis, K.T.; Geromichalos, G.D.; Dimitriadis, K.A.; Kortsaris,A.H. Optimization of the sulforhodamine B colorimetric assay. *Journal of Immunological Methods* **1997**, *208* (2), 27, 151–158.

[18]. Zor, T.; SelingerZ. Linearization of the Bradford Protein Assay Increases Its Sensitivity: Theoretical and Experimental Studies. *Analytical Biochemistry*. **1996**, 236(2), 302–308.

[19]. Ward, E.; DeSantis, C.; Robbins, A.; Kohler, B.; Jemal, A. Childhood and adolescent cancer statistics, 2014.*A Cancer Journal for Clinicians* **2014**, *64* (2), 83–103.

[20]. Luetke, A.; Meyers, P. A.; Lewis, I.; Juergens, H. Osteosarcoma treatment–Where do we stand? A state of the art review. *Cancer Treatment Reviews* **2014**, *40* (4), 523–532.

[21]. Thangapazham,R. L.; Sharma, A.; Maheshwari,R. K. Multiple molecular targets in cancer chemoprevention by curcumin. *The AAPS Journal* **2006**; 8 (3), E443-E449.

[22]. Shi, M.; Cai, Q.; Yao, L.; Mao, Y.; Ming, Y.; Ouyang, G. Antiproliferation and apoptosis induced by curcumin in human ovarian cancer cells. *Cell Biology International* **2006**, *30*, 221-226.

[23]. Karunagaran, D.; Rashmi, R.; Kumar, S.T.R. Induction of apoptosis by curcumin and its implications for cancer therapy. *Current Cancer Drug Targets*, **2005**, 5, 117-129.

[24]. Ireson, C. R.;L. Jones, D. J.; Orr, S.; Coughtrie, M. W. H.; Boocock, D. J.; Williams, M. L.; Farmer, P. B.; Steward, W. P.; Gescher, A. J. Metabolism of the cancer chemopreventive agent curcumin in human and rat intestine. *Cancer Epidemiology, Biomarkers & Prevention* **2002**, 11, 105-111.

[25]. Hevus, I.; Modgil, A.; Daniels, J.; Kohut, A.; Sun, C.; Stafslien, S.; Voronov, A. Invertible Micellar Polymer Assemblies for Delivery of Poorly Water-Soluble Drugs. *Biomacromolecules* **2012**, *13*, 2537-2545.

[26]. Chignell, C.F.; Bilski, P.; Reszka, K.J.; Motten, A.G.; Sik, R.H.; Dahl, T.A. Spectral and photochemical properties of curcumin. *Photochemistry and Photobiology* **1994**, *59*(3), 295-302.

[27]. Leo, A.; Hansch, C.; Elkins, D. Partition coefficients and their uses. *Chemical Reviews* **1971**, *71* (6), 525–616.

[28]. Alexandridis, P.; Lindman, B. *Amphiphilic Block Copolymers: Self-Assembly and Applications*, Elsevier Science B.V., Amsterdam, **2000**, 448 p.

[29]. Pedersen, J.S.; Svaneborg, C. Scattering from block copolymer micelles. *Current Opinion in Colloid & Interface Science* **2002**, 7, 158–166.

[30]. Svensson, B.; Olsson, U.; Alexandridis, P.; Mortensen, K. A. A SANS investigation of reverse (water-in-oil) micelles of amphiphilic block copolymers. *Macromolecules* **1999**, 32, 6725–6733.

[31]. Goldmints, I.; Yu, G-E.; Booth, C.; Smith, K.A.; Hatton, T.A. Structure of (Deuterated PEO)−(PPO)−(Deuterated PEO) Block Copolymer Micelles As Determined by Small Angle Neutron Scattering. *Langmuir* **1999**, *15*, 1651–1656.

[32]. Kohut, A.; Voronov, A. Hierarchical Micellar Structures from Amphiphilic Invertible Polyesters: ^{1}H NMR Spectroscopic Study. *Langmuir* **2009**, *25* (8), 4356 – 4360.

[33]. Kositza, M. J.; Bohne, C.; Alexandridis, P.; Hatton, T. A.; Holzwarth, J. F. Dynamics of micro-and macrophase separation of amphiphilic block copolymers in aqueous solution. *Macromolecules* **1999**, *32*, 5539–5551.

[34]. Yang, L.; Alexandridis, P. Physicochemical aspects of drug delivery and release from polymer-based colloids. *Langmuir* **2000**, *16*, 4819–4829.

CHAPTER 5. PEG AND CHOLESTEROL-CONTAINING PYROMELLITATES: SYNTHESIS, SELF-ASSEMBLY

(Based on manuscript published in *Macromolecular Chemistry and Physics* **2013**, 214 (23), 2761-2767)

5.1. Abstract

In this study, a new synthetic route for two different amphiphilic macromolecular structures containing hydrophilic PEG and lipophilic cholesterol fragments is described. The novelty of the synthesis is in combining hydrophilic and lipophilic fragments in a backbone using functional groups of the pyromellitic dianhydride (PMDA) molecule. The ability of the new oligomers to undergo self-assembly and solubilization of lipophilic molecules in an aqueous medium is compared. The new oligomers form self-assemblies capable of solubilizing lipophilic "guest" molecules in an aqueous medium. Higher solubilization capacity and biodegradability, as well as other properties (size distribution, ζ-potential), make the synthesized macromolecules good candidates for biomedical applications.

Using the developed approach, amphiphilic macromolecules with regulated surface activity can be synthesized by combining PEG of varying lengths with different hydrophobic fragments (for example, fatty alcohols) in the backbone.

5.2. Introduction

Being a key component of eukaryotic cell membranes, water-insoluble cholesterol possesses high thermodynamic affinity for biomembranes and is able to change their permeability and fluidity. [1] It has been shown that cholesterol molecules contribute to the stability of lipid rafts (membrane receptors sites) [2], and regulate a variety of membrane proteins, including multiple receptors and ion channels. [3-5] Water-soluble derivatives of cholesterol can self-assemble to form aggregates, micelles and liquid crystalline phases [6-10]. They are interesting objects for biomimicry research, studying the interactions with biomembranes and practical biomedical applications, including drug delivery [11].

It is generally anticipated that the hydrophobic nature of cholesterol moieties facilitates a broad variety of polymeric self-assemblies in an aqueous medium.[11] To synthesize water-soluble macromolecules with cholesterol moieties and generate their self-assembly in an aqueous medium, one can combine fragments of cholesterol with hydrophilic ones—for example, PEG. The PEG is highly biocompatible and provides stealth behavior by decreasing the interaction with blood, thus making it the only polymer currently approved as a therapeutic agent at the point of drug delivery. [12]

Micelles with a biocompatible PEG corona and a cholesterol core can be formed from commercially available cholesterol-PEG copolymers. [13-14] Depending on PEG length, different polymer morphologies (vesicles and nanofibers) were observed for well-organized architectures from diblock copolymers based on PEGs and polycholesteryl acryloyloxy ethyl carbonate [15]. Examples of PEG-functionalized cholesterols show that the properties of micelles can be tailored with specific binding abilities and release kinetics for the delivery of hydrophobic drugs, plasmids, and nucleic acids [13, 14, 16-19].

Even though a variety of cholesterol-PEG macromolecules have been synthesized, the methods used to synthesize the macromolecules do not provide direct control over the macromolecular hydrophilic-lipophilic balance (HLB) and, thus, they do not provide direct control over their surface activity and self-assembly.

The goal was to develop a new synthetic route employing pyromellitic dianhydride functional groups in order to attach hydrophilic PEG and lipophilic cholesterol fragments in a controllable manner in the backbone. The further goal was to demonstrate the self-assembly and ability of the new oligomers to solubilize poorly water-soluble molecules in an aqueous medium.

Two different molecular structures of the oligomers (Scheme 5.1) were prepared. First, the oligomer consisting of the PEG fragment linked to the cholesterol through the PMDA spacer (PEG-PMDA-Chol, PPC) was synthesized. Another structure (Chol-PMDA-PEG-PMDA-Chol, CPPPC) can be viewed as a gemini-like molecular configuration. [20] Most geminis (often, low molecular weight surface-active compounds) are composed of a spacer connecting two amphiphilic moieties towards the end of the hydrophobic tail and near the hydrophilic fragment. Such a configuration provides a striking ability to form micellar assemblies at a concentration of more than an order of magnitude lower than molecules with a conventional alternated distribution of hydrophilic and hydrophobic fragments [20].

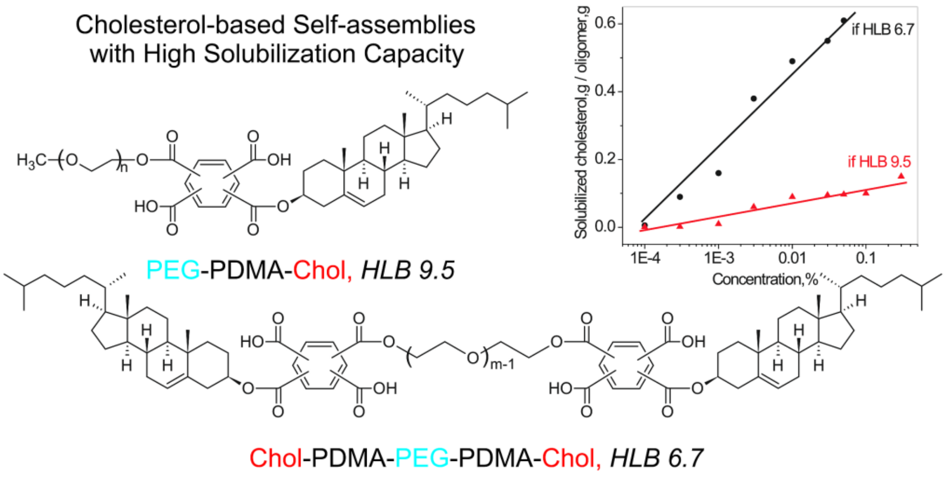

Scheme 5.1. Molecular structures of the cholesterol-base oligomers.

It is assumed that cholesterol fragments form a highly hydrophobic interior of assemblies in aqueous solutions and serve to solubilize poorly water-soluble lipophilic molecules. The latter can include various hydrophobic drugs, dyes for bioimaging, etc. Additionally, the cholesterol moieties are expected to affect the interaction between the self-assemblies and the biomembranes.

In this work, a synthetic route for two different molecular structures of the oligomers containing hydrophilic PEG and lipophilic cholesterol fragments was developed and the ability of the oligomers to undergo self-assembly and solubilization of lipophilic molecules in an aqueous medium was compared. Using the developed approach, amphiphilic macromolecules with regulated surface activity can be synthesized by combining PEG of varying lengths with different hydrophobic fragments (for example, fatty alcohols) in the backbone.

5. 3. Experimental

5.3.1. Abbreviations

PMDA – pyromellitic dianhydride, PEG – poly(ethylene glycol), TEA – triethylamine, Chol – cholesterol, DMFA – dimethylformamide, PPC – PEG-PMDA-Chol oligomer, CPPPC – Chol-PEG-PMDA-PEG-Chol oligomer, PDI – polydispersity index.

5.3.2. Materials

PMDA (97%) was purchased from Alfa Aesar (Ward Hill, MA) and used precisely as it was received. PEG (molecular weight of 600 g/mol, Sigma-Aldrich), PEG methyl ether (molecular weight 550 g/mol, Sigma-Aldrich), and Chol (Alfa Aesar, 95%) were dried by azeotropic distillation in benzene. TEA (Sigma Aldrich, ≥ 99%) was purified by simple distillation. Pyrene (Alfa Aesar, 98%), acetone-d6 and chloroform-d (Sigma-Aldrich, 99.9% atom D), DMFA (Sigma-Aldrich, 99.8%), methanol (anhydrous, VWR), and sodium chloride (Amresco, 99.9%) were used as received. An Amplex Red Cholesterol Assay Kit was purchased from Molecular Probes, Inc., Eugene, OR and was used as received.

5.3.3. Synthesis of Oligomers

For the synthesis of PPC, a mixture of 27.5 g (0.05 mol) methoxy PEG and 10.8 g (0.05 mol) PMDA was dissolved in 68.3 g of DMFA. Subsequently, 0.2 g (≈ 2 mmol) of TEA was added in order to catalyze the reaction. The mixture was stirred for 24 hours at 80°C. Afterwards, 19.3 g (0.05 mol) of dry Chol was added to the mixture and stirred at the same temperature until conversion, determined by pH-metric titration, reached 97–99%. The resulting product was dried under vacuum and purified (yield: 56% of pure PPC).

For the synthesis of CPPPC, 15.0 g (0.025 mol) of PEG-600 and 13.1 g (0.06 mol) of PMDA were dissolved in 85 g of DMFA. Subsequently, 0.2 g (≈ 2 mmol) of TEA was added to catalyze the reaction. The mixture was stirred for 24 hours at 80°C. Afterwards, 29.0 g (0.075 mol) of dry Chol was added to the mixture and stirred at the same temperature until conversion, determined by pH-metric titration, reached 97–99%. The resulting product was dried under vacuum and purified (yield: 69% of pure CPPPC).

Purification Procedure of PPC. After synthesis, the product was dried in a vacuum, dissolved in acetone, filtrated, and dried again. It was then dissolved in water (1:19) with the addition of sodium carbonate until a pH 8.0 was reached. Next, sodium chloride was added to the mixture (1 g NaCl per 10 ml), and PPC was precipitated at a pH of 2.0, by adding 5% w/v hydrochloric acid, and centrifuged. The collected PPC was dissolved in water and reprecipitated.

The product was dried at 60°C in an oven, dissolved in acetone, and filtrated to remove residues of the sodium chloride. The acetone solution was concentrated in a vacuum, precipitated by hexane, and dried to yield pure CPP.

Purification Procedure of CPPPC. After the synthesis product was dried in a vacuum, it was dissolved in an acetone-methanol mixture (1:2 v/v) and filtrated. The filtrated product was dried and dissolved in water (1:4) with the addition of sodium carbonate until a pH of 8.0 was reached. Next, sodium chloride was added to the mixture (1g NaCl per 10 ml), and the CPPPC was precipitated at a pH of 2.0, by adding 5% w/v hydrochloric acid, and centrifuged. The collected CPPPC was dissolved in water and reprecipitated twice using the technique previously described. The product was dried at 60°C in an oven, dissolved in benzene, and filtrated to remove residues of the sodium chloride. The benzene solution was dried in a vacuum to produce pure CPPPC.

5.3.4. Oligomers Characterization

To confirm chemical structure of the synthesized oligomers, ^{1}H NMR spectra were recorded on a JEOL ECA 400 MHz NMR spectrometer using $CDCl_3$ as a solvent. ESI high-resolution mass spectra were obtained using a Bruker Daltonics BioTOF mass spectrometer. The critical aggregation concentration of the synthesized oligomers was measured using solubilization of the fluorescent probe, pyrene, as described elsewhere. [21] The fluorescence excitation spectra, λ_{em} = 390 nm, were accumulated using a Fluoromax-3 fluorescence spectrometer (Jobin Yvon Horiba) with an integration time of 0.5 nm/s. Critical aggregation concentration values were determined after fitting the semi-logarithmic plots of the intensity ratio $I_{336.5}/I_{333}$ vs. log concentration to the sigmoidal curve.

Size distribution and the zeta potential of oligomeric assemblies and mixed micelles were measured using a Malvern Zetasizer Nano-ZS90 at 25 ÷0.1 C and pH 6.5 ± 0.05. The final numbers represent an average of a minimum of five (size) or ten (zeta potential) individual measurements.

5.3.5. Determination of Solubilized Cholesterol

To determine Chol solubilization in oligomeric self-assemblies, a sample of 4% w/w Chol solution in benzene was mixed with 5 ml of aqueous oligomer solutions at different concentrations (at a pH of 6.5 ± 0.05). Open vials were stirred at room temperature for 4 hours to evaporate the benzene. After the evaporation of the benzene, the solutions were stirred in closed vials for 24 hours to equilibrate them. The content of the solubilized product was determined using an Amplex Red Cholesterol Assay Kit (Molecular Probes, Inc.), as described below.

The Amplex Red Cholesterol Assay Kit provides a sensitive and simple fluorometric method for detecting very low concentrations of cholesterol using a series of enzymatic reactions (Scheme 5.2) [21, 22]. During the analysis, free cholesterol is oxidized by cholesterol oxidase to yield H2O2 and the ketone products. The H_2O_2 is then detected using 10-acetyl-3,7-dihydroxyphenoxazine (Amplex Red reagent), a sensitive and stable probe for H_2O_2 [22]. In the presence of horseradish peroxidase (HRP), Amplex Red reagent reacts with H_2O_2 with a 1:1 stoichiometry to produce fluorescent resorufin [21, 22]. Being dependent on the concentration of the absorbing substance, solutions of resorufin possess one of the highest known values of Kreft’s dichromaticity index, which presents itself as the solution’s hue [23].

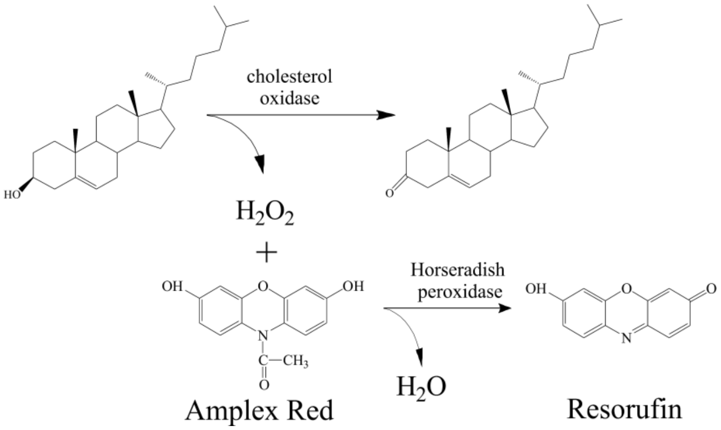

Scheme 5.2. Enzymatic reactions during cholesterol determination.

A 20 mM stock solution of Amplex Red was prepared by dissolving Amplex Red reagent in a corresponding quantity of dimethyl sulfoxide (DMSO). The reaction buffer was comprised of 0.1 M sodium phosphate (pH 7.01), 0.05 M sodium chloride, 5 mM cholic acid, and 0.1% Triton® X-100 and was prepared from a concentrate supplied in the kit. Enzyme stock solutions—horseradish peroxidase (HRP), cholesterol oxidase (CO), and cholesterol esterase (CE)—were prepared by dissolving the supplied concentrates in a corresponding amount of reaction buffer. To generate the oxidation processes (Scheme 5.2), a working solution was prepared by mixing 75 µl of the Amplex Red reagent solution, 50 µl of the HRP solution, 50 µl of the CO solution, and 5 µl of the CE solution in 4.82 ml of the reaction buffer.

Next, 1 mL of the prepared working solution and a final concentration of 150 µM of the Amplex Red reagent were mixed with 1 ml of the analyzed solution of solubilized cholesterol or a cholesterol standard.

The reaction mixture was incubated for 30 minutes at 37°C and was protected from light. The fluorescence spectra of the reaction mixtures were recorded using a Fluoromax-3 fluorescence spectrometer (Jobin Yvon Horiba) with 90° geometry and a slit opening of 0.5 nm.

Fluorescence was measured using excitation at 560 ± 10 nm and fluorescence detection at 590 nm. Spectra were accumulated with an integration time of 0.5 nm/s. Standard cholesterol solutions were used to build the calibration curve in order to determine cholesterol concentrations in the analyzed samples.

5.3.6. Oligomer Degradation in Aqueous Media

0.1 g of oligomer was dissolved in 10 ml of phosphate buffer (pH 7.01) and stirred at 40°C for defined time. The degradation of ester bonds and subsequent formation of carboxylic groups in each oligomer sample was followed by pH-metric titration at room temperature. Determined acid number of hydrolized samples were compared to acid numbers of blank samples to plot the degradation profile.

5.4. Results and Discussion

5.4.1. Synthesis and Self-Assembly of PEG and Cholesterol-Containing Oligomeric Pyromellitates

Synthesis of the oligomers (Scheme 5.1) involves a two-step acylation reaction. The novelty of the synthetic approach is in employing PDMA functional groups, which enable the attachment of different oligomeric fragments to each side of the dianhydride molecule. The synthetic route provides an opportunity to facilitate control of HLB and macromolecular surface activity, simply by (1) employing hydrophilic fragments (in this work, PEG macromolecules) of varying molecular length and/or (2) synthesizing macromolecules with one or two hydrophobic fragments (in this work, Chol). In the first reaction step, PMDA interacts with PEG to form a monoester that contains the residual anhydride group. In the second reaction step, the latter group has been used for the acylation of the cholesterol molecule in order to form the final product.

Using the monofunctional PEG in the first step leads to the formation of diesters with PEG and cholesterol termini (PPC) (Scheme 5.3A). Utilizing the bifunctional PEG results in the synthesis of gemini-like tetraesters with terminal cholesterol fragments (CPPPC) (Scheme 5.3B). Both products contain carboxylic groups that enable the pH control of aqueous solubility.

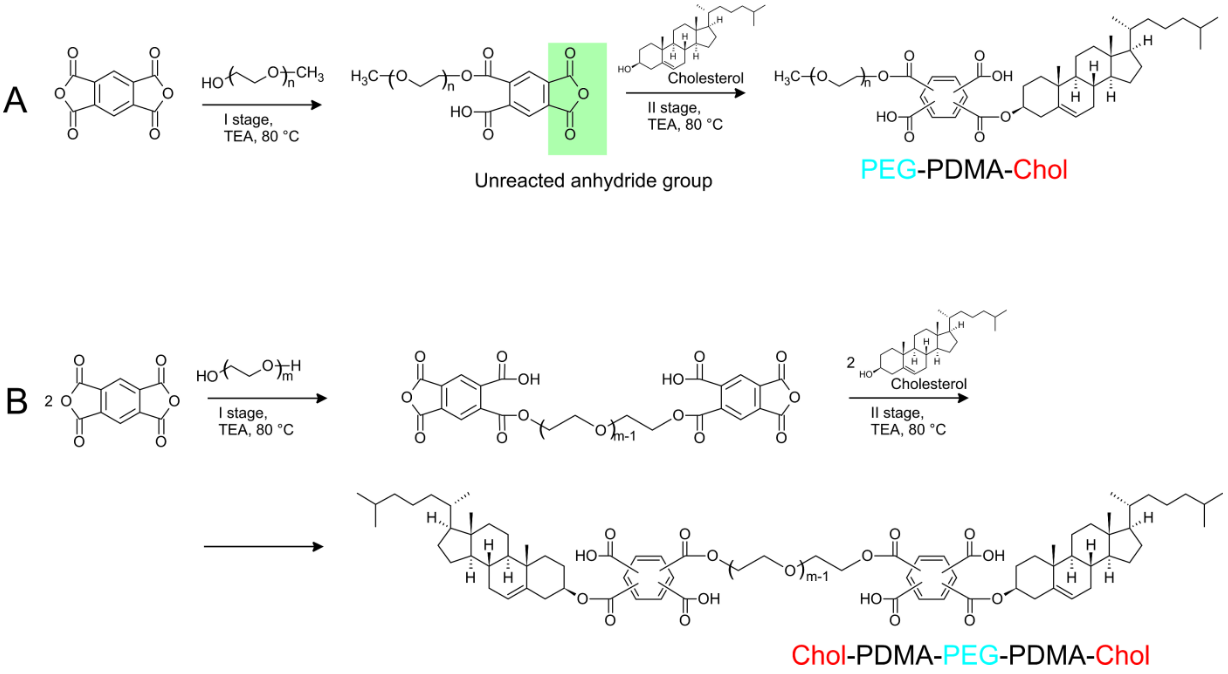

Scheme 5.3. PPC (A) and CPPPC (B) synthesis.

For PPC synthesis, an equimolar ratio of PEG methyl ether, PDMA, and cholesterol was used. To synthesize the gemini-like CPPPC, PEG—which contains two reactive functional groups—was chosen as a hydrophilic fragment, and a 1:2.4:3 ratio of PEG:PDMA:Chol was used.

The oligomers were characterized using ^{1}H NMR and mass spectrometry. As representative examples, the ^{1}H NMR spectrum and mass spectrum of a PPC diester are shown in Fig.5.1. The mass spectrum confirms the chemical composition of the expected structure. Using mass spectra, the molecular weight of the oligomers can be calculated. Values of molecular weight of 1,778 g/mol for the tetraester structure and 1,188 g/mol for the diester structure were determined (Fig.5.1). Generally, the results from ^{1}H NMR spectroscopy and mass spectrometry were in agreement, which was shown by comparing the integrals of the corresponding signals in the ^{1}H NMR spectrum. In the ^{1}H NMR spectrum (Fig.5.1) of the CPP/CPPPC in $CDCl_3$, peaks corresponding to protons of the PEG chains appear at 3.65 ppm (m, 44/44H, $CH_2OC\mathit{H}_2C\mathit{H}_2OCH_2$), 3.69 ppm (t, 2/4H, $C(O)OCH_2C\mathit{H}_2O$), and 4.24 ppm (t, 2/4H, $C(O)OC\mathit{H}_2CH_2O$). Cholesterol protons show themselves as peaks at 0.8–2.6 ppm (m, 43/86H), 4.85 ppm (m, 1/2H, $OC\mathit{H}(CH_2)_2$), and 5.42 ppm (m, 1/2H, $C{=}C\mathit{H}CH_2$). A peak at 3.37 ppm is attributed to a methyl group of an mPEG fragment (s, 3H, $C\mathit{H}_3O$).

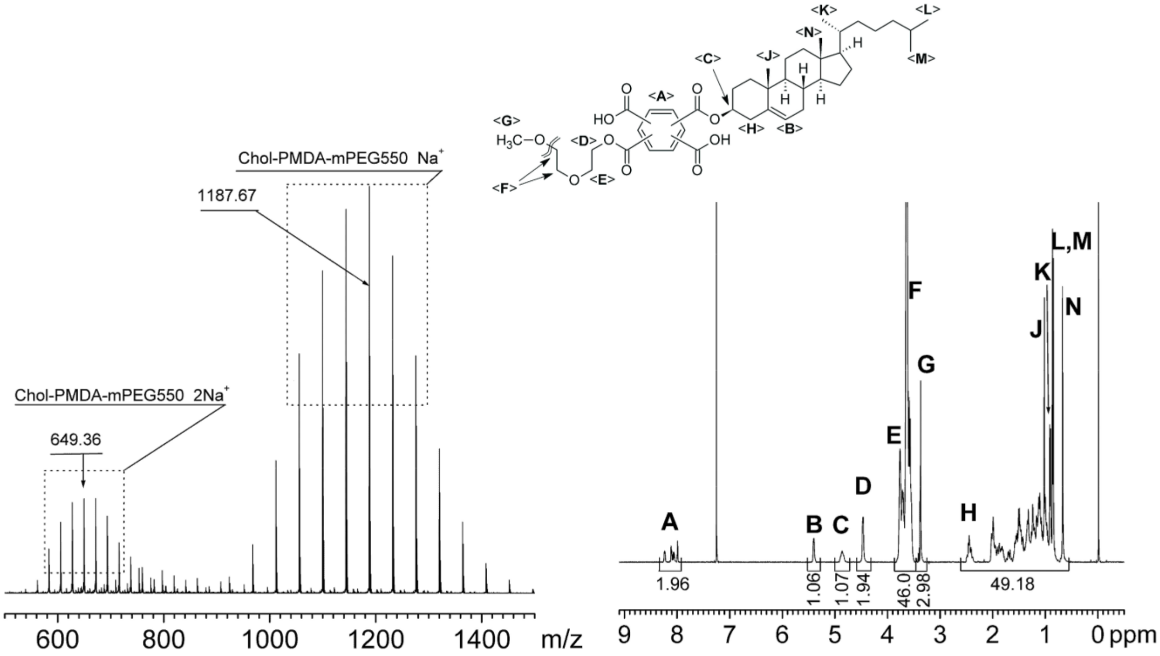

Fig.5.1. Mass and ^{1}H NMR spectrum of a PPC.

To achieve the self-assembly of oligomers in an aqueous solution, their surface activity was targeted. To this end, the HLB of the oligomers was varied during the synthesis by changing their chemical structure (PPC and CPPPC). The HLB of the final products was calculated using the Griffin formula [24]. As a result, macromolecules show different values of HLB (9.5 for PPC and 6.7 for CPPPC). Both oligomers were observed to reduce the surface tension of the water from 72.8 mN/m to 45–48 mN/m (data not shown), which indicates the surface activity of the synthesized products. To demonstrate the self-assembling of oligomers in an aqueous medium, the solubilization of pyrene—a common fluorescent probe for monitoring the association behavior of amphiphilic macromolecules—was performed [25, 26].

The pyrene excitation spectra were recorded in the wavelength range of 300–360 nm and plotted the intensity ratios $I_{336.5}/I_{333}$ as a function of the oligomer concentration in the aqueous solution.

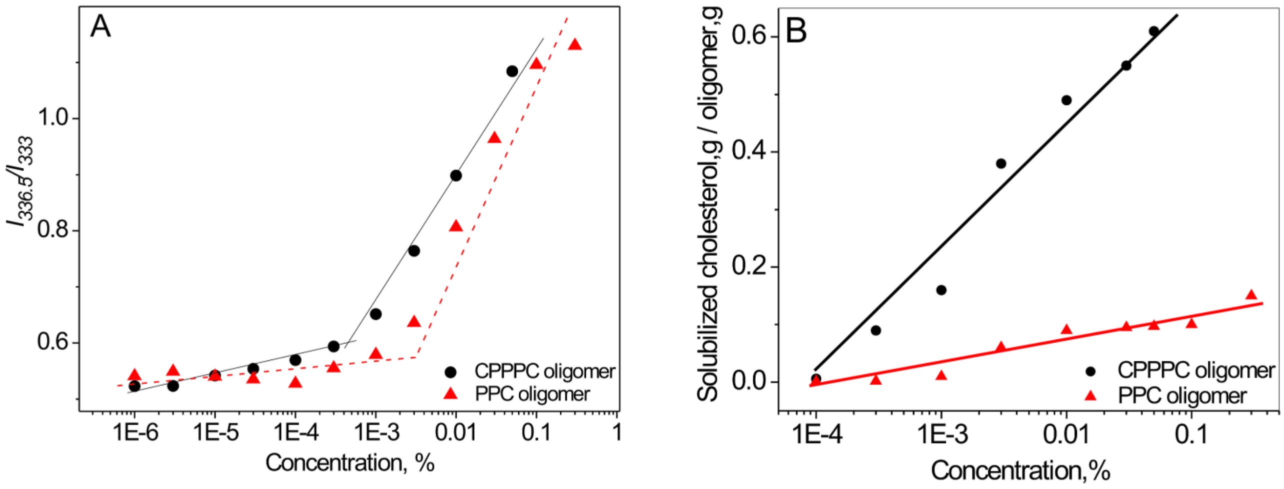

Fig.5.2. The intensity ratio $I_{336.5}/I_{333}$ of the excitation spectra of pyrene in solutions vs. oligomer concentration (A). Amount of cholesterol solubilized in oligomeric assemblies vs. oligomer concentration (B).

A red shift of the fluorescence excitation spectra from 333–336.5 nm with an increasing concentration indicates the transfer of pyrene molecules from the water to the self-assemblies and corresponds to the critical aggregation concentration. Changing the oligomer structure results in a significant difference in the pyrene solubilization. More hydrophobic tetraester macromolecules self-assemble at 2.5 x 10^{-6} mol/L (4.5 mg/L), whereas aggregation of PPC begins at around 2.6 x 10^{-5} mol/L (30 mg/L) (Fig.5.2A). These data are in agreement with HLB and show the higher self-assembling activity of more hydrophobic oligomer CPPPC. Additionally, in the case of a strong dilution by a large volume of systemic circulation in the human body, a very low critical aggregation concentration of CPPPC can facilitate high-aggregative stability in the solution.

Lipophilic cholesterol was chosen in order to evaluate the ability of the assemblies to solubilize the water-insoluble molecules in the aqueous solution. The employed technique of determining solubilized cholesterol in assemblies is based on the oxidation of cholesterol by cholesterol oxidase. The employed technique yields hydrogen peroxide. This technique allows for the detection of the H_2O_2 by 10-acetyl-3,7-dihydroxyphenoxazine (Amplex Red reagent) using fluorescence spectroscopy [27]. Cholesterol is insoluble in water, but in the presence of oligomeric assemblies, it was solubilized, as indicated by the characteristic shift of fluorescence intensity at 590 nm (Fig.5.2C). Thus, the assemblies provide a microenvironment capable of sequestering cholesterol molecules in water. Of note is that the tetraester assemblies show remarkable solubilization capacity (max. loading 59 ± 2.2% w/w.) by being able to incorporate of cholesterol per weight oligomer (Fig.5.2B).

Smaller solubilization capacity was recorded for the more hydrophilic diester assemblies (max. loading 15 ± 0.3% wt.). The latter can be explained by the differences in the chemical structure between two oligomers—in particular by the presence of two cholesterol fragments in the CPPPC. These fragments are expected to be a driving force for the solubilization. The marked difference in the solubilization ability of PPC and CPPPC also correlates with HLB values. To this end, the more hydrophobic oligomer demonstrates stronger aggregation behavior and greater ability to sequester hydrophobic molecules from water. The mechanism of solubilization in the assemblies is the subject of further detailed studies.

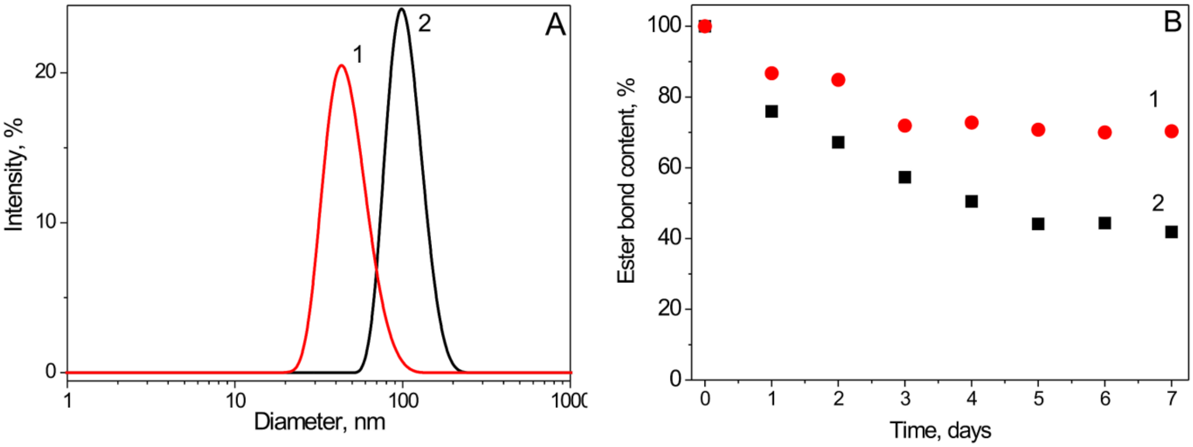

Fig.5.3. Size distribution of oligomeric assemblies as determined by dynamic light scattering (A) for PPC (1), and CPPPC (2) at 0.003% w/w. Hydrolytic degradation (B) of PPC (1) and CPPPC in PBS (pH 7.01) (2).

Using DLS, the size distributions of assemblies were characterized (Fig.5.3A). Small size (50 and 100 nm fof PPC and CPPPC, respectively) and unimodal size distribution (PDI is 1.2 for PPC, 1.18 for CPPPC) indicate that assemblies from both oligomers can be considered as nanocarriers for poorly water-soluble molecules in different biomedical applications.

Analysis of the ζ-potential shows that the assemblies have a negative surface charge (-57.9 mV ± 1.9 mV for PPC, -58.2 mV ± 2.1 mV for CPPC) and can potentially provide greater adhesion to gastrointestinal mucus and more interactions with cellular linings, thus facilitating the bioadhesion between the potential carriers and intestinal epithelial cells. [28]

Being related to hydrolytic cleavage of ester bonds, biodegradability is an important factor of potential biomedical applications of polyesters [29-30]. It has been shown that the polyester macromolecules can degrade in vivo by hydrolytic mechanism [31]. To demonstrate biodegradability of the synthesized macromolecules, the hydrolysis of oligomer ester bonds in phosphate buffer (pH 7.01) was studied by monitoring the subsequent formation of carboxylic groups by pH-metric titration. As a result, PPC and CPPPC exhibit different degradation rates (higher for CPPPC) over the tested period of time. Over the course of 11 days ester bonds cleavage reaches 62 ± 3% and 37 ± 4% for CPPPC and PPC respectively what is comparable to the reported values for polyesters (Fig.5.3B) [32-34].

5.4.2. Fabrication and testing of Mixed Micelles from Cholesterol-Containing Pyromellitates and AIP Macromolecules

In Chapters 3 and 4 the invertible micellar assemblies (IMAs) from amphiphilic invertible polymers (AIP) were shown to effectively incorporate hydrophobic cargo molecules. Moreover, *in vitro* testing of IMAs loaded with drug (curcumin) on normal cells and different osteosarcoma (bone cancer) cells was used to demonstrate therapeutic effect of curcumin-loaded IMAs (micellar curcumin) as drug carriers, whereas the normal bone cells remain viable in presence of micellar curcumin.

Several parameters are important for the successful application of polymeric colloids, such as IMAs, in drug delivery, including size and size distribution, micellar capacity and stability upon administration, delivery mechanism, etc [36-38]. In order to efficiently regulate some of these parameters mixed polymeric micelles can be fabricated from a combination of AIP and amphiphilic oligomers. The possible advantages of mixed polymeric micelles over single-component self-assemblies (IMAs) may include significantly improved thermodynamic and kinetic stability and regulated loading capacity [36-38].

In this work in order to improve the loading capacity of IMAs, novel synthesized oligomers (PPC, CPPPC) were applied in combination with selected AIP (PEG600-PTHF650) to fabricate mixed polymeric micelles.

Mixed micelles from PEG600-PTHF650 and oligomers (PPC or CPPPC) were prepared using thin film method. Following this method, PEG600-PTHF650 and PPC or CPPPC were dissolved in carbon tetrachloride at selected concentrations. The solvent was removed by rotary evaporation at 60°C for 1 h to obtain a solid film. The residual carbon tetrachloride was evaporated overnight in vacuum. The resultant thin film was hydrated with Millipore water to fabricate mixed PEG600-PTHF650/oligomer micelles with the chosen concentrations of PEG600-PTHF650 and PPC or CPPPC.

The dynamic light scattering (DLS) measurements indicate the presence of a single group of nanostructures, thus, confirming the formation of mixed PEG600-PTHF650/oligomer micelles (Fig.5.4). The size of the mixed micelles (Fig.5.5) is larger than the size of IMAs (see Chapter 3) but smaller than the size of oligomeric self-assemblies (see Chapter 5.4.1). As expected, the size of mixed micelles increases when being loaded with curcumin (Fig.5.5).

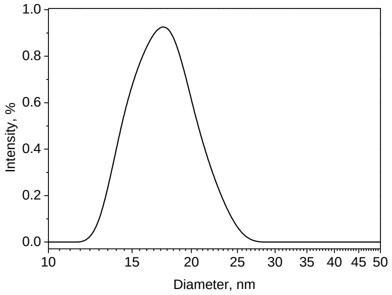

Fig.5.4. Selected size distribution of PEG_{600}-$PTHF_{650}$ (1% w/v)/PPC (0.003% w/v) mixed micelles, determined by DLS.

To load curcumin into mixed micelles, PEG_{600}-$PTHF_{650}$, PPC or CPPPC and methanol solution of curcumin (5 mg/ml) were mixed in carbon tetrachloride at selected concentrations.

The carbon tetrachloride was removed by rotary evaporation at 60°C for 1 h to obtain a solid film. The residual carbon tetrachloride was evaporated overnight in vacuum. The resultant thin film was hydrated with Millipore water to fabricate mixed PEG_{600}-$PTHF_{650}$/oligomer micelles loaded with curcumin. Unincorporated curcumin was removed by filtration through 0.45 μm filters.

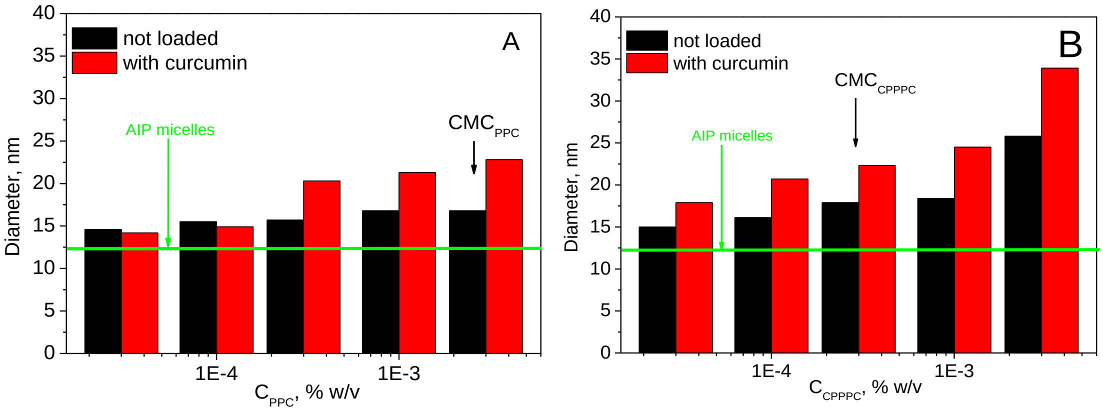

Fig.5.5. Size of loaded and non-loaded mixed micelles prepared from PEG_{600}-$PTHF_{650}$ (1 w/v) and different concentration of PPC (A) and CPPPC (B), determined using DLS.

As it is shown in Fig.5.6., the curcumin-loading capacity of mixed PEG_{600}-$PTHF_{650}$/oligomer micelles is larger in comparison to the capacity of single-component IMAs from PEG_{600}-$PTHF_{650}$. Increase of maximal loading capacity from 10% w/w (PEG_{600}-$PTHF_{650}$ IMAs) to 26% w/w (mixed PEG_{600}-$PTHF_{650}$/CPPPC micelles) can be attributed to the formation of larger hydrophobic moieties from the combination of hydrophobic PTHF fragments of AIP and hydrophobic cholesterol fragments of amphiphilic oligomer.

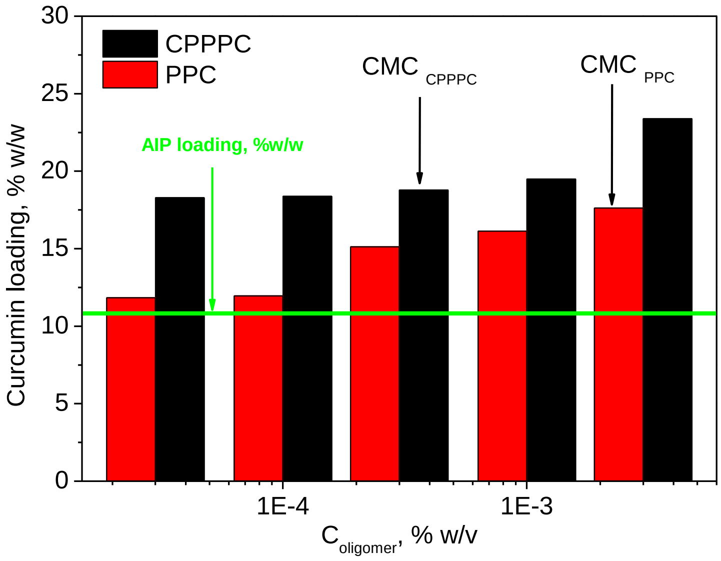

Fig.5.6. Curcumin loading into the mixed micelles prepared from PEG_{600}-$PTHF_{650}$ (1 w/v) and different concentration of PPC and CPPPC determined using UV-vis spectroscopy.

Next experimental aspect of characterization of curcumin-loaded mixed micelles is testing the chemical stability of micellar curcumin. At neutral and basic pH more than 90% of curcumin decomposes to (4'-hydroxy-3'-methoxyphenyl)-2,4-dioxo-5 hexanal, ferulic acid and feruloyl methane within 30 minutes [46]. In current study the chemical stability of micellar curcumin was monitored using UV-vis spectroscopy. Fig.5.7. represents the release of the curcumin from the curcumin-loaded PEG_{600}-$PTHF_{650}$/oligomer micelles. Similarly to curcumin loading determination, UV-vis spectroscopy was used to track the possible release of curcumin molecules from PEG_{600}-$PTHF_{650}$/oligomer micelles over time as the change of absorbance value. The obtained results indicate that the amount of released curcumin over 20 days is smaller 3% of initial loading. Such stability allows the drug to remain in blood circulation for prolonged time which can be promising for drug delivery applications.

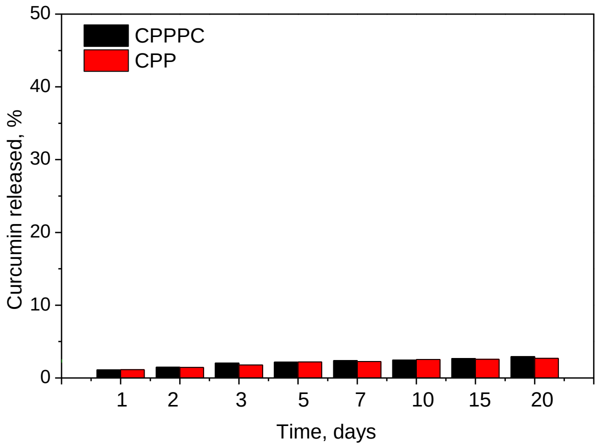

Fig.5.7. Chemical stability of curcumin-loaded mixed micelles prepared from PEG$_{600}$-PTHF$_{650}$ (1 w/v) and PPC (0.003% w/v) or CPPPC (0.001% w/v) determined using UV-vis spectroscopy.

Future studies would include the detailed structural characterization of mixed micelles fabricated from PPC or CPPPC and selected AIPs. SANS and NMR spectroscopy (^{1}H NMR and 2D NOESY) can be used to investigate the morphology and composition of fabricated AIP/oligomer mixed micelles before and after loading with curcumin. In addition, colloidal characterization (surface tension, stability testing) can give more insights into the behavior of mixed micelles in solutions. Finally, *in vitro* testing of curcumin-loaded mixed polymeric micelles can provide the information on their therapeutic effect as drug carriers.

5.5. Conclusions

In summary, a synthetic route for two different molecular structures of amphiphilic oligomers containing hydrophilic PEG and lipophilic cholesterol fragments was developed and the ability of the oligomers to undergo self-assembly and solubilization of lipophilic molecules in an aqueous medium was tested. Novelty of the synthetic route is in employing pyromellitic dianhydride functional groups to attach hydrophilic and lipophilic fragments to each side of the dianhydride molecule.

Using the developed synthetic route, macromolecules capable of self-assembling and solubilizing lipophilic "guest" molecules in an aqueous medium were synthesized. The high solubilization capacity of the assemblies and their biodegradability, as well as other properties (size distribution, ζ-potential) make the amphiphilic oligomers good candidates for studying the interactions with biomembranes and practical biomedical applications, including drug delivery. It is assumed that by facilitating the combination of PEG of varying molecular lengths with different hydrophobic fragments (for example, cholesterol, fatty alcohols), the developed approach can be applied to the synthesis of a variety of amphiphilic macromolecules with a regulated surface activity.

Amphiphilic oligomers (PPC, CPPPC) were combined with selected AIP (PEG600-PTHF650) for the fabrication of mixed micelles. The curcumin-loading capacity of PEG600-PTHF650/oligomer mixed micelles increased to 26% w/w in comparison with 10% w/w capacity of single-component PEG600-PTHF650 IMAs.

5.6. References

[1]. Klok, H.A.; Hwang, J.J.; Iyer, S.N.; Stupp, S.I. Cholesteryl-(L-lactic acid) building blocks for self-assembling biomaterials. *Macromolecules,* **2002**, *35*, 746-759.

[2]. Heino, S.; Lusa, S.; Somerharjju, P.; Ehnholm, C.; Olkkonen, V.M.; Ikonen, E. PEG and Cholesterol-Containing Pyromellitates: Synthesis and Self-Assembly. *Proceedings of the National Academy of Sciences of the USA,* **2000**, *97,* 8375-8380.

[3]. Klausen, T.K.; Hougaard, C.; Hoffmann, E.K.; Pedersen, S.F. Cholesterol modulates the volume-regulated anion current in Ehrlich-Lettre ascites cells via effects on Rho and F-actin. *American Journal of Cell Physiology* **2006**, *291*, 757–771.

[4]. Levitan, I.; Christian, A.E.; Tulenko, T.N.; Rothblat, G.H. Membrane cholesterol content modulates activation of volume-regulated anion current in bovine endothelial cells. *The Journal of General Physiology* **2000**, *115*, 405–416.

[5]. Maxfield, F.R.; Tabas, I. Role of cholesterol and lipid organization in disease. *Nature*, **2005**,*438*, 612–621.

[6]. Ringsdorf, H.; Schlarb, B.; Venzmer, J. Molecular architecture and function of polymeric oriented systems: models for the study of organization, surface recognition, and dynamics of biomembranes. *Angewandte Chemie International Edition* **1988,** *27*, 113-158.

[7]. Zhou, Y.; Briand, V.A.; Sharma, N.; Ahn, S.K.; Kasi R.M.; Polymers comprising cholesterol: synthesis, self-assembly, and applications. *Materials,* **2009**, *2*, 636-660.

[8]. Shibaev, V.P.; Plate, N.A.; Freidzon, Y.S. Thermotropic liquid crystalline polymers. I. Cholesterol-containing polymers and copolymers. *Journal of Polymer Science,* **1979,** *17,* 1655-1670.

[9]. Shibaev, V.P.; Talroze, R.V.; Karakhanova, F.I.; Plate, N.A. Thermotropic liquid crystalline polymers. II. Polymers with amino acid fragments in the side chains. *Journal of Polymer Science,* **1979,** *17,* 1671-1684.

[10]. Yamaguchi, T.; Asada, T. Dependence of the packing structure of mesogenic groups on the flexible spacer length of liquid-crystalline side-chain polymers. *Macromolecules,* **1989,** *22,* 1141-1144.

[11]. Yusa, S.I. Self-Assembly of Cholesterol-Containing Water-Soluble Polymers. *International Journal of Polymer Science,* **2012**, doi:10.1155/2012/609767

[12]. Knop, K.; Hoogenboom, R.; Fischer, D.; Schubert, U.S. Poly(ethylene glycol) in drug delivery: pros and cons as well as potential alternatives. *Angewandte Chemie International Edition* **2010**, *49*, 6288–6308.

[13]. Xu, J.P.; Ji, J.; Chen, W.D.; Shen, J.C. Novel biomimetic polymersomes as polymer therapeutics for drug delivery. *Journal of Controlled Release* **2005**, *107*(3), *502–512*

[14]. Qian, X.Q.; Lai, J.Y.; Zhan, S.L.; Zhang, J.; Wang, L.Q.; Tu, K.H. Novel MePEG-Chol and MepPEG-St mixed micellar systems for drug delivery: Preparation and characterization. *Rare Metal Materials and Engineering* **2008**, *37*, 655-658.

[15]. Pinol, R.; Jia, L.; Gubelini, F.; Levy, D.; Albouy, P-A.; Keller, P.; Cao, A.; Min-Hui, L. Self-Assembly of PEG-b-Liquid Crystal Polymer: The Role of Smectic Order in the Formation of Nanofibers. *Macromolecules,* **2007**, *16*, 5625-5627.

[16]. Chern, C.S.; Chiu, H.C.; Chuang, Y.C. Synthesis and characterization of amphiphilic graft copolymers with poly(ethylene glycol) and cholesterol side chains. *Polymer International* **2004**, *53*, 420-429.

[17]. Wang, Y.; Ke, C.Y.; Beh, C.W.; Liu, S.Q.; Goh, S.H.; Yang, Y.Y. The self-assembly of biodegradable cationic polymer micelles as vectors for gene transfection. *Biomaterials* **2007**, *28*, 5358-5368.

[18]. Thompson, C.J.; Ding, C.X.; Qu, X.Z.; Yang, Z.Z.; Uchegbu, I.F.; Tetley, L.; Cheng, W.P. The effect of polymer architecture on the nano self-assemblies based on novel comb-shaped amphiphilic poly(allylamine). *Colloid & Polymer Science* **2008**, *286*, 1511-1526.

[19]. Liu, L.; Guo, K.; Lu, J.; Venkatraman, S.S.; Luo, D.; Ng, K.C.;. Ling, E.A.; Moochhala, S.; Yang, Y.Y. Biologically active core/shell nanoparticles self-assembled from cholesterol-

terminated PEG–TAT for drug delivery across the blood–brain barrier. *Biomaterials* **2008**, *29*, 1509-1517.

[20]. Novel surfactants. In: K.Holmberg, B.Jonsson, B.Krinberg, B.Lindmann, *Surfactants and Polymers in Aqueous Solution*, *John Wiley and Sons*, LtD, **2002**, 228-235.

[21]. Zhou, M.; Diwu,Z.; Panchuk-Voloshina, N.; Haugland, R.P. A Stable Nonfluorescent Derivative of Resorufin for the Fluorometric Determination of Trace Hydrogen Peroxide: Applications in Detecting the Activity of Phagocyte NADPH Oxidase and Other Oxidases. *Analytical Biochemistry* **1997**, 253, 162–168.

[22]. Mohantya, G.; Jaffeb, J.S.; Schulmana, E.S.; Raible, D.G. A highly sensitive fluorescent micro-assay of H_2O_2 release from activated human leukocytes using a dihydroxyphenoxazine derivative. *Journal of Immunological Methods* **1997**, 202, 133–141.

[23]. Kreft, S; Kreft, M. Quantification of dichromatism: a characteristic of color in transparent materials. *Journal of the Optical Society of America,* **2009**, *A26,* 1576–1581.

[24]. Kohut, A.; Sieburg, L.; Vasylyev, S.; Kudina, O.; Hevus, I.; Stafslien, S.; Daniels, J.; Kislenko, V.; Voronov, A. *In Amphiphiles: Molecular Assembly and Applications*; Nagarajan, R., Ed.; ACS Symposium Series 1070; American Chemical Society: Washington, DC, **2011**; pp 205−224.

[25]. Griffin, W.C. Classification of surface-active agents by “HLB”. *Journal of the Society of Cosmetic Chemists* **1949**, *1*, 311-326

[26]. Wilhelm, M.; Zhao, C.L.; Wang, Y.; Xu, R.; Winnik, M.A.; Mura, J.L.; Riess, G.; Croucher, M.D. Poly(styrene-ethylene oxide) block copolymer micelle formation in water: a fluorescence probe study. *Macromolecules* **1991**, *24*, 1033−1040.

[27]. Schmitz, C.; Mourran, A.; Keul, H.; Moller, M. Synthesis and association behaviour of linear block copolymers with different microstructures but the same composition. *Macromolecular Chemistry and Physics* **2008**, *209*, 1859−1871.

[28]. Drake, M.; Amundson, M. Z. Fluorometric method for the enzymatic determination of cholesterol. *Journal of Biochemical and Biophysical Methods* **1999**, *38* (1), 43–52

[29]. Lo, C.L.; Lin, K.M.; Huang, C.K.; Hsiue, G.H. Mixed micelles formed from graft and diblock copolymers for application in intracellular drug delivery. *Advanced Functional Materials* **2006,** *16*, 2309-2316.

[30]. Okada, H.; Toguchi, H. Biodegradable Microspheres in Drug Delivery. *Critical Reviews in Therapeutic Drug Carrier Systems* **1995**, *12*, 1–99.

[31]. Li, S.; Vert, M. in: Scott, G.; Gilead, D. (Eds.), *Degradable Polymers*. Chapman and Hall, London, **1995**, Chapter 4, 43–87.

[32]. Anderson, J.; Shive, M. Biodegradation and biocompatibility of PLA and PLGA microspheres. *Advanced Drug Delivery Reviews* **1997**, *28*, 5-24.

[33]. Grizzi, I.; Garreau, H.; Li, S.M.; Vert, M. Hydrolytic degradation of devices based on poly(DL-lactic acid) size-dependence. *Biomaterials* **1995**, *16*, 305–311.

[34]. Vert, M.; Li, S.M.; Garreau, H. Hydrolytic degradation of devices based on poly(DL-lactic acid) size-dependence. *Journal of Biomaterials Science, Polymer Edition* **1995,** *8*, 639–649

[35]. Vert, M.; Li, S.M.; Garreau, H. Attempts to map the structure and degradation characteristics of aliphatic polyesters derived from lactic and glycolic acids. *Macromolecular Symposia* **1995,** *98*, 633–642.

[36]. Allen, C.; Maysinger, D.; Eisenberg, A. Nano-engineering block copolymer aggregates for drug delivery. *Colloids and Surfaces B: Biointerfaces* **1999**, *16*, 3–27.

[37]. Kim, S.; Shi, Y.; Kim, J.; Park, K.; Cheng, J. New inhibitors of the mammalian target of rapamycin signaling pathway for cancer. *Expert Opinion on Drug Delivery* **2010**, *7*, 49–62.

[38]. Rapoport, N. Physical stimuli-responsive polymeric micelles for anti-cancer drug delivery. *Progress in Polymer Science* **2007**, *32*, 962–90.

[39]. Lo, C.L.; Lin, K.M.; Huang, C.K.; Hsiue, G.H. Mixed micelles formed from graft and diblock copolymers for application in intracellular drug delivery. *Progress in Polymer Science* **2006,** *16*, 2309-2316.

[40]. Okada, H.; Toguchi, H. Critical Reviews in Therapeutic Drug Carrier Systems. *Critical Reviews in Therapeutic Drug Carrier Systems* **1995**, *12*, 1–99.

[41]. Li, S.; Vert, M. in: Scott, G.; Gilead, D. (Eds.), *Degradable Polymers*. Chapman and Hall, London, **1995**, 43–87.

[42]. Anderson, J.; Shive, M. Biodegradation and biocompatibility of PLA and PLGA microspheres. *Advanced Drug Delivery Reviews* **1997**, *28*, 5-24.

[43]. Grizzi, I.; Garreau, H.; Li, S.M.; Vert, M. Hydrolytic degradation of devices based on poly(DL-lactic acid) size-dependence. *Biomaterials* **1995**, *16*, 305–311.

[44]. Vert, M.; Li, S.M.; Garreau, H. Hydrolytic degradation of devices based on poly(DL-lactic acid) size-dependence. *Journal of Biomaterials Science, Polymer Edition* **1995,** *8,* 639–649

[45]. Vert, M.; Li, S.M.; Garreau, H. Attempts to map the structure and degradation characteristics of aliphatic polyesters derived from lactic and glycolic acids. *Macromolecular Symposia* **1995,** *98,* 633–642.

[46]. Kumar, A.; Ahuja, A.; Ali, J.; Baboota, S. Recent advances in protein and peptide drug delivery systems. *Current Drug Delivery* **2007**, *4*(2), 141-151.

CHAPTER 6. AMPHIPHILIC OLIGOMERS BASED ON DIESTERS OF PYROMELLITIC ACID FOR THE SOLUBILIZATION OF LIPOPHILIC AGENTS

(Published in *International Journal of Theoretical and Applied Nanotechnology* **2013**, *1* (2), 17-25)

6.1. Abstract

New amphiphilic oligomeric surfactants, diesters of pyromellitic acid (DEPA), were synthesized from pyromellitic dianhidryde, polyethylene glycol methyl ethers of different chain lengths, and alkanols/cholesterol. The synthesis resulted in amphiphilic oligomers containing hydrophilic (polyethylene glycol methyl ether, MPEG) and hydrophobic (residues of alkanol/cholesterol) fragments with a defined length. DEPA oligomers were shown to form micelles in an aqueous solution, and that the surface activity of DEPA depends on the nature and length of its hydrophilic and hydrophobic constituents (the hydrophilic-lipophilic balance of DEPA). Above their critical micelle concentration, the DEPA oligomers solubilize water-insoluble substances (including the lipophilic drug, curcumin), which confirms their potential for improving the solubility of poorly water-soluble (lipophilic) agents (drugs), for example in drug delivery systems.

6.2. Introduction

The development of a drug delivery platform based on polymer micelles for transporting hydrophobic (water-insoluble) drugs to pathological cells is a novel approach that has the potential to address the limitations of traditional drug delivery systems [1]. Recent studies resulted in the development of a large number of chemotherapeutic drugs and other therapeutic agents for the treatment of a wide range of cancer, cardiovascular and inflammatory diseases. However, the therapeutic potential of these agents is limited, primarily due to their poor solubility in aqueous media. To overcome this problem, significant research efforts have been recently made to develop novel nanotherapeutic modalities, including amphiphilic molecular assemblies: micelles, vesicles, and liposomes. These nanomodalities possess physico-chemical characteristics that can potentially fulfill the requirements of efficient drug delivery by providing colloidal dissolution of lipophilic agents in the micellar hydrophobic interior, while stabilizing the agent in aqueous media through the hydrophilic outer part of the micelles.

The previous studies demonstrate the synthesis of amphiphilic comb-like macromolecules through the polymer-analogous reactions of α-olefin - maleic anhydride copolymers with MPEG to obtain alternating hydrophilic (MPEG) and lipophilic (alkyl) side chains, in a polymeric surfactant backbone [2]. In aqueous solution, these polymeric surfactants self-assemble into micellar structures that can solubilize poorly water-soluble substances (lipophilic dyes, aromatic hydrocarbons), thus improving their solubility in water.

In this study, new oligomeric surfactants, the amphiphilic diesters of pyromellitic acid (DEPA), were synthesized from pyromellitic dianhidryde, polyethylene glycol methyl ethers with different chain lengths, and alkanols/cholesterol (Fig.6.1). The synthesis resulted in amphiphilic surface active oligomers, including diblock oligomers, containing hydrophilic (polyethylene glycol methyl ethers, MPEG) and hydrophobic (residues of alkanol/cholesterol) fragments with a defined length. It is expected that the inner (solubilizing) part of the oligomeric micelles consists of the DEPA hydrophobic constituents, while the micellar stabilizing exterior is from MPEG chains, which are known to provide micellar stability and longevity in the bloodstream. Additional control over the DEPA micellization is provided by the variation in hydrophilic (different MPEG lengths) and hydrophobic (butyl, octyl, cetyl, cholesteryl moieties) fragments in the DEPA molecule during the synthesis. In this way, the variation of the hydrophilic-lipophilic balance (HLB) of DEPA was achieved to considerably influence surface activity, and broaden the physico-chemical properties of the DEPA micelles. Additionally, it is expected that a controlled number of ester bonds in the DEPA molecules can provide biodegradability to the molecules of the synthesized oligomer surfactants. Choosing cholesterol, an essential structural component of the cell membrane, as one of the DEPA hydrophobic fragments, targets a potentially enhanced interaction between the oligomeric micelles and the biological membranes.

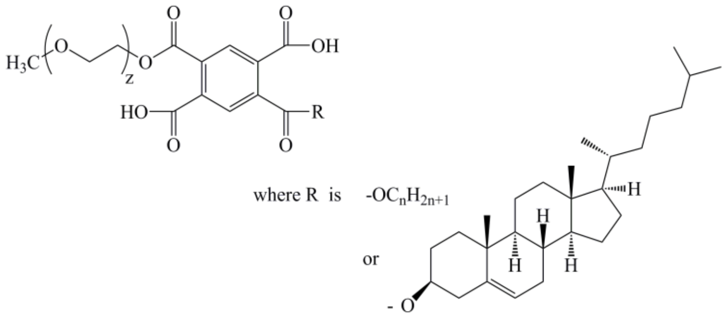

Fig.6.1. Chemical structure of DEPA. n = 3 ÷ 15, z = 7 ÷ 45.

Recently, several studies have focused on the development of amphiphilic surfactants capable of solubilizing and delivering the curcumin (a phytochemical agent that occurs naturally in plants) as an antitumor agent, and thereby increase its bioavailability and efficacy in cancer treatment [3, 4]. The clinical development of curcumin is, however, still hindered due to the drug’s insolubility in water, restricting the use of the curcumin. Hence, oligomeric surfactants can be considered as novel and promising biomaterials in solubilizing water-insoluble drugs, including curcumin, for further improvement in the administration of lipophilic agents.

6.3. Experimental

6.3.1. Materials

Pyromellitic dianhydride (PMDA, 97%) was purchased from Sigma Aldrich and used as received. Polyethylene glycols methyl esters (Aldrich, ≥98%) with molecular weight of 350 g/mol (MPEG350), 550 g/mol (MPEG550), and 750 g/mol (MPEG750) and cholesterol (Chol) (Aldrich) were purified by dissolving them in benzene (30% solution) followed by a distillation of the benzene-water azeotropic mixture at 393K. Primary aliphatic alcohols (PAA) (Sigma Aldrich, ≥98%), 1-butanol (But) and 1-octanol (Oct), were purified by boiling them with CaO for 4 hours and 2 days, respectively, and subsequent distillation over magnesium chips. Cetyl alcohol (Cet) (Aldrich) was used without purification. Dimethylformamide (DMFA) (Sigma Aldrich, anhydrous, 99.8%) was used as received. Triethylamine (TEA) (Sigma Aldrich, ≥99%) was purified by simple vacuum distillation. Curcumin (Overseal Natural Ingredients Ltd), 4-methyl-2-pentanone (Sigma Aldrich, ACS reagent, ≥98.5%), acetone-d_6 and chloroform-d (Aldrich, 99.9 atom % D) were used without purification. A fluorescent probe, pyrene (Alfa Aesar, 98%) was used as received.

6.3.2. Synthesis of DEPAs

Oligomeric diesters of pyromellitic acid were synthesized using a two-step esterification of PMDA, with primary aliphatic alcohols (Alc)/Cholesterol (Chol) and MPEG. The synthesis was carried out in DMFA in the presence of a catalyst TEA (0.02 mol/l), at 353K in an argon atmosphere. For the synthesis of Alc-PMDA-MPEG, 1M solution of aliphatic alcohol and PMDA in DMFA was stirred at a 1:1 ratio during 24 hours. Afterwards, an equimolar quantity of MPEG was added to the mixture and stirred for another 24 hours during the 2nd reaction stage.

For the synthesis of Chol-PMDA-MPEG, 1M solutions of MPEG and PMDA in DMFA were first stirred at a 1:1 ratio for 24 hours. Afterwards, an equimolar quantity of cholesterol was added to the mixture and stirred for another 24 hours during the 2nd reaction stage. Reaction conversion (97-99% at both stages) was controlled by the content of carboxyl groups, determined by pH-metric titration of 0.6 mL reaction mixture (diluted in excess DMFA) by 0.1 N aqueous sodium hydroxide.

After the synthesis, DMFA was distilled from the reaction mixture using a rotary evaporator. Alc-PMDA-MPEG esters were purified by multiple precipitations from the acetone solution into hexane, and washed using 4-methyl-2-pentanone to remove any side products, as well as MPEG and PMDA residues (final product yield 75-85%). Chol-PMDA-MPEG was purified by filtering the acetone solution to remove the cholesteryl pyromellititate esters (insoluble in acetone) and by using multiple precipitation from acetone into hexane to remove the residual cholesterol. The precipitate was dried, dissolved in aqueous sodium carbonate solution, and precipitated by adding a 5% HCl solution and excess of saturated NaCl solution. (The final product yield was 50-60%). Purified DEPAs were dried at 328K.

6.3.3. FTIR Spectroscopy

The FTIR spectra of synthesized oligomers were recorded in a thin layer deposited from the benzene solution on a potassium bromide tablet, using a Thermo Scientific Nicolet Fourier Transform Infrared Spectrometer, in the range of 400-4000 cm^{-1} with compensation of atmospheric CO_2 and H_2O.

6.3.4. NMR Spectroscopy

NMR spectra of oligomers were recorded in acetone-d_6 and chloroform-d (Chol-PMDA-MPEG550) solutions using a 500 MHz Varian Inova spectrometer.

6.3.5. Surface Tension to Determine CMC of DEPAs

The surface tension measurements were performed by drop shape analysis on pendant drops with a Contact Angle/Surface Tension Analyzer, First Ten Angstroms (FTÅ125) to determine the CMC of the DEPAs. Measurements were carried out at room temperature for the oligomer solutions of various concentrations (10^{-7}% – 1% w/w). Aqueous DEPA solutions were prepared by dissolving the DEPA in Millipore water (18Ω) and further adjusting the pH using a 15% w/w aqueous sodium carbonate solution. All glassware was washed in a 1 N NaOH bath and thoroughly rinsed with Millipore water before use.

6.3.6. Fluorescence Spectroscopy to Determine CMC of DEPAs

Alternatively, the critical micelle concentration of DEPAs was measured using the solubilization of a fluorescent probe, pyrene, using a previously reported method [5, 6]. The spectra were taken using a Fluoromax-3 Fluorescence Spectrometer (Jobin Yvon Horiba) with 90° geometry, and a slit opening of 0.5 nm. For fluorescence excitation spectra, λ_{em} = 390 nm was chosen. Spectra were accumulated with an integration time of 0.5 nm/s. Critical micelle concentration values were determined after fitting the semi-logarithmic plots of intensity ratio $I_{336.5}/I_{333}$ versus log concentration to the sigmoidal curve.

6.3.7. Curcumin Solubilization in DEPA Micelles

To determine curcumin solubilization, a sample of curcumin powder was mixed with different oligomer concentration solutions in a phosphate buffer (pH 6.58), and stirred at room temperature for 48 hours. Excessive curcumin was filtered. The UV-vis spectra of curcumin-solubilized oligomer solutions were recorded using Varian Cary 5000 at 293K. The concentration of solubilized curcumin was determined from the absorption spectra at characteristic 470 nm wavelength, using a calibration curve. The calibration curves were built after recording the UV−vis spectra of a set of curcumin solutions of known concentrations in the 1-octanol.

6.3.8. Solubilization of Non-Polar Solvents in DEPA Micelles

To study the solubilization of hexane/benzene in DEPA micelles, 0.01 ml of hexane/benzene was gradually added, every 2 days, to 20 mL of aqueous oligomer solution. The optical density (D) of the DEPA aqueous solutions were measured using the Photoelectric Colorimeter K 77 (λ = 535 nm) every two days, before adding a new portion of hexane/benzene. The procedure was repeated 10-15 times until the solution became turbid. The experimental values of D were plotted versus the volume of hexane/benzene added and the solubilization amount was determined as a slope change.

6.4. Results and Discussion

6.4.1. DEPA Synthesis and Characterization

Fig.6.2A, B shows the chemical structures of the diesters of pyromellitic acid (A- Alc-PMDA-MPEG, B -Chol-PMDA-MPEG) that were synthesized and used in this study for the formation of micelles and the further solubilization of lipophilic agents.

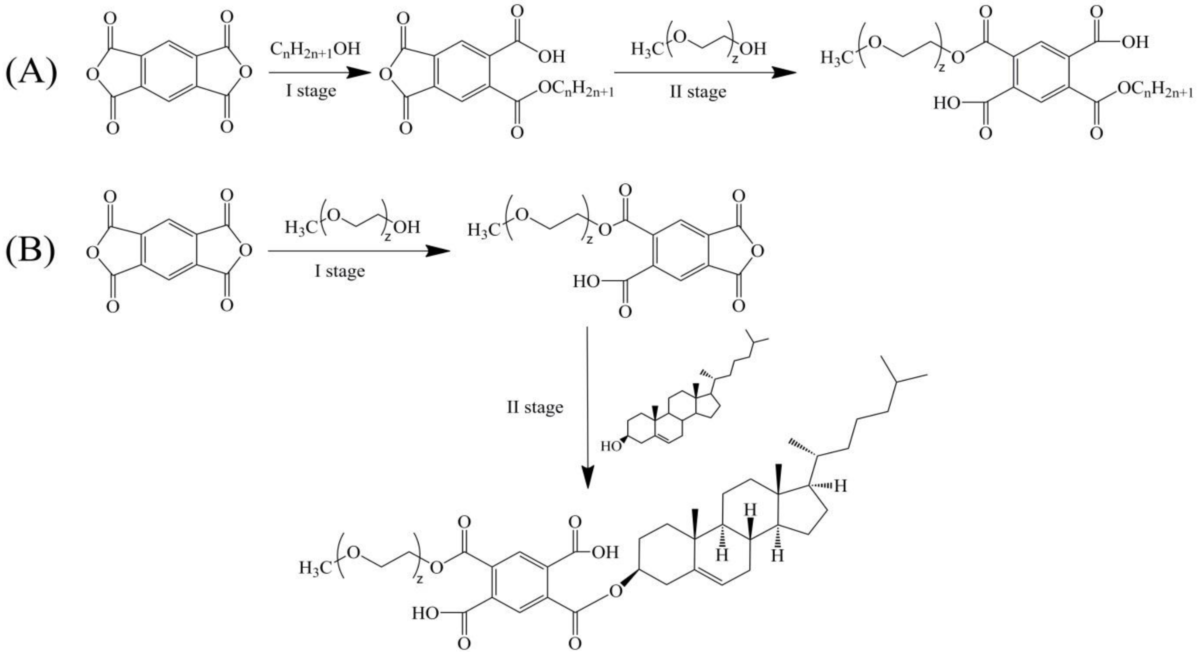

Fig.6.2. Synthesis of DEPA (A - Alc-MPEG-PMDA, B - Chol-MPEG-PMDA).

The chemical structure of the DEPAs was confirmed using FT-IR and ^{1}H NMR spectroscopy (Fig.6.3).

Corresponding to methyl and methylene groups, the characteristic bands for aromatic rings, ester groups and ether fragments on the FTIR spectra (Fig. 6.3, Tables 6.1, 6.2) confirmed the chemical structure of the Alc/Chol -PMDA-MPEG oligomers.

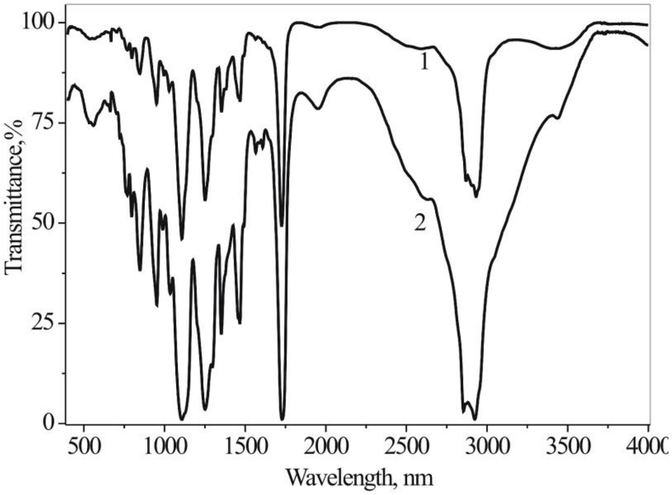

Fig.6.3. FTIR spectra of DEPAs (1 - Chol-PMDA-MPEG550, 2 - Cet-PMDA-MPEG550).

Table 6.1. Characteristic bands on FTIR spectra of Alc-PMDA -MPEG oligomers.

Wavenumber, cm^{-1}	**Group**
3426 ÷ 3438	COOH group near aromatic ring
2927 ÷2921	CH_3 (alkyl)
2854 ÷2869	CH_2 (alkyl)
1957÷1950	Overtone band for substituted aromatic ring
1729 ÷1727	C=O (ester)
1612 ÷1616	Aromatic ring
1467 ÷1456	CH_2 (alkyl)
1253 ÷1249	C-O- (ester)
1106 ÷1105	C-O-C (ether)
953÷951	C-H (aromatic) (CH out-of-plane bending)
760 ÷750	CH_2 (alkyl)

The chemical structure and composition of the synthesized products was confirmed using ^{1}H NMR spectroscopy. ^{1}H NMR spectra of Cet-PMDA-MPEG550 and Chol-PMDA-MPEG550, along with chemical shifts of protons, are represented in Fig.6.4 and 6.5 with Table 6.3 showing good agreement with the published data [7,8].

Table 6.2. Characteristic bands on FTIR spectra of Chol-PMDA –MPEG550.

Wavenumber, cm^{-1}	Group
3400 ÷ 3500	COOH group near aromatic ring
2931	CH_3 (alkyl)
2870	CH_2 (alkyl)
1726	C=O (ester)
1468	CH_2 (alkyl)
1354	alkyl
1252	OC-O- (ester)
1107	C-O-C (ether)
841	C-H (aromatic) (CH out-of-plane bending)

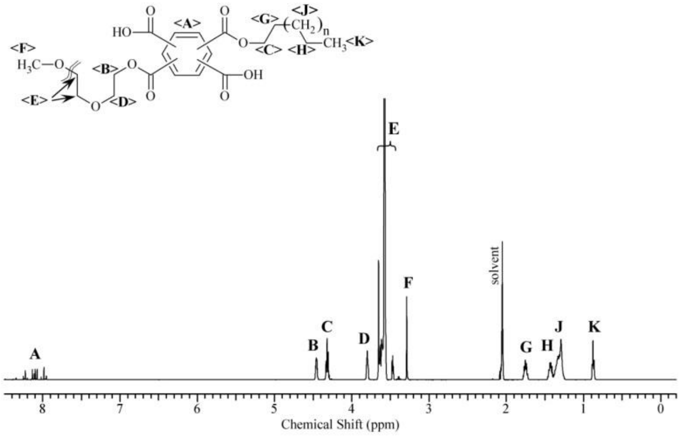

Fig.6.4. Typical ^{1}H NMR spectrum of But-PMDA-MPEG550 (n=0), Octy-PMDA-MPEG550(n=3) and Cet-PMDA-MGEG550 (n=11).

As can be seen from the data, the protons' signals for the MPEG550 fragment (E) show a chemical shift of 3.57 ppm for all synthesized diesters. An integral for the protons G (methylene groups of the alkyl fragment) was assigned as 2.0 (Table 6.3) and divided by two (since there are two protons in the methylene group).

The MPEG550 fragment contains approximately 44 protons, thus the integral for E protons should be divided by 44. The ratio of G/2 to E/44 for the synthesized products is : for But-PMDA -MPEG550: [G/2]:[E/44] = [2.00 / 2]: [44.34 / 44] = 1.00, for Oct-PMDA-MPEG550: [G/2]:[E/44]= [2.00 / 2]: [46.50 / 44] = 0.94; within Cet-PMDA-MPEG550:

[G/2]:[E/44]= [2,06 / 2]: [52.0 / 44] = 0.87. Hence, the ratio of the proton group's intensity (i.e. ratio of protons' intensities for the hydrophilic and lipophilic chains) is in good agreement with the theoretical values, confirming the synthesis and further successful purification of the DEPA oligomers. To this end, the acylation reaction of aliphatic alcohols and polyethylene glycol methyl ethers by PMDA can be employed for the synthesis of new amphiphilic oligomers based on diesters of pyromellitic acid.

Table 6.3. ^{1}H NMR characterization of oligomers[a].

#	Assignment[a]	Chemical Shift, ppm	Number of protons	Sample Integral		
				But-PMDA-MPEG550	**Oct-PMDA-MPEG550**	**Cet-PMDA-MPEG550**
1	K	0.85-0.95	3	2.48	2.30	2.48
2	H	1.38-1.47	2	2.00	10.46	35.88
3	J	1.27-1.37	- / 8 / 24[b]	-		
4	G	1.70-1.78	2	2.00	2.00	2.06
5	C	4.29-4.33	2	1.94	2.34	2.84
6	A	7.90-8.50	2	1.28	1.62	1.40
7	B	4.40-4.45	2	1.70	1.92	2.04
8	D	3.80	2	46.72	47.12	51.98
9	E	3.45-3.70	44			

[a] Assignment of protons corresponds to Fig.6.4.

[b] Value corresponds to the composition of sample: But-PMDA-MPEG550, Octy-PMDA-MPEG550 or Cet-PMDA-MPEG550.

Signals for the methyl groups' (chemical shift 0.85-0.86 ppm) and methylene groups' (1.02-1.99 ppm) protons, corresponding to the signals of protons in alkyl and cyclic fragments of cholesterol, respectively, were observed in the Chol-PMDA-MPEG550 NMR spectrum (Fig.6.5). A group of signals with a chemical shift in a range 3.63 ÷ 3.76 ppm corresponds to the methylene groups' protons in the MPEG550 fragments, while signals with a chemical shift of 3.37 ppm correspond to the methyl protons of the same fragment. Signal with a chemical shift of

4.46 ppm corresponds to the protons of the PEG methylene groups (D) in α position. Multiplet at 4.86 ppm depicts cholesterol fragment proton in α position to the carboxylate group (C). The signal at 5.40 ppm corresponds to the proton at the carbon atoms forming the double bond in cholesterol (B). Signals in the range 7.99÷8.23 ppm correspond to the protons of the aromatic fragment. The assignment of chemical shifts is confirmed by a ratio of the integrals for the MPEG and the cholesterol fragments: $(I\ MPEG:45)/(I\ Chol/44) \approx (49:45) / (49.18:44) \approx 0\ 99$, where 45 and 44 are the number of protons in MPEG550 and the cholesterol fragments respectively. Moreover, the integral for one proton C is 1.07, two protons D is 1.94, two protons A is 1.96, further confirming the structure of the product.

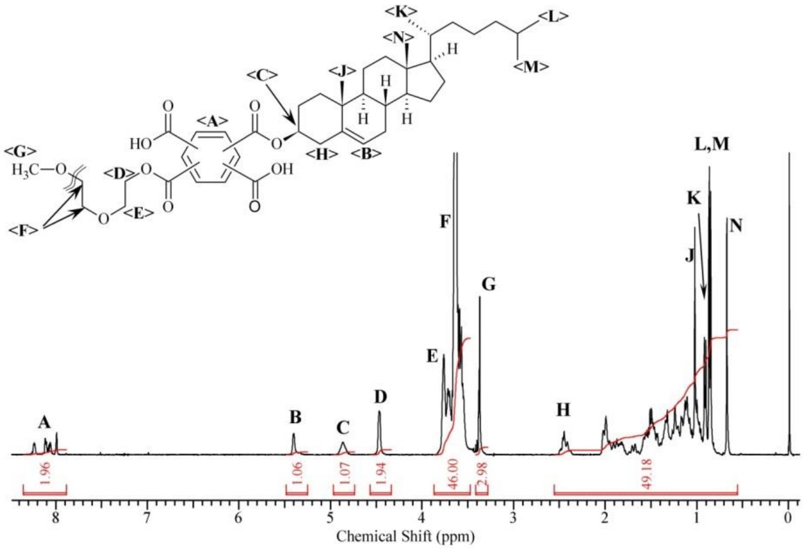

Fig.6.5. ^{1}H NMR spectrum of Chol- PMDA-MPEG550 oligomer.

6.4.2. Surface Activity of DEPA Oligomers

Amphiphilic behavior of the synthesized Alc-PMDA-MPEG and Chol-PMDA-MPEG oligomers is expected from having lipophilic alkyl/cholesterol fragments and hydrophilic MPEG fragments, simultaneously in the DEPA chemical structure. Broad surface activity for synthesized DEPAs was targeted to achieve a varying capacity of micelles in the solubilization of lipophilic agents in water. To this end, the HLB of the DEPAs was varied by changing the length of the hydrophilic and hydrophobic fragments in the oligomer molecule between 6.1 and 14.2, as calculated [8]. To confirm the formation of micelles from DEPAs in the aqueous solution, CMC values were determined by using surface tension measurements and the solubilization of pyrene. Molecular weight, hydrophilic lipophilic balance and critical micelle concentration of DEPAs (determined by using surface tension measurements) are shown in Table 6.4.

Table 6.4. Chemical structure and characteristics of DEPAs used in this study.

Lipophilic fragment		**Hyprophilic MPEG, MW**	**Oligomer, MW**	**HLB**	**CMC, mmol/L**
Code	**Formula**				
Oct	$-C_8H_{17}$	350	715	11,2	13.6
Oct	$-C_8H_{17}$	550	915	12.7	11.7
Cet	$-C_{16}H_{33}$	550	1027	8.9	2.0
Chol	$-C_{27}H_{45}O$	550	1188	6.1	0.8
Oct	$-C_8H_{17}$	750	1115	14.2	11.1
Cet	$-C_{16}H_{33}$	750	1227	10.4	2.0

Pyrene is a well-known fluorescent probe for studying the association behavior of amphiphilic polymers [5, 6]. Depending on the environment of the pyrene, a red shift of the absorption band, with enhanced excitation intensity, was observed due to the migration of the probe from the hydrophilic to the hydrophobic region of the polymer micelles. Pyrene excitation spectra were monitored in the wavelength range of 300−360 nm. From the pyrene excitation spectra, the intensity ratios $I_{336.5}/I_{333}$ were plotted as a function of oligomer concentration

(Fig.6.6). A red shift of the fluorescence excitation spectra from 333 to 336.5 nm, with an increasing DEPA concentration in aqueous solution, indicates the solubilization of pyrene within the micellar hydrophobic environment, and the transfer of pyrene molecules from the water to the micelles. The sharp increase in the intensity ratio corresponds to the critical micelle concentration for each DEPA composition.

CMC values correlate with the chemical structure and HLB of the DEPAs. Changing the length of both the hydrophobic and hydrophilic fragments in the DEPA molecules results in a significant difference in recorded CMC values, both when using surface tension measurements and through the solubilization of the fluorescence probe.

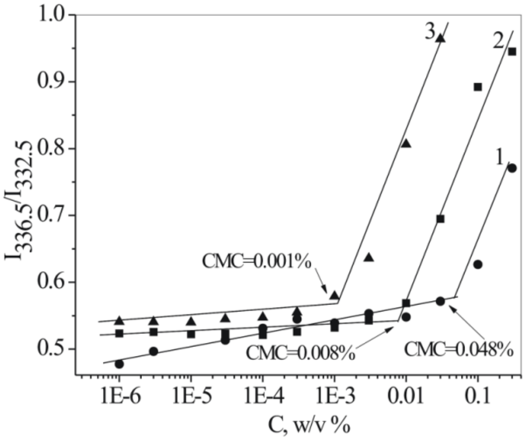

Fig.6.6. The intensity ratio $I_{336.5}/I_{333}$ of the excitation spectra of pyrene in DEPA solutions vs DEPA concentration to determine CMC (1 – Oct-PMDA-MPEG550, 2 – Cet-PMDA-MPEG550, 3 – Chol- PMDA-MPEG550).

Determined using surface tension measurements CMC generally increases with an increasing HLB, and shows strong dependence on the length and nature of the DEPA hydrophobic fragment. The highest surface activity was recorded for the Chol-PMDA-MPEG550 oligomer. Three oligomers based on MPEG550 and different hydrophobic fragments, were chosen for CMC measurements using fluorescence probe solubilization. Fig.6.6 shows that this method gives, in general, lower values for CMC, but with the same trend, indicating higher surface activity of more hydrophobic oligomer and lower CMC. The CMC for the oligomers varies between 1 x 10^{-3} mol/L and 4.8 x 10^{-2} mol/l.

This observation indicates that synthesized DEPA molecules are surface active and form micelles in aqueous solution due to the aggregation of single oligomeric molecules in assemblies at different concentrations, depending on the HLB (chemical structure) of the oligomers.

6.4.3. Solubilization of Lipophilic Agents Using DEPA Micelles

The ability of DEPA micelles to solubilize otherwise insoluble substances in water was demonstrated using two non-polar solvents, hexane and benzene, both immiscible with water. In the presence of DEPA micelles, both non-polar solvent molecules were immediately extracted into an aqueous phase, which was accompanied by clear changes in the DEPA aqueous solution turbidity. Using spectrophotometry, it was demonstrated that hexane and benzene molecules can be physically incorporated within the hydrophobic interior of the DEPA micelle in aqueous solutions in significant quantities (6-8 moles of solvent/mol DEPA).

Having established the DEPA micelles' ability to solubilize insoluble substances in water, four oligomeric surfactants, with different surface activity, were chosen to demonstrate the capability of their micellar solutions to be loaded with the molecules of a lipophilic drug, poorly water-soluble curcumin. All chosen DEPAs demonstrated that curcumin can be successfully solubilized by the DEPA micellar assemblies (Fig.6.7). The amount of the solubilized drug differs significantly for different DEPA surfactants, showing a general tendency to increase in relation to the increasing length of the hydrophobic fragments.

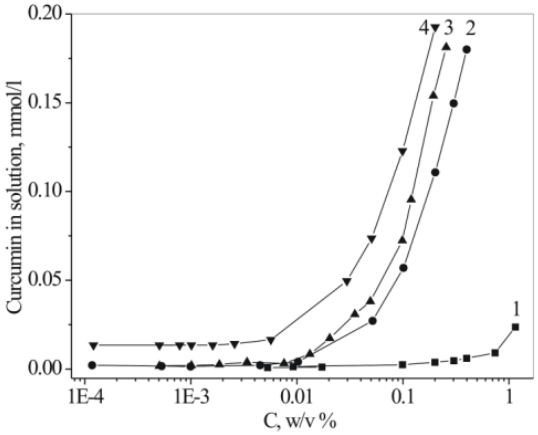

Fig.6.7. Curcumin solubilization vs. DEPA concentration in aqueous solution (1 – Oct-PMDA-MPEG750, 2 – Cet-PMDA-MPEG750, 3 – Cet-PMDA-MPEG550, 4 – Chol- PMDA-MPEG550).

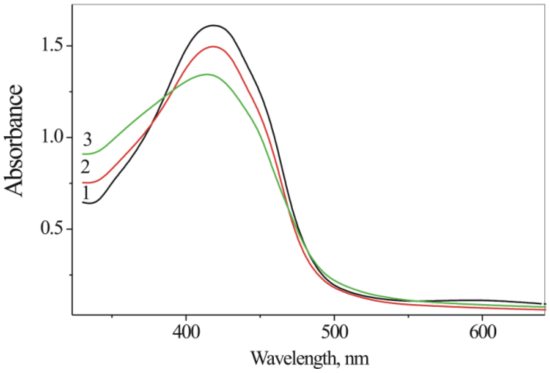

Fig.6.8. UV-vis spectra of micellar curcumin-loaded Cet-PMDA-MPEG550 aqueous solution (0.2% w/v) (pH 6.5, room temperature). 1 – 2 days, 2 – 14 days, 3 – 23 days.

In addition, the DEPA micelles stabilize curcumin molecules in an aqueous medium and prevent drug decomposition. It is known that curcumin is stable at an acidic pH, but is not stable at neutral and basic pH. In these conditions it decomposes to (4′- hydroxy-3′-methoxyphenyl)-2,4-dioxo-5-hexanal, ferulic acid, and feruloyl methane [9]. It has been demonstrated that more than 90% of the curcumin rapidly decomposes within 30 min of placement in phosphate buffered saline at pH 7.2.

In this work, the stability of the curcumin loaded in DEPA micellar assemblies was monitored by UV−vis spectroscopy. The data show that the change in absorbance of the curcumin-loaded DEPA micelles is small, confirming a good stability of micellar curcumin. In particular, very low curcumin decomposition degree was observed for micellar formulation based on Cet-PMDA-MPEG550 during 560 hours (Fig.6.8).

6.5. Conclusions

A new class of amphiphilic oligomers, surface active diesters of pyromellitic acid, was synthesized using pyromellitic dianhidryde, polyethylene glycol methyl ethers of different chain lengths, and alkanols/cholesterol.

The synthesis resulted in amphiphilic oligomers containing hydrophilic (polyethylene glycol methyl ethers, MPEG) and hydrophobic (residues of alkanol/cholesterol) fragments of defined lengths. DEPA oligomers demonstrated the ability to form micelles in an aqueous solution, and the surface activity of DEPA depends on the nature and length of the hydrophilic and hydrophobic constituents (the hydrophilic-lipophilic balance of DEPA). Above their critical micelle concentration, the DEPA oligomers solubilize water-insoluble substances (including a lipophilic drug, curcumin), which confirms their potential in improving the solubility of poorly water-soluble (lipophilic) agents (drugs), for example in drug delivery systems. Additionally, it was demonstrated that loading in DEPA micelles significantly increases the stability of poorly water-soluble drug, curcumin at neutral pH in aqueous media. It is expected that DEPA micellar nanomodalities possess physico-chemical characteristics that can potentially fulfill the requirements (including size distribution, chemical structure, "capacity" in terms of the encapsulated cargo) of efficient drug delivery by providing colloidal dissolution of lipophilic agents in the micellar hydrophobic interior, while stabilizing the agent in aqueous media through the hydrophilic outer part of the micelles.

6.6. References

[1]. Sinha, R.; Kim, G. J.; Nie, S. Shin D M Nanotechnology in cancer therapeutics: bioconjugated nanoparticles for drug delivery. *Molecular Cancer Therapeutics* **2006**, *5*, 1909-1917.

[2]. Kudina, O.; Budishevska, O.; Voronov, A.; Kohut, A.; Khomenko, O.; Voronov, S. Synthesis of New Amphiphilic Comb-Like Copolymers Based on Maleic Anhydride and α-Olefins. *Macromolecular Symposia* **2010**, *298*, 79–84.

[3]. Leung, M. H. M.; Colangelo, H.; Kee, T. W. Encapsulation of curcumin in cationic micelles suppresses alkaline hydrolysis. *Langmuir* **2008**, 24, 5672-5675.

[4]. Bisht, S.; Feldmann, G.; Soni, S.; Ravi, R.; Karikar, C.; Maitra, A.; Maitra, A. Polymeric nanoparticle-encapsulated curcumin (“nanocurcumin”): a novel strategy for human cancer therapy. *Nanobiotechnology* **2007**, *5*, 3-21.

[5]. Schmitz C, Mourran A, Keul H and Möller M Synthesis and association behaviour of linear block copolymers with different microstructures but the same composition. *Macromolecular Chemistry and Physics* **2008**, *209*, 1859–1871.

[6]. Wilhelm, M.; Zhao, C. L.; Wang, Y. .; Xu, R.; Winnik, M. A.; Mura, J. L.; Riess, G.; Croucher, M. D. Poly(styrene-ethylene oxide) block copolymer micelle formation in water: a fluorescence probe study. *Macromolecules* **1991**, *24*, 1033–1040.

[7]. Davies, J. T.; Rideal, E. K. *Interfacial Phenomena.* Academic Press: New York, **1961**.

[8]. Brown, D. W.; Floyd, A. J.; Sainsbury, M. J. *Organic Spectroscopy*. John Wiley and Sons: New York, 1988.

[9]. Kumar. A.; Ahuja, A.; Ali, J.; Baboota, S. *Critical Reviews in Therapeutic Drug Carrier Systems* **2010**, *27*, 279– 312.

CHAPTER 7. HIGHLY EFFICIENT PHASE BOUNDARY BIOCATALYSIS WITH ENZYMOGEL NANOPARTICLES

(Published in *Angewandte Chemie International Edition* **2014**, *53* (2), 483–487)

7. 1. Abstract

The enzymogel nanoparticles made of a magnetic core and polymer brush shell demonstrate a novel type of remote controlled phase-boundary biocatalysis that involves remotely directed binding to and engulfing insoluble substrates, high mobility, and stability of the catalytic centers. The mobile enzymes reside in the polymer brush scaffold and shuttle between the enzymogel interior and surface of the engulfed substrate in the bioconversion process. Biocatalytic activity of the mobile enzymes is preserved in the enzymogel while the brush-like architecture favors the efficient interfacial interaction when the enzymogel spreads over the substrate and extends substantially the reaction area as compared with rigid particles.

7.2. Introduction

The major difference between enzymatic biocatalysis in living organisms and manmade phase-boundary catalysis is the dynamics of the catalytic centers [1]. These differences are caused by the limitations of solid phase catalysis are due to poor mobility of the catalytic centers resulting in a net loss of biocatalytic activity as compared with soluble enzymes that can more readily reach the surface of insoluble substrates and adjust spatial orientation at the phase boundary [2]. Enzymatic catalysis is vital for the regulation of chemical reactions in cells. Nature provides numerous examples of compartmentalized enzymatic reactions that are used in different metabolic pathways and localized in different cellular compartments where the organelles' internal environment is optimized to maintain the highest level of enzyme activity and selective transport of reactants and synthesized products. The enzymes are confined in compartments, although they are in motion which is vital for their biological functions to secure access to spatially organized catalytic sites in the folded protein molecules [1]. Intracellular enzymatic catalysis is controlled within the cellular membrane through regulation of pH, ionic strength, and the presence of inhibitors through gated transport across the membrane. Remarkably, natural living systems demonstrate other examples of enzymatic catalysis when enzymes are secreted and released by cells and organisms to the cell environment. Extracellular biocatalytic activity of secreted enzymes *in vitro* is strongly affected by the environmental conditions. Typically, cell-secreted enzymes are effectively lost after a limited period of time because of diffusion, degradation, or nonproductive binding. The lost enzymes are replaced by new secreted proteins. However, in industrial technologies initial enzyme costs are high enough to warrant recovery and reuse of enzymes but such processes are often too costly [3].

Biocatalytic enzymogel was developed which is designed as a core–shell nanoparticle with a superparamagnetic core and a polymer brush scaffold loaded with enzymes. The enzymogel demonstrates a novel type of phase-boundary biocatalysis with a unique combination of properties including a) biocatalysis involving enzymes in the particle, b) stimuli- triggered release of enzymes to the nanoparticles surrounding and extracapsular biocatalysis, c) biocatalytic conversion of substrates contacting the enzymogel when the enzymes act to bridge the particle and the substrate and engulf the substrate, and d) stimuli-triggered reattachment of released enzymes for their reuse. The enzymogel nanoparticle mimics catabolism of either internal or extracapsular substrates. This versatility turns the particle into a universal biocatalytic “supercapsule” for a number of applications such as synthesis of biofuels; the storage, delivery and reuse of enzymes in biotechnology; and in multifunctional biomaterials when enzymogel nanoparticles could be remotely guided to the surface of drug-loaded containers or temporal implants (absorbable sutures) and degrade them upon contact.

A few approaches to solve the problem of enzyme delivery and recycling have been developed to date: 1) immobilization of enzymes on solid nonporous supports and 2) encapsulation of enzymes using semipermeable capsules. Immobilization of enzymes on supports may provide a simple way to recover and reuse them which will significantly reduce costs for many industrial processes of biotechnology [2]. Enzymes can be immobilized using methods either fixing their interaction with a carrier (physical or covalent binding to support), or carrier-free cross-linking methods; both approaches bring a history of advantages and disadvantages widely reported in literature [4]. In many cases, however, immobilization may result in changing the enzyme structure and altering their activity, specificity, and selectivity [5]. Attachment to the carrier by strong covalent binding can irreversibly deactivate enzymes or lower the catalytic performance [6]. Physical adsorption of enzyme molecules may also lower enzyme activity resulting from considerable changes in the enzyme structure both on flat [7] and colloidal supports [8-9]. Therefore, carrier surface modification in order to prevent a direct contact between the support and the immobilized enzyme is being explored [10]. Specifically, an approach has been recently reported that would preserve enzymatic activity after immobilization on support by attachment (covalent or physical) of enzymes to a soft polymer network (gel lattice) [11-12]. It also includes stimulus-responsive polymer networks that undergo conformational changes in response to changing environment pH, temperature, and the ionic strength [13-15]. The immobilization (encapsulation) of enzymes in gels can protect enzymes from structural alterations and subsequent deactivation, but the process suffers from low enzyme loading as well as low enzyme diffusivity in the host matrix.

7.3. Experimental

7.3.1. Materials

Tert-butyl acrylate (TBA), ascorbic acid, copper bromide, N,N,N′,N″,N″-pentamethyldiethylenetriamine (PMDTA), methylsulfonic acid, toluene, dichloromethane, methylethylketone (MEK), hydrogen peroxide, ethanol, α-bromoisobutyryl bromide (BIB), triethylamine, ethylenediamine, sodium dodecyl sulphate (SDS), methylamine, ferrous (II) chloride tetrahydrate, ferrous (III) chloride hexahydrate, sodium silicate, tetraethyl orthosilicate (TEOS), ammonium hydroxide solution Bradford reagent, sodium azide (Sigma-Aldrich BioUltra Reagents, ≥99.5%), albumin from bovine serum (BSA, lyophilized powder, ≥96%) were purchased from Sigma-Aldrich and used as received. 3-glycidoxypropyl-trimethyl-ethoxysilane (GPES) was purchased from GELEST Inc. Citric buffers were prepared from sodium citrate dihydrate (ACS reagent, ≥99.5%, BDH), citric acid (ACS reagent, ≥99.5%, Sigma-Aldrich) and Millipore water (18Ω). Cellulase (CEL) enzyme stock solution (40 % w/w) NS 50013 from Novozymes Corporation, Bagsvaerd, Denmark were diluted in buffered solutions and stabilized with 0.04% NaN_3.

Alexa Fluor® 594 Protein Labeling Kit was obtained from Invitrogen, Life Technologies Corporation. Filter paper was purchased from Whatman#1 (VWR International).

Highly polished silicon wafers (Semiconductor Processing, Union Miniere USA Inc.) were cleaned twice with ethanol and twice with dichloromethane in an ultrasonic bath for ten minutes each time. Then the wafers were cleaned in a hot (60℃) NH_4OH: H_2O_2:H_2O (1:1:5) mixture for one hour and rinsed with Millipore Water (18 MΩ cm) several times.

7.3.2. Synthesis of Enzymogels

Synthesis of silica particles. The silica particles were synthesized using the Stöber method [16]. Ammonium hydroxide (19.0 mL) was added to 200.0 mL of ethanol under stirring. Then, 12.0 mL of TEOS was added in three portions of 4 mL each. The particles were formed within 1 hour, and the dispersion was left overnight with continued stirring. The particles were subsequently cleaned by three cycles of centrifugation and redispersion in pure ethanol using ultrasonication. The final concentration of the particles was 18 mg/mL, as determined by thermogravimetric analysis. The particles were characterized using dynamic light scattering (DLS), scanning electron microscopy (SEM) and transmission electron microscopy (TEM) methods. Synthesis was conducted by Dr. S. Minko group in Clarkson University (Potsdam, NY).

Synthesis of magnetic nanoparticles. The synthesis was reported in Ref. [17] $FeCl_2 \cdot 4H_2O$ (1.59 g) and SDS (0.575 g) were added to 100ml of distilled water at 50°C. The reactants were stirred for 3 hours. Then, the product was cooled to 4°C and stored for 24 hours. The formed ferrous dodecyl sulfate precipitate was washed with cold water and collected using vacuum filtration. The filtrate was dried in a vacuum for three days. Ferrous dodecyl sulphate (180 mg) and methylamine (2.4 ml) were added to 40 ml of distilled water at 80°C and stirred continuously for 3 hours. Then, the formed iron oxide particle suspension was cooled to room temperature, and 20 µl of sodium silicate was added to the particle suspension and stirred overnight with sonication for 5 minutes every 4 hours. The particles were washed with ethanol:water 1:4 (v/v) and redispersed in the solution of ethanol:water 2:1 (v/v). TEOS (100 µl) was added to the particle suspension and stirred overnight continuously. Then, the particles were washed with ethanol:water 1:4 (v/v) and redispersed in the solution of ethanol:water 2:1 (v/v). The particles were characterized using DLS, SEM and TEM. Synthesis was conducted by Dr. S. Minko group in Clarkson University (Potsdam, NY).

7.3.3. Grafting of Polyacrylic Acid (PAA) Brushes

Functionalization of particles with amino groups. Silica particles or silica coated magnetic nanoparticles were dispersed in 3% by volume solution of GEPS in MEK for 16 hours at room temperature, separated by centrifugation and rinsed in ethanol several times. Then, the particles were treated by ethylenediamine to react with epoxy group on the surface and functionalize the surface of particles with amino groups.

Initiator immobilization. The functionalized particles were treated in a mixture of 2% w/v solution by volume of triethylamine and a 1% w/w solution by volume of BIB in dichloromethane for 2 hours at room temp (a successful reaction should turn the solution yellow) and rinsed with sequential washing of chloroform, ethanol and Millipore H_2O.

Synthesis of the brushes. Grafting of TBA was carried out using ATRP mechanism. Samples were incubated in the presence of copper bromide (0.8mM), PMDTA (4 mM) and ascorbic acid (25mM) at room temperature at 70°C for 1 hour for 50% w/w TBA in MEK. In order to convert TBA to PAA, samples were hydrolyzed by immersion in a 1.5% w/w solution by volume of methylsulfonic acid in dichloromethane. After 2 minutes, samples were then rinsed in dichloromethane and ethanol for 10 minutes. The particles with grafted brushes were characterized using DLS, SEM and cryo-TEM (Scheme 7.1). The same polymerization conditions were used to synthesize brushes on the surface of Si-wafers for all reference experiments. The brushes on Si-wafers were characterized using ellipsometry. Synthesis was conducted by Dr. S. Minko group in Clarkson University (Potsdam, NY).

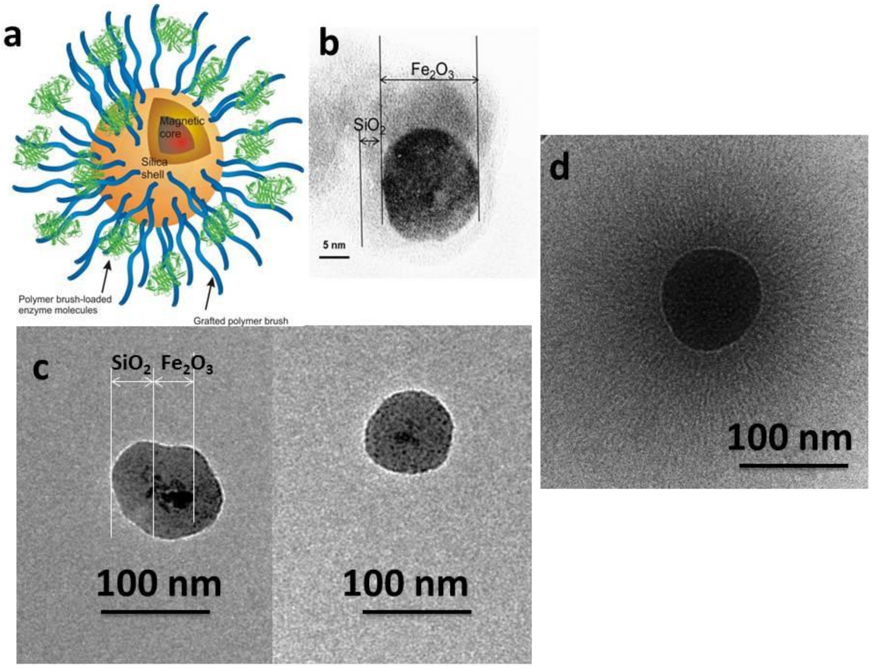

Scheme 7.1. The hairy particle (a) of the enzymogel consists of a magnetic core, silica shell and PAA brush; TEM images of particles with different silica shell thicknesses of a few nanometers (b) to tens nanometers (c) were synthesized and decorated with PAA brushes (cryo-TEM in water at pH 7 (d)). Data obtained by Dr. S. Minko group in Clarkson University (Potsdam, NY).

7.3.4. Cellulase (CEL) Loading and Release

Cellulase loading into the enzymogels. 40 mg of brush-decorated particles was mixed overnight with 100 μl of cellulase stock solution in 1.5 ml of citric buffer (pH 4.0). The loaded enzymogels were separated using centrifugation at 15,000 rpm for 15 min (VWR Scientific microcentrifuge (model V). The particles were dispersed afterwards in 1.5 ml of citric buffer (pH 4.8) and used as a stock dispersion of the loaded particles in experiments. Cellulase loading was estimated using a standard Bradford assay [18]. For this purpose, a standard calibration plot was created by serial dilutions of 1 mg/ml BSA protein standard in a range 0.1 - 1.4 mg/ml and recording absorbance spectra of the BSA solutions at 595 nm using Varian Cary 5000 UV-VIS-NIR spectrometer. To determine cellulase loading, 0.1 ml of the liquid dispersion phase was mixed with 3 ml of the Bradford Reagent, gently stirred, and incubated at room temperature for 15 minutes. Cellulase concentration in each tested liquid dispersion phase was calculated using the calibration.

$$Loading,\% = \frac{C_i - C_r}{C_i} \times 100\% \qquad (7.1)$$

where C_i is the initial cellulase concentration in solution before the loading and C_r is the cellulase concentration in liquid disperse phase after the loading, mg/mL.

Cellulase release from the enzymogels. To release enzymes from the enzymogels, 15 ml of the stock dispersion of the enzymogels was loaded in Slide-A-Lyser Dialysis Casette (3,500 MWCO) to gradually change pH from 4 to 7. Dialysis with citric buffer (pH 7.0) was carried out overnight with 3 changes of dialysis buffer (after 1, 2 and 4 hours of dialysis). The particles were separated using Precision Durafuge 100 centrifuge at 5,000 rpm for 15 min. Liquid phase was analyzed to determine cellulase release using Bradford assay.

7.3.5. Hydrolysis of Cellulose

Hydrolytic activity of a cellulose-loaded enzymogels was tested in several cycles (72 hours each) at 50ºC and pH 4.80 ± 0.05. The stock dispersion of the enzymogels was mixed with citrate buffer at pH 4.8 (total sample volume 10 mL) and sonicated for 5 min in Branson B5510 ultrasonic bath. 50 mg of Whatman#1 filter paper was added to sonicated dispersion, and it was stirred at 300 rpm and 50ºC for 72 hours. Afterwards, the enzymogels were separated using centrifugation; magnetic enzymogels were separated with a permanent magnet (1T). The liquid phase was sampled after each hydrolytic cycle to determine concentration of cellulose and sugar yield.

Fermentable sugars quantification. Fermentable sugars (cellobiose, glucose, arabinose and galactose, Table 7.1) yield in each cycle of enzymatic hydrolysis were analyzed using HPLC, Waters (Milford, MA) system with Bio-Rad (Hercules, CA) Aminex HPX-87P HPLC column (water as mobile phase at a flow rate 0.6 mL/min and temperature 50°C) and refractive index detector (temperature 85°C). Prior to HPLC, 1 mL of liquid dispersion phase was centrifuged and filtered using a 0.25 μm nylon filter (Pall Corporation, West Chester, PA).

Table 7.1. Compositions of fermentable sugars in the course of biocatalytic hydrolysis of cellulose using enzymogel (% w/w).

Time, min	**Cellobiose, %**	**Glucose, %**	**Xylose, %**	**Galactose, %**	**Arabinose, %**
30	36.2	56.3	0.1	1.2	6.3
60	25.1	66.9	2.4	0.0	5.6
120	15.0	76.8	0.0	2.8	5.4
180	15.7	74.7	2.6	3.8	3.2
240	13.4	85.4	0.0	0.0	1.2
300	11.9	85.4	0.0	0.0	2.7
1440	1.2	96.5	0.5	0.1	1.7
2880	1.3	97.3	1.1	0.1	0.2
4320	0.2	98.9	0.2	0.1	0.6

7.3.6. Cellulase Labeling and Fluorescence Recovery after Photobleaching (FRAP) Experiments

Cellulase labeling. Alexa Fluor® 594 protein labeling kit was used to label cellulase with Alexa Fluor 594 dye. A 2 mg/mL cellulase solution was prepared by dilution of the stock solution with 0.1 M sodium bicarbonate. 50 μL of 1 M bicarbonate was added to 0.5 mL of the diluted cellulase solution to adjust pH 8. The diluted cellulase solution was stirred with the dye for one hour at room temperature. Non-reacted dye was removed using purification resin (Bio-

Rad BioGel P-30) and PBS buffer (0.1 M potassium phosphate, 1.5 M NaCl, pH 7.2, with 2 mM sodium azide). Absorbance of solutions at 280 nm and 590 nm was used to calculate the concentration of cellulose and covalently attached dye.

Fluorescence recovery after photobleaching (FRAP) experiments. An Olympus BX61 microscope equipped with 20X and 40X water immersion objectives was used in the experiments. An AsRed2 filter cube and bright field cube were used for fluorescent and bright field images, respectively. The samples with the labeled cellulose loaded PAA brushes were immersed in citric buffer at pH 4.8. Photobleaching was performed by exposing the sample to laser light at wavelength 590 nm; excited fluorescence intensity was monitored immediately after the photobleaching, after 1, 3 hours and then after 7 days. The intensity of laser beam was attenuated using beam profiler (less than 5%) to avoid any possible bleaching during recovery monitoring.

Recorded images were analyzed using ImageJ software. The surface mobility rate (MR) and diffusion coefficient (D) were calculated after converting recovery signals to the concentrations of enzymes [19].

7.3.7. Adsorption Experiments

The estimation of the cellulose adsorption based on changes of the PAA-brush thickness was verified using thermogravimetric analysis (Q500 Thermogravimetric Analyzer, TA Instruments Inc). The analysis was performed at the ramp rate of 10°C/min rates from room temperature to 700°C at nitrogen flow rate of 15ml/min.

Adsorption kinetics. Adsorption and desorption kinetics in a typical CEL concentration range was monitored with in situ ellipsometry on the surface of a reference sample of the PAA brush grafted to the Si-wafer substrate. Experiments were performed by Dr. S. Minko group in Clarkson University (Potsdam, NY).

7.3.8. Cellulase Grafting to Nanoparticles (Reference Sample)

200 nm silica nanoparticles (1.9 g) were dispersed in 100 ml of ethanol using ultrasonication. Afterward, the particles were separated by precipitation using centrifugation (10,000 rpm, for 10 min) and transferred to a dry MEK using ultrasonication. In the next step, the nanoparticles were silanized by 2% (3-glycidyloxypropyl) trimethoxysilane (GPS) in dry MEK overnight and rinsed 3 times by MEK and dichloromethane. Finally, particles were treated with 2% ethylenediamine in dichloromethane for 2 h and rinsed three times with dichloromethane, ethanol and water. The particles were separated by centrifugation and dried in vacuum oven at 60°C overnight. The silica particles modified with amino groups (100 mg) were rinsed three times with 10 ml of phosphate buffer (pH 7.4, coupling buffer). After the final wash cycle, the particles were dispersed in 10 ml of phosphate buffer containing 10% w/w of glutaraldehyde. The mixture was left to react for 1 hour at room temperature. Unreacted glutaraldehyde was removed by rinsing the particles three times with 10 ml of phosphate buffer. The particles were dispersed in 10 ml of the coupling buffer and mixed with a 0.5% w/w cellulase solution. Mixture reacted for 4 h at a vigorous mixing. Glycine (0.2 M) and cyanoborohydride (10 nM) were added to deactivate unreacted glutaraldehyde. Excess of protein and reactants was removed by three repetitive rinsing of the particles with 10 ml of citric buffer (pH 3.8). The amount of cellulase grafted to nanoparticles was estimated using a standard Bradford assay as described above.

7 3.9. Magnetic Separation of Enzymes for Reuse

The stages of magnetic separation were applied for the experiments with multiple cycles of fermentation and reuse of the same fraction of enzymes (Fig.7.1).

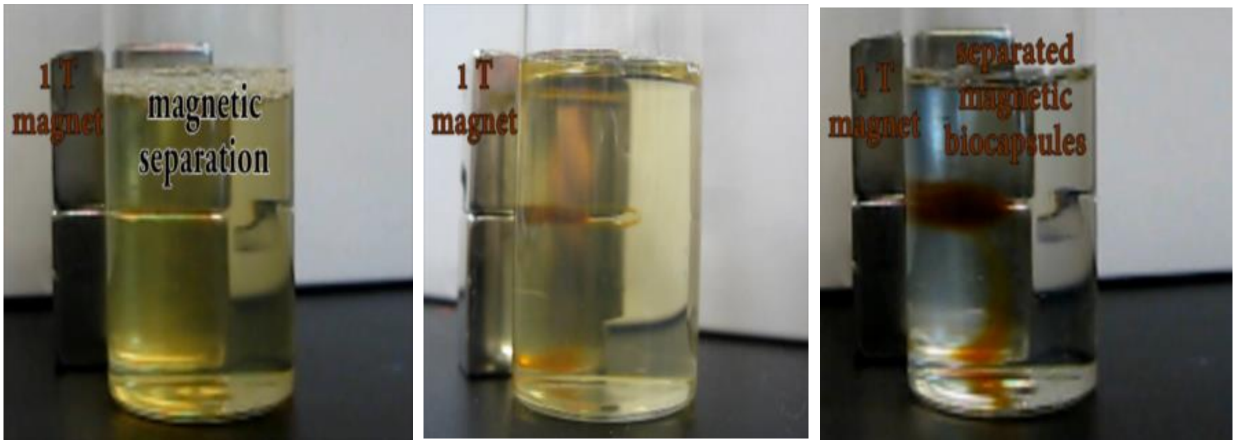

a) b) c)

Fig.7.1. Magnetic separation of enzymogels: immediately after attachment of the magnet (a), in 12 h (b) and 24 h (c) in the magnetic field. The brown colored enzymogel was collected on the walls of the glass container; the greater amount of the material was collected at the poles.

Multicycle fermentation with pH-triggered release and capture of CEL. In this experiment, CEL was released from biomass at pH and then after fermentation for 72 h the CEL was captured at pH. The total amount of CEL in the brush, fractions of released and captured CEL are shown in orange, red and blue bars respectively (Fig.7.2). The amount of the captured enzymes diminishes in each cycle. The amount of sugars produced in the cycles is shown in Fig.7.3.

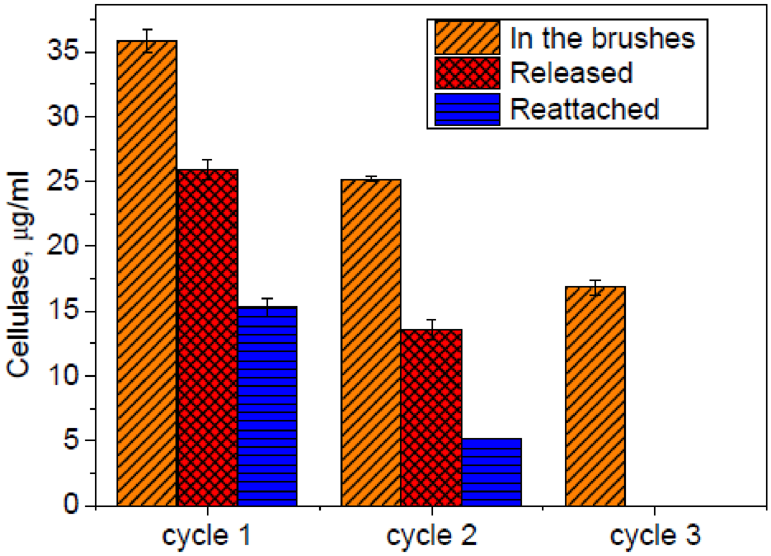

Fig.7.2. Loading, release (at pH 4) and capture (at pH 7) of cellulase enzymes in fermentation cycles. Orange bars show the initial amount of CEL in the brush and the total amounts of CEL in the enzymogel after reattachment (capture) of CEL from the biomass, in the first, second and third cycles, respectively. Red bars show the amount of CEL released from the brush into biomass at pH 7 in the first and the second cycles (no release was conducted after the third cycle). Blue bars show the amounts of CEL captured at pH 7 adjusted after fermentation in the first and the second cycles.

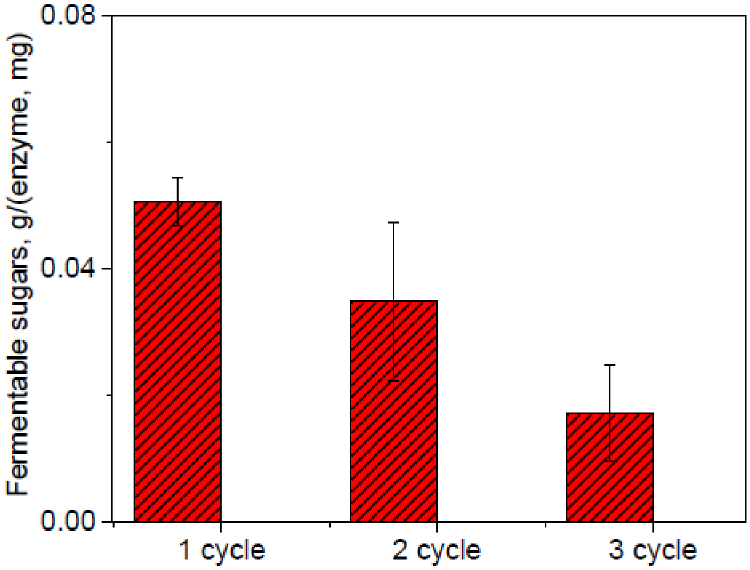

Fig.7.3. Amount of sugars produced in each cycle (20 µg/ml CEL) that corresponds to cycles in Fig.7.2.

7. 4. Results and Discussion

One of the most efficient ways to ensure higher loading and mobility of enzyme molecules with polymer-based carriers is to attach them to soft, flexible polyelectrolyte brushes—arrays of polymer chains end-tethered to colloidal particles at high grafting density [20-24]. It has been shown that the ionic strength in the system is the decisive parameter in enzyme adsorption of polyelectrolyte brushes grafted onto solid supports [23-24]. The native secondary structure [23-24] and the activity [25-26] of the adsorbed enzyme molecules are preserved, thus making colloidal particles decorated with densely tethered polyelectrolyte chains promising carriers for enzyme recovery and reuse by a gradual release of enzymes from the brush after increasing the ionic strength [27]. Another recent study has demonstrated that protein molecules adsorbed on polyelectrolyte brushes are not "frozen" in terms of protein dynamics, but undergo changes probably because of the presence of repulsive electrostatic interactions [28]. Although a variety of immobilization methods using polymer networks has been designed and tested, it is still challenging to develop stable, efficient, and economically feasible hybrid biocatalytic systems for repeated enzyme recovery and recycling without activity loss for biotechnological and medical applications.

The proposed design of enzymogel nanoparticles includes a core–shell structure with an inorganic core and a polymer brush shell (Fig.7.4a). A typical example is represented by a 100±10 nm silica core with a 30±5 nm (in the dry state) poly(acrylic acid) (PAA) brush. To enable magnetic separation of the enzymogel particles, the core was made of one or few 15 nm g-Fe_2O_3 superparamagnetic particles that were enveloped by a silica shell. The PAA brush was synthesized by surface-initiated polymerization of tert-butylacrylate and the subsequent hydrolysis of poly(tert-butylacrylate). In an aqueous environment in a pH range from 5 to 7 the enzymogel particle has a homogeneous, swollen, negatively charged PAA brush which is clearly observable in cryo-TEM images (Fig.7.4b). The PAA shell shrinks at pH 4.5 but still maintains a net negative charge (Fig.7.4c). PAA is a weak polyelectrolyte with a monomer unit pK_a of 4.5 and is negatively charged in a pH range of 4 to 8 which is optimal for the highest enzymatic activity for most enzymes. The enzymogel can be loaded with positively charged enzymes in this pH range (Fig.7.5). In a working example, the cellulase (CEL) enzymes were used to cleave cellulose molecules and convert them into glucose for biofuel or biochemical production [29-30]. CEL is typically isoelectric at pH 4.9 and, thus, attains a moderate positive charge at pH 4.5. CEL was loaded into the enzymogel particles at pH 4.5 (Fig.7.4d). The loading of the enzyme is reversible and a major portion of it can be released at pH 7 and a high ionic strength. Adsorption and desorption kinetics in a typical CEL concentration range [31] were monitored with in situ ellipsometry on the surface of a reference sample of the PAA brush grafted to the Si-wafer substrate (Fig.7.5) and using the Bradford assay, particle size analysis methods and thermogravimetric analysis for adsorption/desorption of CEL by the enzymogel. The amount of the attached enzymes can reach about 300% of the PAA by weight. Desorption reaches about 80% of the adsorbed amount and depends on the ionic strength and pH. The pH-triggered uptake/release is reproducible.

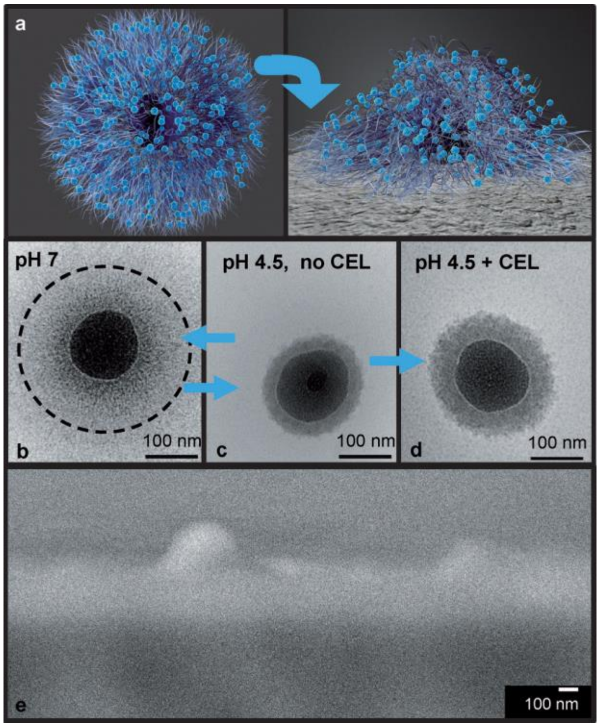

Fig.7.4. An enzymogel nanoparticle schematic a) of the particle that consists of an iron oxide core, a silica shell, and a PAA brush loaded with enzymes: the particle with spherical symmetry in solution and interacting with a solid substrate; cryo-TEM images of the particle with a 120 nm in diameter silica core and b) swollen and c) shrunken PAA brush at pH 7 and pH 4.5, respectively. d) The brush is uniformly loaded with CEL enzymes at pH 4.5. e) The spreading of the brush over the substrate surface is shown in the SEM image. Data obtained by Dr. S. Minko group in Clarkson University (Potsdam, NY).

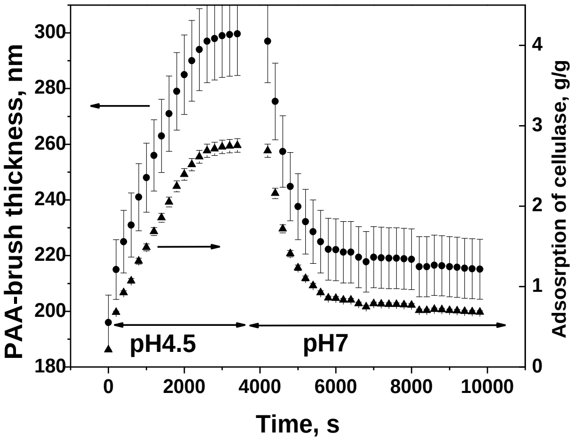

Fig.7.5. Adsorption at pH 4.5 and 1.4 mg/ml CEL and desorption at pH 7 of CEL kinetics on a 32 ± 2 nm thick PAA brush grafted to the surface of a Si-wafer shown as a change in the brush thickness and CEL loading per PAA weight. Data obtained by Dr. S. Minko group in Clarkson University (Potsdam, NY).

It was found that cellulases are readily adsorbed by PAA brushes at pH 4 and show almost no absorption at pH 7. The pH dependence of adsorption can be explained by considering the isoelectric point of the protein and the dissociation constant of poly(acrylic acid). In fact, cellulase has an isoelectric point of pH 4.9, thus adsorption at a low pH is likely caused by formation of hydrogen bonds and electrostatic interactions between the positively charged protein and weakly charged PAA (pK_α of 5.5 for monomers). A reduced adsorption at pH 7 is due to the electrostatic repulsion between the negatively charged protein and PAA.

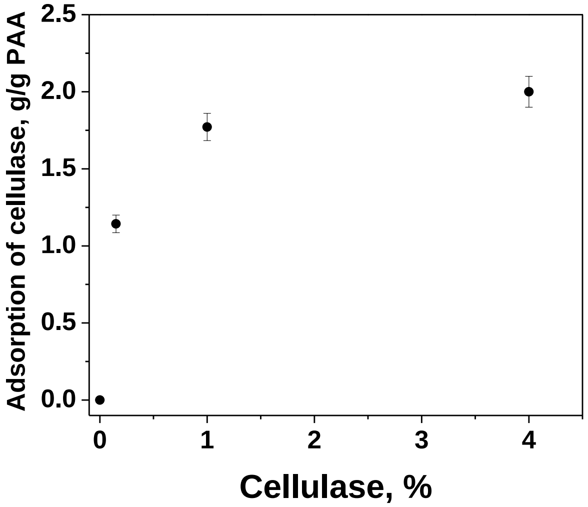

Fig.7.6. Adsorption isotherm for cellulase enzymes on the PAA brush (a Si-wafer grafted brush) plotted vs. concentration of cellulose at pH 4, 20°C. Data obtained by Dr. S. Minko group in Clarkson University (Potsdam, NY).

The adsorption isotherm in Fig.7.6 (at pH 4) showed that the saturation of protein layer with the cellulase was observed at cellulase concentration greater than 1% (w/w). It was found that adsorption of cellulase at pH 4 increases with thickness of the poly(acrylic acid) brush (Fig.7.7a). The normalized thickness of the cellulase layer (ratio of the adsorbed cellulase to the grafted polymer brush) decreases with thickness of the PAA brush (Fig.7.7b). Thinner brushes are characterized with a larger normalized enzyme load. This effect can be explained by entropic penalty for loading densely grafted brushes with enzymes.

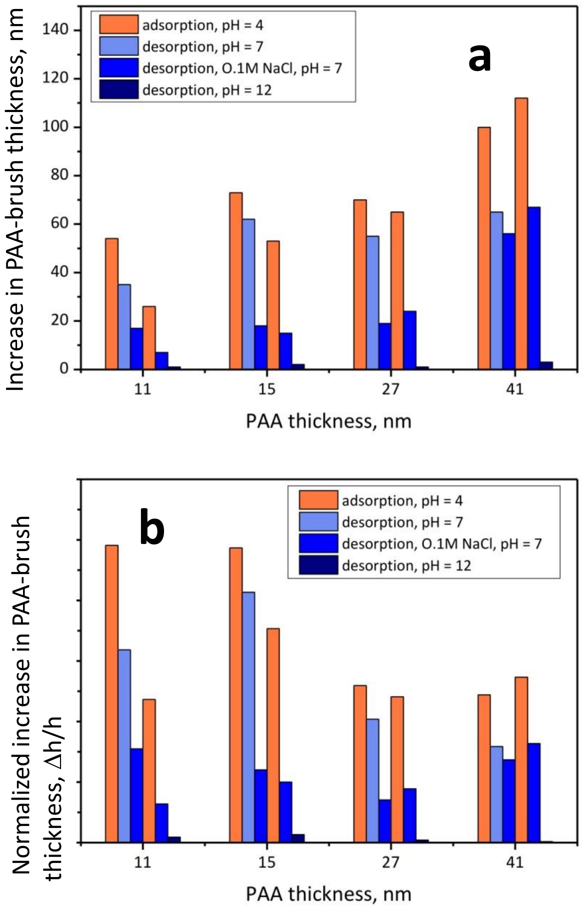

Fig.7.7. Cyclic adsorption-desorption equilibrium at different pH and salt concentration plotted as an increase in the PAA-brush thickness (2 cycles), Δh (a) and a normalized increase in the brush thickness, Δh/h vs. PAA-brush thickness, h. Data obtained by Dr. S. Minko group in Clarkson University (Potsdam, NY).

The incubation of the polymer brushes with adsorbed cellulase in aqueous buffer at pH 7 results in desorption of a small amount of the protein. A considerable but incomplete desorption was observed in 0.1 M NaCl aqueous solutions (pH 7). The enzyme can be repeatedly adsorbed and desorbed at pH 4 and pH 7, respectively. The enzyme can be completely extracted from the brush at pH 12.

Cellulase exchange between the enzymogel and solution was studied using a dye-labeled cellulase via optical spectroscopy. Two experiments were designed to test the exchange (Table 7.2). First (Experiment A on Fig.7.8 and Table 7.2), labeled cellulase was attached on polymer brushes and dispersed in solution of non-labeled cellulase (Fig.7.8A). In the second experiment (Experiment B on Fig.7.8 and Table 7.2), non-labeled cellulase was attached on polymer brush-decorated silica and dispersed in solution of labeled cellulase (Fig.7.8B). For both tests, a small change of absorbance was recorded (Table 7.2).

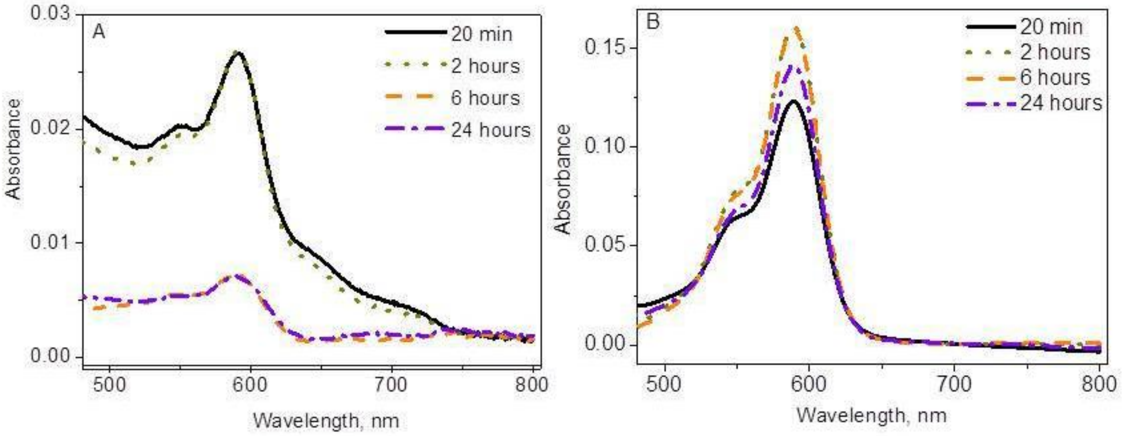

Fig.7.8. UV-vis spectra of dye-labeled cellulose recorded for supernatant after different period of time in two different experiments: (A) enzymogels (0.56 mg/ml) loaded with non-labeled CEL were dispersed in aqueous solution of the dye-labeled CEL (0.56 mg/ml); (B) the enzymogels (0.87 mg/ml) loaded with dye-labeled CEL were dispersed in aqueous solution of the non-labeled CEL (0.87 mg/ml).

Table 7.2. Concentration of labeled cellulase in liquid dispersion phase for tests A and B.

Time	**Cellulase concentration, mg/mL**	
	Test A	**Test B**
20 min	0.05	0.66
2 hours	0.05	0.84
6 hours	0.02	0.83
24 hours	0.01	0.75
48 hours	0.02	0.77

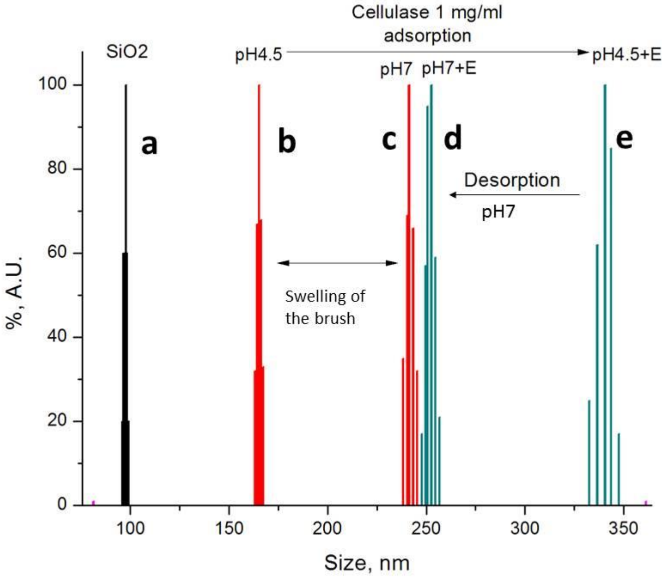

Fig.7.9. Particle size distributions (DLS) for: inorganic core particles (a), enzymogel particles with no enzyme loaded at pH 4.5 (b) and pH 7 (c), after loading with CEL at pH 4.5 (e), and after dersorption (unloading) CEL at pH 7 (d). The particle diameter at the full loading with CEL (e) is overestimated by DLS method (330 nm by DLS vs 250 nm by cryo-TEM). That is explained by particle aggregation when protein adsorption compensates the electrical charge. The broadening of the distribution function indicates aggregation of the particles. Data obtained by Dr. S. Minko group in Clarkson University (Potsdam, NY).

Adsorption experiments with enzymogel particles using DLS method for particle size estimation are in accord with the data for the plane brushes (Fig.7.9). At very high loading of the brushes with CEL, the DLS method overestimates the particle diameter due to the presence of particle aggregates.

The enzymogel loaded with CEL demonstrates a high affinity of CEL to the PAA brush. CEL resides in the brush even after multiple washing in buffer at pH 4.5. Limited leakage (about 5%) of CEL was observed after rinsing of the fully loaded enzymogel particles. About the same amount of CEL was exchanged by dye-labeled CEL indicating a high affinity and quasi-irreversible adsorption of enzymes by the enzymogel under the specified conditions.

An important aspect of enzyme dynamics in the enzymogel particle was discovered from experiments with a fluorescent dye-labeled CEL (FL-CEL). The fluorescence recovery after photobleaching experiments were applied to estimate mobility of CEL in the enzymogel. In this experiment estimated CEL diffusion coefficient in the PAA brush at pH 4.5 is 1.3 ± 10-10 cm2×s-1, similar to the diffusion of the CEL adsorbed on cellulose [32]. Thus, the enzymogel demonstrates a unique combination of very high affinity to the enzyme and mobility of the attached enzymes. A reference PAA brush grafted on a Si-wafer was used as a model scaffold to study the diffusivity of CEL in the brush using a recovery after photobleaching method (Fig.7.10). There are two possible mechanisms for transport of the labeled CEL to the bleached area: (1) diffusion through the brush and (2) desorption of CEL molecules to the bulk solution, diffusion in the solution, and re-adsorption on the bleached area. To distinguish and estimate contributions of those two mechanisms two parallel experiments were conducted with PAA brushes loaded with FL-CEL in equilibrium with a pH 4.5 aqueous solution. In one experiment, an area (about one cm2) was laser-bleached and the fluorescence recovery was monitored using a fluorescent microscope (Fig.7.10a, b). In another experiment, the bleached area was circumscribed by a rectangular scratch using a metal needle, removing a track of the PAA brush from the wafer's surface (Fig.7.10 c,d). For the latter experiment, recovery of the photobleached area can only be achieved via the aforesaid second mechanism.

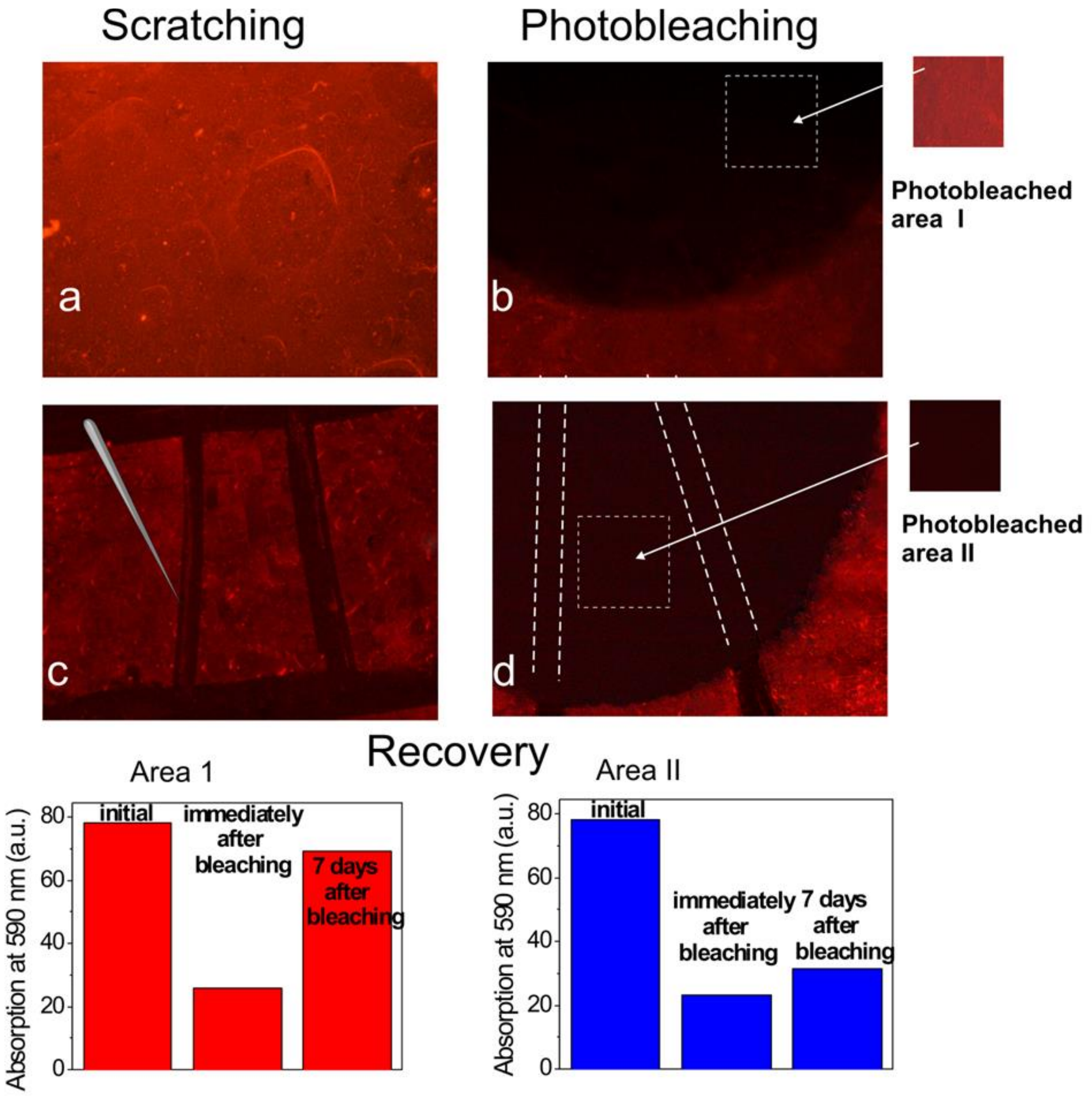

Fig.7.10. Fluorescence recovery after photobleaching experiments (fluorescent microscope images and schematics) with the PAA brush on the Si-wafer loaded with FL-CEL enzymes (a) and scratched to form a rectangular area (b). Both samples were photobleached and recovery of the fluorescent emission from the photobleached areas marked with dashed squares was monitored for 7 days. The images immediately after photobleaching are shown in the panels b and c. Changes of intensity in 7 days are shown in the rectangular inserts. The fluorescent intensities at 590 nm are shown in the insert diagrams for the original samples, immediately after photobleaching and in 7 days after photobleaching. The recovery in the scratched sample (d) is much slower than for the sample in the panel B providing evidence for a dominating recovery mechanism by transport in the brush.

A comparison of the results revealed fluorescence recovery (inserts of the diagrams) two orders of magnitude slower for the experiment with the scratch providing evidence for the major recovery mechanism via transport of enzymes through the brush.

This combination of the high affinity and mobility of CEL in the enzymogel yields multiple benefits for the use of the enzymogel particles with a high loading capacity accompanied by unchanged biocatalytic activity and mobility of the enzymes. This behavior was explained using the properties of the polyelectrolyte brushes and the ampholytic character of the enzymes. The high affinity is caused by counterion release because of the formation of the polyelectrolyte complex which provides a substantial gain of entropic energy and increases the activation barrier for the exchange between molecules in the enzymogel and in the solution. At the same time, the activation energy for translocation of enzymes between PAA segments is decreased due to the ampholytic nature of proteins which simultaneously carry similar and opposite charges to the charge of PAA. The more detailed mechanisms are the subject of further research.

The brush assembled on the magnetic-core nanoparticles was used to hydrolyze cellulose by attracting the enzymes from the solution at pH 4.5 and releasing them into the bioreactor at pH 7 which demonstrated the stimuli-responsive behavior of the enzymogel. The encapsulated CEL retains its biocatalytic activity in the brush and the released CEL retains its biocatalytic activity at the original level. The most remarkable property of the enzymogel is that CEL remains active even when residing in the brush. In Fig.7.11a, biocatalytic activity of CEL in six different systems is compared. The systems are divided into two groups based on a cellulose substrate used: (I–V) hydrolysis of insoluble cellulose (filter paper standard) and (VI–VIII hydrolysis of semi-soluble colloidal dispersion of α-cellulose (MW= 9000 gmol-1).

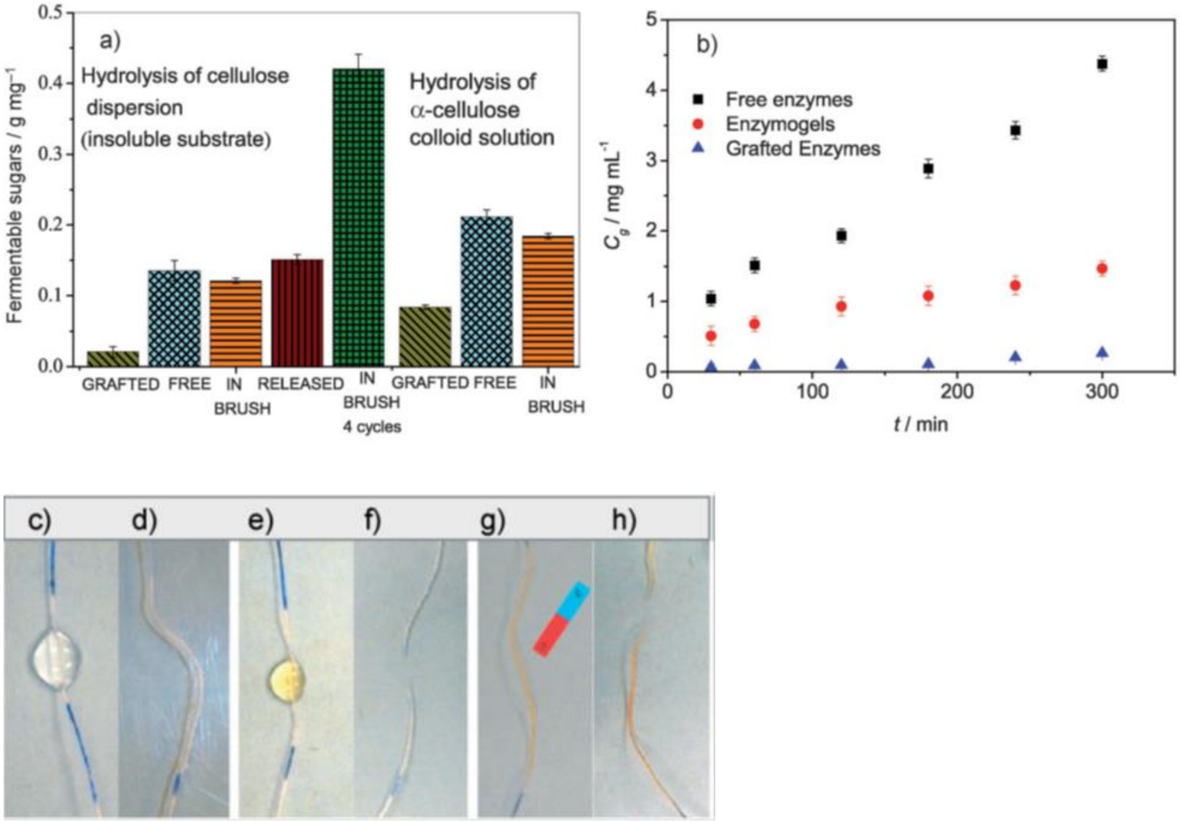

Fig.7.11. Biocatalytic activity of CEL (40 mg×mL^{-1}) in buffer solutions at pH 5.0: a) for insoluble (I–V) and semisoluble colloidal (VI–VIII) cellulose (5 mg×mL^{-1}) presented as amount of synthesized fermentable sugars per CEL (g×mg^{-1}) for CEL dissolved in the buffer (II,VII), CEL grafted to 200 nm silica particles (I,VI), CEL in the PAA brush in the enzymogel nanoparticles (III V and VIII), CEL released from the PAA brush (IV), and after four cycles of the reuse of the same enzymogel particles with a magnetic core (V). b) Kinetics of glucose production shown as glucose concentration (C_g) versus time (t) using free enzymes in solution (squares), grafted enzymes (triangles), and the enzymogel (circles). Degradation of a 500 mm thick cotton floss by deposition of CEL using c) a free CEL enzyme solution, d) when no rupture of the floss was observed for the free enzyme in 14 h, e) the enzymogel, f) rupture was documented for the enzymogel-treated floss in 2.5 h, g) and magnetic field-directed deposition, and h) for the magnetic field-localized enzymogel rupture was documented in 1 h.

In all the systems, the concentration of cellulose and the protein-basis concentration of CEL in buffer solutions at pH 4.8 are the same. In the reference experiments (II and VII), free (unattached) CEL demonstrates a reference level of activity that is higher for colloidal cellulose (VII) than for filter paper (II). The CEL released from the enzymogel retains its activity at the same level (IV). The grafted CEL in both examples (I and VI) is much less active. The difference between VII and VI is likely due to the loss of CEL activity because of grafting, while the difference between I and VI shows the loss of efficiency because of a poor interfacial contact between the filter paper substrate and the grafted enzymes. CEL in the brush demonstrates nearly unchanged level of activity (III and VIII) for both types of cellulose substrates and bioconversion can be repeated in several cycles if the enzymogel is reused (V). The hydrolysis with multiple cycling of release and capture of enzymes in and from the biomass is less efficient because of possible denaturing of enzymes due to alternations in pH.

The results provide evidence that the enzymogel nanoparticles catalyze hydrolysis of cellulose using a new type of phase boundary catalysis (cases III and VIII); the particles are adsorbed on the surface of cellulose fibers and cleave the cellulose chains by enzymes shuttling between the PAA brush interior and the brush–cellulose interface. This shuttling is responsible for the high efficiency of cellulose conversion which is much higher than expected assuming that only CEL located on the exterior of the enzymogel particle could be involved in biocatalysis. The almost unchanged level of CEL activity proves that most enzyme molecules in the enzymogel are involved in the biocatalytic reactions (it is likely that only some fraction of CEL is entrapped at the particle - brush interface that causes a slightly lower sugar yield as compared with free CEL). By comparing the kinetics of glucose production using free CEL, grafted CEL and enzymogel (Fig.7.11b), the mean diameter of contact of the enzymogel particles with the cellulose substrate was estimated. The estimated value is about 140 nm. Such contact area is possible if the CEL loaded brush spreads over the surface of the substrate. The latter was proved with in situ AFM experiments when single enzymogel nanoparticles were examined on the surface of a cellophane film (a model of cellulose substrate). The images of single adsorbed-on-the-substrate nanoparticles using topographical, adhesion and mechanical modulus contrasts are shown in Fig.7.3 a. The spreading of the enzymogel over the substrate is clearly visible on the 3D topography images and topographical cross-sections (Fig.7.13b and c) and on the SEM image (Fig.7.4e). A simple estimation shows that the reaction contact rea of an enzymogel nanoparticle due to the spreading (engulfing) is about an order of magnitude greater than for a solid particle of the same diameter with a traditional method of surface immobilization (grafting) of enzymes. The latter is proved in the reference experiment (Fig.7.11b, triangles).

AFM and SEM experiments demonstrate the structure of the contact area between enzymogel nanoparticles and cellophane substrates. AFM in situ experiments provide dimensions of the contact area in the conditions of biocatalytic conversion. Similar spreading effect was observed for enzymogel particles with no loaded enzymes (Fig.7.13). That explains the mechanism of spreading driven by PAA brush chains. Since CEL and PAA chains compete for the contact with the substrate, the exact area of the contact between enzyme molecules and the substrate should be less than that observed in the images.

Kinetic data was used to estimate an effective contact area for excess of the substrate as:

$$S = \frac{C_e \, N_A a^2}{\frac{R_{FE}}{R_{EG}} N_c} \qquad (7.2)$$

where S is the reaction contact area, C_e is the concentration of enzyme, N_A is Avogadro's number, a is the diameter of enzyme molecule (3 nm), R_{FE} is the rate of glucose synthesis in the presence of free CEL enzyme, R_{EG} is the rate of glucose synthesis in the presence of the same concentrate of CEL enzyme in the enzymogel, N_c is the number of enzymogel particles per volume unit.

For the experimental ratio $R_{FE}/ R_{EG} = 4$ and 180 nm in diameter enzymogel particles at the reaction conditions that correspond to Fig 7. 3 a contact area per particle was calculated as equal to 1.47×10^4 nm^2 with a 138 nm effective diameter of the contact area. Although, this diameter is smaller than the particle diameter because some fraction of the contact area is occupied by PAA chains, it is substantially greater than the contact diameter of a particle that carries enzymes immobilized by traditional methods as shown in the schematic (Fig.7.12). The area of contact with substrates is much larger for enzymogel than for solid particles due to spreading of PAA brushes over the substrate. For solid particles, the contact area S_S can be estimated taking into account a penetration depth of the enzymes into the substrate d. The penetration depth of the enzymes d is limited by the carrier particle and thus cannot exceed a. In the latter case the contact area is (chord theorem):

$$S_s = 2\pi Rd \qquad (7.3)$$

For particles with the same diameter as that for enzymogel nanoparticles, S_S is 1.69×10^3 nm^2. That value is about 10 times smaller than the effective contact area for enzymogel particles. In reality, the area of contact for solid carriers should be even smaller because when $d=a$ enzymes may undergo denaturing and could loss heir catalytic activity. Moreover, the model does not consider surface roughness of the solid carrier that may screen immobilized enzymes.

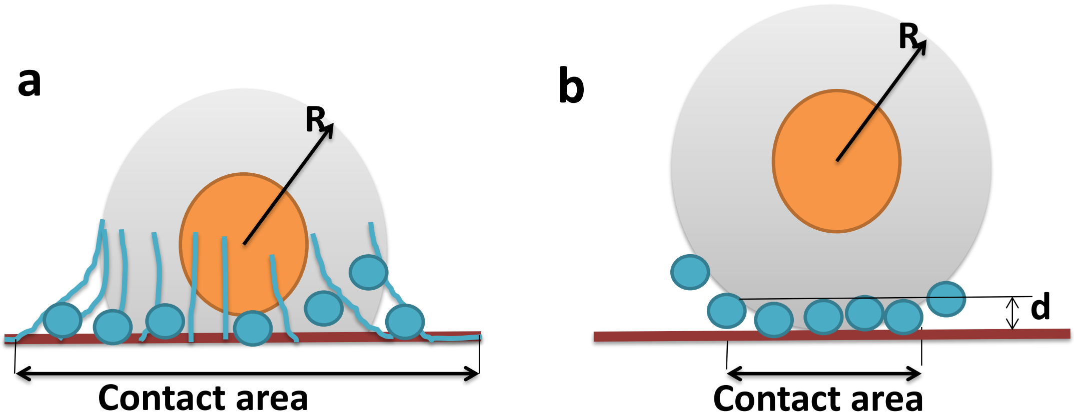

Fig.7.12. Comparison of the contact area of a hairy particle (enzymogel) and a solid particle that carry enzymes.

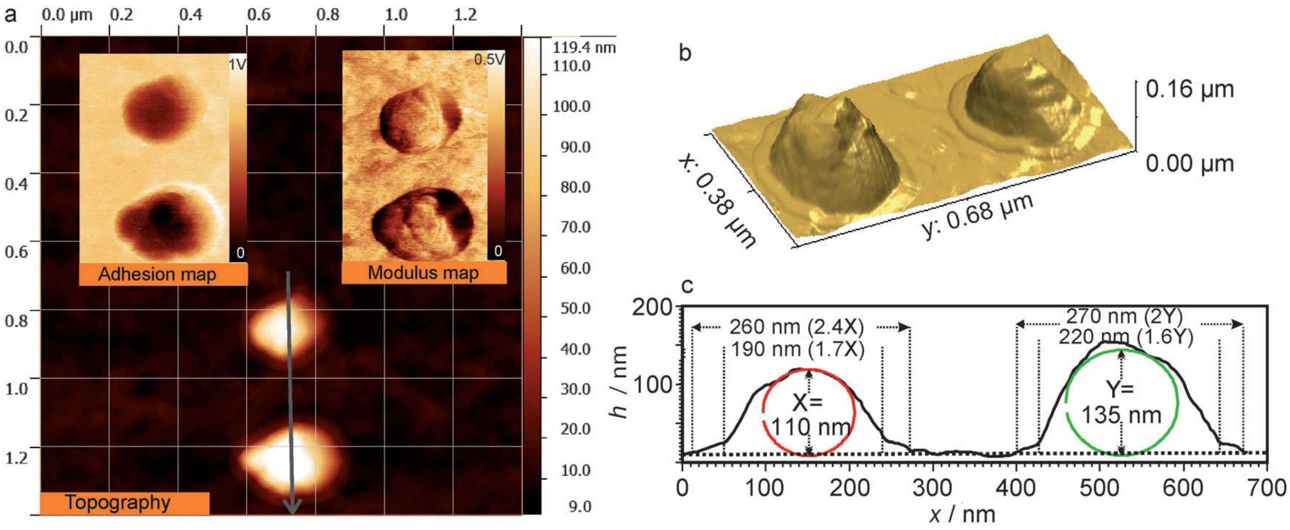

Fig.7.13. AFM imaging of the CEL-loaded enzymogel particles in 10 mm citrate buffer on the surface of a cellophane film using a) topography, modulus, and adhesion contrasts; 3D topographical images of the particles and their topographical cross-sectional profiles (b and c). Data obtained by Dr. S. Minko group in Clarkson University (Potsdam, NY).

The enzymogel nanoparticles provide a unique opportunity for industrial enzyme recovery. Because of the high biocatalytic activity of the enzymes that reside in the enzymogel there is no need to release and extract enzymes. In other words, the enzymogel can be used for biomass conversion. After conversion of the cellulosic biomass, the enzymogel nanoparticles can be magnetically extracted and transferred into a freshly loaded bioreactor for reuse. The experiments demonstrated that this methodology provides an about four-fold increase in glucose per enzyme when compared with the traditional one-way use of CEL for cellulose conversion (Fig.7.11a, V).

Possible applications including biomedical technologies are illustrated using experiments with cotton floss (Fig.7.11c–h). A droplet of a free CEL solution was deposited on the floss (Fig.7.11c) and allowed to dry. In the second experiment, the droplet of enzymogel solution was deposited on the floss and dried. In both cases the concentration of CEL was the same. Then, the floss was immersed in buffer pH 5.5 solution. In 2.5 h, the floss treated with the enzymogel was broken while the one treated with a free enzyme was intact after 14 h. If at the same concentration of CEL the enzymogel was collected on the floss with a magnet, the degradation experiment demonstrated an even faster floss failure after 1 h (Fig.7.11g and h). Thus, application of the enzymogel using a magnetic field can be explored for localized highly efficient bioconversion processes. The possibility of a remote control of the localized biocatalysis opens a new avenue for applications in drug delivery and absorbable implants.

Enzymogel nanoparticles readily adsorb on cellulose substrates like cotton and filter paper when both the substrates and enzymogel are negatively charged in water at pH 5. The cellulose surface is only weakly charged since there are no strong acidic functional groups on the surface. Thermal fluctuations overcome the weak long-range repulsive forces and enzymogel particles strongly interact with the cellulose surface by hydrogen bonds between hydroxyl groups of cellulose and carboxyl groups of PAA brushes.

7. 5. Conclusions

Novel phase boundary biocatalysis was introduced when encapsulated enzyme retains its mobility in a soft hydrophilic polymer carrier and is capable of hydrolyzing insoluble substrates using highly dynamic behavior of the enzyme and their high affinity to the polymer brush of the enzymogel and to the substrate. The enzyme remains encapsulated in the polymer brush and catalyzes the hydrolysis of the insoluble substrates attached to the enzymogel.

7.6. References

[1]. Henzler-Wildman, K.; Kern, D. Dynamic personalities of proteins. *Nature* **2007**, *450*, 964 – 972.

[2]. Bornscheuer, U. T. Enzymimmobilisierung: ein Weg zu verbesserten Biokatalysatoren. *Angewandte Chemie* **2003**, *115*, 3458 – 3459.

[3]. Stewart, J. D. Dehydrogenases and Transaminases in Asymmetric Synthesis. *Current Opinion in Chemical Biology* **2001**, *5*, 120 – 129.

[4]. Hwang, E. T.; Gu, M. B. Enzyme stabilization by nano/microsized hybrid materials. *Engineering in Life Sciences* **2013**, *13*, 49 – 61.

[5]. Rodrigues, R. C.; Ortiz, C.; Berenguer-Murcia, A.; Torres, R.; Fernandez-Lafuente, R. Modifying enzyme activity and selectivity by immobilization. *Chemical Society Reviews* **2013**, *42*, 6290 – 6307.

[6]. Veum, L.; Hanefeld, U. Carrier enabled catalytic reaction cascades. *Chemical Communications* **2006**, 825 – 831.

[7]. Czeslik, C. Factors ruling protein adsorption. *Zeitschrift für Physikalische Chemie* **2004**, *218*, 771 – 801.

[8]. Czeslik, C.; Winter, R. Effect of temperature on the conformation of lysozyme adsorbed to silica particles. *Physical Chemistry Chemical Physics* **2001**, *3*, 235 – 239.

[9]. Norde, W.; Lyklema, J. The adsorption of human plasma albumin and bovine pancreas ribonuclease at negatively charged polystyrene surfaces: I. Adsorption isotherms. Effects of charge, ionic strength, and temperature. *Journal of Colloid and Interface Science* **1978**, *66*, 266 – 276.

[10]. Lu, Y.; Wittemann, A.; Ballauff, M. Supramolecular structures generated by spherical polyelectrolyte brushes and their application in catalysis. *Macromolecular Rapid Communications* **2009**, *30*, 806 – 815.

[11]. Coradin, T.; Nassif, N.; Livage, J. Silica–alginate composites for microencapsulation. *Applied Microbiology and Biotechnology* **2003**, *61*, 429 – 434.

[12]. Kobayashi, J.; Mori, Y.; Kobayashi, S. Novel immobilization method of enzymes using a hydrophilic polymer support. *Chemical Communications* **2006**, 4227 – 4229.

[13]. Ivanov, A. E.; Edink, E.; Kumar, A.; Galaev, I. Y.; Arendsen, A. F.; Bruggink, A.; Mattiasson, B. Conjugation of Penicillin Acylase with the Reactive Copolymer of N-Isopropylacrylamide: A Step Toward a Thermosensitive Industrial Biocatalyst. *Biotechnology Progress* **2003**, *19*, 1167 – 1175.

[14]. Lutz, J.-F.; Akdemir, O.; Hoth, A. Point by point comparison of two thermosensitive polymers exhibiting a similar LCST: is the age of poly(NIPAM) over? *Journal of the American Chemical Society* **2006**, *128*, 13046 – 13047.

[15]. Chiu, Y.-C.; Cheng, M.-H.; Engel, H.; Kao, S.-W.; Larson, J. C.; Gupta, S.; Brey, E. M. The role of pore size on vascularization and tissue remodeling in PEG hydrogels. *Biomaterials* **2011**, *32*, 6045 – 6051.

[16]. Stöber, W.; Fink, A.; Bohn, E. J. Controlled growth of monodisperse silica spheres in the micron size range. *Journal of Colloid and Interface Science* **1968,** *26*, 62-69.

[17]. Levy, L.; Sahoo, Y.; Kim, K. S.; Bergey, E. J.; Prasad, P. N. Nanochemistry: synthesis and characterization of multifunctional nanoclinics for biological applications. *Chemistry of Materials* **2002,** *14* (9), 3715-3721.

[18]. Bradford, M. M. A rapid and sensitive method for the quantitation of microgram quantities of protein utilizing the principle of protein-dye binding. *Analytical Biochemistry* **1976,** *72*, 248–254

[19]. Lopez, A.; Dupou, L.; Altibelli, A.; Trotard, J.; Tocanne, J. F. Fluorescence recovery after photobleaching (FRAP) experiments under conditions of uniform disk illumination. Critical comparison of analytical solutions, and a new mathematical method for calculation of diffusion coefficient D. *Biophysical Journal* **1988,** *53*, 963–970

[20]. Haupt, B.; Neumann, T.; Wittemann, A.; Ballauff, M. Activity of enzymes immobilized in colloidal spherical polyelectrolyte brushes. *Biomacromolecules* **2005**, *6*, 948 – 955.

[21]. Henzler, K.; Haupt, B.; Ballauff, M. Enzymatic activity of immobilized enzyme determined by isothermal titration calorimetry. *Analytical Biochemistry* **2008**, *378*, 184 – 189.

[22]. Becker, A. L.; Welsch, N.; Schneider, C.; Ballauff, M. Adsorption of RNase A on cationic polyelectrolyte brushes: a study by isothermal titration calorimetry. *Biomacromolecules* **2011**, *12*, 3936 – 3944.

[23]. Wittemann, A.; Ballauff, M. Interaction of proteins with linear polyelectrolytes and spherical polyelectrolyte brushes in aqueous solution. *Physical Chemistry Chemical Physics* **2006**, *8*, 5269 – 5275.

[24]. Czeslik, C.; Jansen, R.; Ballauff, M.; Wittemann, A.; Royer, C. A.; Gratton, E.; Hazlett, T. Mechanism of protein binding to spherical polyelectrolyte brushes studied in situ using two-photon excitation fluorescence fluctuation spectroscopy. *Physical Review E* **2004**, *69*, 021401.

[25]. Wittemann, A. Ballauff, M. Secondary structure analysis of proteins embedded in spherical polyelectrolyte brushes by FT-IR spectroscopy. *Analytical Chemistry* **2004**, *76*, 2813 – 2819.

[26]. Wittemann, A.; Ballauff, M. Temperature-induced unfolding of ribonuclease A embedded in spherical polyelectrolyte brushes. *Macromolecular Bioscience* **2005**, *5*, 13 – 20.

[27]. Pessela, B. C. C.; Mateo, C.; Carrascosa, A. V.; Vian, A.; Garca, J. L.; Rivas, G.; Alfonso, C.; Guisan, J. M.; Fernandez-Lafuente, R. One-step purification, covalent immobilization, and additional stabilization of a thermophilic poly-his-tagged β-galactosidase from Thermus sp. Strain T2 by using novel heterofunctional chelate–epoxy sepabeads. *Biomacromolecules* **2003**, *3*, 107 – 113.

[28]. Wittemann, A.; Haupt, B.; Ballauff, M. Controlled release of Proteins Bound to Spherical Polyelectrolyte Brushes. *Zeitschrift für Physikalische Chemie* **2007**, *221*, 113 – 126.

[29]. Hollmann, O.; Steitz, R.; Czeslik, C. Structure and dynamics of α-lactalbumin adsorbed at a charged brush interface. *Physical Chemistry Chemical Physics* **2008**, *10*, 1448 – 1456.

[30]. Lynd, L. R.; van Zyl, W. H.; McBride, J. E.; Laser, M. Consolidated bioprocessing of cellulosic biomass: an update. *Current Opinion in Biotechnology* **2005**, *16*, 577 – 583.

[31]. Zhang, Y.; Liu, Y. Y.; Xu, J. L.; Yuan, Z. H.; Qi, W.; Zhuang, X. S.; He, M. C. High solid and low enzyme loading based saccharification of agricultural biomass. *Bioresources* **2012**, *7*, 345 – 353.

[32]. Jervis, E. J.; Haynes, C. A.; Kilburn, D. G. Surface diffusion of cellulases and their isolated binding domains on cellulose. *The Journal of Biological Chemistry* **1997**, *272*, 24016 – 24023.

CHAPTER 8. KINETIC STUDIES OF ENZYMES IMMOBILIZED ON RESPONSIVE ORGANIC-INORGANIC COLLOID PARTICLES

8.1. Abstract

The hydrolytic performance of enzymogels as novel biocatalytic colloids for the immobilization of cellulase enzymes was compared to performance of free enzymes and enzymes chemically grafted to dispersed carrier particles. Kinetic studies were used to investigate the role of mobility of the immobilized enzymes for their hydrolytic activity. The hydrolysis of cellulose substrate was studied using complementary classical and fractal kinetic models based on Michaelis-Menten equations. In contrast to grafted enzymes, the kinetic parameters (fractal rate orders and Michaelis constant) of enzymogels were found to be close to those of free enzymes. It indicates higher availability of enzymes immobilized in enzymogels and their higher substrate affinity. As a result the efficiency of enzymogels during hydrolysis is close to the efficiency of free enzymes. It can be explained by the ability of enzymogels to facilitate homogeneous distribution of enzymes and their continuous supply towards the cellulose substrate due to the mobility of the enzymes inside the polymer brushes of the enzymogel particle.

8.2. Introduction

Cellulose as the major component of plant cells can be considered the most abundant polysaccharide in nature and a renewable source of biomass [1-3]. The hydrolysis of cellulose-containing materials resulting in production of simple reducing sugars has long been viewed as an abundant food and energy source [2]. However, the commercial applications of biomass hydrolysis have been limited by a number of factors: the high cost of the enzymes involved in the hydrolysis, slow rate of the reaction, inefficient reactors for the complex heterogeneous reaction, etc [1, 2]. To develop efficient scalable technology of the cellulose enzymatic hydrolysis robust rate expression should be derived to fit the experimental data. Such models are needed to calculate hydrolytic reactor configurations and feeding frequencies [2-4].

Chemical and physical properties of cellulose materials vary widely and thus the kinetic modeling of the hydrolysis often requires complicated input of physical and mass transfer parameters [2-3].

The immobilization of cellulase enzymes is a possible approach for large scale commercialization in order to increase their productivity and shelf life. Enzyme immobilization is confinement of enzyme to a phase (matrix/support) different from the phase of overall reaction mixture (i.e. solvent, substrate and/or products) [5]. Several methods were developed for cellulase immobilization influencing the performance of immobilized enzymes. Adsorption and/or carrier-binding method uses water-insoluble carriers such as polysaccharide derivatives, synthetic polymers and glass [6-9]. In grafting method, bi/multifunctional reagents such as glutaraldehyde, bisdiazobenzidine and hexamethylene diisocyanate are used to cross-link/form covalent bonds between the enzyme and the support [10]. Polymer matrixes like collagen, cellulose and κ-carrageenan are used to entrap the enzymes, while the membrane confinement method includes formulation of liposomes and microcapsules to encapsulate the enzymes [10-16]. Apart from being affordable, an ideal support/matrix must encompass characteristics such as inertness, physical strength, stability and ability to reduce product inhibition, non-specific adsorption and microbial contamination [17]. Immobilization generates continuous economic operations, automation, high investment/capacity ratio and fabrication of the product with greater purity [18]. Kinetic modeling of the enzymatic systems with immobilized enzymes can be used to compare their activity and efficiency with respective parameters of free enzymes [19].

Cellulose hydrolysis catalyzed by cellulases is a heterogeneous reaction. Experimental data on cellulose hydrolysis in presence of immobilized cellulases point to various limitations that contribute to decreasing rates of hydrolysis with conversion [19-20]. To analyze the experimental data and investigate the role of enzymes mobility in the immobilized systems the kinetic modeling of the hydrolysis process is an important tool [19-23].

Initial cellulose hydrolysis data often follow the classical Michaelis-Menten model [19-23]. Therefore during the rapid initial hydrolysis (first 60 min of reaction) neither the absorption nor the mass transfer limits the overall reaction rate providing constant number of the substrate on the binding sites of the enzymes resulting in high substrate/enzyme ratio [20-23].

However, the classical approach cannot be used for the extended reaction times, as the experimental data point out to the decrease of reaction rate with the increase of the conversion [2, 24-25]. A number of theories was developed to describe the reactions in such complex systems [23]. Reported kinetic models describing enzymatic hydrolysis of cellulose can be classified into three major types: i. empirical, ii. adsorption-based and iii. fractal kinetic models [23]. Within these models specific systems of equations may or may not include inhibition [26-28], synergy (for enzyme mixtures) [29-31], deactivation [32-33], etc. Empirical models can produce good fits of the experimental data and can be used for the prediction of the expected reaction rates. However, they do not give any insights on the specifics of the enzyme-substrate interactions [23, 34-37]. The adsorption-based kinetic models consider adsorption as the major rate-limiting process during the reaction. This approach gives adequate results only for the reactions catalyzed by the enzymes immobilized on solid supports with small surface areas [23, 38-39] and will not be suitable for nanosized carriers. On the other hand the concept of fractal kinetic takes into account the complex processes contributing to the cellulose hydrolysis: turbulence phenomena, Brownian motion in confined spaces, non-Euclidean shapes of the substrate and non-uniform distribution of components in the system [23, 32, 40-45]. The fractal model was shown to meet the appropriateness criteria for the complex enzymatic systems such as cellulase catalyzed hydrolysis by being systematically structured [41-44]. The fractal approach gives the estimation of data deviation from the classical Michaelis-Menten formalism conserving the basic philosophy of the classical scheme [41-43].

The fractal kinetics approach should not be considered exclusive for the description of the system. In the field of enzymatic kinetics different methods complement each other giving valuable parameters to construct the picture of the intricate mechanisms of the cellulose hydrolysis. The complexity of the enzymatic system, involved in cellulose hydrolysis, especially in case of immobilized enzymes requires structured and multistep kinetic modeling.

The goal of the current study is to investigate the hydrolytic activity of enzymogels as novel biocatalytic colloids using different cellulose substrates (filter paper, dispersed cellulose) and compare it with the behavior of free cellulase enzymes and cellulases chemically grafted to the dispersed carrier particles. In case of grafted enzymes, we assume that the mobility of enzyme macromolecules is restricted by chemical binding to dispersed carrier (silica particles). In the same time the immobilized enzymes may remain mobile inside the polymer brushes of the enzymogel particles (see Chapter 7). Therefore, the kinetic studies of novel biocatalytic colloids (enzymogels) developed in this work can reveal the role of the enzymes mobility in hydrolytic processing. Both classical and fractal kinetic models have been applied for the description of cellulose hydrolysis. The calculated kinetic parameters can be used to explain the higher efficiency of enzymogels and give more insights into their behavior on the cellulose substrates during hydrolysis.

8.3. Experimental

8.3.1. Materials

Tert-butyl acrylate (TBA), ascorbic acid, copper bromide, N,N,N′,N″,N″-pentamethyldiethylenetriamine (PMDTA), methylsulfonic acid, toluene, dichloromethane, methylethylketone (MEK), hydrogen peroxide, ethanol, α-bromoisobutyryl bromide (BIB), triethylamine, ethylenediamine, sodium dodecyl sulphate (SDS), methylamine, ferrous (II) chloride tetrahydrate, ferrous (III) chloride hexahydrate, sodium silicate, tetraethyl orthosilicate (TEOS), ammonium hydroxide solution Bradford reagent, sodium azide (BioUltra Reagents, ≥99.5%), albumin from bovine serum (BSA, lyophilized powder, ≥96%) were purchased from Sigma-Aldrich and used as received. (3-Glycidyloxypropyl) trimethoxysilane (GPES) was purchased from Gelest. Citric buffers were prepared from sodium citrate dihydrate (ACS reagent, ≥99.5%, BDH), citric acid (ACS reagent, ≥99.5%, Sigma-Aldrich) and Millipore water (18Ω). Cellulase enzyme stock solution (40%, w/w) NS 50013 from Novozymes Corporation, Bagsvaerd, Denmark was diluted in buffered solutions and stabilized with 0.04% NaN_3.

8.3.2. Synthesis and Loading of the Enzymogels

Enzymogel particles synthesis. The synthesis of enzymogels is described in Chapter 7.3.2.

Loading of cellulases into the enzymogels. Enzymogel particles loaded with cellulase enzymes as described in Chapter 7. Brush-decorated particles (40 mg) mixed overnight with 100 μl of cellulase stock solution in 1.5 ml of citric buffer (pH 4.0). The cellulase-loaded enzymogels were separated using centrifugation at 15,000 rpm for 15 min (VWR Scientific microcentrifuge (model V). The particles were afterwards dispersed in 1.5 ml of citric buffer (pH 4.8) and used as a stock dispersion in experiments. Cellulase loading was estimated using a standard Bradford assay [46]. For this purpose, a standard calibration plot was developed by serial dilutions of 1 mg/ml BSA protein standard in a range 0.1 - 1.4 mg/ml and recording absorbance spectra of the solutions at 595 nm using Varian Cary 5000UV-VIS-NIR spectrometer. To determine cellulase loading, 0.1 ml of the dispersion was mixed with 3 ml of the Bradford Reagent, gently stirred, and incubated at room temperature for 15 minutes. Cellulase concentration in tested dispersion was calculated using the calibration.

$$Loading,\% = \frac{C_i - C_r}{C_i} \times 100\% \qquad (8.1)$$

where C_i is the initial cellulase concentration in solution before the loading and C_r is the cellulase concentration in dispersion after the loading, mg/mL.

8.3.3. Grafting of Cellulase Enzymes to the Silica Particles

Silica particles with chemically grafted enzymes were used as a reference sample, assuming that chemical grafting may restrict the mobility of enzymes during hydrolysis. To fabricate grafted enzymes 200 nm silica particles (1.9 g) were dispersed in 100 ml of ethanol using ultrasonication. Afterwards, the particles were separated by centrifugation (10,000 rpm, for 10 min), transferred to a dry MEK and sonicated again. In the next step, the silica was silanized using 2% (3-glycidyloxypropyl) trimethoxysilane (GPES) solution in dry MEK overnight and rinsed 3 times by MEK and dichloromethane. Finally, the silanized particles were treated with 2% ethylenediamine solution in dichloromethane for 2 h and rinsed three times with dichloromethane, ethanol and water. The modified silica particles were separated by centrifugation and dried in vacuum oven at 60°C overnight. The dried silica (100 mg) modified with amino groups was rinsed three times with 10 ml of phosphate buffer (pH 7.4, coupling buffer). After the final wash cycle, the modified silica was dispersed in 10 ml of phosphate buffer containing 10% w/w of glutaraldehyde. The mixture was left to react for 1 hour at room temperature. Unreacted glutaraldehyde was removed by rinsing the particles three times with 10 ml of phosphate buffer. The modified silica was dispersed in 10 ml of the coupling buffer and mixed with a 0.5% w/w cellulase solution 4 h. Afterwards glycine (0.2 M) and cyanoborohydride (10 nM) were added to deactivate unreacted glutaraldehyde. Excess of protein and reactants was removed by three repetitive rinsing of the particles using 10 ml of citric buffer (pH 3.8). The amount of cellulase grafted to silica particles was estimated using a standard Bradford assay [32] as described above.

8.3.4. Kinetic Assays

Hydrolytic activity of the cellulase-loaded enzymogels was tested in several cycles (72 hours each) at 50ºC and pH 4.80 ± 0.05. The stock dispersion containing either enzymogels, grafted enzymes or free enzymes was diluted with citrate buffer at pH 4.8 (total sample volume 10 mL) and sonicated for 5 min in Branson B5510 ultrasonic bath. 50 mg of Whatman#1 filter paper (1×6 cm) was added to sonicated dispersion, and it was stirred at 300 rpm and 50ºC. The liquid dispersion phase was sampled over time to determine the glucose content which is known as the reliable measure of cellulase enzymes performance [2].

8.3.5. Glucose Quantification

Glucose yield during enzymatic hydrolysis was analyzed using HPLC, Waters (Milford, MA) system Bio-Rad (Hercules, CA) Aminex HPX-87P HPLC column (water as mobile phase at a flow rate 0.6 mL/min and temperature 50°C) and refractive index detector (temperature 85°C). Prior to HPLC, 1 mL of dispersion was centrifuged and filtered using a 0.25 μm nylon filter (Pall Corporation, West Chester, PA).

8.4. Results and Discussion

8.4.1. Linear Mass-Action Hydrolysis Kinetics During Hydrolysis of Cellulose Substrates

The classical Michaelis-Menten scheme was developed for the mass action reaction systems – i.e. mixtures with homogeneous distribution of the components. The main quasi steady-state assumption for this scheme is based on the presence of the excess of the substrate in the system. The classical model was used to describe the experimental data for the initial fast hydrolysis - first 60 minutes of reaction [19-23, 47-49]. It can be explained by the abundance of enzyme binding sites on the substrate proving higher substrate/enzyme ratio. Hence, during the rapid initiation stage of hydrolysis neither the absorption rate nor mass transfer processes rates are limiting the overall reaction rate [21-23, 47-49].

Kinetic calculations based on classical Michaelis-Menten formalism [19, 20] are widely used for the description of enzymatic reactions. In conventional mass action kinetics rate laws are expressed as rational functions of product and enzyme concentrations [19, 47-49]. For basic enzymatic reaction (Scheme 8.1) the Michaelis-Menten equation can be represented as eq. 8.2. [19, 48]:

$$E + S \underset{k_{-1}}{\overset{k_1}{\rightleftharpoons}} ES \xrightarrow{k_2} E + P$$

Scheme 8.1. Michaelis reaction scheme. E – enzyme, S – substrate, P – product, ES – enzyme-substrate complex; k_1, k_{-1}, k_2 – equilibrium constants [19, 47].

$$k_2[E]t = P(t) - K_m \ln\left(1 - \frac{P(t)}{[S]}\right) \qquad (8.2)$$

where $K_m = \frac{k_{-1} + k_2}{k_1}$ is the Michaelis constant [19, 47-49] quantifying the affinity of the enzyme molecules towards the substrate, *P(t)* is the glucose concentration at time *t*, and *[S]* is the substrate concentration.

In practice equation 8.2 is rewritten as equation 8.3 in order to calculate K_m by fitting the experimental data to the double reciprocal plots of $1/V_o$ *vs* $1/[S]$ (Lineweaver-Burk plots, Fig.8.2) [2].

$$V_o = \frac{V_{\max}[S]}{K_m + [S]} \qquad (8.3)$$

where V_0 – is the initial reaction rate, V_{max} – maximal reaction velocity.

The initial reaction rates were calculated as the slopes of the kinetic plots for the initial stage of the hydrolysis (Fig.8.1) and used to develop Lineweaver-Burk plots by plotting velocity vs the substrate concentration in double-reciprocal form (Fig.8.2).

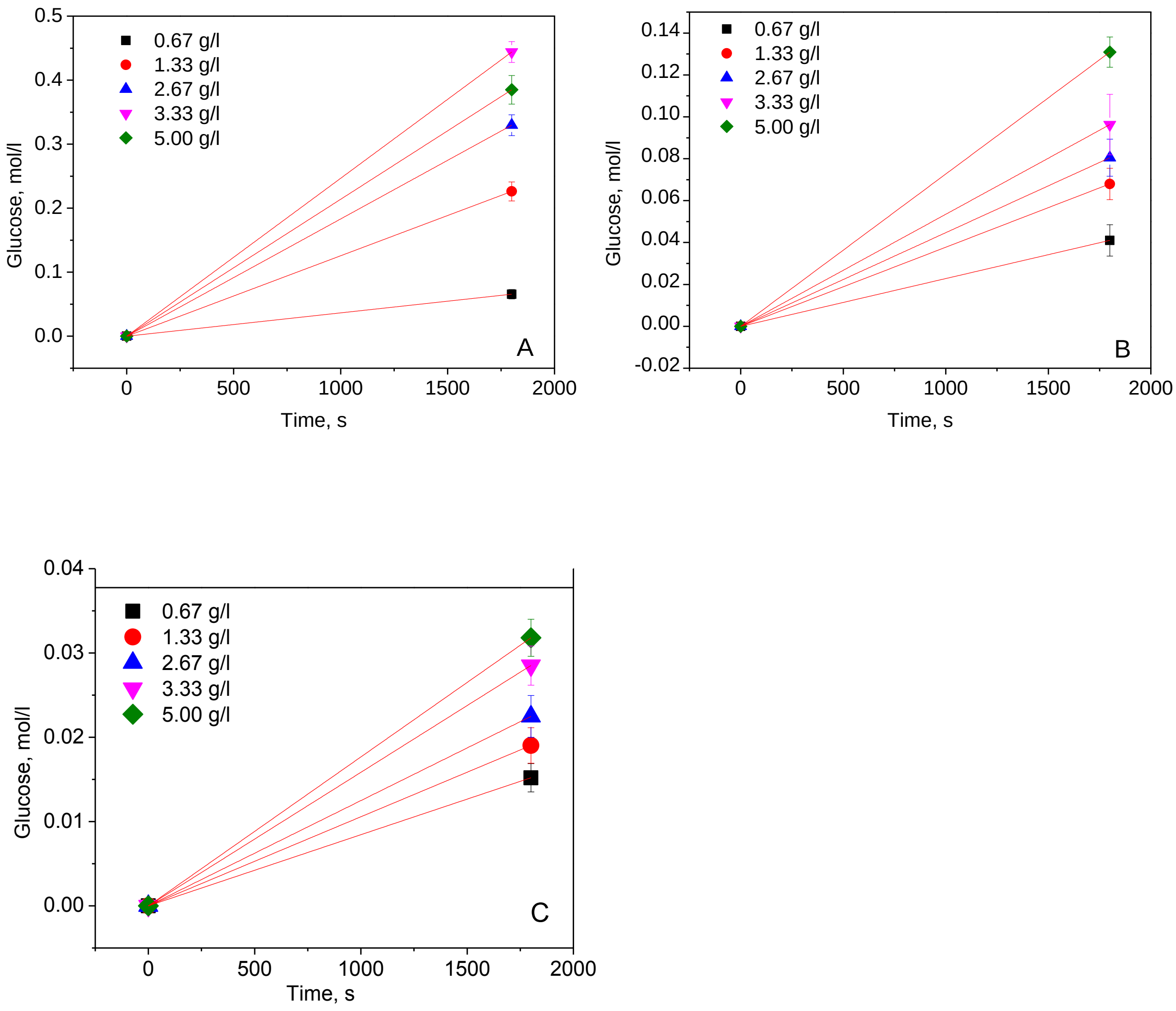

Fig.8.1. Selected kinetic plots at concentration 20 μg/ml and filter paper substrate. A – free enzymes, B – enzymogels and C – grafted enzymes.

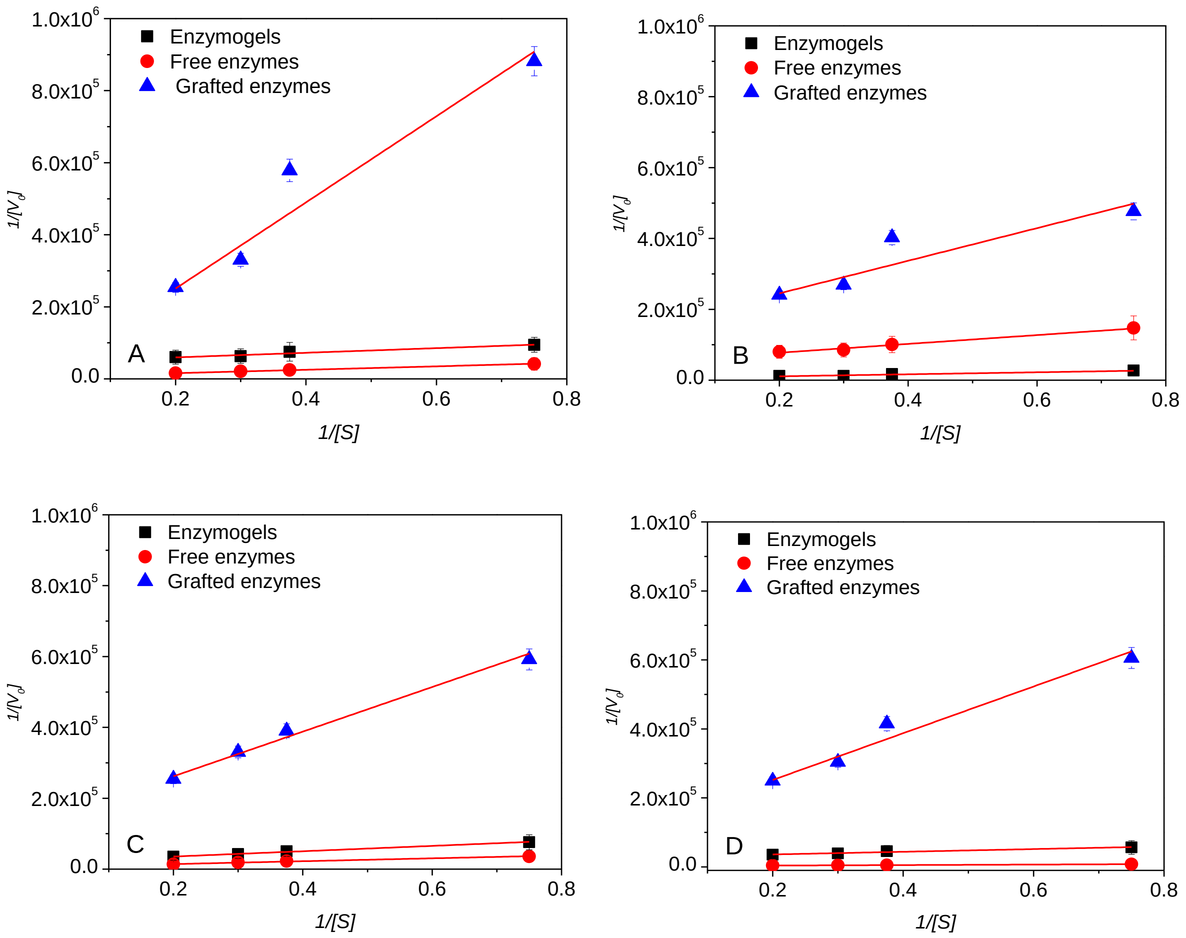

Fig.8.2. Lineweaver-Burk plots for the immobilized and free cellulases at 20 μg/ml (A – on filter paper, B – on dispersed cellulose) and at 40 μg/ml (C – on filter paper, D – on dispersed cellulose).

The data on the Lineweaver-Burk plots (Fig.8.2) indicate significantly lower velocity values for the grafted cellulase enzymes when compared to the data for enzymogels and for the free enzymes in the same reaction conditions. This effect can be explained by the different diffusion limitations for the different enzymatic systems towards the heterogeneous substrate during the hydrolysis. In order to perform the catalytic action, the cellulase enzymes first need to diffuse towards the substrate and adsorb on it. In case of grafted enzymes the mobility of the cellulases is mainly defined by the mobility of the carrier particles chosen for cellulase immobilization. Thus the limited mobility can result in lower diffusion rates and more pronounced diffusion limitation for the grafted enzymes towards the substrate. In case of enzymogels, prior studies indicate that cellulase enzymes remain mobile inside the soft polymer brushes of the enzymogel particles. It is assumed that this specific mobility of cellulase in polymer brushes may facilitate continuous supply of enzymes towards the substrate surface during hydrolysis. The latter fact can explain the increase of overall efficiency of enzymogels during hydrolysis when compared to chemically grafted cellulases, where the enzymes are not mobile.

The values of Michaelis constant Km calculated from the Lineweaver-Burk using eq. 8.3 are presented in Fig.8.3. For free enzymes the calculated Km values are consistent with the Km values reported for similar cellulase-catalyzed hydrolytic systems [21, 36, 47, 50]. Moreover, in case of free enzymes the calculated Km values depend only on the substrate type and are concentration independent which is consistent with the postulates of classical Michaelis-Menten formalism [21, 36]. The latter means that enzyme/substrate ratio is large enough to overcome the diffusion effects on the surface of non-soluble cellulose substrate.

For the grafted enzymes calculated Km values are constant at two different concentrations on two different substrates. It can be explained by the restricted mobility of the cellulases grafted to the surface of silica, so the diffusion of the cellulase molecules is mainly controlled by the slow diffusion of silica particles towards the substrate.

In the systems with uniform distribution and free diffusion of soluble substrate and enzymes the Km values are constant at all enzyme concentrations according to the rate expression of Michaelis-Menten mass-action kinetics [21, 22]. In the same time for enzymogels the calculated Km values depend on the nature of the substrate and concentration of the cellulases which contradicts the assumptions of classical Michaelis-Menten mass-action kinetics about the constant enzyme/substrate ratio during the reaction. Due to the insoluble nature of cellulose substrate, the large domains of the substrate are not exposed to enzymogels during the hydrolysis reaction. The complexity of the cellulose hydrolysis in presence of enzymogels can be further increased by the diffusion of enzymogel particles to the substrate surface and by the diffusion of enzymes inside the carrier (the mobility of the enzymes). Therefore, the accessibility of substrate surface and the mobility of enzyme molecules in reaction media can be considered as the major rate-determining factors during the cellulose hydrolysis in presence of enzymogels. In order to take into account these spatial restrictions the kinetic model describing enzymogels as immobilizing support should include the additional dimension – fractal dimension (see below) [21]. In this study the kinetics of cellulose hydrolysis was modeled using fractal kinetic approach, with non-integer order rate expressions corresponding to fractal dimensions [21, 22].

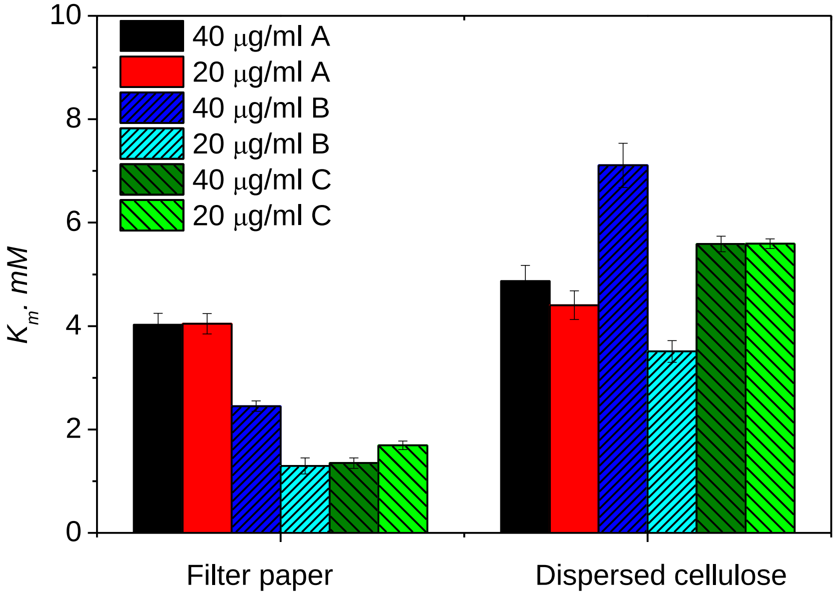

Fig.8.3. Michaelis constant for A – grafted enzymes, B – enzymogels, C – free enzymes on different cellulose substrates (filter paper, dispersed cellulose) at two different enzyme concentrations.

8.4.2. Fractal Kinetic Calculations for the Free Enzymes, Enzymogels and Grafted Enzymes During Hydrolysis of Cellulose Substrates

Fractal kinetic approach is commonly used to describe the reactions taking place in spatially constrained media – such as heterogeneous systems. Since non-soluble cellulose substrates are transformed into soluble products during the hydrolysis, the kinetics of the hydrolytic reaction can be described by fractal kinetic models [23, 41-43]. The fractal models take into account catalytic actions accompanied by the diffusion on the non-ideal (not flat) substrate surfaces [23, 40-44] and can be used to describe the hydrolytic system at extended reaction times [19-23].

In this work the hydrolytic activity of immobilized enzymes (enzymogels and grafted enzymes) is compared with free enzymes. The physical immobilization of cellulases on polymer brushes of the enzymogels and chemical grafting of enzymes to the dispersed silica support result in additional spatial constrains for the hydrolytic performance of cellulases. To this end fractal kinetics can be effectively used for the description of reactions catalyzed by immobilized enzymes. The inaccessible and non-reactive portions of the cellulose substrate can be considered as spatial constraints increasing the fractal character (heterogeneity) of the hydrolysis. The fractal character can be quantified as the deviation from the linear behavior of the kinetic curves and estimated as fractal dimension parameter [39-44].

The fractal dimension of the system can be calculated using empirical first-order equation 8.4 [23, 32]:

$$P(t) = [S_O]\left(1 - \exp\left(-k \times t^{(1-h)}\right)\right) \qquad (8.4)$$

where *P(t)* is the product concentration at time *t*, *[S$_o$]* – is the initial substrate concentration, *k* – is the reaction rate constant, *h* – is the fractal dimension parameter.

Equation 4 was used to fit the obtained kinetic data in order to compute the values of fractal dimension parameter (Fig.8.4). Correlation coefficients for the fitting were in the range 0.88÷0.95, thus validating the fit of the experimental data by the selected model.

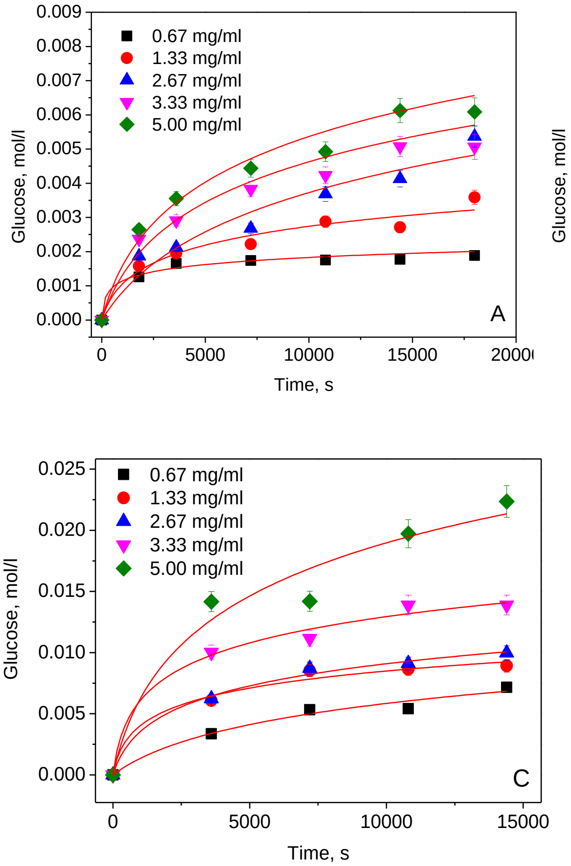

Fig.8.4. Selected kinetic curves representing the experimental data and their fits by the fractal model for the samples of A – free enzymes, B – enzymogels and C – grafted enzymes at cellulase concentration 20 μg/ml and dispersed cellulose substrate.

The fractal dimension parameter (FDP) values depend on the spatial distribution of the components in the reaction mixture [40-44]. Hence plotting values of FDP as function of the substrate concentration can be used to observe the change of the spatial restrictions in the system during hydrolysis. Fig.8.5 represents the FDP plotted as a function of concentration for two different cellulose-containing substrates. In case of filter paper (Fig.8.5A) for each of the enzymatic systems (free cellulases, enzymogels and grafted cellulases) the shape of plotted curves is similar at both tested concentrations. However, for the filter paper the behavior of three tested enzymatic systems (shape of the respective curve) is different. For the free cellulases the FDP values are almost constant, whereas for enzymogels and grafted cellulases the FDP values decrease with the increase of substrate concentration. Constant FDP for the free cellulase enzymes (soluble in reaction media) can be explained by the homogeneous distribution of free cellulases in reaction media. They can easily diffuse towards the substrate with constant diffusion rate providing continuous supply of the catalyst and constant fractal dimension. Lower FDPs for the grafted enzymes and enzymogels indicate increasing degree of inhomogeneity. The difference in behavior between free and immobilized cellulases can be explained by the increasing complexity of the hydrolytic reaction for the filter paper. The degrading filter paper fibers may result in time-dependent inhomogeneity of the reaction media.

The alternatively selected substrate is crystalline α-cellulose (dispersed cellulose). Unlike filter paper fibers, crystalline α-cellulose is dispersed in reaction media and keeps the reaction conditions homogeneous. Hence, in this case (Fig.8.5 B) all tested the enzymatic systems demonstrate similar behavior. The observed maximum for FDPs is close to 1 for all experiments and corresponds to the reaction conditions with almost no spatial constrains (nearly homogeneous system) due to the abundance of enzyme in the system and the availability of the substrate surface for the hydrolysis. This behavior is similar to the reported phenomena when lower FDP values before maximum correspond to cluttering by the excessing enzyme molecules and lower FDP values after maximum correspond to cluttering by the excessive substrate [21, 41-44].

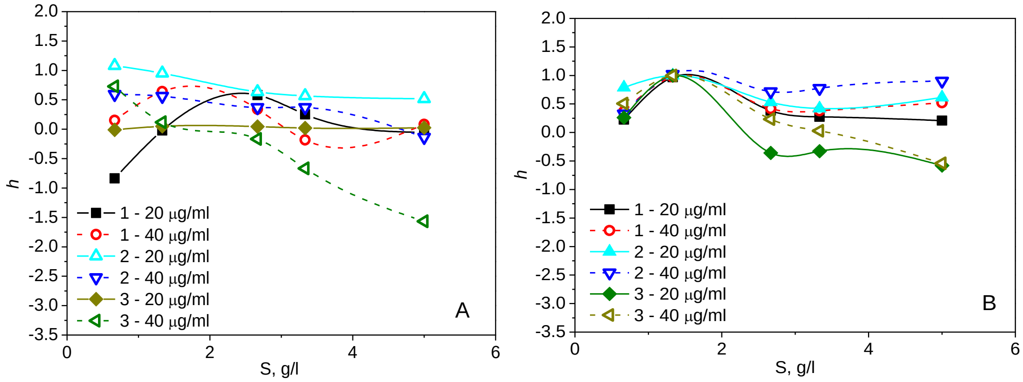

Fig.8.5. Fractal dimension parameter at different substrate concentrations. A – filter paper, B – dispersed cellulose. 1 – enzymogels, 2 – free cellulases, 3 – grafted cellulases. Standard deviations for the calculations do not exceed 5%.

To distinguish between the effect of the substrate and the enzymatic immobilization Michaelis-Menten formalism was applied taking into account the inhomogeneity of the system by using the concepts of the fractal media (fractal rate orders). Michaelis-Menten kinetic model in fractal media involves the power law formalism when the enzyme-catalyzed reaction is described by apparent (fractal) rate orders (eq. 8.5) [42-43, 51-52].

$$\frac{d(ES)}{dt} = \alpha_1 \times [E]^{g_e} \times [S]^{g_s} - (\alpha_2 + \beta_1)(ES) \quad (8.5)$$

where g_e and g_s – fractal rate order with respect to the enzyme and substrate; α_1, α_2 and β_1 – constants developed for the fractal kinetic model [42-43, 51-52], *(ES)* – concentration of enzyme-substrate complex; *[E]*, *[S]* – concentration of enzyme and substrate.

The kinetic fractal rate order (KFRO) g_e and g_s depends on the degree of dimensional restrictions in the reaction media [42-43]. The values of the KFRO can be used to estimate the spatial restrictions during the reaction (Scheme 8.2) and include the cases when reaction occurs either in the whole volume of the reactor (3D space) or is restricted to the 2D surface or even a single fiber (1D). The homogeneous monomolecular reactions are considered unaffected by the dimensional restrictions and occur in 3D reaction space. The KFROs for such reactions is

$g_e=g_s=1$. If at least one of the calculated orders g_e or g_s is exactly 2.46, the reaction can be considered taking place on a two-dimensional surface. If either g_e or g_s is exactly 3 reaction is taking place in one-dimensional channel. If either g_e or g_s is less than 1 or greater than 3 the reaction media is clustered or dispersed (non-ordered fractal or percolation clusters) [41-44].

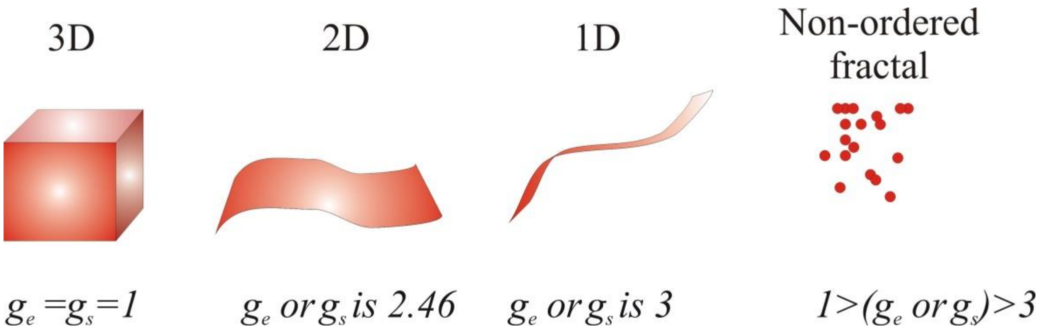

Scheme 8.2. Manifestation of fractal orders by the spatial restriction of the reaction [41-44].

The KFROs can be calculated from the Michaelis-Menten equation for the fractal media (eq. 8.5). From the equation (8.5) fractal Michaelis constant (K_f) can be defined as equation 8.6 [3]:

$$K_f = \left(\frac{\alpha_2 + \beta_1}{\alpha_1}\right)^{1/g_s} \left(\frac{V_{\max}}{\alpha_2}\right)^{(1-g_e)/g_s} \qquad (8.6)$$

From the eq. 8.5, the fractal rate law (eq. 8.5) can be expressed as [43]:

$$\left(\frac{S}{K_f}\right)^{g_s} = \left(\frac{v_o}{V_{\max}}\right)\left(1 - \frac{v_o}{V_{\max}}\right)^{g_e} \qquad (8.7)$$

where V_{max} is the maximal reaction velocity, v_o is the initial reaction velocity.

Kinetic data were plotted in log-log coordinate system (Fig.8.6) to calculate the kinetic parameters defining the rate law (Tables 8.1 and 8.2).

The plotted kinetic data for the extended reaction times resemble the behavior of the cellulases at initial hydrolysis stages (first 60 minutes) – i.e. reaction velocities for the grafted enzymes are significantly lower than for the enzymogels and for free enzymes.

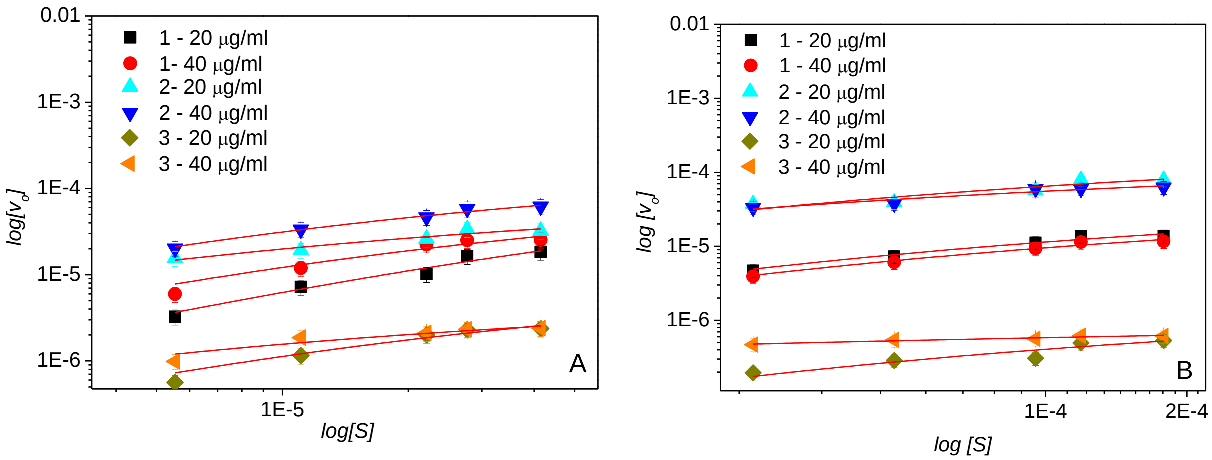

Fig.8.6. Experimental data fitted with the fractal mode (eq. 8.5) for the calculation of fractal kinetic parameters. A – filter paper substrate, B – dispersed cellulose substrate[2]; 1 – enzymogels, 2 – free cellulases, 3 – grafted cellulases.

The resulting K_f values can be used to calculate effective Michaelis constant, taking into account the fractal constrains during hydrolysis (Table 8.2) [43].

$$K_{m\,eff} = K_f \times 2^{(g_e-1)/g_e} \qquad (8.8)$$

Tables 8.1 and 8.2 represent the calculated fractal kinetic parameters for the tested cellulases. KFROs g_e and g_s can be used to estimate the contribution of specific enzymatic system and heterogeneous cellulose substrate to the overall inhomogeneity of the reaction mixture [43-44].

---

[2] Reaction rate was calculated using empirical rate expression $P(t) = \left(\frac{[S_0]}{k}\right)\ln\left(1 + \frac{v_0 kt}{[S_0]}\right)$, where *P(t)* is the product concentration at time *t; [S_o]* –substrate concentration, v_o – the initial rate and *k* is the rate retardation constant [9, 22]

Table 8.1. Kinetic fractal orders*.

Cellulase concentration, µg/ml	**KFRO**	**Enzymogels**		**Free cellulases**		**Grafted cellulases**	
		Filter paper	**Dispersed cellulose**	**Filter paper**	**Dispersed cellulose**	**Filter paper**	**Dispersed cellulose**
20	g_s	0.92	0.96	0.46	0.63	0.38	0.55
40	g_s	0.077	0.092	0.42	0.59	0.0013	0.0026
	g_e	*1.29*	*1.29*	*1.47*	*1.25*	*3.64*	*3.31*

*average standard deviation does not exceed 5% of respective fractal order value

The values of g_e for the enzymogels and free cellulases are similar and close to unity when compared to grafted cellulases. This indicates uniform enzyme distribution on the substrate during hydrolysis [41-44]. In case of enzymogels uniform distribution of enzymes can be solicitated by their mobility inside the polymer brushes. Higher g_e values (greater than 3) for grafted cellulases are typical for highly clustered or aggregated systems [41-43]. It can be explained by the restricted mobility of the cellulases grafted to the support and/or aggregation of silica carriers.

For the tested free and immobilized cellulases the values of g_s are independent on the nature of the substrate (filter paper or dispersed cellulose). The rapid decrease of g_s with the increasing of cellulase concentration for the enzymogels and grafted cellulases can be explained by the possible diffusion limitations of cellulases inside the enzymogels brushes and aggregation of the silica particles for the chemically grafted enzymes.

In fractal kinetic approach effective Michaelis constant (K m eff) is the measure of the affinity of enzymes towards the substrate, similar to the Michaelis constant in classical mass-action approach [22, 23]. The calculated K m eff is concentration independent (Table 8.2) and can be used to estimate the net substrate affinity of the enzymatic systems. The lower K m eff values for the dispersed cellulose indicate higher affinity of the enzymatic system and can be attributed to its higher surface area when compared to the filter paper. Notably, the values of K m eff for the free cellulases and enzymogels for both substrates are close and significantly lower than that of grafted cellulases. This higher substrate affinity of enzymogels can be attributed to the above-mentioned behavior of the enzymogels on the substrate due to flexibility of PAA macromolecules of polymeric brushes and their ability to spread over the substrate surface (see Chapter 7). Such behavior increases the surface area of the contact between the enzymogel particles and the substrate. Mobile cellulase molecules in enzymogel can migrate within the layer of the increased contact between the particle and substrates, thus facilitating the hydrolysis. Since the cellulase molecules are mobile, the continuous supply of these enzymes may increase the overall efficiency of the hydrolysis in presence of the enzymogels.

Table 8.2. Fractal kinetic parameters.

Parameter	**Cellulase concentration, µg/ml**	**Enzymogels**		**Free cellulases**		**Grafted cellulases**	
		Filter paper	**Dispersed cellulose**	**Filter paper**	**Dispersed cellulose**	**Filterd paper**	**Dispersed cellulose**
$K_{m\ eff}, mM$*	20	0.68	1.8×10^{-4}	0.6	1.5×10^{-4}	5.83	75×10^{-4}
	40	0.42	0.98×10^{-4}	0.81	7.0×10^{-4}	5.84	19×10^{-4}
$V_{m\ eff}\times10^{-6}$, $mol\times l^{-1}\times s^{-1}$**	20	25.2	9.27	2.1	0.77	4.49	0.51
	40	38.05	8.46	73.98	10.87	14.33	1.46

*****average standard deviation does not exceed 6%.
******average standard deviation does not exceed 5%.

Similar to the K m eff, Vm eff (i.e. effective maximal velocity) takes into account the fractal-like reaction media and can be used to evaluate the reaction velocity. The calculated Vm eff values for the enzymogels and free enzymes in same conditions (substrate type and enzyme concentration) are significantly higher than for the grafted enzymes. It supports the assumption about the significance of the enzyme mobility for the efficiency of the immobilized enzymatic system. Apparently, in the enzymogels, the cellulases can diffuse towards the substrate just as effectively as the free cellulases. At the concentration 20 μg/ml the Vm eff of enzymogels is higher than even Vm eff of the free enzymes. It can be explained by fact that the immobilization of the enzymes on the enzymogel polymer brushes may create local concentration maxima.

The calculated fractal kinetic parameters – KFRO, $K_{m\ eff}$ and $V_{m\ eff}$ indicate higher substrate affinity and continuous availability of cellulase molecules during the cellulose hydrolysis in presence of the enzymogels.

8. 5. Conclusions

The hydrolytic performance of enzymogels as novel biocatalytic colloids for the immobilization of cellulase enzymes was compared to performance of free enzymes and enzymes chemically grafted to dispersed carrier particles. Kinetic studies were used to investigate role of mobility of the immobilized enzymes for their hydrolytic activity. The hydrolysis of cellulose substrate was studied using complementary classical and fractal kinetic models based on Michaelis-Menten equations. In contrast to grafted enzymes, the kinetic parameters (fractal rate orders and Michaelis constant) of enzymogels are close to the parameters of free enzymes, indicating higher availability of enzymes immobilized in enzymogels and their higher substrate affinity. As a result the efficiency of enzymogels during hydrolysis is close to the efficiency of free enzymes. It can be explained by the ability of enzymogels to facilitate homogeneous distribution of enzymes and their continuous supply towards the cellulose substrate due to the enzymes mobility inside the polymer brushes of the enzymogel particle.

8.6. References

[1]. Galbe, M.; Zacchi, G. A review of the production of ethanol from softwood. *Applied Microbiology and Biotechnology* **2002**, *59*, 618–628.

[2]. Lynd, L.R.; Laser, M.S.; Bransby, D.; Dale, B.E.; Davison, B.; Hamilton, R.; Himmel, M.; Keller, M.; McMillan, J. D.; Sheehan, J.; Wyman, C. E. How biotech can transform biofuels. *Nature Biotechnology* **2008**, *26*, 169–172.

[3]. Sun, Y.; Cheng, J. Hydrolysis of lignocellulosic materials for ethanol production: a review. *Bioresource Technology* **2002**, *83*, 1-11.

[4]. Himmel, M.E.; Ding, S.Y.; Johnson, D.K.; Adney, W.S.; Nimlos, M.R.; Brady, J.W.; Foust, T.D. Biomass recalcitrance: engineering plants and enzymes for biofuels production. *Science* **2007**, *315*, 804–807.

[5]. Datta, S.; Christena, L. R.; Rajaram, S.Y. R. Enzyme immobilization: an overview on techniques and support materials. *3Biotech* **2013**, *3*(1), 1–9

[6]. Adhami, A.J.H.; Bryjak, J.; Greb-Markiewicz, B.; Peczynska-Czoch, W. Immobilization of wood-rotting fungi laccases on modified cellulose and acrylic carriers. *Process Biochemistry* **2002**, *37*, 1387–1394.

[7]. Rosa, C.C.; Cruz, H.J.; Vidal, M.; Oliva, A.G. Optical biosensor based on nitrite reductase immobilised in controlled pore glass. *Biosensors and Bioelectronics* **2002**, *17*, 45–52.

[8]. Wu, S.C.; Lia, Y.K. Application of bacterial cellulose pellets in enzyme immobilization. *Journal of Molecular Catalysis B: Enzymatic* **2008**, *54*, 103–108.

[9]. Cordeiro, A.L.; Lenk, T.; Werner, C. Immobilization of Bacillus licheniformis α-amylase onto reactive polymer films. *Journal of Biotechnology* **2011**, *154*, 216–221.

[10]. Lee, D.H.; Park, C.H.; Yeo, J.M.; Kim, S.W. Lipase immobilization on silica gel using a cross-linking method. *Journal of Industrial and Engineering Chemistry* **2006**, *12*, 777–782.

[11]. Katwa, L.C.; Ramakrishna, M.; Rao, M.R.R. Spectrophotometric assay of immobilized tannase. *Journal of Biosciences* **1981**, *3*, 135–142.

[12]. Wang, H.Y.; Hettwer, D.J. Cell immobilization in κ-carrageenan with tricalcium phosphate. *Biotechnology and Bioengineering* **1982**, *14*, 1827–1838.

[13]. Tümtürk, H.; Karaca, N.; Demirel, G.; Şahin, F. Preparation and application of poly(N, N-dimethylacrylamide-co-acrylamide) and poly(N-isopropylacrylamide-co-acrylamide)/κ-Carrageenan hydrogels for immobilization of lipase. *International Journal of Biological Macromolecules* **2007**, *40*, 281–285

[14]. Rochefort, D.; Kouisni, L.; Gendron, K. Physical immobilization of laccase on an electrode by means of poly(ethyleneimine) microcapsules. *Journal of Electroanalytical Chemistry* **2008**, *617*, 53–63.

[15]. Jegannathan, K.R.; Jun-Yee, L.; Chan, E.S.; Ravindra, P. Production of biodiesel from palm oil using liquid core lipase encapsulated in κ-carrageenan. *Fuel* **2010**, *89*, 2272–2277.

[16]. Klein, M.P.; Scheeren, C.W.; Lorenzoni, A.S.G.; Dupont, J.; Frazzon, H. P.F. Ionic liquid-cellulose film for enzyme immobilization. *Process Biochemistry* **2011**, *46*, 1375–1379

[17]. Spahn, C.; Minteer, S.D. Enzyme immobilization in biotechnology. *Recent Patents on Engineering* **2008**, *2*, 195–200

[18]. D’Souza, S.F. Immobilized enzymes in bioprocess. *Current Science* **1998**, *77*, 69–79

[19]. Michaelis, L.; Menten, M.L. Die kinetik der invertinwirkung. *Biochemische Zeitschrift* **1913**, *49*, 333–69.

[20]. Laidler, K.J. Theory of the transient phase in kinetics, with special reference to enzyme systems. *Canadian Journal of Chemistry* **1955**, *33*, 1614–1624.

[21]. Bezerra, F.; Dias, A. A. Discrimination Among Eight Modified Michaelis-Menten Kinetics Models of Cellulose Hydrolysis With a Large Range of Substrate/Enzyme Ratios, Inhibition by Cellobiose. *Applied Biochemistry and Biotechnology* **2004**, *112*, 173-184.

[22]. Gan, Q.; Allen, S.J.; Taylor, G. Kinetic dynamics in heterogeneous enzymatic hydrolysis of cellulose: an overview, an experimental study and mathematical modeling. *Process Biochemistry* **2003**, *38*, 1003-1018

[23]. Bansal, P.; Hall, M.; Realff, M.J.; Lee, J.H. Modeling cellulase kinetics on lignocellulosic substrates. *Biotechnology Advances* **2009**, *27*, 833–848

[24]. Hodge, D.B.; Karim, M.N.; Schell, D.J.; McMillan, J.D. Model-based fed-batch for high-solids enzymatic cellulose hydrolysis. *Applied Biochemistry and Biotechnology* **2009**, *152*, 88-107.

[25]. Hong, J.; Ye, X.; Zhang, Y.H.P. Quantitative determination of cellulose accessibility to cellulase based on adsorption of a non-hydrolytic fusion protein containing CBM and GFP with its applications. *Langmuir* **2007**, *23*, 12535–12540.

[26]. Caminal, G.; Lopez-Santin, J.; Sola, C. Kinetic modeling of the enzymatic hydrolysis of pretreated cellulose. *Biotechnology and Bioengineering* **1985**, *27*, 1282–1290.

[27]. Drissen, R.E.T.; Maas, R.H.W.; Maare, M.J.E.; Kabel, M.A.; Schols, H.A. Tramper, J.; Beeftink, H. H. A generic model for glucose production from various cellulose sources by a commercial cellulasecomplex. *Biocatalysis and Biotransformation* **2007**, *25*, 419–429.

[28]. Donggyun, S.;Yoo. A.; Kim, S.W.; Yang, D.R. Cybernetic modeling of simultaneous saccharification and fermentation for ethanol production from steam-exploded wood with Brettanomyces custersii. *Journal of Microbiology and Biotechnology* **2006**, *16*, 1355–1361.

[29]. Chakraborty, S. A.; Gaikwad, A. Mixing effects in cellulase-mediated hydrolysis of cellulose for bioethanol production. *Industrial & Engineering Chemistry Research* **2010**, *49* (21), 10818–10825

[30]. Fenske, J.J.; Penner, M.H.; Bolt, J.P. A simple individual-based model of insoluble polysaccharide hydrolysis: the potential for auto synergism with dual-activity glycosidases. *Journal of Theoretical Biology* **1999**, *199*, 113–118.

[31]. Mansfield, S.D.; Meder, R. Cellulose hydrolysis — the role of monocomponent cellulases in crystalline cellulose degradation. *Cellulose* **2003**, *10*, 159–169.

[32]. Väljamäe, P.; Sild, V.; Pettersson, G.; Johansson, G. The initial kinetics of hydrolysis by cellobiohydrolases I and II is consistent with a cellulose surface — erosion model. *European Journal of Biochemistry* **1998**, *253*, 469–475.

[33]. Yang, B.; Willies, D.M.; Wyman, C.E. Changes in the enzymatic hydrolysis rate of avicel cellulose with conversion. *Biotechnology and Bioengineering* **2006**, *94*, 1122–1128.

[34]. Chang, V.S.; Holtzapple, M.T. Fundamental factors affecting biomass enzymatic reactivity. *Applied Biochemistry and Biotechnology* **2000**, *84–86*, 5-37.

[35]. Kim, S.; Holtzapple, M.T. Effect of structural features on enzyme digestibility of corn stover. *Bioresource Technology* **2006**, *97*, 583–591.

[36]. Ohmine, K.; Ooshima, H.; Harano, Y. Kinetic study on enzymatic hydrolysis of cellulose by cellulase from Trichoderma Viride. *Biotechnology and Bioengineering* **1983**, *25*, 2041–2053.

[37]. O'Dwyer, J.P.; Zhu, L.; Granda, C.B.; Chang, V.S.; Holtzapple, M.T. Neural network prediction of biomass digestibility based on structural features. *Biotechnology Progress* **2008**, *24*, 283–292.

[38]. Movagarnejad, K.; Sohrabi, M.; Kaghazchi, T.; Vahabzadeh, F. A model for the rate of enzymatic hydrolysis of cellulose in heterogeneous solid–liquid systems. *Biochemical Engineering Journal* **2000**, *4*, 197–206.

[39]. Kadam, K.L.; Rydholm, E.C.; McMillan, J.D. Development and validation of a kinetic model for enzymatic saccharification of lignocellulosic biomass. *Biotechnology Progress* **2004**, *20*, 698–705.

[40]. Fogler, H.S. *Elements of Chemical Reaction Engineering*. Prentice Hall, **2005**.

[41]. Kopelman, R. Rate processes on fractals, theory, simulations and experiments. *Journal of Statistical Physics* **1986**, *42*, 185–200.

[42]. Kopelman, R. Fractal reaction kinetics. *Science* **1988**, *241*, 1620–1626.

[43]. Savageau, M.A. Michaelis–Menten mechanism reconsidered, implications of fractal kinetics. *Journal of Theoretical Biology* **1995**, *176*, 115–124.

[44]. Savageau, M. A. Development of fractal kinetic theory for enzyme-catalysed reactions and implications for the design of biochemical pathways. *Biosystems* **1998**, *47*, 1–2, 9–36

[45]. Xu, F.; Ding, H. A new kinetic model for heterogeneous (or spatially confined) enzymatic catalysis: contributions from the fractal and jamming (overcrowding) effects. *Applied Catalysis A: General* **2007**, *317*, 70–81.

[46]. Bradford, M. M. A rapid and sensitive method for the quantitation of microgram quantities of protein utilizing the principle of protein-dye binding. *Analytical Biochemistry* **1976,** *72*, 248–254

[47]. Gan, Q.; Allen, S.J.; Taylor, G. Kinetic dynamics in heterogeneous enzymatic hydrolysis of cellulose: an overview, an experimental study and mathematical modeling. *Process Biochemistry* **2003**, *38*, 1003-1018

[48]. Huang AA. Kinetic studies on insoluble cellulose-cellulase system. *Biotechnology and Bioengineering* **1975**, *17*, 1421-1433.

[50]. Peitersen, N.; Ross, E.W. Mathematical model for enzymatic hydrolysis and fermentation of cellulose by Trichoderma. *Biotechnology and Bioengineering* **1979**, *21*, 997-1017.

[51]. Gusakov, A. V.; Sinitsyn, A. P. Kinetics of the enzymatic hydrolysis of cellulose, A mathematical model fora batch reactor process. *Enzyme and Microbial Technology* **1985**, *7*, 346-352

[52]. Berry, H. Monte Carlo simulations of enzyme reactions in two dimensions, fractal kinetics and spatial segregation. *Biophysical Journal* **2002**, *83*, 1891–901.

CHAPTER 9. CONCLUSIONS AND FUTURE WORK

9.1. Conclusions

The goal of the current work is to develop and characterize several groups of RPBC with different morphological complexity and explore their potential in drug delivery and bioconversion. The role of RPBC morphology for these specific applications is discussed in details. Three groups of RPBC were fabricated: i. polymeric micelles; ii. mixed polymeric micelles; iii. hybrid polymer-inorganic particles. All fabricated RPBCs contain polymeric component in their structure. The dissertation investigates how the changes of the responsive polymeric component are reflected in morphological properties of RPBC.

The first group of RPBC, polymeric micelles, were formed by the self-assembly of amphiphilic invertible polymers (AIPs) developed in our group. AIPs self-assemble into invertible micellar assemblies (IMAs) in solvents of different polarity. Hydrophilic−lipophilic balance of the AIP macromolecules affects their surface activity and the ability to self-assemble into IMAs. IMAs are able to rapidly change their conformation and structure in response to changes in solvent polarity. SANS measurements were used to obtain detailed quantitative parameters of the IMAs morphologies in solvents of different polarity (Chapter 3). The model-dependent fitting of SANS data have shown that IMAs have cylindrical core-shell morphology both in polar and non-polar media. The size and detailed composition of the IMAs was determined in aqueous and toluene solutions. It has been confirmed that the hydrophobic effect (or solvophobic interactions) is the major driving force for the AIP self-assembly in water. The longer -$(CH_2)_{10}$- sequences of dodecanedioic acid undergo stronger interactions compared to shorter -$(CH_2)_8$- fragments of sebacic acid, resulting in closer packing in the core and the formation of smaller assemblies. Furthermore, the SANS data demonstrated the ability of IMAs to invert their structure in response to the change of solvent polarity. PEG and aliphatic dicarboxylic acid fragments of AIP macromolecules tend to replace each other in the core and shell of the IMAs. In toluene solutions, the PEG species move from the shell to the interior (core) of the assemblies, whereas hydrophobic aliphatic dicarboxylic acid moieties tend to relocate from the core to the exterior (shell) of the assemblies. In aqueous solution at 15°C, the IMA mixed core is composed from aliphatic dicarboxylic acid, PEG moieties, and the PEG-based shell. When the temperature increases, the IMAs composition changes, the hydration level (water content) in the micellar core significantly decreases as a result of the progressive loss of water by the macromolecules, followed by dehydrated PEG fragments in the shell entering the interior of the assemblies when the temperature increases from 15°C to 25°C and then to 35°C.

^{1}H NMR spectroscopy and SANS techniques were used to investigate the morphology of IMAs after the solubilization of hydrophobic (poorly water-soluble) cargo depending on the chemical structure of the solubilized molecules (Chapter 4). The IMAs were shown to incorporate cargo molecules in a different manner either in core or in the shell of micellar structures. Such selective incorporation can potentially be promising for the fabrication of multifunctional therapeutic formulations, where two different active therapeutic agents are delivered at the same time. Loaded with natural drug curcumin IMAs were tested in vitro as drug carriers on human and mice osteosarcoma cell lines. Curcumin-loaded IMAs were found to be cytotoxic against multiple osteosarcoma (bone cancer) cell lines whereas normal bone cells remain viable in presence of micellar curcumin.

Mixed polymeric micelles represent another, more complex, RPBC morphology (Chapters 5 and 6). They were fabricated from AIPs and amphiphilic oligomers synthesized in this work from pyromellitic dianhydride, polyethylene glycol methyl ethers, and alkanols/cholesterol. The higher solubilization capacity of the oligomeric assemblies and their biodegradability, as well as small size and narrow size distribution of their assemblies makes the oligomers good candidates for biomedical applications, including drug delivery. In this work, the ‘proof of concept’ study has shown that the fabrication of mixed micelles from selected AIP macromolecules and amphiphilic oligomers containing cholesterol notably increases curcumin-loading capacity when compared to single-component IMAs (from 10% w/w to 26% w/w per polymer unit).

Hybrid polymer-inorganic particles (enzymogels) represent RPBC group with another, even more complex morphology, designed in this work for bioconversion (cellulose hydrolysis) (Chapter 7). The enzymogel particles are made of silica-coated magnetic core surrounded by responsive polyacrylic acid (PAA) brushes grafted to the surface of silica. The PAA brushes are loaded with cellulase enzymes immobilized using physical interactions between proteins and PAA macromolecules. The enzymogels catalyze the hydrolysis of cellulose and can be magnetically recovered from the reaction mixture at the end of each hydrolytic cycle. As a result of this work, the enzymogels introduced novel phase boundary catalysis mechanism. The immobilized enzyme macromolecules retain theirs mobility in a polymer brush and are capable of hydrolyzing insoluble cellulose into fermentable sugars using this highly dynamic behavior as well as high affinity to both polymer brushes and to the substrate The study demonstrated that such RPBCs can be used multiple times during hydrolysis and provide an about four-fold increase in glucose production per unit of the enzyme in comparison to free enzymes.

To investigate the role of immobilized enzymes mobility for their hydrolytic activity, kinetic studies were conducted (Chapter 8). For this purpose, the hydrolytic performance of enzymogels was compared to the performance of free enzymes and enzymes chemically grafted to dispersed carrier particles (silica particles). The hydrolysis was studied using complementary classical and fractal kinetic models based on Michaelis-Menten equations. In contrast to grafted enzymes, the kinetic parameters (fractal rate orders and Michaelis constant) of enzymogels are closer to the parameters of free enzymes, indicating higher availability of enzymes immobilized in enzymogels and their higher cellulose substrate affinity. As a result, the efficiency of enzymogels during hydrolysis is closer to the efficiency of free enzymes.

In summary, the increase in morphological complexity for RPBC can be considered as a tool in regulating the interaction between the responsive polymeric component of RPBC and cargo molecules (for example, hydrophobic drugs or enzymes). The results of this study can be used to fabricate and/or optimize the RPBC structures with an appropriate morphology and properties for the specific applications in drug delivery and bioconversion.

9.2. Future Work

9.2.1. Mathematical Modeling of Interaction between AIP with Different Composition and Solvents during Self-Assembly

The main goal of the studies would be to use a mathematical modeling approach to determine the driving forces (inter- and intramolecular interactions) of IMA self-assembly and inversion (when the solvent polarity is changed). To investigate the formation and invertibility of IMAs a linear-free energy relationship (LFER) approach can be employed. The LFER approach is based on the application of linear-free energy relationship regression analysis on the set of viscometry data. Viscosity of polymeric solutions can be used to probe the molecular properties: molecular size, shape, inter- and intramolecular interactions. Since the viscosity is an internal thermodynamical property of a solution that relates to the forces resisting to flow, linear free energy relationship (LFER) can be extended to the set of viscosity data. LFER approach is based on deriving the linear correlation between colloidal property (viscosity) and its characteristics (descriptors) to correlate and foresee various inter- and intramolecular interactions, as well as AIP-solvent interactions. The values of correlation coefficients in LFER model can give the quantitative description of the tested inter- and intramolecular interactions. The LFER approach can be used to propose the model describing interactions between macromolecules in solution during the formation of polymeric micelles and the interactions between the micelles and the solvent. By comparing the calculated LFER regression coefficients for the tested AIP and concentration range, modeling can reveal the dominating role of specific intermolecular or intermolecular interactions in the formation and behavior of AIP micellar structures in solvents with different polarity.

9.2.2. Exploration of the Biological Pathway of Selective Cytotoxicity of Curcumin-Loaded IMAs

In vitro studies of curcumin-loaded IMAs (Chapter 4) revealed their cytotoxicity towards multiple bone cancer cell lines. The goal of further studies would be to establish the biological pathway of cytotoxicity (curcumin digestion in cells) to explore the potential of curcumin-loaded IMAs for cancer therapy. According to the previous research described in this work, a number of pathways was detected for the digestion of curcumin in cancer cells. However, the presence of IMAs used as carrier for curcumin, can change the course of these pathways. Hence, a detailed investigation is required to establish the mechanism of cancer treatment by micellar curcumin. The investigation would include assays for specific biochemical pathway that might be affected my micellar curcumin: Wnt pathway, effect on kinase enzymes, transcription and growth factors.

The knowledge of specific pathways of the cancer treatment by curcumin-loaded IMAs can be used to predict the fundamental effect of micellar curcumin on a whole human organism. Such fundamental knowledge can justify the feasibility of using micellar curcumin in clinical cancer therapy.

9.2.3. Detailed Structural Investigation of Mixed Micelles from Amphiphilic Invertible Polymers and Novel Amphiphilic Oligomers

The experiments from Chapter 6 demonstrate successful fabrication of mixed micelles from selected AIP (PEG_{600}- $PTHF_{650}$) and synthesized in this work amphiphilic oligomers (PPC, CPPPC) with an increased curcumin-loading capacity. However, for the applications in drug delivery further detailed examination is needed. That is why, it is suggested to conduct SANS measurements as well as ^{1}H NMR and 2D NOESY experiments in order to investigate the morphology and composition of mixed micelles after loading with a drug. In addition, colloidal characterization (surface tension, stability testing) can give more insights about the behavior of mixed micelles in solutions. Finally, *in vitro* testing of curcumin-loaded mixed polymeric micelles can provide the information on their therapeutic effect as drug carriers.

9.2.4. Immobilization of Mixture of Cellulolytic Enzymes into the Enzymogel Particles

In this work (Chapters 7 and 8) enzymogels were used for the immobilization of one type of cellulolytic enzymes – endocellulases. However, in nature the complete hydrolysis of cellulose is carried out by the mixture of several types of cellulolytic enzymes (cellulases). Often, cellulolytic enzymes in mixtures are combined in multi-enzyme complexes called cellulosomes. In these multienzyme complexes enzymes act synergistically increasing the efficiency of the hydrolytic process. By immobilizing several types of cellulolytic enzymes on each enzymogel particle we would mimic natural cellulosome in the diverse enzyme localization of different immobilized cellulases inside the carriers and the synergy of their hydrolytic action. It is expected to enhance the hydrolytic efficiency. In the same time, unlike natural cellulosomes, artificial cellulosomes can be magnetically recovered from the reaction mixture and reused in several hydrolytic cycles.

The goal of the future enzymogels studies would be to create and characterize artificial cellulosomes by immobilizing different cellulolytic enzymes on the each enzymogel particle in order to ensure the synergistic action of immobilized enzymes.

The studies would include the structural characterization of artificial cellulosomes as well as testing of their enzymatic performance using biocatalytic assays.